

DISSERTATION

Hole Trapping and the Negative Bias Temperature Instability

ausgeführt zum Zwecke der Erlangung des akademischen Grades
eines Doktors der technischen Wissenschaften

eingereicht an der Technischen Universität Wien
Fakultät für Elektrotechnik und Informationstechnik
von

WOLFGANG GÖS



Wien, im Dezember 2011

Kurzfassung

Mit der Miniaturisierung der MOS-Transistoren ist ein neues Phänomen zum Vorschein gekommen, welches als *Negative Bias Temperature Instability* (NBTI) bezeichnet wird und sich zu einem ernsthaften Zuverlässigkeits- bzw. Lebensdauerproblem entwickelt hat. Der komplexe Mechanismus hinter NBTI ist derzeit noch nicht vollständig geklärt. Es konnte jedoch Einigkeit darüber erzielt werden, dass Ladungsträger im Substrat von Oxiddefekten eingefangen werden und dort bis zum Ende der Stressperiode verbleiben. Dieser Vorgang ist mit einer Verschiebung der Schwellspannung verbunden, welche die Bauteilcharakteristiken beeinflusst und die Lebensdauer der Bauteile empfindlich verkürzt. Es wird vermutet, dass diese Ladungsträger während der Relaxationsphase wieder von den Oxiddefekten emittiert werden und daher die Schwellspannung wieder zu ihrem ursprünglichen Wert zurückkehrt. Die Einfang- und Emissionsprozesse während der Stress- sowie der Relaxationsphase werden als Charge-Trapping bezeichnet und rücken ins Zentrum der Untersuchungen dieser Arbeit.

Charge-Trapping basiert auf einem Transfer der Ladungsträger zwischen dem Kanal und den Defekten. Zahlreiche, in der Literatur vorgestellte Modelle beschreiben diesen Ladungstransfer auf unterschiedlichem theoretischen Niveau. Diese Modelle werden im Zuge dieser Arbeit hinsichtlich der NBTI nochmals überprüft und in einem bestehenden Bauteilsimulator zum Vergleich mit Experimenten eingebaut. Diese Evaluierung basiert auf einer Liste von Kriterien, welche die besonderen Merkmale des Bauteilverhaltens für zum Beispiel unterschiedliche Einsatztemperaturen, Gatespannungen oder Stresszeiten beinhalten.

Im einfachsten Modell basiert der Ladungstransfer auf elastischem Tunneln von Elektronen, welche ihre Energie während des Übergangs beibehalten. Diese Art von Ladungstransfer bildet die Basis des Elastic-Tunneling-Modells dar, welches als erste Möglichkeit für ein NBTI-Modell untersucht wird. Ein spezielles Augenmerk wurde dabei auf das Temperaturverhalten des Modells gelegt, was eine genauere Untersuchung der Quantisierungseffekte im Kanal eines MOS-Transistors erfordert. In den neuesten Bauteiltechnologien wurde die Oxiddicke auf ein paar wenige Nanometer reduziert, sodass frühere Untersuchungen um den Einfluss des Tunnelns vom und zum Gatekontakt erweitert werden müssen.

Ausgeklügeltere Konzepte berücksichtigen die Tatsache, dass die atomistische Defektkonfiguration eine entscheidende Rolle während eines Ladungstransfers spielt. Nachdem ein Defekt einen Ladungsträger vom Substrat eingefangen hat, unterzieht er sich einer Strukturrelaxation, welche eine Stärkung, eine Schwächung oder sogar einen Bruch von Atombindungen verursachen kann.

Interessanterweise hat diese Relaxation auch eine Verschiebung des Traplevels zur Folge — eine Tatsache, die bisher unberücksichtigt geblieben ist. Mit Hilfe von First-Principles-Simulations kann gezeigt werden, dass einige Defekte eine solche Traplevelverschiebung aufweisen, deren Effekt auf die Trappingdynamik detailliert untersucht werden muss. Weiters, wird auch ein neues Modell entwickelt, welches diese Traplevelverschiebung berücksichtigt und basierend auf den zuvor genannten experimentellen Kriterien evaluiert wird.

Die realistischste Beschreibung des Ladungstransfers ist die Non-radiative-Multiphonon-Theory —ursprünglich für die Lichtabsorption von Molekülen entwickelt und später für den Ladungsträgereinfang und der Ladungsträgeremission in Festkörpern verallgemeinert. Diese Art von Prozessen setzt eine Aktivierung über eine thermische Barriere voraus und führt daher zu einer Temperaturabhängigkeit, die im Fall von elastischem Tunneln nicht vorhanden ist. In dieser Arbeit wird eine vereinfachte Variante dieses Prozesses für das Two-Stage-Model verwendet. In diesem wird Charge-Trapping mit einer Wasserstoffreaktion als gekoppelt angenommen. Auch wenn dieses erweiterte Modell erfolgreich die Verschiebung der Schwellspannung bei NBTI-Experimenten in Simulationen reproduzieren kann, spiegelt es gemäß der Time-Dependent-Defect-Spektroscopy (TDDS) nicht korrekt die mikroskopischen Prozesse wider. In einer erweiterten Variante des Two-Stage-Models wurde diese Schwäche durch ein Verfeinern der Beschreibung des Ladungstransfers und durch die Berücksichtigung von metastabilen Zuständen in diesem Modell behoben. Mit diesen Modifikationen liefert das verbesserte Two-Stage-Model eine Erklärung für die Rauschphänomene, welche in Random-Telegraph-Noise- und TDDS-Messungen beobachtet wurden.

Zusammenfassend lässt sich sagen, dass Charge-Trapping in NBTI für verschiedene Erklärungen des Ladungstransfers untersucht wurde. Es wird gezeigt, dass die verbesserte Variante des Two-Stage-Models konsistent mit einer Reihe von der in NBTI- und Rauschmessungen beobachteten Merkmalen ist. Aus diesem Grund wird dieses Modell als die beste Beschreibung von Charge-Trapping aus der heutigen Sicht angesehen.

Abstract

With the continuing miniaturization of MOS transistors, a phenomenon called the negative bias temperature instability (NBTI) has evolved into a serious reliability concern. In the newest device technologies, its detrimental impact complicates reliable lifetime projection of the devices. Even though this fact has aroused large industrial and scientific interest, the complex mechanism behind NBTI has only been partially clarified so far. At least it has been agreed that substrate charge carriers are captured in oxide or interface defects and remain there until the end of the stress period. This is associated with a threshold voltage shift, which affects the device characteristics and considerably shortens the device lifetime. During relaxation, the same charge carriers are suspected to be emitted from the oxide defects so that the threshold voltage returns towards its initial value. The capture and emission of charge carriers during stress and relaxation are known under the name charge trapping and will be the focus of this thesis.

Charge trapping involves a transfer of charge carriers between the channel and defects. Several different models from literature describe this charge transfer at various levels of sophistication. They are re-examined in the light of NBTI and incorporated into an existing device simulator for comparison to measurements. This evaluation is based on a list of criteria, which include particular features of the device behavior under different operation temperatures, gate biases, and stress times.

In the simplest model, the charge transfer is based on elastic tunneling, which involves an electron whose energy must be preserved during a transition. This kind of a charge transfer reaction is the basis for the elastic tunneling model, studied as the first candidate for NBTI. A special focus is put on the temperature behavior of this model, requiring an investigation of the quantization effect within the channel of a MOS transistor. Furthermore, the oxide thicknesses have been downsized to a few nanometers in modern MOS technologies so that previous investigations must be extended to account for elastic tunneling to and from the gate contact.

A more sophisticated concept also accounts for the fact that the defect configuration plays a crucial role in the charge transfer process. After a defect has captured a charge carrier from the substrate, it undergoes structural relaxation, including strengthening, weakening, or even breaking of bonds. Most importantly, this relaxation results in a shift of the trap level — a fact that has remained unconsidered so far. Using first principles simulations, it is proven that several defects have a large level shift whose effect on the trapping dynamics needs to be studied in more detail. A new model is developed, which accounts for the level shift and is evaluated based on the list of experimental criteria mentioned before.

The most realistic description of the charge transfer is given by nonradiative multiphonon (NMP) theory, which has initially been developed for light absorption of molecules and later generalized to charge capture and emission in solids. This kind of process involves an activation over a thermal barrier and thus leads to a temperature dependence, which is missing in the case of the elastic tunneling model for instance. In this thesis, a simplified variant of this process is used for the so-called two-stage model, in which charge trapping is coupled to a hydrogen reaction. Even though this model can successfully reproduce the threshold voltage shift observed in NBTI experiments, it does not reflect the correct microscopic processes as shown by time-dependent defect spectroscopy (TDDS). In an extended variant of the two-stage model, this deficiency has been overcome by refining the description of the charge transfer process and incorporating a metastable state in this model. With these modifications, the improved two-stage model can also give an explanation of the noise phenomena observed in random telegraph noise and TDDS measurements.

In conclusion, hole trapping in NBTI is investigated using different explanations for the charge transfer. It is demonstrated that the refined variant of the two-stage model is consistent with the plenty of experimental features seen in NBTI and noise measurements. For this reason, this model is expected to be the best description of hole trapping from the present perspective.

Acknowledgements

This thesis would not have attained such a scientific level without the generous assistance of a large number of people. Thus, I feel indebted to those who have assisted me and I would like to thank them for their support during the last years.

First and foremost I want to express my deep gratitude to my adviser *Prof. Grassner* for providing me the opportunity to join his research group. Furthermore, he was always eager to create a stimulating atmosphere and never missed an opportunity to offer a few encouraging words. Furthermore, it has been a pleasure to see how a small scientific group, that started from scratch, has achieved considerable progress in its field, and gained international importance over the years.

I want to thank *Prof. Selberherr* and *Prof. Langer* for providing excellent working conditions, for the possibility to work at such a prestigious place, and for the opportunity to attend several international scientific conferences. Furthermore, I owe gratitude to *Prof. Süss*, who is willing to serve on my examination committee.

I am thankful to my numerous colleagues, named individually in the following. First, I want to thank *Franz Schanovsky*, who always took the time to discuss highly challenging and lengthy topics about theoretical physics and let me participate in his knowledge about first principles codes and numerical algorithms. Furthermore, I value *Paul Wagner's* elaborate comments on linguistic issues and enjoyed conversations with him about swimming techniques. I have to thank *Oliver Triebel* for his altruistic attitude in several situations. In particular, he assisted me with my operating system and happily joined in philosophical debates during lunch time. Furthermore, it was a pleasure to work with *Philipp Hehenberger* who frequently entered into debates about recent football games. Special thanks go to *Markus Karner*, who patiently introduced me to numerous versions of the Vienna-Schrödinger-Poisson solver. I acknowledge *Oskar Baumgartner* and *Zlatan Stanojevic* for their support during complicated implementations in the Vienna-Schrödinger-Poisson solver as well as for their help in preparing programming lectures. Furthermore, I am grateful to *Robert Entner*, *Martin Wagner*, *Markus Bina*, and *Johann Cervenka* for their sustained efforts in complicated computer affairs. I further thank *Victor Sverdlov*, who shared his comprehensive knowledge and valuable wisdom to help resolve some lengthy derivations. Last but not least, I want to name my long-lasting roommates *Martin Vasicek* and *Stanislav Tyaginov*, who never lost their sense of humor — even when imminent submission deadlines were looming.

I very much appreciate *Prof. Pantelides'* kind offer of a research visit at the Vanderbilt University in Nashville to gain knowledge about first-principles simulations in his group. Furthermore, I want to thank *Dr. Mittendorfer* for his patient introduction into density functional calculations at the center of computational material science.

Above all, I want to express my deep gratitude to my family, in particular to my parents, who gave me the possibility to attend a university. They continuously encouraged me during my education and my whole life — even supporting my crazy triathlon ambitions. I also want to thank my friends, especially *Johannes Csmarits*, who accompanied me during my student days and curiously followed my life as a researcher.

Acronyms

| | | |
|-----------------------------|-----|---|
| <i>a</i> – SiO ₂ | ... | Amorphous silicon dioxide |
| CDW | ... | Coupled double well |
| <i>c</i> – SiO ₂ | ... | Crystalline silicon dioxide |
| DFT | ... | Density functional theory |
| ESR | ... | Electron spin resonance |
| ETM | ... | Elastic tunneling model |
| H | ... | Hydrogen |
| HDL | ... | Harry-Diamond-Laboratories |
| LSM | ... | Level shift model |
| MPFAT | ... | Multiphonon field assisted tunneling |
| MOSFET | ... | Metal oxide semiconductor field effect transistor |
| MSM | ... | Measure-stress-measure |
| NBTI | ... | Negative bias temperature instability |
| NMP | ... | Nonradiative multi-phonon (process) |
| O | ... | Oxygen |
| OTF | ... | On-the-fly |
| RD | ... | Reaction diffusion |
| RDD | ... | Reaction dispersive diffusion |
| RTN | ... | Random telegraph noise |
| Si | ... | Silicon |
| SiO ₂ | ... | Silicon dioxide |
| SiON | ... | Silicon Oxynitride |
| SRH | ... | Shockley-Read-Hall |
| TDDS | ... | Time-dependent defect spectroscopy |
| TSM | ... | Two stage model |
| TWM | ... | Triple well model |
| WKB | ... | Wenzel-Kramers-Brillouin |

Physical Quantities

| Symbol | Unit | Description |
|-----------------|-----------------|---|
| a | 1 | Kinetic exponent in the RD model |
| A_{ab} | s^{-1} | Electronic matrix element in the Franck-Condon approximation |
| A_p | V | Prefactor of the permanent component in the NBTI fit formula |
| A_r | V | Prefactor of the recoverable component in the NBTI fit formula |
| A_{yz} | m^2 | Interface area in the yz-plane |
| B | 1 | Parameter in the empirical relation of the universal recovery |
| c_n | m^3s^{-1} | Electron capture coefficient |
| c_p | m^3s^{-1} | Hole capture coefficient |
| c_p^{NMP} | m^3s^{-1} | Hole capture coefficient in the NMP model |
| $c_{p,0}^{NMP}$ | m^3s^{-1} | Temperature independent prefactor of c_p^{NMP} |
| C_{ox} | $CV^{-1}m^{-2}$ | Areal gate capacitance |
| D_c | m^2s^{-1} | Diffusion coefficient in the RDD model |
| D_{c1D} | J^{-1} | Density of states of a one-dimensional, confined electron gas |
| D_{c3D} | $m^{-2}J^{-2}$ | Density of states of a three-dimensional, confined electron gas |
| D_{it} | $m^{-2}J^{-1}$ | Interface trap density of states |
| D_n | $m^{-3}J^{-1}$ | Electron density of states in the conduction band |
| $D_{n,1D}$ | $m^{-1}J^{-1}$ | Density of states of a one-dimensional electron gas |
| $D_{n,1D+2D}$ | $m^{-3}J^{-2}$ | Product of $D_{n,1D}$ and $D_{n,2D}$ |
| $D_{n,2D}$ | $m^{-2}J^{-1}$ | Density of states of a two-dimensional electron gas |
| D_{ox} | $m^{-2}J^{-1}$ | Oxide trap density of states |
| D_p | $m^{-3}J^{-1}$ | Hole density of state in the valence band |
| $D_{p,c3D}$ | $m^{-2}J^{-2}$ | Density of states of a three-dimensional, confined hole gas |
| $D_{p,1D}$ | $m^{-1}J^{-1}$ | Density of states of a one-dimensional hole gas |
| $D_{p,1D+2D}$ | $m^{-3}J^{-2}$ | Product of $D_{p,1D}$ and $D_{p,2D}$ |
| $D_{p,2D}$ | $m^{-2}J^{-1}$ | Density of states of a two-dimensional hole gas |
| D_X | m^2s^{-1} | Diffusion coefficient of the species X in the RD model |
| e_n | m^3s^{-1} | Electron emission coefficient |
| e_p | m^3s^{-1} | Hole emission coefficient |
| e_p^{NMP} | m^3s^{-1} | Hole emission coefficient in the NMP model |
| $e_{p,0}^{NMP}$ | m^3s^{-1} | Temperature independent prefactor of e_n^{NMP} |
| E | J | Electron energy in the band edge energy diagram |
| E_{act} | J | Activation energy |
| E_b | J | Electron energy in the conduction/valance band |
| E_c | J | Conduction band edge energy |
| E_c^{DFT} | J | Conduction band edge energy in DFT calculations |
| $E_{c,0}$ | J | Conduction band edge energy in the flat band case |
| E_d | J | Demarcation energy |

| Symbol | Unit | Description |
|----------------|----------------|---|
| E_{ds} | J | Dissociation barrier in the reaction-limited model |
| E_{dsm} | J | Mean value of the dissociation barriers in the reaction-limited model |
| E_f | J | Fermi energy |
| E_i | J | Energy of the electron system in the state i |
| $E_{n,i}$ | J | Energy of a channel electron in the quasi-bound state i |
| $E_{p,i}$ | J | Energy of a channel hole in the quasi-bound state i |
| E_{q_1/q_2} | J | Switching trap level for a transition from charge state q_1 to q_2 |
| E_t | J | Trap level |
| $E_{t,0}$ | J | Trap level in the flat band case |
| $E_{t,1}$ | J | Trap level of the oxygen vacancy in the TSM |
| $E_{t,2}$ | J | Trap level of the E' center in the TSM |
| E'_t | J | Trap level in the NMP model |
| $E_{tot,ij}$ | J | Energy of the combined system of electrons and nuclei in the state ij |
| E_v | J | Valence band edge energy |
| E_v^{DFT} | J | Valence band edge energy in DFT calculations |
| $E_{v,0}$ | J | Valence band edge energy in the flat band case |
| E_x | J | x -component of electron energy E |
| E_{xc} | J | Exchange-correlation energy |
| f_{ab}^{LSF} | 1 | Lineshape function |
| $f_{aab\beta}$ | 1 | Franck-Condon factor |
| $f_{eq,i,n}$ | 1 | Equilibrium occupancy for the trap n |
| f_i | 1 | Occupancy of a trap in state i |
| $f_{i,n}$ | 1 | Occupancy for the trap n in state i |
| f_{it} | 1 | Interface trap occupancy |
| f_n | 1 | Electron occupancy |
| f_{ox} | 1 | Oxide trap occupancy |
| f_p | 1 | Hole occupancy |
| f_t | 1 | Trap occupancy |
| f_t^{eq} | 1 | Equilibrium trap occupancy |
| $f_{t,2}$ | 1 | Electron occupancy of the E' center in the TSM |
| f_{FD} | 1 | Fermi-Dirac distribution |
| F_{ox} | Vm^{-1} | Oxide field |
| F_c | Vm^{-1} | Reference field for the MPFAT mechanism |
| $F_{ox,r}$ | Vm^{-1} | Oxide field during relaxation |
| $F_{ox,s}$ | Vm^{-1} | Oxide field during stress |
| \mathbf{F} | 1 | Trap occupancy for a set of states |
| \mathbf{F}_i | N | Force on atom i |
| g_H | $m^{-3}J^{-1}$ | Hydrogen trap density of states in the RDD model |
| g_v | 1 | Degeneracy of the valley v |
| H | m^{-3} | Hydrogen concentration in the RDD model |
| H | Am^{-1} | Magnetic field strength |
| H | J | General hamilton operator in the derivation of Fermi's golden rule |

| Symbol | Unit | Description |
|------------------------|------------------|--|
| H_c | m^{-3} | Free hydrogen concentration in the RDD model |
| H_{ch} | J | Hamilton operator of the channel in the derivation of Fermi's golden rule |
| \hat{H}_{tot} | J | Hamilton operator of an atomic system |
| I_D | A | Drain current |
| I_{D0} | A | Initial drain current |
| k | m^{-1} | Electron wavevector |
| k | 1 | Coupling constant between τ_{cap} and τ_{em} in Yang's model |
| k_f | s^{-1} | Forward rate of a reaction/transition |
| $k_{f,0}$ | s^{-1} | Attempt frequency in the reaction-limited model |
| k_r | s^{-1} | Reverse rate of a reaction/transition |
| $k_{x/y/z}$ | m^{-1} | $x/y/z$ -component of the electron wavevector |
| L_x | m | Length of the substrate in the x -direction |
| m_n | m | Effective mass of the electrons |
| $m_{n,v}$ | m | Effective mass of the electrons for the valley index v |
| m_p | m | Effective mass of the holes |
| $m_{p,v}$ | m | Effective mass of the holes for the valley index v |
| m_t | m | Tunneling mass of the charge carriers |
| M | kg | Oscillator mass in the harmonic approximation |
| $M_{a\alpha b\beta}$ | J | Matrix element for a vibronic transition from state $a\alpha$ to state $b\beta$ |
| M_{if} | J | Matrix element for a transition from state i to state f |
| n | m^{-3} | Electron density |
| n_p | 1 | Power law exponent of permanent component in the NBTI fit formula |
| n_r | 1 | Power law exponent of recoverable component in the NBTI fit formula |
| n_{RD} | 1 | Power law exponent in the RD model |
| N_a | m^{-3} | Acceptor concentration |
| N_c | m^{-3} | Effective conduction band weight |
| $N_{c,H}$ | m^{-3} | Effective density of conduction states in the RDD model |
| N_d | m^{-3} | Donor concentration |
| N_{it} | m^{-2} | Concentration of interface states per area |
| $N_{\text{it},0}$ | m^{-2} | Initial concentration of interface states per area |
| N_{ox} | m^{-2} | Number of oxide charges per area |
| N_t | m^{-3} | Trap density |
| N_v | m^{-3} | Effective valence band weight |
| N_x | 1 | Number of states for a free electrons/holes gas in the x -direction |
| N_{yz} | 1 | Number of states for a free electrons/holes gas in the yz -plane |
| N_{xyz} | 1 | Number of states for a free electrons/holes gas in the xyz -volume |
| p | m^{-3} | Hole density |
| p_{ij} | s^{-1} | Transition probability from state i to state j |
| q | m | Configuration coordinate |
| q_i | m | Configuration coordinate at the energy minimum i |
| Q_{it} | Cm^{-2} | Areal interface charges |
| Q_{ox} | Cm^{-2} | Areal oxide charges |

| Symbol | Unit | Description |
|-------------------------------------|-----------------|--|
| $r_{a\alpha b\beta}$ | s^{-1} | Vibronic transition rate from state $a\alpha$ to state $b\beta$ |
| $r_{\text{cap,e}}$ | s^{-1} | Electron capture rate |
| $r_{\text{cap,h}}$ | s^{-1} | Hole capture rate |
| r_e | s^{-1} | Electron tunneling rate |
| $r_{\text{eq},ij,n}$ | s^{-1} | Transition rate r_{ij} of a trap n during equilibrium conditions |
| $r_{e,q_1/q_2}$ | s^{-1} | Electron tunneling rate from the charge state q_1 to q_2 in the LSM |
| $r_{\text{em,e}}$ | s^{-1} | Electron emission rate |
| $r_{\text{em,h}}$ | s^{-1} | Hole emission rate |
| r_{ij} | s^{-1} | Rate for the transition $T_{i \rightarrow j}$ |
| r_h | s^{-1} | Hole tunneling rate |
| $r_{h,q_1/q_2}$ | s^{-1} | Hole tunneling rate from the charge state q_1 to q_2 in the LSM |
| R_i | 1 | Ratio of the vibration frequencies in an NMP transition |
| \mathbf{r}_i | m | Spatial coordinates of electron i |
| \mathbf{R} | s^{-1} | Transition rate matrix |
| \mathbf{R}_i | m | Spatial coordinates of atom i |
| s | $K^{-1}V^{-1}m$ | Scaling factor for stress/relaxation curves |
| s_r | $K^{-1}V^{-1}m$ | Scaling factor s during relaxation |
| s_s | $K^{-1}V^{-1}m$ | Scaling factor s during stress |
| s_0 | 1 | Prefactor of the scaling factor s |
| S | 1 | Action in the WKB method |
| S_i | 1 | Huang-Rhys factor for an NMP transition $T_{i \rightarrow j}$ |
| t | s | Time |
| t_{ox} | m | Thickness of the insulator |
| t_r | s | Relaxation time |
| t_s | s | Stress time |
| t_0 | m | First measurement point during stress |
| T | K | Temperature |
| TC_c | 1 | Transmission coefficient for tunneling through the conduction band |
| TC_v | 1 | Transmission coefficient for tunneling through the valence band |
| T_{eq} | K | Temperature during equilibrium conditions |
| $T_{i \rightarrow j}$ | s^{-1} | Transition from state i to state j |
| $T_{i \leftrightarrow j}$ | s^{-1} | Transitions between the states i to state j |
| $T_{i \rightarrow j \rightarrow k}$ | s^{-1} | Chain of the transitions $T_{i \rightarrow j}$ and $T_{j \rightarrow k}$ |
| T_r | K | Temperature during relaxation |
| T_s | K | Temperature during stress |
| \hat{T}_e | J | Electron kinetic energy operator |
| \hat{T}_n | J | Nucleus kinetic energy operator |
| U | J | Adiabatic potential of an atomic system |
| U^q | J | U for charge state q |
| U_i | J | U in the minimum configuration of state i |
| ν_{eff} | J | Effective electron potential |
| $\nu_{\text{th},n}$ | ms^{-1} | Thermal velocity of the electrons |

| Symbol | Unit | Description |
|-----------------|------------------------------|---|
| $\nu_{th,p}$ | ms^{-1} | Thermal velocity of the holes |
| \mathbf{v}_i | ms^{-1} | Velocity of atom i |
| V | J | Defect potential |
| V_{ch} | J | Channel potential in the derivation of Fermi's golden rule |
| V_{eq} | J | Gate bias during equilibrium conditions |
| V_{EP} | J | Interatomic empirical potential |
| V_G | V | Gate bias |
| V_i | J | Energy of the system in state i in the TWM and the CDW |
| $V_{i,0}$ | J | Initial energy of the system in state i in the TWM |
| V_r | V | Gate bias during relaxation |
| V_s | V | Gate bias during stress |
| V_{th} | V | Threshold voltage |
| V_{th0} | V | Initial threshold voltage |
| V_{th}^{OTF} | V | Threshold voltage extracted from OTF measurements |
| V_{th0}^{OTF} | V | Initial threshold voltage extracted from OTF measurements |
| V_{tr} | J | Trap potential in the derivation of Fermi's golden rule |
| \hat{V}_{en} | J | Operator for the electron-nucleus Coulomb interactions |
| \hat{V}_{ee} | J | Operator for the electron-electron Coulomb interactions |
| \hat{V}_{nn} | J | Operator for the nucleus-nucleus Coulomb interactions |
| WKB_c | 1 | WKB factor for tunneling through the conduction band |
| WKB_v | 1 | WKB factor for tunneling through the valence band |
| x | m | Direction perpendicular to the substrate-insulator interface |
| x_{if} | m | Position of the substrate-insulator interface |
| $x_{n,0}$ | m | Characteristic tunneling length for electrons |
| $x_{p,0}$ | m | Characteristic tunneling length for holes |
| x_t | m | Position of the trap |
| x_B | m | Position of the tunneling hole front |
| X | m^{-3} | Density of the diffusing species X in the RD model |
| y | m | Direction parallel to the substrate-insulator interface |
| z | m | Direction parallel to the substrate-insulator interface |
| Z_c | 1 | Charge state of the diffusing species X in the RD model |
| Z_H | 1 | Charge state of the diffusing species in the RDD model |
| α | 1 | Characteristic exponent in the reaction-limited model |
| β | 1 | Parameter in the empirical relation of the universal recovery |
| γ | JN^{-1} | Field dependence factor of the thermal barrier in the TSM |
| Δ | J | Stress parameter in the TWM |
| Δ_i | J | Stress parameter in the CDW model |
| Δt | s | Time step in molecular dynamics |
| ΔD_{it} | $\text{m}^{-2}\text{J}^{-1}$ | Change in the interface trap density of states |
| Δf_i | 1 | Change in the trap occupancy in state i |
| Δf_{ox} | 1 | Change in the oxide trap occupancy |
| Δf_t | 1 | Change in the trap occupancy |

| Symbol | Unit | Description |
|-----------------------|-------------------|--|
| ΔE_b | J | Energy barrier for charge trapping in the model of Kirton and Uren |
| $\Delta E_{b,1}$ | J | Energy barrier for hole capture of the oxygen vacancy in the TSM |
| $\Delta E_{b,2}$ | J | Energy barrier for hole capture of the E' center in the TSM |
| $\Delta E_{b,3}$ | J | Relaxation barrier to the oxygen vacancy in the TSM |
| $\Delta E_{b,4}$ | J | Thermal barrier for the hydrogen transition in the TSM |
| ΔE_t | J | E_t referenced to the substrate valence bandedge |
| $\Delta E'_t$ | J | E'_t referenced to the substrate valence bandedge |
| ΔN_{it} | m^{-2} | Change in the number of interface charges per area |
| ΔN_{ox} | m^{-2} | Change in the number of oxide charges per area |
| ΔQ_{it} | Cm^{-2} | Change in the areal interface charges |
| ΔQ_{ox} | Cm^{-2} | Change in the areal oxide charges |
| ΔV_{th} | V | Change in the threshold voltage |
| $\Delta V_{th,r}$ | V | Change in the threshold voltage during relax |
| $\Delta V_{th,s}$ | V | Change in the threshold voltage during stress |
| ΔV_{th}^{OTF} | V | Change in threshold voltage extracted from OTF measurements |
| $\Delta U_{b,ij}$ | J | NMP barrier for the transition $T_{i \rightarrow j}$ |
| ϵ | Fm^{-1} | Electric permittivity |
| ϵ_i | J | Energy level of the bound state i |
| ϵ_i^{KS} | J | Kohn-Sham eigenvalue |
| ϵ_{ij} | J | Energy barrier for the transition $T_{i \rightarrow j}$ in the NMP model |
| ϵ_{q_1/q_2} | J | Thermodynamic trap level for a transition from charge state q_1 to q_2 |
| $\epsilon_{T2'}$ | s | Energy difference between the state 2 and 2' in the NMP model |
| $\zeta_{n/p,i}$ | 1 | Square root of the WKB factor |
| μ | $s^{1/2}$ | Mean value of the distribution of τ in Yang's model |
| μ_c | $m^2V^{-1}s^{-1}$ | Mobility in the RD model |
| μ_X | $m^2V^{-1}s^{-1}$ | Mobility of the diffusing species X in the RDD model |
| ν | 1 | Valley index |
| ν_0 | s^{-1} | Attempt frequency |
| ξ | 1 | Normalized relaxation time |
| π_i | 1 | Occupation probability for being in state i |
| Π | 1 | Occupation probability for set of states |
| Π_{eq} | 1 | Equilibrium occupation probability for set of states |
| ρ | Cm^{-3} | Charge density |
| ρ_t | m^{-3} | Density of traps |
| ρ_H | $m^{-3}J^{-1}$ | Trapped hydrogen density in the RDD model |
| ρ_0 | Cm^{-3} | Ground state charge density |
| σ | $s^{1/2}$ | Spread of the distribution of τ in Yang's model |
| σ_{ds} | J | Spread of dissociation barrier in the reaction-limited model |
| σ_n^{TSM} | m^2 | Cross section for an electron transition in the TSM model |
| $\sigma_{n,yz}$ | m^2 | Cross section for an electron tunneling in the ETM |
| $\sigma_{n,0}^{TSM}$ | m^2 | Temperature-independent prefactor of σ_n^{TSM} |
| σ_p^{SRH} | m^2 | Cross section for a hole transition in the SRH model |

| Symbol | Unit | Description |
|-----------------------------|--------------------|---|
| σ_p^{NMP} | m^2 | Cross section for a hole transition in the eNMP model |
| σ_p^{TSM} | m^2 | Cross section for a hole transition in the TSM model |
| $\sigma_{p,yz}$ | m^2 | Cross section for hole tunneling in the ETM |
| $\sigma_{p,0}^{\text{SRH}}$ | m^2 | Temperature-independent prefactor of σ_p^{SRH} |
| $\sigma_{p,0}^{\text{NMP}}$ | m^2 | Temperature-independent prefactor of σ_p^{NMP} |
| $\sigma_{p,0}^{\text{TSM}}$ | m^2 | Temperature-independent prefactor of σ_p^{TSM} |
| τ | s | Transition time constant in the reaction-limited and the Yang model |
| $\tau_{\text{cap}}^{1'}$ | s | Hole capture time constant over the state $1'$ in the eNMP model |
| $\tau_{\text{cap}}^{2'}$ | s | Hole capture time constant over the state $2'$ in the eNMP model |
| τ_{cap} | s | Capture time constant |
| $\tau_{\text{cap,e}}$ | s | Electron capture time constant |
| $\tau_{\text{cap,h}}$ | s | Hole capture time constant |
| $\tau_{\text{c,min}}^{1'}$ | s | Minimal $\tau_{\text{cap}}^{1'}$ in the eNMP model |
| $\tau_{\text{c,min}}^{2'}$ | s | Minimal $\tau_{\text{cap}}^{2'}$ in the eNMP model |
| τ_{em} | s | Emission time constant |
| $\tau_{\text{em}}^{1'}$ | s | Hole emission time constant over the state $1'$ in the eNMP model |
| $\tau_{\text{em}}^{2'}$ | s | Hole emission time constant over the state $2'$ in the eNMP model |
| $\tau_{\text{em,e}}$ | s | Electron emission time constant |
| $\tau_{\text{em,h}}$ | s | Hole emission time constant |
| $\tau_{\text{e,min}}^{1'}$ | s | Minimal $\tau_{\text{em}}^{1'}$ in the eNMP model |
| $\tau_{\text{e,min}}^{2'}$ | s | Minimal $\tau_{\text{em}}^{2'}$ in the eNMP model |
| $\tau_{n,0}^{\text{TSM}}$ | s | Electron capture time constant as defined in the TSM model |
| $\tau_{p,0}^{\text{ETM}}$ | s | Hole capture time constant as defined in the ETM |
| $\tau_{p,0}^{\text{NMP}}$ | s | Hole capture time constant as defined in the eNMP model |
| $\tau_{p,0}^{\text{SRH}}$ | s | Hole capture time constant as defined in the SRH model |
| $\tau_{p,0}^{\text{TSM}}$ | s | Hole capture time constant as defined in the TSM model |
| $\bar{\tau}_{n,0}$ | s | Reduced electron capture time in the ETM |
| $\bar{\tau}_{p,0}$ | s | Reduced hole capture time in the ETM |
| Υ_i | $\text{m}^{-3N/2}$ | Wavefunction of the combined system of N electrons and M nuclei |
| φ | V | Electric potential |
| φ_s | V | Surface potential |
| ϕ | J | Potential energy of electrons/holes |
| $\phi_{1/2}$ | J | Left/Right border of the tunnel barrier |
| Φ_{ij} | $\text{m}^{-3N/2}$ | Wavefunction of an N nuclei system in state i |
| ψ_i | $\text{m}^{-1/2}$ | Single-electron wavefunction in state i |
| ψ_i^{KS} | $\text{m}^{-1/2}$ | Kohn-Sham orbitals |
| $\psi_{n,i}$ | $\text{m}^{-1/2}$ | Electron channel wavefunction of the quasi-bound state i |
| $\psi_{p,i}$ | $\text{m}^{-1/2}$ | Hole channel wavefunction of the quasi-bound state i |
| Ψ_i | $\text{m}^{-3N/2}$ | Wavefunction of an N electron system in state i |
| Ψ_0 | $\text{m}^{-3N/2}$ | Wavefunction of an N electron system in the ground state |
| ω | s^{-1} | Oscillator frequency in the harmonic approximation |

Physical Constants

| | | | |
|-----------------|-----|-----------------------------------|---|
| g_0 | ... | Gyromagnetic factor for electrons | 2.0023193 |
| h | ... | Planck's constant | $6.6260755 \times 10^{-34}$ Js |
| \hbar | ... | Reduced Planck's constant | $h/(2\pi)$ |
| k_B | ... | Boltzmann's constant | 1.380662×10^{-23} JK ⁻¹ |
| q_0 | ... | Elementary charge | $1.6021892 \times 10^{-19}$ C |
| m_e | ... | Electron rest mass | $9.1093897 \times 10^{-31}$ kg |
| ε_0 | ... | Dielectric constant | $8.8541878 \times 10^{-12}$ AsV ⁻¹ m ⁻¹ |
| μ_B | ... | Bohr magneton | $9.2740092 \times 10^{-24}$ JT ⁻¹ |

Contents

| | |
|--|-------------|
| Kurzfassung | i |
| Abstract | iii |
| Acknowledgements | v |
| Acronyms | vii |
| Physical Quantities | ix |
| Physical Constants | xvii |
| 1 Introduction | 1 |
| 1.1 Definition of NBTI | 1 |
| 1.2 Two Main Contributions to NBTI | 2 |
| 1.3 NBTI Experiments | 2 |
| 1.3.1 Measure-Stress-Measure Technique | 3 |
| 1.3.2 On-The-Fly Measurements | 3 |
| 1.3.3 Electron Spin Resonance | 4 |
| 1.3.4 Time Dependent Defect Spectroscopy | 5 |
| 1.4 Phenomenological Findings | 7 |
| 1.5 A Modeling Perspective | 11 |
| 1.5.1 Reaction-Diffusion Model | 11 |
| 1.5.2 Dispersive Transport | 15 |

| | | |
|----------|--|-----------|
| 1.5.3 | Reaction-Limited Models | 15 |
| 1.5.4 | Triple-Well Model | 17 |
| 1.5.5 | Combined Models | 18 |
| 1.5.6 | Conclusion | 19 |
| 2 | Fundamentals of Charge Trapping | 21 |
| 2.1 | Tunneling — A Process Depending on Device Electrostatics | 22 |
| 2.2 | Franck-Condon Theory | 25 |
| 2.3 | The Level Shift | 28 |
| 2.4 | Nonradiative Multi-Phonon Theory | 30 |
| 2.5 | Effective Rates into Single Traps | 32 |
| 2.5.1 | Elastic Electron Tunneling | 32 |
| 2.5.2 | Shockley-Read-Hall Theory | 35 |
| 3 | Applied Methods | 39 |
| 3.1 | Schrödinger-Poisson Solver | 39 |
| 3.2 | From Rates to Degradation Curves | 42 |
| 3.3 | Density Functional Theory | 45 |
| 3.3.1 | Introduction | 45 |
| 3.3.2 | The Basic Concepts of DFT | 46 |
| 3.3.3 | Simulation Details | 47 |
| 3.4 | Empirical Potential Molecular Dynamics | 50 |
| 3.4.1 | Fundamentals of Molecular Dynamics | 50 |
| 3.4.2 | Procedure for Structure Generation | 51 |
| 4 | Elastic Tunneling Model | 55 |
| 4.1 | A Phenomenological Trapping Model | 56 |
| 4.2 | Elastic Tunneling | 58 |

| | | |
|----------|--|------------|
| 4.2.1 | The Behavior of A Single Trap | 59 |
| 4.2.2 | Spatially and Energetically Distributed Traps | 62 |
| 4.2.3 | Time Behavior during Stress | 64 |
| 4.2.4 | Time Range of Trapping | 67 |
| 4.2.5 | Oxide Field Dependence | 67 |
| 4.2.6 | Time Behavior during Relaxation | 68 |
| 4.2.7 | Investigation of the Temperature Dependence using a Quantum Refinement . . | 70 |
| 4.2.8 | Charge Injection from the Gate | 73 |
| 4.2.9 | Width of the Trap Band | 75 |
| 4.3 | Conclusion | 77 |
| 5 | Level Shift Model | 79 |
| 5.1 | Defects in $a - \text{SiO}_2$ | 80 |
| 5.1.1 | Oxygen Vacancy | 80 |
| 5.1.2 | E'_γ Center and Variants | 82 |
| 5.1.3 | Hydrogen Atom | 84 |
| 5.1.4 | Hydrogen Bridge | 86 |
| 5.2 | The Level Shift Model | 88 |
| 5.2.1 | Model Evaluation | 92 |
| 5.2.2 | Conclusion | 100 |
| 6 | SRH-Based Models | 101 |
| 6.1 | McWhorter Model | 102 |
| 6.2 | Standard Model of Kirton and Uren | 103 |
| 6.3 | Two Stage Model | 106 |
| 6.3.1 | Physical Description of the Model | 106 |
| 6.3.2 | Model Evaluation | 108 |
| 6.3.3 | Quantum Mechanical Simulations | 113 |

| | | |
|----------|---|------------|
| 6.3.4 | Capture and Emission Time Constants | 116 |
| 6.4 | Conclusion | 118 |
| 7 | The Extended Nonradiative Multi-Phonon Model | 119 |
| 7.1 | Transition Rates according to the NMP Theory | 119 |
| 7.2 | States of a Bistable Defect | 123 |
| 7.3 | Model Evaluation | 126 |
| 7.4 | Analytics Derivation of the Capture and Emission Time Constants | 128 |
| 7.5 | Explanation for Noise in TDDS Measurements | 135 |
| 7.6 | Discussion | 136 |
| 7.7 | Conclusion | 139 |
| 8 | Conclusion and Outlook | 141 |
| A | Physical Basics | 145 |
| A.1 | Fermi's Golden Rule | 145 |
| A.2 | Wenzel-Kramers-Brillouin Method | 147 |
| A.3 | WKB Formulas for Different Shapes of Energy Barriers | 148 |
| A.4 | Density of States | 150 |
| | Bibliography | 153 |
| | Own Publications | 165 |
| | Curriculum Vitae | 173 |

1

Introduction

1.1 Definition of NBTI

The negative bias temperature instability (NBTI) falls into the category of reliability issues which considerably affect the device behavior of metal oxide semiconductor field effect transistors (MOSFETs). After its discovery several decades ago, NBTI has risen to one of the most serious reliability concerns for modern CMOS technologies and has therefore increasingly attracted industrial as well as scientific interest. In its idealized form it occurs when the device is subjected to elevated temperatures and high gate voltages while the remaining terminals are grounded. Temperatures typically encountered in practice range from 0°C to 300°C, while the field across the dielectric reaches values up to approximately 10MV/cm. These conditions, usually referred to as stress, have detrimental effects on the device characteristics, for instance a shift in the threshold voltage V_{th} and a change in the subthreshold slope. However, as soon as the stress conditions are removed, the device characteristics are found to recover, meaning that the device parameters slowly revert towards their initial values. For operating stress conditions outside these parameter ranges, NBTI occurs in a combination with other reliability phenomena, such as hot carrier degradation [1–3] or time-dependent dielectric breakdown [4, 5] among others.

Interestingly, NBTI becomes increasingly pronounced for modern devices: First, the aggressive down-scaling of device geometry goes hand in hand with higher electric fields across the dielectric. Second, compact device integration gives rise to high power dissipation and thus to high operating temperatures. Both strong fields as well as increased temperatures enhance the NBTI device degradation. Also, the introduction of new technologies, especially nitrided oxides, has turned out to reduce other reliability issues but enhances NBTI [6, 7]. On the other hand, advances in device

processing improved the oxide reliability, which is accompanied by a reduction of defects at the interface as well as in the dielectric. Even to date, NBTI has eluded our detailed understanding regarding the phenomenological behavior as well as the underlying microscopic origins.

1.2 Two Main Contributions to NBTI

The change in the threshold voltage V_{th} , the signature of NBTI, originates from trapped charges which are immobile and therefore cannot carry any drain current. Hence, the central question arises whether NBTI must be ascribed to charges trapped at the Si/SiO₂ interface (interface traps), in the dielectric (oxide traps), or even a combination thereof.

Interface traps stem from the lattice mismatch caused by the abrupt transition from crystalline bulk silicon to amorphous SiO₂. Even the amorphous nature of modern high-quality oxides is not fully capable of compensating the lattice mismatch through the flexibility of its bonding network. As a result, a certain fraction of Si atoms cannot establish four bonds to their neighbor atoms and thus leave behind unsaturated bonds, the so-called dangling bonds [8,9]. The corresponding orbitals can carry up to two electrons and feature two trap levels found to lie within the substrate bandgap. Three different types of interface defects are observed experimentally: P_b centers have been found at (111)Si/SiO₂ interfaces, while P_{b0} and P_{b1} centers are present at the technologically more relevant (100)Si/SiO₂ interfaces [8, 10, 11]. The creation or annealing of charged interface states induces a non-negligible threshold voltage shift ΔV_{th} , which is considered as an undesired degradation by engineers. However, these states can be eliminated by exposure to a hydrogen ambient, where the interfacial dangling bonds are passivated and their corresponding energy levels are shifted out of the substrate bandgap [10, 12].

There exists a series of traps, such as cycling positive charges [13], anti-neutralization positive charges [13], border traps [14], switching traps [15, 16], oxide traps, E' centers [17], and K_n centers [18]. However, no precise distinction has been made between them. Experimentally, these traps are characterized by either their trapping time constants or their defect structures. Furthermore, their properties have been found to strongly depend on the local environment of their host material, such as E' centers in amorphous SiO₂ [19,20]. Nevertheless, all these types of oxide traps have been linked to the NBTI phenomenon [21, 22] since they are capable of exchanging charge carriers with the substrate. Electron or hole injection is assumed to proceed by some kind of elastic [23] or inelastic trapping mechanism [24] into spatially and/or energetically distributed traps. Ongoing research is now dealing with the exact physical description of this process, including all dependences on the oxide field and the temperature.

1.3 NBTI Experiments

In the past, a series of distinct measurement techniques has been established, which includes direct-current current-voltage measurements, measure-stress-measure (MSM) technique, on-the-fly (OTF)

measurements, capacitance-voltage measurements, charge-pumping, and electron-spin-resonance (ESR). Each of them is suited and thus employed for the analysis of NBTI. part from equipment issues, these measurement techniques strongly differ in the information they provide. In the following, their basic experimental setup and principle functioning are outlined and their specific shortcomings are discussed.

1.3.1 Measure-Stress-Measure Technique

The measure-stress-measure (MSM) technique has traditionally been employed to probe NBTI experimentally [25, 26]. Before the real measurement of NBTI degradation starts, an $I_D(V_G)$ curve is taken by scanning the device in a range around the initial threshold voltage V_{th0} . Then the device is subjected to stress bias and only interrupted by short intervals with the gate bias brought back to V_{th0} . During these short measurement intervals, the drain current I_D is monitored and converted to a threshold voltage shift ΔV_{th} based on the initially scanned $I_D(V_G)$ curve [25]. Alternatively, V_{th} can be directly obtained by enforcing the initial threshold current I_{D0} [27] or by the shift of complete $I_D(V_G)$ curves recorded using ultra-short pulses [28, 29].

However, the MSM method suffers from an unavoidable measurement delay [30], which is defined as the time interval between the removal of stress and the first measurement of the drain current. The degradation within this time is not covered by the measurements and so usually leads to an underestimation of the threshold voltage shift. As pointed out in [31], the different delay times seriously affect the interpretation of the degradation data, for instance, the exponent of a time power-law as discussed in Section 1.4. Thus minimizing the measurement delay has long been the subject of numerous studies [27].

1.3.2 On-The-Fly Measurements

On-the-fly (OTF) measurements try to circumvent the unintentional measurement delay and are therefore often regarded as the method of choice for experimentally investigating NBTI. In this method, the gate bias is maintained in the linear regime during the entire measurement run while the drain bias is held at a small but constant level. Alternatively, short voltage pulses can be applied to the drain during measurements only. In both cases, the device degradation is monitored based on the drain current I_{Dlin} . Since the threshold voltage is of central interest for NBTI, the drain current has to be converted to V_{th} using extrapolation schemes [32, 33]. The simplest is based on the SPICE level 1 compact model

$$\Delta V_{th}^{OTF} = \frac{I_D - I_{D0}}{I_{D0}} (V_G - V_{th0}^{OTF}), \quad (1.1)$$

where I_{D0} and V_{th0}^{OTF} denote I_D of the first measurement point [34, 35] and V_{th} of the undegraded device, respectively. This compact model neglects mobility variations [35–37] ascribed to the scattering of charge carriers at the trapped charges close at the interface. However, this model benefits from the fact that, in contrast to other extrapolation schemes, only I_{D0} has to be recorded. More

complex extrapolations schemes accounting for mobility variations have been proposed but require the determination of the full $I_D V_G$ curve. Note that these $I_D V_G$ curves must be measured before stress, thereby already causing a non-negligible amount of degradation, which is not accounted for in the extrapolation scheme.

1.3.3 Electron Spin Resonance

Electron spin resonance (ESR) is a powerful tool to identify paramagnetic defects, which are characterized by an unpaired electron in their orbitals. This electron is associated with a spin whose response to an external magnetic field is measured in ESR experiments. For instance, such paramagnetic defects can be Si-dangling bonds at the Si/SiO₂ interface (the so-called P_b centers) [8, 10, 11, 38] or in the dielectric (the numerous variants of E' centers) [39–44]. It thereby gives chemical and structural information about the defect under investigation and provides insight into the chemical processes occurring in the dielectrics. In this measurement technique, the defects in the sample are subjected to a large but slowly varying magnetic field H , which splits their energy levels according to the Zeeman effect. An unpaired electron residing in one defect orbital has two possible orientations - namely either parallel or anti-parallel to the magnetic field. The energetical separation of these two orientations equals

$$\Delta E = g_0 \mu_B H, \quad (1.2)$$

where μ_B denotes the Bohr magneton and g_0 the gyromagnetic factor. Due to energetical considerations, the defect electron preferably aligns parallel to the magnetic field. Furthermore, the sample is additionally exposed to a microwave radiation $\nu \sim 9 - 10$ GHz, thereby delivering an energy of $h\nu$ to the electron. In the case of resonance, the condition $h\nu = g_0 \mu_B H$ is satisfied and the electron change the orientation of its spin, which causes as a peak in the ESR absorption spectrum. The most frequently employed measurement technique records the ESR signal with respect of the slowly varying magnetic field H . Note that this measurement technique is limited to defects that have only one electron in their orbitals. Therefore, changing the charge state via electron or hole capture will render these defects “ESR-inactive”. Conversely, defects with either no or two electrons in the corresponding orbital can be made “ESR-active” by a charge capture event.

Additional structural information of the investigated defect is available via second-order effects: In solids, the spin-orbit interactions vanish for the ground state in solids but affect the excited states. They alter the gyromagnetic factor to an angle-dependent g -tensor, which reflects the symmetry of the paramagnetic center. Hence, angle-dependent measurements allow the identification of defects on the basis of this symmetry [8, 45]. In this way, it has been revealed that the central Si atoms of P_b and P_{b0} centers are tetrahedrally back-bonded to three other Si atoms. In contrast, P_{b1} centers exhibit a lower symmetry, which is traced back to a surface dimer bond. Another second order effect arises from electron-nuclear hyperfine interactions. Due to different orientations of the nuclei magnetic moments, additional characteristic peaks emerge in the ESR spectrum. For instance, the relative heights of these features — more precisely, a ratio of 1/20 — is a special signature for the element Si. Therefore all variants of P_b centers could be identified as Si dangling bonds. In the context of NBTI, a

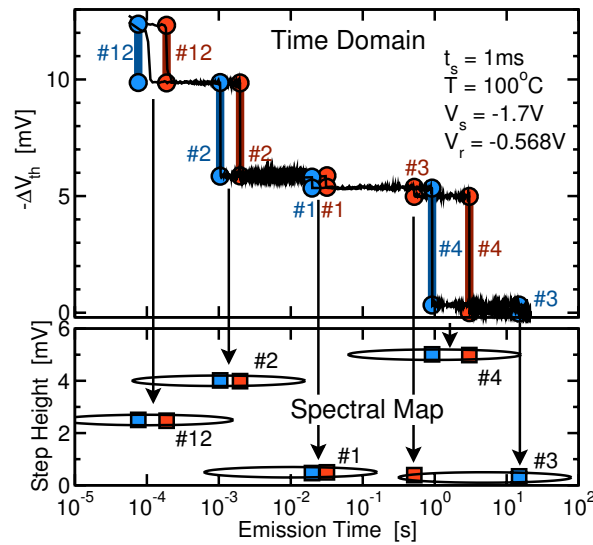


FIGURE 1.1: The time evolution of the threshold voltage shift for a small-area pMOSFET during recovery. The recorded recovery traces (black lines) in the top panel have several steps marked by the red or blue lines, respectively. The corresponding spectral map shows the emission times vs. the step height. Note that there are regions (ellipses) with an accumulation of points. Each of them can be assigned to one individual defect within the device.

series of investigations address hydrogen reactions with P_b centers as well as hydrogenated variants of E'_γ centers, namely 10.4 G doublet and the 74 G doublet [40, 41, 46]. Another variant of ESR is spin dependent recombination (SDR) [18, 47], in which the recombination via deep traps in the substrate bandgap is hampered due to a magnetic alignment of electrons in the conduction band and in the trap. With this method, it has been suggested that K_N centers play an important role in the NBTI degradation of silicon oxynitrides.

1.3.4 Time Dependent Defect Spectroscopy

With the technical advances in the MOSFET technology during the last several years, the device geometries of MOSFETs have been continuously shrunk and reached a point where the device degradation is dominated by the occurrence of single charging or discharging events [48–50]. As shown in Fig. 1.1, each of these events appears as a step in the recovery traces. Interestingly, one can clearly recognize that those steps differ significantly in their heights. This can be ascribed to the fact that the random distribution of dopants produces a spatially varying electrical potential inside the channel. The resulting inhomogeneous current density from source to drain is frequently referred to as the percolation current path, which is unique for each device. The lateral position of a charged trap within the gate area determines the step height in the drain current and the threshold voltage shift. This height is the signature of each defect and can thus be used for the identification of a single trap. This fact has motivated the use of the so-called spectral maps [51–53], in which the frequency of emission events is plotted vs. d and τ_{em} (see the lower panel of Fig. 1.1). These maps reveal the

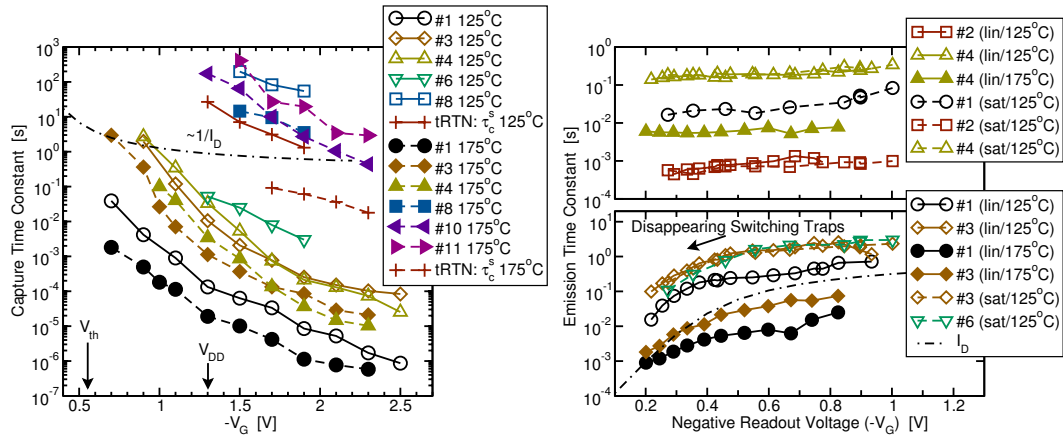


FIGURE 1.2: **Left:** The capture time constants τ_{cap} as a function of V_G for a number of defects at different temperatures extracted from a single device. Open and closed symbols mark measurements carried out at 125°C and 175°C, respectively. The τ_{cap} curves show a strong field acceleration and temperature activation. However, the observed field acceleration does not follow the $1/I_D \approx 1/p$ dependence (dot-dashed line) as predicted by the conventional SRH model. **Right:** The same as in the left figure but for the emission time constants τ_{em} . The two distinct field dependences (upper and lower panel) suggest the existence of two types of defects present in the oxide. However, the defect #1 shows different field behaviors depending on whether the device is operated in the linear or the saturation regime during the measurement. This suggests that the electrostatics within the device are responsible for the two distinct field dependences. It is noteworthy that the drop in τ_{em} goes hand in hand with the decrease of the interfacial hole concentration p (dot-dashed line).

characteristic emission times for certain stress conditions, which can be varied for the investigation of field and temperature dependence of τ_{cap} and τ_{em} (Fig. 1.2).

TDDS has lead to several essential findings [51–54] outlined in the following:

- (i) The plot in Fig. 1.2 reveals that the defects exhibit a strong, nearly exponential voltage dependence of τ_{cap} . Empirically, this dependence can be described by $\exp(-c_1 F_{\text{ox}} + c_2 F_{\text{ox}}^2)$. However, it differs from defect to defect, implying that it is related to certain defect properties.
- (ii) The time constant plots show a marked temperature dependence, which becomes obvious by the downward shift of the τ_{cap} curves for higher temperatures. The activation energies E_{act} extracted from Arrhenius plots are about 0.6 eV.
- (iii) τ_{em} of most defects is unaffected by changes in V_G (“normal” behavior).
- (iv) A few defects show a drop in τ_{em} towards lower V_G (“anomalous” behavior).
- (v) The τ_{em} of both types shows a temperature activation with a large spread ($E_{\text{act}} = 0.6 - 1.4$ eV).

One should keep in mind that some defects exhibit an exponential oxide field dependence of τ_{em} in normal random telegraph noise (RTN) measurements [55]. This difference to TDDS findings may arise from the fact that these defects are not assessable by the TDDS measurements.

Astonishingly, several TDDS recovery traces display RTN only after stressing [51]. The noise at one recovery trace is physically linked to defects — in this case hole traps — which continuously exchange charge carriers with the substrate. After a while, the RTN signal vanishes and does not reoccur during the remaining measurement time. The termination of the noise signal is ascribed to hole traps which change to their neutral charge state and remain therein. In [51], this kind of noise has been termed temporary RTN (tRTN) since it occurs only for a limited amount of time.

A similar phenomenon called anomalous RTN (aRTN) has been discovered in the early studies of Kirton and Uren [56]. Therein, electron traps have been observed, which repeatedly produce noise for random time intervals. During the interruptions of the signal, the defects dwell in their negative charge state so that no noise signal is generated. The behavior of these traps has been interpreted by the existence of a metastable defect state.

1.4 Phenomenological Findings

Before embarking on detailed physical models, the focus is now put on a phenomenological understanding of NBTI. In this respect, special attention is put on the functional form of the time evolution of ΔV_{th} depending on gate bias and temperature. Long term extrapolation does not only allow lifetime projection relevant for industrial purposes but also should be viewed as a touchstone for subsequent modeling attempts.

Grasser *et al.* [24] recognized that the recorded threshold voltage curves follow the same pattern at different stress temperatures and voltages. Therefore, these curves can be scaled so that they overlap for the stress and the relaxation phase. Mathematically, this can be described by

$$\Delta V_{th}(t_s, t_r, F_{ox,s}, T) = s(T, F_{ox,s}) \cdot \Delta V_{th}^0(t_s, t_r). \quad (1.3)$$

The scaling factor $s(T, F_{ox,s})$ represents the temperature (T) and oxide field ($F_{ox,s}$) dependence, which is best approximated by

$$s(T, F_{ox,s}) \approx s_0 T^2 F_{ox,s}^2. \quad (1.4)$$

$\Delta V_{th}^0(t_s, t_r)$ mimics a universally valid shape of the threshold voltage curves. A series of stress sequences for different temperatures are depicted in Fig. 1.3 in order to illustrate the common pattern of the threshold voltage data. As a proof for scalability, all curves line up to one curve by dividing them by their corresponding $s(T, F_{ox,s})$. As demonstrated in Fig. 1.3, the initial part of the stress phase shows a logarithmic behavior up to a stress time $t_{s,0} \sim 1$ s while the subsequent part follows a power-law with an exponent of $n = 0.11$ afterwards. The stress phase [24] can be expressed as

$$\Delta V_{th,s}(t_s, t_r, F_{ox,s}, T) = \begin{cases} s_s(T, F_{ox,s}) \cdot \log_{10}(t_s / t_0), & t_s \leq t_{s,0} \\ t_s^n, & t_s > t_{s,0} \end{cases}, \quad (1.5)$$

where t_0 denotes the first stress measurement point. However, Huard [57] reported that, for some devices, the scalability property is violated for the long term degradation with stress times larger $t_{s,0} \sim$

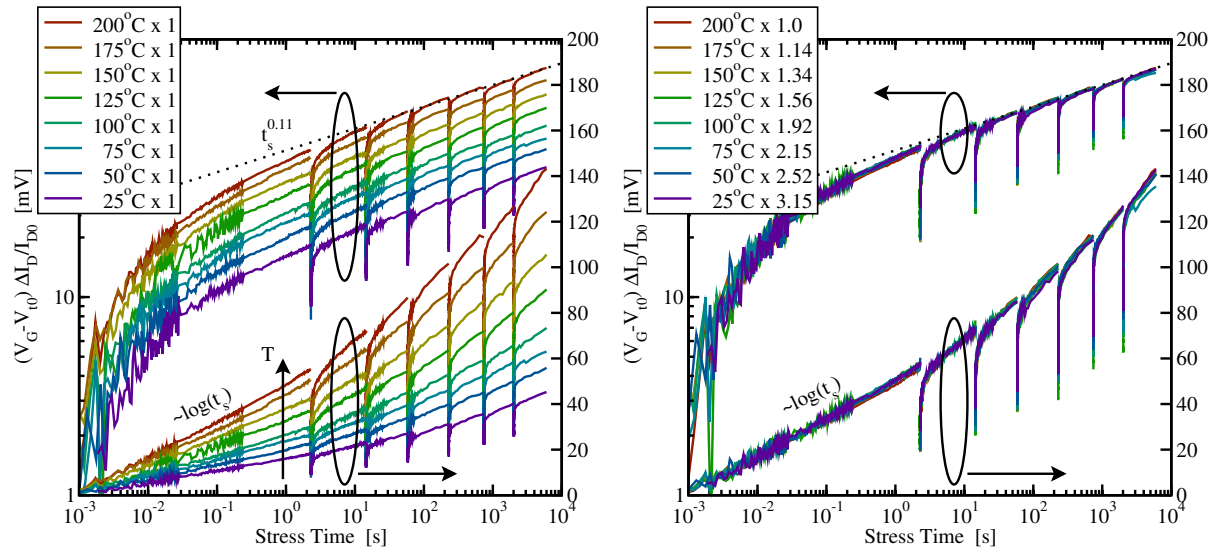


FIGURE 1.3: **Left:** The degradation of the drain current recorded for various stress temperatures (25 – 200°C) applying the extended MSM (eMSM) scheme [25,26]. In this method, the investigated device is subject to exponentially growing stress intervals ($V_G = -2V$) with interruptions of 12s (visible as spikes in the plots). During stress, the OTF technique is employed, in which the degradation of threshold voltage is estimated using the expression $\Delta V_{th}^{OTF} \approx (V_G - V_{th0})(I_D - I_{D0})/I_{D0}$. During the short relaxation periods, the drain current is converted to the threshold voltage using a initially recorded $I_D(V_G)$ curve. **Right:** The same data as in the left figure, where each curve is multiplied with a suitably chosen factor. All curves share the same shape as proven by the nearly perfect overlap. Note that the degradation lost during the short stress interruptions is restored within less than one decade and thus does not affect the extracted exponent n of the time power-law.

10s. Depending on the details of the fabrication process, the long term part has a scaling factor, which is estimated as

$$s(T, F_{ox,s}) \approx s_0 \exp\left(-\frac{E_{act}}{k_B T}\right) F_{ox,s}^4 \quad (1.6)$$

with E_{act} being an activation energy of 0.15 – 0.25 eV.

In the context of the universal behavior, special attention has been paid to the recovery phase. This was motivated by the notion that NBTI underlies reversible reaction kinetics. The degradation during the stress phase was assumed to be caused by the combination of a forward and a reverse rate. Therefore, the kinetics during stress were supposed to cover the whole physics, however, the individual contributions of the forward and the reverse rate are obscured. By contrast, only the reverse rate is activated during the relaxation phase, which is thus more suited for analyzing NBTI. In the following, some observations on the relaxation phase are summarized:

- The recovery already sets in before the shortest measurable relaxation time of about 1 μs .
- The recovery slows down before reaching the pre-stress level.
- The recovery data follow a universal curve when plotted as a function of $\xi = t_r / t_s$.

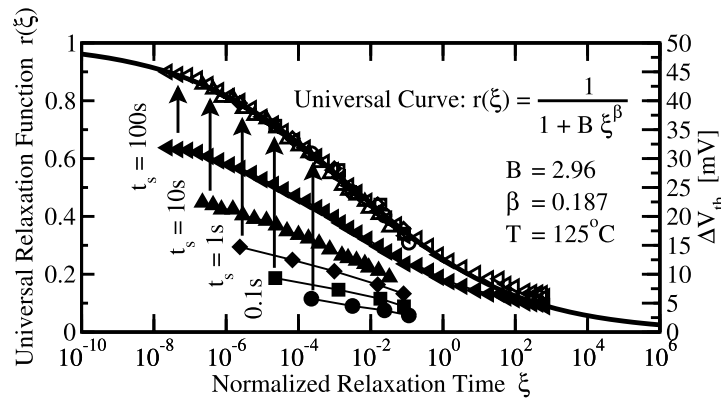


FIGURE 1.4: Relaxation data measured with the fast MSM technique of Reisinger [27]. Note that all relaxation curves line up to one single curve and thus follow a universal behavior according to equation (1.7) after they have been normalized as indicated by the upwards arrows.

These observations suggest the following procedure to process the recorded NBTI recovery data: First, the relaxation curves must be normalized to their last respective stress points, which are generally unknown but can be obtained using the back-extrapolation method proposed in [31]. Second, the relaxation times have to be scaled to their last accumulated stress time. The resulting curve can be best analytically described by the empirical relation [31] (cf. Fig. 1.4)

$$r(\xi) = \frac{1}{1 + B \xi^\beta} \quad (1.7)$$

with $\xi = t_r/t_s$, $B = 0.3 - 3$, and $\beta = 0.15 - 0.2$. In a further step, the universal relaxation is extended by the so-called permanent component [26, 28, 58] attributed to a mechanism with another physical origin. This permanent component, however, is ascertained to be a slowly recovering component rather than a constant contribution and is best represented by a power-law [59]. Separating the permanent from the recoverable component $P(t_s)$, the degradation during stress can be written as

$$\Delta V_{th,s}(t_s, t_r, F_{ox,s}, T) = s_s(T, F_{ox,s}) \cdot \log_{10}(t_s/t_0) + P(t_s) \quad (1.8)$$

with t_0 being the first stress measurement point. Alternatively, it can also be formulated as

$$\Delta V_{th}(t_s) = A_r t_s^{n_r} + A_p t_s^{n_p} \quad (1.9)$$

$A_{r/p}$ is the prefactor of a power law with exponent $n_{r/p}$, where the subscripts r and p refer to the recoverable or the permanent component, respectively. Note that n_p is larger than n_r in equation (1.9) indicating that the permanent component becomes dominant at large stress times [59]. The impact of the permanent component is demonstrated in Fig. 1.5, where the long term recovery tails deviate from the universal curve. However, universality is regained by accounting for the permanent component. For times longer than 1 ms, the relaxation data can be well approximated by a logarithmic behavior [60, 61] using the expression

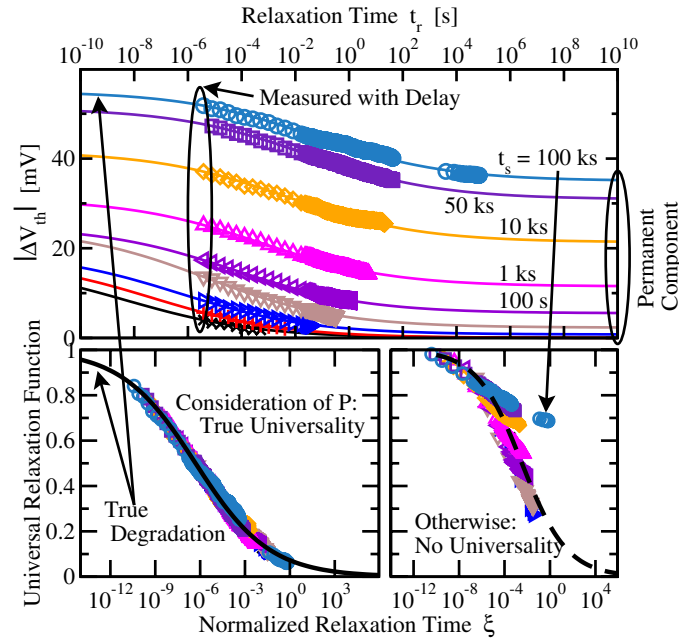


FIGURE 1.5: MSM data for the relaxation phase [62]. **Top:** The raw data as a function of $\xi = t_r/t_s$ clearly indicate the existence of a permanent component. **Bottom Right:** The same as in the top panel but scaled to the last stress value and normalized to the stress time. One can clearly recognize the deviation from the universal behavior $r(\xi)$. **Bottom Left:** Only a combination of a recoverable and a permanent component can reproduce the expected universal behavior.

$$\Delta V_{th,r}(t_s, t_r, F_{ox,s}, T) = s_r(T, F_{ox,s}) \cdot \log_{10}(1 + C t_s/t_r) + P(t_s) \quad (1.10)$$

with C being a parameter. The first term at the right hand side of equation (1.10) represents the recovering component, which shows a nearly logarithmic behavior, and compares well with the short term part of expression (1.7) [31, 60]. In [61] the prefactors $s_s(T, F_{ox,s})$ and $s_r(T, F_{ox,s})$ have been extracted from the eMSM data in Fig. 1.3 for the time range 1 ms... 1 s during stress and 1 ms... 100 ms during relaxation. A comparison of the prefactors has revealed a certain ratio $s_s/s_r > 1$, meaning that the stress and relaxation curves have different slopes. This asymmetry has long remained unrecognized but rules out several proposed NBTI models.

The logarithmic and power-law-like part of the stress curve along with the two components during recovery raise the question whether NBTI is governed by two mechanisms with one of them dominating in each of the time regimes. If this is the case, each of these mechanisms is highly likely to be subject to different field and temperature acceleration. Then the transition between these regimes should be controllable by varying the temperature and the electric field. However, no such transition has been observed so far. In [63], it has been argued that NBTI must be caused by either a single process or two tightly coupled ones. In the latter case, the interplay of both process enforces a single field dependence and temperature dependence without any transitions.

1.5 A Modeling Perspective

So far, only empirical relations, emerging from an experimental perspective but lacking any profound physical justification, have been presented. Now the focus is put on an in-depth microscopic understanding of the NBTI phenomenon. Hence, a series of modeling approaches are discussed in the following, where each of them is traced back to the creation of either interface charges and/or oxide charges.

The relation between the threshold voltage shift and the created charges can be expressed as

$$\Delta V_{th}(t) = - \frac{\Delta Q_{it}(t) + \Delta Q_{ox}(t)}{C_{ox}} \quad (1.11)$$

with C_{ox} being the areal gate capacitance. The change in interface charges $\Delta Q_{it}(t)$ is given by

$$\Delta Q_{it}(t) = q_0 \int \Delta D_{it}(E_t, t) f_{it}(E_f, E_t, t) dE_t. \quad (1.12)$$

$\Delta D_{it}(E_t, t)$ denotes the change in the time-dependent density of interface states at an energy level E_t and f_{it} corresponds to their occupancy. In equation (1.12) it has been presumed that the temporal charging and discharging of the interface states are negligible since both processes already occur on much shorter timescales than that typically covered by NBTI. The interface traps can hold up to two electrons and exhibit two distinct energy levels, namely one acceptor and one donor level. Accordingly, they are also referred to as amphoteric traps [9, 64, 65], which behave as either a donor or an acceptor by definition (cf. Fig. 1.6). Starting from midgap, a shift of the Fermi level towards the conduction band charges the interface states negatively, while they become positively charged if the Fermi level is moved in the opposite direction.

In addition to interface charges, also oxide-trapped charges [68–70] impact the threshold voltage shift. According to the current understanding of oxide-traps, charges are stored in preexisting defects whose occupation is governed by the quantum mechanical trapping dynamics. The contribution of the oxide traps to ΔV_{th} can be evaluated using

$$\Delta Q_{ox}(t) = q_0 \int \int D_{ox}(x, E_t, t) \Delta f_{ox}(x, E_t, t) (1 - x/t_{ox}) dx dE_t, \quad (1.13)$$

where $D_{ox}(x, E_t, t)$ is the density of trap states and Δf_{ox} represents the change in the trap occupancy. It is commonly assumed that oxide traps have larger time constants compared to interface states. For instance, this can be related to the depth of the trap location or the energetical position within the bandgap. Then the structural disorder of $a - \text{SiO}_2$ gives rise to a wide spread of trap levels assumed in several NBTI models [24].

1.5.1 Reaction-Diffusion Model

First serious modeling attempts date back to the so-called reaction-diffusion (RD) model [71, 72], which has been refined successfully in later studies [25, 60, 68, 73, 74]. It relies on an interface reaction

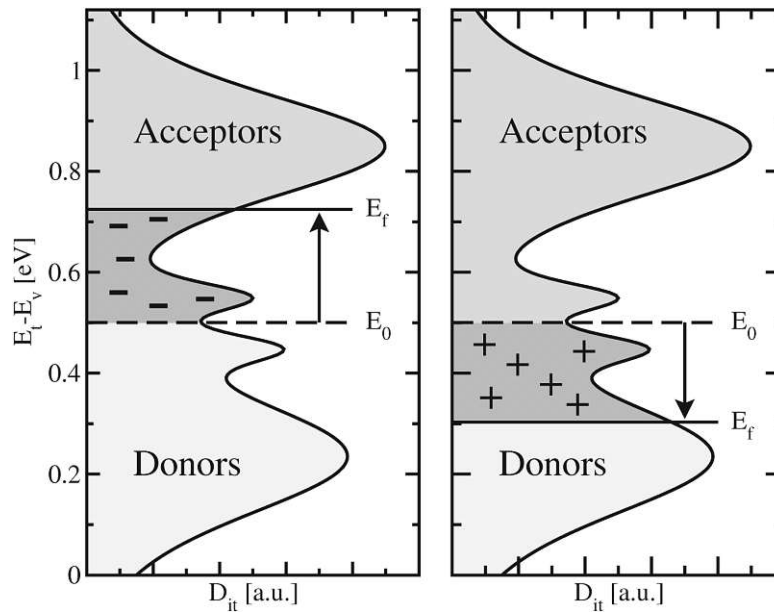


FIGURE 1.6: A schematic representation of the donor and acceptor distribution within the bandgap of Si. Energy levels for $+/0$ transitions, termed donor states, are located below midgap while energy levels for $0/-$ transitions, acceptor states, are predominantly found above midgap. The spread of the peaks in the trap distribution [10, 38] has been speculated to originate from the disorder of the atomic structure at the interface. Note that in addition to the interface states density, a band tail states density exponentially decays into the bandgap. They are ascribed to stretched Si-Si bonds due to the disorder at the Si/SiO₂ interface [66, 67].

involving the interfacial Si dangling bonds (present in the form of P_b centers) together with some sort of hydrogen species. Initially, nearly all of the P_b centers are supposed to be passivated through a hydrogen anneal step. This means that their unsaturated Si atoms has established a bond to a nearby hydrogen atom H, thereby shifting the electrically active trap levels out of the substrate bandgap. Upon application of stress, the Si – H bonds (P_bH) can break due to the presence of an electric field, thereby activating the forward reaction of



With the breakage of the Si – H bonds, the trap levels associated with the unsaturated Si atoms are shifted back into the bandgap. Since the released hydrogen atoms can easily rebond to the P_b centers, the reaction (1.14) is in equilibrium, resulting in a fixed ratio of the concentration of P_b centers, hydrogen atoms, and Si – H bonds. The released hydrogen atoms can also diffuse away and are thus not available for the passivation of the interfacial Si dangling bonds according to reverse reaction of (1.14). This results in a temporally increasing concentration of P_b centers, measured as a degradation in NBTI. After the removal of stress, the forward reaction of (1.14) is suppressed while the reverse mode dominates the reaction dynamics. It is important to note here that the dynamics in the RD model are eventually governed by the hydrogen diffusion but not by the interface reaction, which has

been assumed to be in equilibrium. An alternative reaction involves molecular hydrogen H_2 [75–77] and presumes that atomic hydrogen dimerizes instantaneously right at the interface according to



Thus, the generation of interface states is described by the electro-chemical reaction

$$\partial_t N_{it} = k_f(N_{it,0} - N_{it}) - k_r N_{it} X^{1/a}. \quad (1.17)$$

N_{it} and $N_{it,0}$ denote the surface concentration of interface states and its initial concentration, respectively. k_f and k_r stand for the field and temperature dependent forward and the reverse rate of the interface reaction. The kinetic exponent a determines the migrating hydrogen species X , that is, 1 for atomic H^+ and H^0 , and 2 for molecular H_2 . Within the RD framework, the interface reaction (1.17) is assumed to be in equilibrium and thus determines the ratio between X at the interface and N_{it} . However, the basis of the RD model is the transport equation (1.18) for the migrating species X . It is described by the drift-diffusion equation

$$\partial_t X = D_X \partial_x^2 X + Z_X \mu_X F_{ox} \partial_x X, \quad (1.18)$$

which is coupled to the interface reaction via the boundary condition

$$a \partial_t N_{it} = D_X \partial_x X + Z_X \mu_X F_{ox} X. \quad (1.19)$$

D_X , μ_X , and Z_X are the diffusion coefficient, the mobility, and the charge state of the species X , respectively. Within the time regime of interest, the dynamics of the interface reaction are governed by the interfacial hydrogen concentration, which in turn is controlled by hydrogen diffusion to and from the interface.

A solution of equation (1.17)-(1.19) can be found as

$$\Delta V_{th} \approx t^{n_{RD}}, \quad (1.20)$$

where n_{RD} is referred to as the time exponent. In the case of H^0 , the RD model yields a time exponent n_{RD} of 1/4, which is only compatible to measurements obtained with a relatively long delay. In more recent studies with a shorter delay, a time exponents close to 1/6 is obtained, as predicted by the RD model for H_2 . However, thorough examinations of the stress/relaxation curves show large discrepancies between the RD theory and the universal relaxation (cf. Fig. 1.7). While the recovery in experiments covers at least 12 decades, the RD model is limited to about 3 decades. This rules out this model as a reasonable explanation for NBTI. Some attempts to remedy this deficiency have been put forward:

- Since the gate thicknesses of modern MOSFET technologies have been downsized to a few nanometer, the hydrogen is supposed to reach the gate interface during stress. In a new two-region RD model [60, 77], it is assumed that the hydrogen can enter the poly-gate where it continues to diffuse with a lower diffusivity. This extension introduces spurious features, such as kinks or bumps into the degradation curves of the threshold voltage, which are in contradiction to the universal shape of the ΔV_{th} curves seen in experiments.

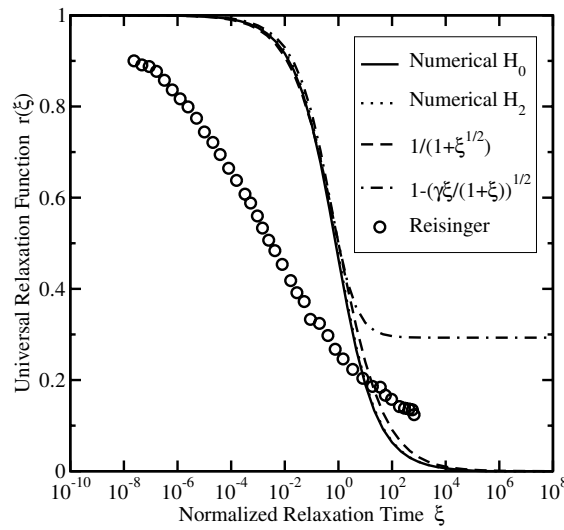


FIGURE 1.7: A comparison between simulations, analytical results, and measurement data following universal relaxation [60]. The circles mark measurement data while lines corresponds to simulations. Irrespective of the particular hydrogen species, the recovery according to RD theory extends to only 3 decades which is in strong contrast to experimental findings.

- The two-interface RD model [60, 78] is based on the assumption that atomic hydrogen released from the substrate interface reacts with Si – H bonds at the gate interface and then migrates inside the poly-gate with a lower diffusivity. This extension results in a power law with an exponent of $1/6$ during stress but yields a bump during relaxation. As in the case of the two-region, such a feature has not been observed in experiments.
- In a further variant of the RD model, the dimerization to molecular hydrogen does not occur due to an interface reaction but can take place over the whole bulk oxide. This assumption leads to an initial time exponent which changes from $1/3$ to $1/6$ for larger stress times in agreement with some measurements [74, 79]. However, the recovery remains the same as for the standard RD model and therefore does not follow the universal relaxation.

Experimentally, the most convincing proof that NBTI is not explained by the RD model comes from the TDDS [51, 53]. The spectral maps show clusters which are fixed on the emission time axis for a certain temperature and evolve with increasing stress time. By contrast, the RD model predicts clusters that extend towards larger emission times for rising stress times. Theoretical first-principles calculations of the Pantelides group [80–83] predict too high dissociation barrier for the interface reactions (1.14) and (1.15-1.16). In contradiction to the assumption of the RD model, Tsetseris *et al.* [81–83] proposed that the interface reaction can be initiated by protons originating from the substrate.

1.5.2 Dispersive Transport

In order to explain the long recovery tails seen in experiments, a refinement of the hydrogen transport in the RD model has been proposed. Due to the exposure to a hydrogen ambient during device fabrication, a large background concentration of hydrogen has to be expected. However, this background concentration would strongly enhance the reverse mode of the interface reaction so that no device degradation could occur. According to dispersive transport, a large fraction of the hydrogen particles is bonded to traps and thus cannot participate in the interface reaction. The retarded release of the strongly bonded particles during recovery [84] should bring the required long recovery tails. The hydrogen transport has been modeled to proceed over single trap levels, in which the particles dwell most of their time. Diffusion only takes place when the hydrogen atoms are released from their traps. This kind of transport is referred to as dispersive transport. Its formulation relies on multiple trapping theory [85–87] and was combined with the interfacial hydrogen reaction to the reaction dispersive diffusion (RDD) model [68, 73]. The overall hydrogen $H(x, t)$ concentration is split into a contribution of free hydrogen $H_c(x, t)$ in a conduction state and hydrogen $\rho_H(x, E_t, t)$ residing at traps with an energy level E_t :

$$H(x, t) = H_c(x, t) + \int \rho_H(x, E_t, t) dE_t. \quad (1.21)$$

The trap dynamics are expressed by balance equations for each trap

$$\partial_t \rho_H(E_t) = \frac{\nu_0}{N_{c,H}} (g(E_t) - \rho_H(E_t)) H_c - \nu_0 \exp\left(-\frac{E_c - E_t}{k_B T}\right). \quad (1.22)$$

with ν_0 being the attempt frequency, E_c the conduction state for hydrogen, and $N_{c,H}$ the effective density of conduction states. $g(E_t)$ stands for an exponential trap distribution. Only the free hydrogen as a migrating species X is accounted for in the diffusion equation:

$$\partial_t H_c = D_c \partial_x^2 H_c(x, t) + Z_c \mu_c F_{ox} \partial_x H_c(x, t) + \int \partial_t \rho_H(E_t) dE_t. \quad (1.23)$$

Here, the last term reflects the generation of free hydrogen, which escaped from their traps. The particular variants of the RDD model primarily differ in the postulate whether the free hydrogen H_c in the conduction state [25, 88] or the total hydrogen concentration H [37, 89] can enter the interface reaction (1.19). As pointed out in [31], neither variant of the RDD model can explain the long relaxation tails, irrespective of the assumed hydrogen species (see Fig. 1.8).

1.5.3 Reaction-Limited Models

The previous models rest on the assumption that hydrogen diffusion ultimately governs the generation of interface states. Another modeling approach assumes the interface reaction as the rate-limiting step. Due to the amorphous structure of SiO_2 , the Si–H bonds at the interface are subjected to a wide spread of bond lengths and angles, which are both related to large variations of bond strengths. In order to account for this fact, the associated dissociation barriers E_{ds} [38, 58, 69, 90] are taken to be

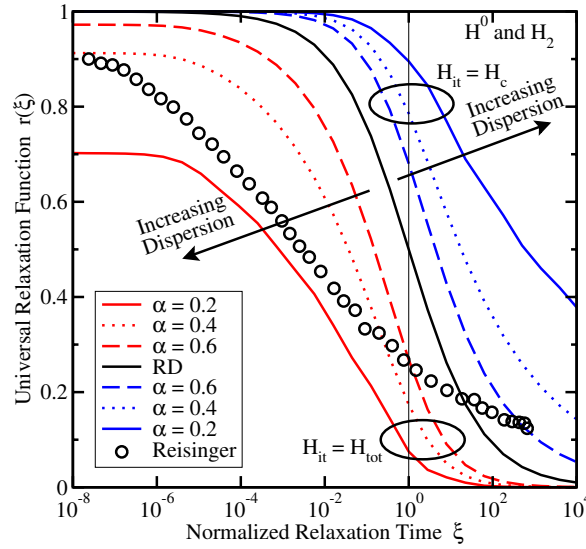


FIGURE 1.8: Simulated recovery curves for the RDD model based on either H (red) or H_c (blue) for various dispersion parameters α . In the case of H_c the recovery is predicted to end too early while it sets in too late for the H_c . As a consequence, this model is not capable of reproducing the long lasting relaxation of NBTI.

distributed rather than single-valued. According to transition state theory, the bond breakage rates follow an Arrhenius law and can be expressed as

$$k_f(E_{ds}) = k_{f,0} N_{it,0} \exp\left(-\frac{E_{ds}}{k_B T}\right), \quad (1.24)$$

where $k_{f,0}$ is an attempt frequency. Neglecting the corresponding reverse rate, simple first-order interface kinetics deliver

$$N_{it} = N_{it,0} (1 - \exp(-k_f(E_{ds}) t)) . \quad (1.25)$$

With a Fermi-derivative function for the distributions of dissociation barriers

$$g(E, E_{dsm}, \sigma_d) = \frac{1}{\sigma_{ds}} \frac{\exp\left(\frac{E - E_{dsm}}{\sigma_{ds}}\right)}{\left(1 + \exp\left(\frac{E - E_{dsm}}{\sigma_{ds}}\right)\right)^2}, \quad (1.26)$$

the interface state generation follows

$$\Delta N_{it} \approx N_{it,0} \frac{1}{1 + \left(\frac{t}{\tau}\right)^{-\alpha}} \quad (1.27)$$

with

$$\tau = 1/k_{f,0} \exp(E_{dsm}(F_{ox})/k_B T), \quad (1.28)$$

$$\alpha = k_B T / \sigma_{ds}. \quad (1.29)$$

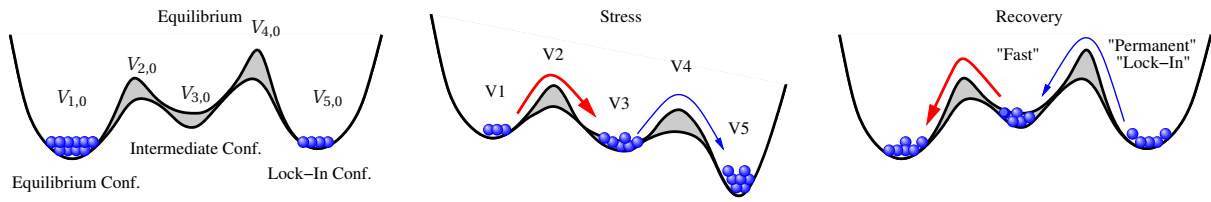


FIGURE 1.9: The schematic of the TWM. The double well represents the Born Oppenheimer surface with three stable configuration (states 1, 3, and 5 with the energies $V_{1,0}$, $V_{3,0}$, and $V_{5,0}$) and their separating barriers ($V_{2,0}$ and $V_{4,0}$). Transitions between two configurations or rather states are indicated by the arrows. Upon application of stress, the energies V_i are shifted down in energy according to $V_i = V_{i0} - i \times \Delta(T)$ with $\Delta(T)$ being a parameter and the defects move from state 1 to 5. When switching back to equilibrium conditions (recovery), the defects return to the state 1.

The field dependence is incorporated in the mean dissociation barrier E_{dm} , while the temperature activation originates from the spread σ_{ds} of the distribution (1.26). Due to a missing reverse rate k_r , this model cannot explain relaxation and must thus be assigned to the permanent component of NBTI. In an improved variant of this model [60], the rate equation (1.25) was extended by a reverse reaction with distributed barriers. Then the universal relaxation behavior can be accurately reproduced but the degradation during the stress phase is drastically underestimated ($n \sim 0.03$). Therefore, this model falls short of capturing both the stress and the relaxation phase at the same time.

1.5.4 Triple-Well Model

So far, the prolonged degradation and recovery are ascribed to the dispersive nature of either the interface reaction or the hydrogen transport in the oxide. Since both modeling attempts remained fruitless, a new model has been developed, which combines the dispersive interface reaction with a diffusion-like mechanism. The concept of the Born Oppenheimer energy surface [91–93] motivated the idea of the triple-well model (TWM) [94, 95] where the stable sites of hydrogen along with their separating barriers are represented in one common energy diagram (see Fig. 1.9). The dynamics of this system are expressed by coupled rate equations with Arrhenius-like expressions for transition rates following transition state theory. In a simplified mathematical model, there exist three states corresponding to an equilibrium, an intermediate and a lock-in configuration, which are connected in series. While the temperature activation is already incorporated in Arrhenius-type transition rates, the field acceleration is assumed to be due to an energetical downward shift of the intermediate and the lock-in states along with their connecting barriers (see Fig. 1.9). For instance, this shift can be related to breaking bonds with a dipole moment whose energy contribution depends on the oxide field.

During stress the hydrogen particles travel from the equilibrium towards the lock-in configuration, where a considerable fraction remains in the intermediate state. After the stress is removed, particles from the intermediate state first return to the equilibrium configuration. This fraction of particles correspond to the recoverable component of NBTI. The return of the other particles from the lock-

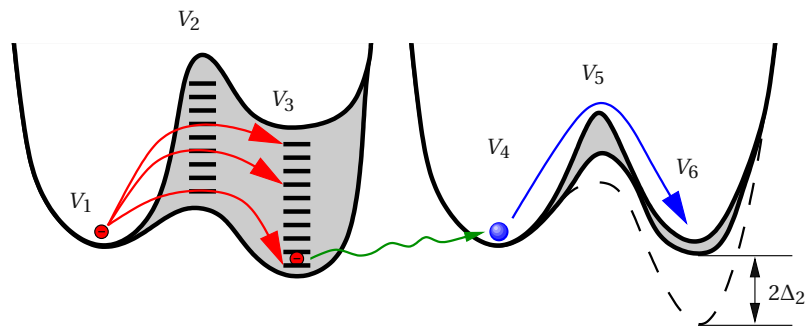


FIGURE 1.10: Schematic of the coupled double well model (CDW). The left well corresponds to the first step, which is described by a temperature-activated hole trapping process (V_1 - V_2 - V_3). The distribution of V_3 represents the spread in the hole trap levels, where V_2 reflects the required activation energies for this process. The field acceleration of the hole capture process was modeled by the term $\exp(-\Delta_1(F_{ox}))$, where the temperature-independent Δ_1 referred to as the stress parameter. The second step (V_4 - V_5 - V_6) mimics the release of hydrogen analogously to the description of the TWM.

in configuration occur at longer timescales and corresponds to the permanent or rather the slowly recoverable component of NBTI. In SiO_2 , the first transition mimics the interface reaction involving the hydrogen atom initially bonded to a P_b center, while the lock-in reflects the hydrogen diffusion away from the interface. In contrast to previous models, the triple-well model cannot only reproduce the complicated stress/relaxation pattern but also exhibits the correct temperature activation.

1.5.5 Combined Models

Investigations of the universal recovery (see Section 1.4) have revealed that there exists a permanent in addition to a recoverable component, where each of them are caused by their own physical mechanism. As a result, some sort of hole trapping into defects was suggested as the recoverable component and assumed to be due to elastic tunneling of holes into preexisting traps [58]. By contrast, a hydrogen reaction like the Si – H bond breakage in the RD model was ascribed to the permanent component. However, both mechanisms were assumed to be tightly coupled and therefore do not take place independently according the argumentation in Section 1.4.

A more promising approach assumes hole trapping “triggering” a hydrogen reaction as illustrated in Fig. 1.10. This model [24] relies on thermally activated tunneling into precursor defects. The captured charge weakens the hydrogen bond to the defect and thus causes the release of hydrogen. The last step corresponds to the permanent component of NBTI since the reaction of the defect with hydrogen requires considerably larger times compared to the hole trapping or detrapping process. Even though unprecedented accuracy is achieved for the stress and the relaxation phase at different temperatures and gate voltages, the field dependence of the stress parameter was phenomenologically introduced but has not been justified so far.

1.5.6 Conclusion

Electrical measurements, in particular MSM and OTF, have allowed to characterize NBTI on a phenomenological basis, but only give little insight into the underlying physical processes. Nevertheless, it has been possible to formulate criteria which can be used to evaluate the candidates for NBTI models (see Section 1.4). Additionally, TDDS experiments have revealed that NBTI is attributed to a superposition of individual charge capture or emission events with certain field and temperature dependences. In contrast to MSM and OTF, the TDDS findings shed light on the microscopic processes behind NBTI and therefore give an additional criteria for any NBTI model.

Despite of all this experimental information, none of the NBTI models proposed so far could fully explain all the findings from the aforementioned measurements. This is especially true for the RD model along with all its variants based on a dispersive nature of the interface reaction and/or the hydrogen reaction. As a consequence, the focus of this thesis is put on some kind of charge trapping as a possible explanation for NBTI.

1. INTRODUCTION

2

Fundamentals of Charge Trapping

As pointed out in Section 1.2, all tested variants of the RD model have been ruled out. Alternatively, the NBTI phenomenon may be ascribed to charge trapping into the oxide — a process that also involves tunneling of electrons and holes, respectively [22,57]. However, the underlying microscopic mechanism has only been vaguely understood so far and the developed models are often oversimplified [70, 96, 97].

This chapter provides a brief overview of miscellaneous charge trapping mechanisms at a microscopic level. On the one hand, these mechanisms involve electrons and holes located in the inversion layer of a MOSFET. Therefore, it will be necessary to address the electrostatics of such devices considering quantum mechanical effects, such as the formation of subbands and the penetration of the charge carriers into the dielectric. On the other hand, there are traps, whose properties are highly sensitive to the exact defect configuration. As a consequence, the defects must be addressed using an atomistic theory, which considers the structural relaxation of the defects and the thermal lattice vibrations for instance. The above considerations will lead to three basic charge trapping processes, which will be tested as a possible explanation for NBTI in this thesis.

These processes allow for a vast number of different transitions from the conduction or the valence band into one trap.. In the second part of this chapter, all possible transitions will be incorporated in compact rate expressions, which can be used for device simulation.

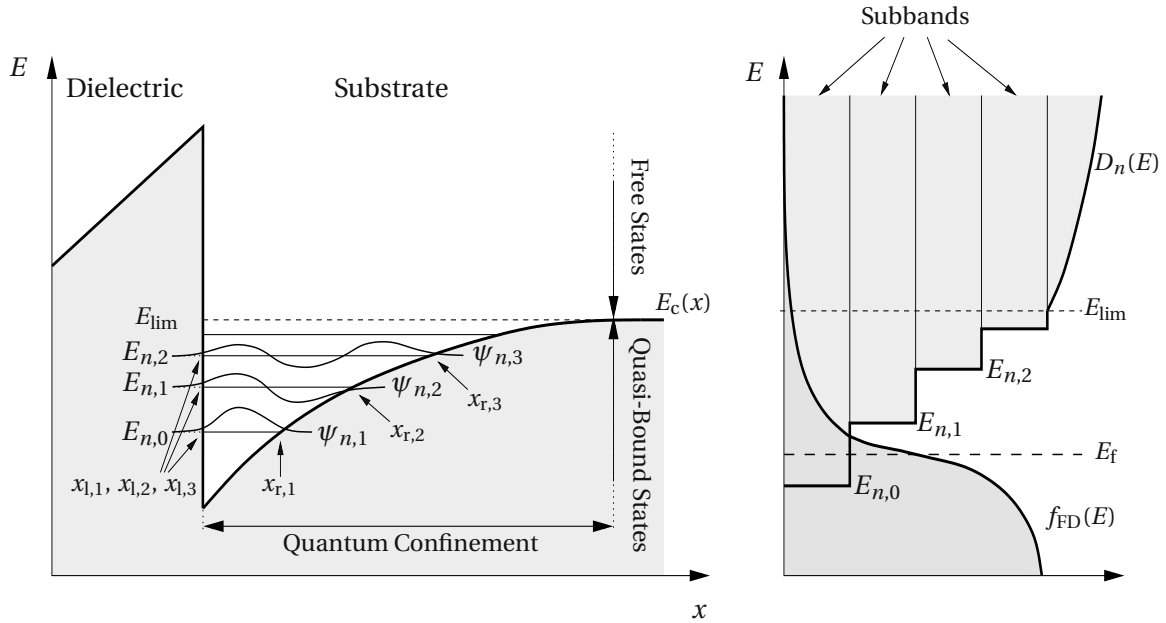


FIGURE 2.1: **Left:** A schematic band diagram of the inversion layer. The wavefunctions of the quasi-bound states $\psi_{n,0}, \psi_{n,1}, \psi_{n,2}, \dots$ are spatially confined between the dielectric on the left-hand side and the conduction band on the right-hand side. The free states encounter no boundary on the right-hand side and are energetically located above the quasi-bound states $E_{n,0}, E_{n,1}, E_{n,2}, \dots$ at the conduction band edge deep in the substrate (E_{lim}). **Right:** Schematic of the DOS $D_n(E)$ and the Fermi-Dirac distribution $f_{FD}(E)$. Each quasi-bound state associated with its own subband, resulting in a stepped DOS. The Fermi energy E_f places the Fermi-Dirac distribution relative to the DOS and determines the occupation of each state.

2.1 Tunneling — A Process Depending on Device Electrostatics

Since NBTI is triggered by the electric field F_{ox} across the dielectric, much importance is attached to the electrostatics within the device. Since source and drain are grounded during NBTI stress, the electrical potential remains almost constant along the interface so that the charge carriers face the same conditions for charge trapping over the entire channel area. As a consequence, the description of this process can be reduced to a one-dimensional problem (in the x -direction) where the electrostatics are only governed by the gate bias. The corresponding band diagram of a MOSFET with a p-doped silicon substrate biased in inversion is depicted in Fig. 2.1 (left). Due to the potential difference between substrate and gate, the band edges are strongly bent close to the interface so that the conduction band $E_c(x)$ forms a potential well. The electrons therein are confined to a small region close to the interface, which results in the build-up of discrete quasi-bound states $E_{n,1}, E_{n,2}, E_{n,3}, \dots$ as shown in Fig. 2.1. The energetical separation between these states narrows towards higher energies and changes to a continuum of free states at the energy E_{lim} . In the two other dimensions (yz -plane), the channel electrons behave as free particles and can therefore carry a current in these directions. The combination of quasi-bound and free states yields subbands as illustrated in Fig. 2.1 (right). Therefore, steps appear in the electron density of states (DOS) $D_n(E)$, where each step belongs to one subband. The occupation probability of a state is given by Fermi-Dirac statistics, which apply

as long as thermal equilibrium prevails. This is certainly the case for NBTI conditions, where the channel does not carry any appreciable current. Indeed, small and short channel current pulses, required in some measurement techniques to assess the NBTI degradation, lead to an overpopulation of high energy states. However, at the end of each pulse, the redistribution of the charge carriers back to equilibrium proceeds quickly and thus has not been noticed in experiments up to now. For this reason, electrons are assumed to obey the Fermi-Dirac statistics during NBTI conditions.

There exist several approximate methods to obtain the wavefunctions of bound states, however, each of them suffers from oversimplifications in certain regions. The first approach makes use of the Airy functions [98], which are solutions of the Schrödinger equation when the inversion layer is approximated by triangular potential well. Even though these functions satisfactorily reproduce the oscillatory behavior within the channel, they lack the exponential tails penetrating into the dielectric. This is due to the fact that the discontinuity at the interface is approximated by an infinitely high barrier. Another approach is provided by Gundlach's method [99] that focuses on the part of the wavefunctions located within the dielectric. The channel electrons, however, are modeled as free particles in a constant potential and thus the effect of the electric field within the channel is not considered in this method. The third analytical approach relies on the Wentzel-Kramers-Brillouin (WKB) approximation [100, 101] (see Appendix A.2), which stems from a semi-classical derivation. However, this approximation breaks down at the classical turning points $x_{l/r,1}$, $x_{l/r,2}$, $x_{l/r,3}$... where the energies of the quasi-bound states $E_{n,1}$, $E_{n,2}$, $E_{n,3}$, ... fall below the conduction band edge $E_c(x)$. This problem can be overcome using Langer's method [102], which yields reasonable results — even in a region close to the classical turning points — and is thus frequently applied for the calculation of the tunneling probability. The most interesting part of the wavefunctions lies in the region left to the interface where the WKB approximation is often simplified assuming a trapezoidal, a triangular, or even a rectangular energy barrier (see Appendix A.3). The above deficiencies can be overcome by numerically solving the Schrödinger equation for the whole region including the substrate and the dielectric. This, for instance, is carried out in a Schrödinger-Poisson solver, which also considers the electrostatics within the device (see Chapter 3).

The injection of electrons into the dielectric is hindered in crystal and amorphous structures due to the absence of any quantum states within their bandgap. Atomic arrangements, where the symmetry of the regular structure is broken, are termed defects. During processing they unavoidably arise in large abundance and are distributed over the whole oxide. Furthermore, these defects have orbitals that can potentially introduce energy levels within the insulator bandgap and are thus capable of capturing and emitting substrate charge carriers. The band edges of the dielectric are large energy barriers for the charge carriers in the substrate. Since the band offset between the substrate and the dielectric has values of several electron volts, thermal activation over these barriers is negligible when there is only a small bias applied between source and drain. However, the wavefunctions of the charge carriers feature quickly decaying tails into the oxide. This implies a non-zero probability of encountering charge carriers within the dielectric, meaning that they penetrate into the dielectric and can be captured by defects. The rates of such transitions are given by Fermi's golden rule.

$$r_{if} = \frac{2\pi}{\hbar} |M_{if}|^2 \delta(E_i - E_f) \quad (2.1)$$

The subscripts i and f denote the initial and the final state of the tunneling electron. M_{if} is a matrix element, which is associated with the transition and can be calculated as

$$M_{if} = \langle \psi_i | V | \psi_f \rangle. \quad (2.2)$$

The term $\delta(E_i - E_f)$ in equation (2.1) guarantees energy conservation before and after the transition. This kind of process is commonly referred to as ‘elastic’, where this term only refers to the energy of the exchanged electron.

Tewksbury [23] provided an expression for matrix element assuming a constant oxide field within the dielectric and a constant potential within the substrate. In his derivation, the trap was approximated by a δ -type potential

$$V(x) = E_c(x) - V_\delta \delta(x - x_t) \quad (2.3)$$

with $\delta(x)$ being the Dirac delta function. $E_c(x)$ and $V_\delta(x)$ are the conduction band edge in the oxide and the depth of the trap potential, respectively. The form of this potential implies that the integral in the matrix element only contributes directly at the center of the trap. Then the matrix element has the form

$$M_{if} = C \sqrt{k_x} \exp \left(- \int_{x_{if}}^{x_t} K_x(x') dx' \right), \quad (2.4)$$

where k_x and $K_x(x)$ are defined as the wavevectors within the substrate and the dielectric, respectively.

$$k_x^2 = \frac{2m_n}{\hbar^2} (E_x - V(x)) \quad (2.5)$$

$$K_x^2(x) = \frac{2m_t}{\hbar^2} (V(x) - E_x) \quad (2.6)$$

E_x denotes the energy of the electrons in the x -direction and C is a normalization constant. x_t stands for the spatial depth of a trap measured from the substrate-oxide interface and x_{if} is the position of the interface. m_t represents the tunneling mass and m_n is the electron mass in the conduction band. Note that the exponential term in equation (2.4) is the dominant factor in the matrix element. For slowly varying $K_x(x)$, it decays with increasing trap depth — a behavior characteristic for all kinds of tunneling processes. The WKB integral in its exponent originates from the phase factor of the channel wavefunction, whose corresponding wavevector $K_x(x)$ is often approximated to be constant for simplicity [23]. Due to the reduction to a one-dimensional problem, the δ -type trap potential covers the entire plane parallel to the interface. To correct for this shortcoming, Tewksbury introduced a capture cross section following the Freeman approach [103].

Lundstrom *et al.* [104] derived an expression of the matrix element assuming a step-potential for $E_c(x)$ and a three-dimensional δ -type trap potential [104].

$$M_{if} = C \sqrt{\frac{k_x K}{m_t^2 k_x + m_n^2 K_x}} e^{-K_x(x_t - x_{if})} \quad (2.7)$$

$$K^2 = \frac{2m_t}{\hbar^2} (V_0 - E) \quad (2.8)$$

$$K_x^2 = K^2 + k_y^2 + k_z^2 \quad (2.9)$$

V_0 stands for the height of the potential step. The wavevectors parallel to the interface are referred to as k_y and k_z . Due to the constant potential energy within the dielectric, the WKB integrand is reduced to a simple multiplication $K_x(x_t - x_{if})$. Keep in mind that the kinetic energy of the electrons perpendicular to the interface enters the exponential term in contrast to equation (2.4). The sum of this matrix element over all conduction band states assuming a free Fermi gas delivers a tunneling time constant of the form

$$\frac{1}{\tau(E, x)} = \frac{1}{\tau_0(K, k_x^2 + k_y^2 + k_z^2, x)} e^{-K(x_t - x_{if})}, \quad (2.10)$$

where the prefactor τ_0 is shown to weakly depend on the trap energy $E_t = E_x$ and the trap depth x_t . Note that wavevector K , the equivalent quantity to K_x in the one-dimensional case, enters the exponential term again.

The mechanism of pure elastic electron tunneling is often used as the standard explanation of charge trapping in MOSFETs. Over the time, several simplified expressions of tunneling rates have been published in numerous distinct charge trapping models [105, 106] and will be touched on for completeness below. Christenson *et al.* [106] used Shockley-Read-Hall statistics in order to investigate the low frequency noise spectrum of a MOS transistor. His hole capture rates incorporate a tunneling probability through a rectangular potential barrier depending on the depth of a trap x_t .

$$r = cn \exp\left(-\frac{2}{\hbar} \sqrt{2m_t W} x_t\right), \quad (2.11)$$

where c and W stand for a capture coefficient and the barrier height, respectively. A further improvement has been achieved by Scharf [97], who accounted for the energy dependence of the tunneling charge carriers.

$$r = \frac{1}{\tau_0(E, x_t, T)} \exp\left(-2 \int_{x_{if}}^{x_t} k(E) dx\right) \quad (2.12)$$

Here, the integral extends from the semiconductor-oxide interface x_{if} to trap depth x_t . Note that the second factor on the right-hand side of equation (2.12) corresponds to a WKB factor and reflects the exponentially decaying tunneling probability with increasing trap depth. However, this factor has been phenomenologically introduced by Scharf but does not arise from a rigorous derivation. The approximation provided by Tewksbury is the most suited one for the application to MOSFETs since it accounts for the energy and depth dependence and uses a convenient one-dimensional formulation of tunneling.

2.2 Franck-Condon Theory

Charge trapping models found in literature usually assume elastic electron tunneling, which ignores the atomic configuration of the defects. In the Franck-Condon theory [107–110], however, changes in the defect configuration play a crucial role in the charge trapping process. For instance, this theory predicts that the defect levels can be subject to a shift [111–114] (discussed in Section 2.2). In order

to support the physical understanding of such trapping processes, one has to deal with the basics of microscopic theories, which provide the most complete description of a physical process, such as charge trapping.

Therefore, the Schrödinger equation [91, 92] for a system involving electrons and nuclei is taken as a starting point. Its Hamiltonian \hat{H}_{tot} can be formulated as

$$\hat{H}_{\text{tot}}(\{\mathbf{R}_l\}, \{\mathbf{r}_m\}) = \hat{T}_e + \hat{V}_{\text{en}}(\{\mathbf{R}_l\}, \{\mathbf{r}_m\}) + \hat{V}_{\text{ee}} + \hat{T}_n + \hat{V}_{\text{nn}}(\{\mathbf{R}_l\}), \quad (2.13)$$

where the subscripts n and e refer to nuclei and electrons, respectively. \mathbf{r}_i and \mathbf{R}_j are the coordinates of a certain electron m or a certain nucleus l , respectively, whereas the curly braces stand for the whole set of coordinates, such as $\mathbf{r}_1, \mathbf{r}_2, \mathbf{r}_3, \dots$ for $\{\mathbf{r}_m\}$. The Hamiltonian \hat{H}_{tot} contains all contributions from the electrons (\hat{T}_e) and nuclei (\hat{T}_n) kinetic energies as well as from the Coulombic electron-electron \hat{V}_{ee} , nucleus-nucleus \hat{V}_{nn} , and electron-nucleus \hat{V}_{en} interactions. Then, the Schrödinger equation reads

$$\hat{H}_{\text{tot},j}(\{\mathbf{R}_l\}, \{\mathbf{r}_m\}) \Upsilon_j(\{\mathbf{R}_l\}, \{\mathbf{r}_m\}) = E_{\text{tot},j} \Upsilon_j(\{\mathbf{R}_l\}, \{\mathbf{r}_m\}), \quad (2.14)$$

where the energy of the whole system of the electrons and the nuclei is denoted as $E_{\text{tot},j}$. It is important to note at this point that the wavefunctions $\Upsilon_j(\{\mathbf{R}_l\}, \{\mathbf{r}_m\})$ depend on all positions of the electrons as well as the nuclei and thus the equation (2.14) cannot be solved due to its mathematical complexity.

In order to obtain an approximate solution, one usually employs the Born-Oppenheimer approximation, also known as the adiabatic approximation [91, 92], which states that the electrons move much faster than the nuclei. In this picture, the electrons instantaneously adapt to each atomic configuration and the motion of the nuclei can be neglected for the solution of the electron system. Based on this assumption the wavefunction $\Upsilon_j(\{\mathbf{R}_l\}, \{\mathbf{r}_m\})$ can be split into an electron ($\Psi_i(\{\mathbf{R}_l\}, \{\mathbf{r}_m\})$) and a nuclei ($\Phi_{ij}(\{\mathbf{R}_l\})$) part.

$$\Upsilon_j(\{\mathbf{R}_l\}, \{\mathbf{r}_m\}) = \sum_i \Psi_i(\{\mathbf{R}_l\}, \{\mathbf{r}_m\}) \Phi_{ij}(\{\mathbf{R}_l\}) \quad (2.15)$$

In a further consequence, this ansatz separates the electron and nuclei system, which are then characterized by the so-called ‘electronic’ and ‘vibrational’ states, respectively. The electron system is described by the electronic Schrödinger equation with a fixed nuclei configuration $\{\mathbf{R}_l\}$.

$$(\hat{T}_e + \hat{V}_{\text{en}}(\{\mathbf{R}_l\}, \{\mathbf{r}_m\}) + \hat{V}_{\text{ee}}(\{\mathbf{r}_m\}) + \hat{V}_{\text{nn}}(\{\mathbf{R}_l\})) \Psi_i(\{\mathbf{R}_l\}, \{\mathbf{r}_m\}) = E_i(\{\mathbf{R}_l\}) \Psi_i(\{\mathbf{R}_l\}, \{\mathbf{r}_m\}) \quad (2.16)$$

$\Psi_i(\{\mathbf{R}_l\}, \{\mathbf{r}_m\})$ stands for the many-electron wavefunction, which is a function of the electron coordinates $\{\mathbf{r}_m\}$. The nuclei have fixed positions $\{\mathbf{R}_l\}$ and enter the equation (2.16) as parameters only. Consequently, their positive charges form an external potential $\hat{V}_{\text{en}}(\{\mathbf{R}_l\}, \{\mathbf{r}_m\})$ to the electron system. The eigenvalues $E_i(\{\mathbf{R}_l\})$ of equation (2.16) re-enter the Schrödinger equation of the nuclei system,

$$(\hat{T}_n + E_i(\{\mathbf{R}_l\})) \Phi_{ij}(\{\mathbf{R}_l\}) = E_{\text{tot},ij} \Phi_{ij}(\{\mathbf{R}_l\}), \quad (2.17)$$

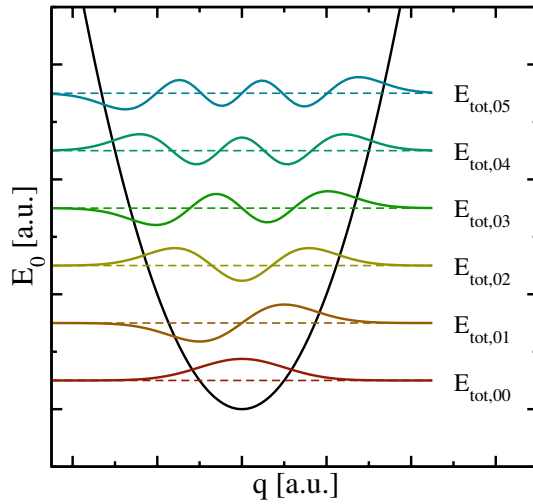


FIGURE 2.2: The configuration coordinate diagram of a nuclei system in a parabolic adiabatic potential (black solid line). The ordinate represents the total energy $E_{\text{tot},0j}$, where the electron system is assumed to be in its ground state. The abscissa is the configuration coordinate q , which describes the atomic configuration $\{\mathbf{R}_l\}$. The quantum mechanical nature of the nuclei is reflected in the formation of wavefunctions $\Phi_{0j}(\{\mathbf{R}_l\})$ (colored lines), each of which has its corresponding discrete energies $E_{\text{tot},0j}$.

and act as an external potential, in which the nuclei move. This potential is therefore referred to as the adiabatic potential or the potential energy surface. The nuclei in the Schrödinger equation (2.17) are treated as quantum mechanical particles. Therefore, they cannot be visualized as being to be located at certain points in space but are described by their wavefunctions $\Phi_{ij}(\{\mathbf{R}_l\})$. Furthermore, the energy spectrum of the nuclei system is quantized and includes discretized excitations known as lattice vibrations in crystals. In quantum chemistry, the nuclei system is frequently visualized in so-called configuration coordinate diagrams (see Fig. 2.2). The ordinate of these diagrams represents the total energy $E_{\text{tot},0j}$ presuming that the electron system is in its ground state. The abscissa is the configuration coordinate q , which summarizes the nuclei configuration $\{\mathbf{R}_l\}$ in one quantity. It is important to note here that the coupling of the two Schrödinger equations (2.16) and (2.17) results in so-called ‘vibronic’ states, which are combinations of the electronic and the vibrational states and are defined by the wavefunctions $\Psi_i(\{\mathbf{R}_l\}, \{\mathbf{r}_m\}) \cdot \Phi_{ij}(\{\mathbf{R}_l\})$ and their corresponding energy $E_{\text{tot},ij}$.

According to the Franck-Condon principle [107–110], these vibronic transitions involve a change in the electronic as well as in the vibrational state. The corresponding rate can be calculated using Fermi’s golden rule (see Appendix A.1)

$$r_{a\alpha b\beta} = \frac{2\pi}{\hbar} M_{a\alpha b\beta}^2 \delta(E_{\text{tot},a\alpha} - E_{\text{tot},b\beta}), \quad (2.18)$$

$$M_{a\alpha b\beta} = \left| \left\langle \Phi_{a\alpha}(\{\mathbf{R}_l\}) \left| \left\langle \Psi_a(\{\mathbf{R}_l\}, \{\mathbf{r}_m\}) \right| V' \right| \Psi_b(\{\mathbf{R}_l\}, \{\mathbf{r}_m\}) \right\rangle \right| \Phi_{b\beta}(\{\mathbf{R}_l\}) \right| \quad (2.19)$$

with V' being the perturbation operator. $a\alpha$ and $b\beta$ denote the initial and the final vibronic state, respectively, where the latin and greek symbols refer to the electronic and vibrational states.

According to the Franck-Condon approximation, the matrix element $M_{a\alpha b\beta}$ can be separated into two factors:

$$M_{a\alpha b\beta} = \left| \left\langle \Phi_{a\alpha}(\{\mathbf{R}_l\}) \left| \Phi_{b\beta}(\{\mathbf{R}_l\}) \right\rangle \right| \cdot \left| \left\langle \Psi_a(\{\mathbf{R}_l\}, \{\mathbf{r}_m\}) \left| V' \right| \Psi_b(\{\mathbf{R}_l\}, \{\mathbf{r}_m\}) \right\rangle \right| \quad (2.20)$$

Using the above equation, the transition rate (2.19) can be rewritten as

$$r_{a\alpha b\beta} = A_{ab} f_{a\alpha b\beta}, \quad (2.21)$$

$$A_{ab} = \frac{2\pi}{\hbar} \left| \left\langle \Psi_a(\{\mathbf{R}_l\}, \{\mathbf{r}_m\}) \left| V' \right| \Psi_b(\{\mathbf{R}_l\}, \{\mathbf{r}_m\}) \right\rangle \right|^2, \quad (2.22)$$

$$f_{a\alpha b\beta} = \left| \left\langle \Phi_{a\alpha}(\{\mathbf{R}_l\}) \left| \Phi_{b\beta}(\{\mathbf{R}_l\}) \right\rangle \right|^2. \quad (2.23)$$

Here, A_{ab} denotes the electronic matrix element and is associated with an electronic transition, for instance electron or hole tunneling in the case of charge trapping in defects. The Franck-Condon factor $f_{a\alpha b\beta}$ gives the probability of the vibrational transition, which is determined by the overlap of the nuclei wavefunctions. The probability for such a transition is lower than that for the electron transition. Therefore, $f_{a\alpha b\beta}$ becomes the decisive factor in equation (2.21).

2.3 The Level Shift

The Frank-Condon theory provides a theoretically profound description of vibronic transitions and has a wide range of applications in quantum chemistry, such as the calculation of the absorption and fluorescence spectra. In the following, this theory will be employed for the case of charge trapping into oxide defects and will lead to a shift of the defect levels. This level shift can be best explained using a configuration coordinate diagram of a defect (depicted in Fig. 2.3). The neutral defect is represented by the curve $U_0(q)$, which can, for instance, be identified with the formation energy U_f of the defect¹. In equilibrium, the neutral defect takes on its minimum configuration q_1 labeled with A in Fig. 2.3. If the defect is charged positively, one electron has to be removed from the defect and placed within the substrate valence band, for instance at E_v . As a consequence, the electron energy E_v must be added to the defect energy $U_+(q)$ for a correct comparison with $U_0(q)$. But one should consider that vibronic transitions can occur with each conduction or valence band state in the substrate, including the energies $E_{0/+}$ and $E_{+/0}$. As mentioned before, the transition rates for charge trapping can be calculated using the Franck-Condon theory. The corresponding equation (2.21) depends most strongly on the factor $f_{a\alpha b\beta}$, which is determined by the overlap of the nuclei wavefunctions. This factor reaches the largest values for vibrational transitions, whose energies lie close the intersection point (IP) of the adiabatic potentials. In the classical limit, it is even peaked at the energy of this intersection point, at which the vibronic transition is assumed to occur. During a hole capture process, the neutral defect is initially in its equilibrium configuration q_1 (state A in Fig. 2.3). There, the defect has an energy of $U_0(q_1)$, which only intersects with $U_+(q_1)$ when the emitted electron is placed at the energy level $E_{0/+}$ in the substrate valence band. It is emphasized

¹ The formation energy corresponds to the energy required to piece together a defect out of its individual components and can be determined from first-principles calculations, such as density functional theory.

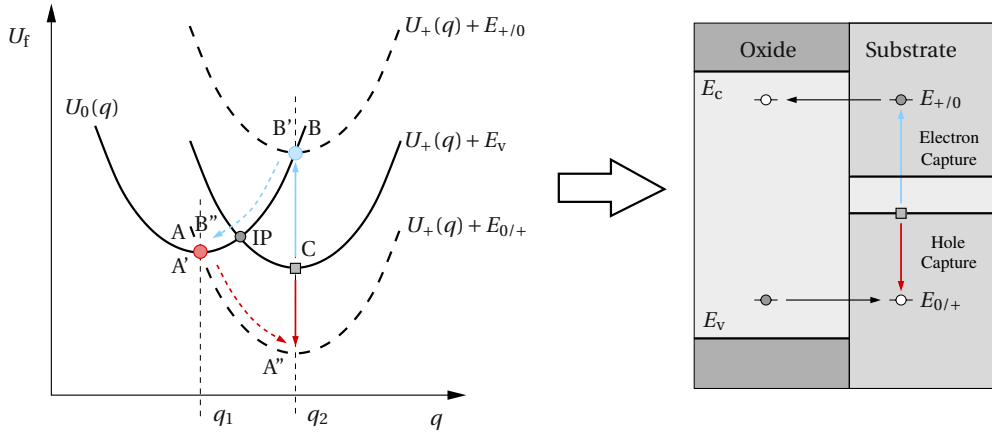


FIGURE 2.3: The configuration coordinate diagram of a defect in its positive and neutral charge state (left) and the corresponding trap levels in the band diagram (right). The solid curves $U_+(q) + E_v$ and $U_0(q)$ represents the adiabatic potentials of the positive and neutral defect system, respectively. In the former case, the tunneling electron is moved to the substrate where it sits at the valence band edge. When the electron has a different energy, for instance $E_{0/+}$ or $E_{+/0}$, the corresponding adiabatic potential is shifted on the energy scale and depicted by the dashed lines. The red and the blue filled circle indicates the points, where the hole and electron trapping process can occur. These points only represent the temporary states, which are realized right after the tunneling process. The band diagram on the right-hand side includes the defect levels extracted from the configuration coordinate diagram (left). The resulting electron ($E_{+/0}$) and hole capture ($E_{0/+}$) level can be separated by several electron Volts, where only one of these two levels can be active at a time. Interestingly, the energy level $E_{+/0}$ must always lie above $E_{0/+}$ due to the positive curvature of the adiabatic potentials.

here that the defect is assumed not to overcome the barrier over the intersection point IP (path $C \rightarrow IP \rightarrow A$ in Fig. 2.3) in the concept of the level shift. During the tunneling transition of the electron, the defect is not capable of adopting the new configuration of the new charge state according to the Franck-Condon principle. Afterwards, it is in the state A' and relaxes to the equilibrium configuration q_2 (state A''). During this process, the defect dissipates the relaxation energy of $U_+(q_1) - U_+(q_2)$ to the heat bath. In the case of an electron capture process, the defect is initially in its equilibrium configuration q_2 labeled with B in Fig. 2.3. A vibronic transition is only allowed, if a substrate electron is excited to the energy $E_{+/0}$ (from state A' to B) by the heat bath. Then the defect plus the electron have an energy of $U_+(q_2) + E_{+/0}$ (state B in Fig. 2.3), which coincides with the energy of the neutral defect $U_0(q_2)$. Analogously to the hole capture process, the defect configuration q_2 is preserved during the tunneling transition (state B'). Afterwards the defect undergoes a structural relaxation to state B'' thereby dissipating an energy of $U_0(q_2) - U_0(q_1)$ to the heat bath. The aforementioned electron levels $E_{0/+}$ and $E_{+/0}$ are usually referred to as switching levels and can be defined as the difference of adiabatic potential energies:

$$E_{0/+} = U_0(q_2) - U_+(q_2) \quad (2.24)$$

$$E_{+/0} = U_0(q_1) - U_+(q_1) \quad (2.25)$$

There is a the shift between energy levels for electron ($E_{+/0}$) and hole ($E_{0/+}$) capture. This difference is ascribed to the fact that the defects have different equilibrium configurations q_1 and q_2 for different

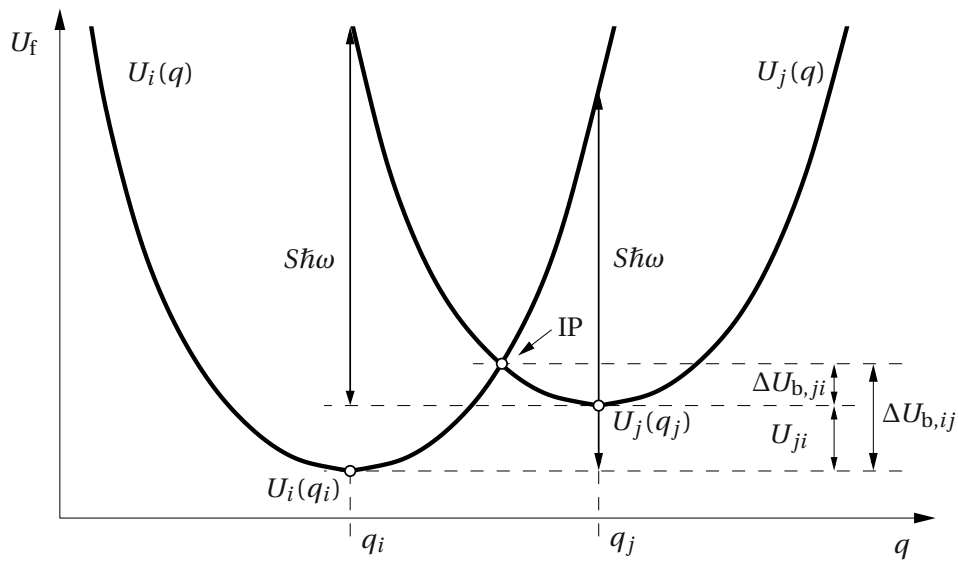


FIGURE 2.4: The configuration coordinate diagram for the NMP model. The two parabolas $U_i(q)$ and $U_j(q)$ show the adiabatic potentials for the case that the electron is located in the channel or the defect, respectively. IP labels the intersection point of $U_i(q)$ and $U_j(q)$, where the NMP process takes place in the classical approximation. The electron capture or emission rates are primarily determined by the NMP barriers $\Delta U_{b,ij}$ and $\Delta U_{b,ji}$, respectively.

charge states of the defect. As a consequence, an ‘elastic’ vibronic transition can only occur at different energies in the configuration coordinate diagram. This requires that the exchanged electron has different energies $E_{+/0}$ and $E_{0/+}$ for electron and hole capture — a fact that has motivated the term ‘level shift’. It is important to note at this point that the above considerations are not restricted to defect transitions between positive and neutral charge states and can in principle be extended to all possible combinations of charge states.

In conclusion, the conventional concept of fixed trap levels must be questioned if a defect has distinct equilibrium configurations for two charge states. Instead, the trap/defect levels depend on their charge state, which can have a considerable impact on the trapping dynamics. Although this concept has not been applied to charge trapping so far, it can give an explanation for trap-assisted tunneling through dielectrics [112, 113].

2.4 Nonradiative Multi-Phonon Theory

For the level shift, it has been implicitly presumed that vibronic transitions always take place at equilibrium configurations of the defects. Thereby, it has been ruled out that the defects are thermally excited² up to the intersection points of their adiabatic potentials (see Fig. 2.4). However, this case has been accounted for in the nonradiative multi-phonon theory (NMP) [107, 115]. This mechanism has

² In solid-state physics, the thermal excitations are associated with a distortion of defects and the absorption of phonons. By contrast, the structural relaxation of defects is related to the emission of phonons.

already been suggested for random telegraph noise and $1/f$ noise in microelectronic devices [56], where only a simplified description of NMP process has been employed. Furthermore, it is also encountered in the context of phonon-assisted tunneling ionization of deep centers [116–118] and discussed on various levels of theoretical sophistication [55, 119–122] including additional second-order effects, such as the Coulomb energy [123–125] and field-enhancement factors [116, 117].

In NMP theory, the equation (2.21) is generalized to account for all possible thermal excitations. Then the equation (2.21) must be rewritten as

$$r_{ab} = A_{ab} f_{ab}^{\text{LSF}}, \quad (2.26)$$

$$f_{ab}^{\text{LSF}} = \text{ave} \sum_{\alpha} f_{a\alpha b\beta}, \quad (2.27)$$

where f_{ab}^{LSF} is referred to as the lineshape function. ‘ave’ denotes the thermal average over all initial vibrational states α and accounts for the thermal excitations using a sum over weighted Boltzmann factors. The lineshape function eventually depends on the Franck-Condon factor and thus on the complicated shape of the adiabatic potentials of the defects. It is noted that these potentials are not assessable via experiments but can also not be calculated using first-principles calculations (see Section 3.3), which would by far exceed the current computational capabilities. However, they can be reasonably approximated using the harmonic approximation when only small displacements from the equilibrium configuration of the defects are considered. In this approximation, the adiabatic potentials are represented as a Taylor expansion whose linear term vanishes close to the equilibrium configuration. As a result, these potentials become parabolic and therefore, describe harmonic oscillators frequently used in solid state physics. A corresponding configuration coordinate diagram for the vibronic transitions of a defect is depicted in Fig. 2.4. The total energies $U_i(q)$ and $U_j(q)$ in Fig. 2.4 include the contributions from the defect atoms along with its immediate surrounding (and the channel region) and therefore correspond to the adiabatic potentials $E_{\text{tot},ij}(\{\mathbf{R}_l\})$. For this reason, their corresponding adiabatic potentials differ only in the location of electron involved in the trapping process. In the case of $U_i(q)$, the electron resides in the channel while, for $U_j(q)$, it is located at the defect site. In the harmonic approximation, the adiabatic potentials can be written as:

$$U_i(q) = \frac{1}{2} M \omega^2 (q - q_i)^2 + U_i \quad (2.28)$$

$$U_j(q) = \frac{1}{2} M \omega^2 (q - q_j)^2 + U_j \quad (2.29)$$

ω stands for the vibrational frequency of the oscillator and determines the curvature of the parabola while M is the mass of the oscillator. Analogously to the previous section, the classical vibronic transitions are assumed to occur at the intersection points of the adiabatic potentials. Therefore, the defect system must be thermally excited from its initial configuration $U_i(q_i)$ to the intersection point IP of the two parabolas in Fig. 2.4. At this point, the total energies $U_i(q)$ and $U_j(q)$ equal and allow for an elastic tunneling transition. From there, the system relaxes to the equilibrium configuration q_j with the energy $U_j(q_j)$. The energy difference between $U_i(q)$ and $U_j(q)$ can be expressed as

$$\begin{aligned} \Delta U(q) &= U_j(q) - U_i(q) \\ &= U_{ji} + S \hbar \omega - \sqrt{2S} \hbar \omega \sqrt{\frac{M\omega}{\hbar}} (q - q_i). \end{aligned} \quad (2.30)$$

$U_{ji} = U_j(q_j) - U_i(q_i)$ is the so-called thermodynamic trap level. It is given relative to the conduction or the valence band edge for electron or hole trapping³ and determines the occupancy of the defect in thermal equilibrium. As demonstrated in Fig. 2.4, the Huang-Rhys factor S is defined by the energy differences $U_j(q_i) - U_j(q_j)$ and $U_i(q_j) - U_i(q_i)$, which are both equivalent to S phonons with an energy of $\hbar\omega$. That is, this quantity determines the intersection point of the parabolas and eventually impacts the probability for an electron transition between the defect and the channel. In the above NMP concept, it has been assumed that the charge state of the defect does not affect the curvatures of $U_i(q)$ and $U_j(q)$. As a result, only a linear term in q appears in equation (2.30). Note that its sign is determined by the relative positions of q_i and q_j but has no physical meaning. The forward and reverse barrier of this process are given by

$$\Delta U_{b,ij} = \frac{(U_{ji} + S\hbar\omega)^2}{4S\hbar\omega} \quad (2.31)$$

and

$$\Delta U_{b,ji} = \frac{(U_{ji} - S\hbar\omega)^2}{4S\hbar\omega}, \quad (2.32)$$

respectively.

The NMP mechanism was suggested several decades ago but has been disregarded in the context of NBTI so far. Nevertheless, this mechanism should be considered as a possible description of charge trapping in NBTI. The underlying theory relies on the complicated quantization effects of the nuclei system and is therefore quite complex in its original variant. However, several convenient and accurate approximations, including the version presented in this section, have been developed over the years and allow for theoretical investigations on a device level.

2.5 Effective Rates into Single Traps

Up to this point, trapping has been defined for transitions from one band state in the substrate into one trap state or vice versa. Each of the possible transitions is associated with one rate entering the trapping dynamics. In order to reduce the set of rate equations, compact analytical expressions for the overall trapping rates into one defect are required. In this section, a derivation of the sought expressions will be presented for the case of elastic as well as inelastic tunneling.

2.5.1 Elastic Electron Tunneling

The derivation below follows the approach of Tewksbury [23] with some slight modifications. For a proper description of charge trapping, Fermi's golden rule is taken as a starting point. This

³ Here it has been implicitly presumed that the electrons or holes lie exactly at the conduction or valence band edge, respectively. However, if quantum confinement in the inversion layer is considered, the band edges must be replaced by the energy of the first quasi-bound state in the respective band.

fundamental law (see Appendix A.1) gives the rate for a transition between a certain initial and final state. In its most general form it reads:

$$r_{tb} = \frac{2\pi}{\hbar} |M_{tb}|^2 \delta(E_t - E_b) \quad (2.33)$$

The subscripts t and b denote a trap or a band state, respectively, and M_{tb} represents the tunneling matrix element. The δ -function indicates that the electron energy before and after the transition must be conserved as it is required for elastic tunneling. In semiconductor devices, the charge carriers captured in the dielectric can originate from several different energy levels of the substrate valence or conduction band. In order to account for their contribution to the whole tunneling rate, the sum over all \mathbf{k} states has to be taken.

$$r = \sum_{\mathbf{k}} \frac{2\pi}{\hbar} |M_{t\mathbf{k}}|^2 \delta(E_t - E(\mathbf{k})) \quad (2.34)$$

Here, E_t and $E(\mathbf{k})$ is the trap level and the electron energy in the substrate, respectively. The subscript t in equation (2.33) has been omitted since only tunneling into and out of a certain trap is considered. The matrix element $M_{t\mathbf{k}}$ involves the trap wavefunction, whose exact form is in general unknown. Often, the calculation of the matrix element is simplified to a one-dimensional δ -type trap potential. Its solution [23],

$$M_{c/v, tk_x}(E_x, x_t) = M_{c0/v0, tk_x}(E_x, x_t) \zeta_{\text{WKB}, c/v}(E_x, x_t), \quad (2.35)$$

consists of the factors

$$M_{c0/v0, tk_x}(E_x, x_t) = \frac{\hbar^2 K_{c/v, x}(E_x, x_t)}{m_t} \sqrt{\frac{k_{c/v, x}(E_x)}{2L_x}} \quad (2.36)$$

and

$$\zeta_{\text{WKB}, c/v}(E_x, x_t) = \exp\left(-\int_{x_{\text{if}}}^{x_t} K_{c/v, x}(E_x, x_t) dx\right) \quad (2.37)$$

with

$$K_{c/v, x}^2(E_x, x) = \frac{2m_t}{\hbar^2} |E_{c/v, \text{ox}}(x) - E_x|, \quad (2.38)$$

$$k_{c/v, x}^2(E_x) = \frac{2m_{n/p}}{\hbar^2} |E_x - E_{c/v, \text{sc}}(x_{\text{if}})|. \quad (2.39)$$

Note that electron and hole tunneling proceed through an energy barrier formed by the oxide conduction and valence band, respectively. The matrix elements for these cases are labeled by 'c' and 'v', accordingly. The second factor $\zeta_{\text{WKB}, c/v}(E_x, x_t)$ of the matrix element in equation (2.35) arises from the exponential decay of the electron wavefunction, which can be derived using the WKB approximation. Since this factor shows a dependence on the carrier kinetic energy $|E_x - E_{c/v, \text{sc}}(x)|$ perpendicular to the interface, the summation over all band states must be split into a one-dimensional and a two-dimensional part (see Appendix A.4):

$$\sum_{\mathbf{k}} = L_x A_{yz} \left(\int_{E_c}^{\infty} \int_{E_c}^E D_{n, 1D+2D}(E_x) dE_x dE + \int_{-\infty}^{E_v} \int_E^{E_v} D_{p, 1D+2D}(E_x) dE_x dE \right), \quad (2.40)$$

$$D_{n/p, 1D+2D}(E_x) = \frac{m_{n/p}}{\pi^2 \hbar^3} \sqrt{\frac{m_{n/p}}{2|E_x - E_{c/v, \text{sc}}(x)|}}. \quad (2.41)$$

In $D_{n/p,1D+2D}(E_x)$ a factor of two has been introduced in order to account for spin degeneracy. Note that the DOS has been derived based on the parabolic band approximation, however, the potential well in the inversion layer gives rise to the formation of subbands (see Section 2.1) and in consequence a different DOS. This means that the equation (2.40) neglects quantization effects in the inversion layer. Nevertheless, inserting the expression (2.40) into equation (2.34) yields

$$r = L_x A_{yz} \frac{2\pi}{\hbar} \left(\int_{E_c}^{\infty} \int_{E_c}^E D_{n,1D+2D}(E_x) |M_{c0,tb}(E_x, x_t)|^2 \zeta_{\text{WKB},c}^2(E_x, x_t) \delta(E_t - E) dE_x dE \right. \\ \left. + \int_{-\infty}^{E_v} \int_E^{E_v} D_{p,1D+2D}(E_x) |M_{v0,tb}(E_x, x_t)|^2 \zeta_{\text{WKB},v}^2(E_x, x_t) \delta(E_t - E) dE_x dE \right), \quad (2.42)$$

which can be simplified to

$$r = L_x A_{yz} \frac{2\pi}{\hbar} \left(\int_{E_c}^{E_t} D_{n,1D+2D}(E_x) |M_{c0,tb}(E_x, x_t)|^2 \zeta_{\text{WKB},c}^2(E_x, x_t) dE_x \right. \\ \left. + \int_{E_t}^{E_v} D_{p,1D+2D}(E_x) |M_{v0,tb}(E_x, x_t)|^2 \zeta_{\text{WKB},v}^2(E_x, x_t) dE_x \right). \quad (2.43)$$

The factor $\zeta_{\text{WKB},v}(E_x, x_t)$ enters the above equation as a square, which corresponds to a transmission coefficient of an electron through an energy barrier [126], and will be referred to as the ‘WKB factor’ in the following.

In this derivation, the calculation of the matrix element has been reduced to a one-dimensional problem in favor of a compact and analytical expression. In order to correct for this approximation, the term $\sigma_{n/p,xy}/A_{yz}$ must be introduced following Freeman’s approach [103].

$$r(E_t) = r_e(E_t) + r_h(E_t) \quad (2.44)$$

$$r_e(E_t) = L_x \frac{2\pi}{\hbar} \int_{E_c}^{E_t} D_{n,1D+2D}(E_x) \sigma_{n,yz} |M_{c0,tb}(E_x, x_t)|^2 \zeta_{\text{WKB},c}^2(E_x, x_t) dE_x \quad (2.45)$$

$$r_h(E_t) = L_x \frac{2\pi}{\hbar} \int_{E_t}^{E_v} D_{p,1D+2D}(E_x) \sigma_{p,yz} |M_{v0,tb}(E_x, x_t)|^2 \zeta_{\text{WKB},v}^2(E_x, x_t) dE_x \quad (2.46)$$

Keep in mind that these equations describe elastic tunneling, meaning that a trap can only exchange charge carriers with those bound states, whose energy E coincides with the trap level E_t — even though E can have different components E_x . In this derivation, the cross-sections $\sigma_{n/p,yz}$ correspond to fitting parameters but can be estimated by analytical expressions presented in [23]. Since the values obtained by these expressions range around 10^{-16} cm^2 and are subject to small variations, the cross-sections are assumed to be constant throughout this thesis.

2.5.2 Shockley-Read-Hall Theory

Compact expressions for inelastic transitions are provided by the framework of the Shockley-Read-Hall (SRH) theory [127]. It has been developed to describe recombination centers in bulk but has also been extended for the case of electron or hole trapping into dielectrics [128]. The following derivation of the SRH rates is generalized to NMP transitions, presuming the case of hole trapping, and starts from equation (2.27).

$$r_{tb}(E) = A_{tb} f_{tb}^{\text{LSF}}(E_t, E_b) \quad (2.47)$$

The trap and the band state involved in the NMP transition are labeled by the subscripts t and b , respectively. E_t denotes the thermodynamic trap level and E_b an arbitrary state in the valence band. Since the NMP theory assumes thermal transitions, the energies of the states t and b may differ, meaning that the trap can in principle exchange charge carriers with the entire valence band. In order to account for this fact, a sum over all band states has to be carried out.

$$r_t(E) = \sum_b A_{tb} f_{tb}^{\text{LSF}}(E_t, E_b) \quad (2.48)$$

Employing to the parabolic band approximation (see Section A.45), the sum over all band states b can be approximated by an integral over the valence band DOS $D_p(E)$, where E can be identified with the energy E_b of the valence band state b (see Appendix A.4).

$$\sum_b = L_x A_{yz} \int_{-\infty}^{E_v} D_p(E) dE \quad (2.49)$$

Using the expression (2.49), the transition rate can be rewritten as

$$r_{tb}(E) = L_x A_{yz} \int_{-\infty}^{E_v} A_{tb}(E) f_{tb}^{\text{LSF}}(E) D_p(E) dE. \quad (2.50)$$

For a hole capture process, one must account for the joint probability that the trap must be occupied by an electron while the band state with an energy E is empty. The first condition is considered by the trap occupancy f_t . The second one can be expressed by

$$f_p = 1 - f_{\text{FD}} \quad (2.51)$$

with f_{FD} being the Fermi-Dirac distribution

$$f_{\text{FD}}(E) = \frac{1}{1 + \exp(\beta(E - E_f))}, \quad (2.52)$$

$$\beta = \frac{1}{k_B T}. \quad (2.53)$$

With this joint probability, one obtains the rate equation for hole capture,

$$\partial_t f_t = -L_x A_{yz} \int_{-\infty}^{E_v} f_t A_{tb}(E) f_{tb}^{\text{LSF}}(E) D_p(E) f_p(E) dE, \quad (2.54)$$

where the ‘minus’ sign on the right-hand side in the above equation reflects the fact that the trap occupancy is decreased by a hole capture event. An analogous argumentation for hole emission yields

$$\partial_t f_t = L_x A_{yz} \int_{-\infty}^{E_v} (1 - f_t) A_{bt}(E) f_{bt}^{\text{LSF}}(E) D_p(E) f_n(E) dE, \quad (2.55)$$

where f_n equals the Fermi-Dirac distribution f_{FD} . Combining the rate equations for hole capture (2.54) and emission (2.55) and using the shorthands

$$c_p(E) = L_x A_{yz} A_{tb}(E) f_{tb}^{\text{LSF}}(E), \quad (2.56)$$

$$e_p(E) = L_x A_{yz} A_{bt}(E) f_{bt}^{\text{LSF}}(E), \quad (2.57)$$

one obtains

$$\partial_t f_t = \int_{-\infty}^{E_v} ((1 - f_t) e_p(E) f_n(E) - f_t c_p(E) f_p(E)) D_p(E) dE \quad (2.58)$$

$$= \int_{-\infty}^{E_v} \left((1 - f_t) \frac{e_p(E)}{c_p(E)} f_n(E) - f_t f_p(E) \right) c_p(E) D_p(E) dE. \quad (2.59)$$

If thermal equilibrium is assumed [127], the trap level E_t is occupied according to the Fermi-Dirac statistics

$$f_t(E) = f_{\text{FD}}(E_t) = \frac{1}{1 + \exp(\beta(E_t - E_t))} \quad (2.60)$$

and detailed balance

$$\partial_t f_t = 0 \quad (2.61)$$

must be employed. Using the identity

$$f_n(E) = \exp(-\beta(E - E_t)) f_p(E) \quad (2.62)$$

one obtains

$$\frac{e_p(E)}{c_p(E)} = \exp(-\beta(E_t - E)). \quad (2.63)$$

Inserting this result back into equation (2.59) yields

$$\partial_t f_t = ((1 - f_t) \exp(-\beta(E_t - E_t)) - f_t) \int_{-\infty}^{E_v} c_p(E) D_p(E) f_p(E) dE. \quad (2.64)$$

The hole capture time constant can be expressed as

$$\frac{1}{\tau_{\text{cap,h}}} = \frac{\int_{-\infty}^{E_v} c_p(E) D_p(E) f_p(E) dE}{\underbrace{\int_{-\infty}^{E_v} D_p(E) f_p(E) dE}_{\equiv \sigma_p^{\text{SRH}} v_{\text{th},p}}} p, \quad (2.65)$$

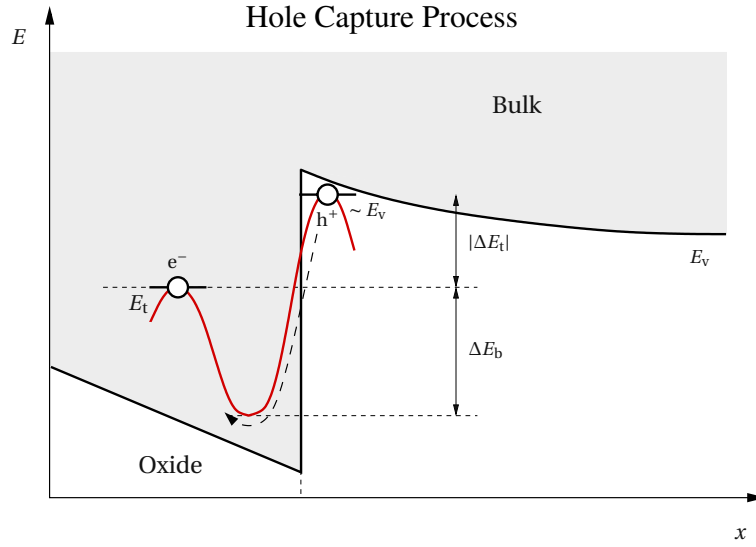


FIGURE 2.5: The transition barrier for a hole capture process with $E_t < E_v$. The hole is initially located in the bulk at an energy level $\sim E_v$. Its capture can be imagined to proceed over a downwards directed barrier of the height $|\Delta E_t| + \Delta E_b$. For this process, an minimum energy of ΔE_t is required to push down the hole from E_v to E_t . As a consequence, the forward barrier is higher than its reverse counterpart by a value of $|\Delta E_t|$. The rest of the barrier height is accounted for by ΔE_b , which is assumed to have a finite value for generality. It is noted here that the SRH theory [127] has been derived without assuming thermal barriers. Therefore, this theory is usually considered for processes proceeding without or with a negligible thermal barrier.

where the first term on the right-hand side of the above equation is defined as the product of a cross section σ_p^{SRH} and the thermal velocity $v_{\text{th},p}$. The definition of the hole emission time constant follows from equation (2.64).

$$\partial_t f_t = (1 - f_t) \underbrace{\sigma_p^{\text{SRH}} v_{\text{th},p} p \exp(-\beta(E_t - E_f))}_{=1/\tau_{\text{em},h}} - f_t \underbrace{\sigma_p^{\text{SRH}} v_{\text{th},p} p}_{=1/\tau_{\text{cap},h}}$$

For the ratio of the time constants, one obtains the well-known relation

$$\frac{\tau_{\text{cap},h}(E)}{\tau_{\text{em},h}(E)} = \exp(-\beta(E_t - E_f)) , \quad (2.66)$$

which is frequently invoked in the context of charge trapping — in particular for NMP models [55, 56, 121, 124, 125]. Note that the quantity σ_p^{SRH} in equation (2.65) contains the matrix element A_{tb} and the Frank-Condon factor $f_{tb}^{\text{LSF}}(E_t, E_b)$. The former is associated with an electron tunneling process and thus often approximated by a WKB factor. The latter is strongly determined by the barrier height of an NMP transition (see Section 2.4). This suggests that also the cross section σ_p^{SRH} in the SRH theory should somehow reflect this barrier dependence. For a hole capture process with $E_t < E_v$ (cf. Fig. 2.5), the barrier height can be split into two components, namely $|\Delta E_t|$ and ΔE_b . The former is defined as

$$\Delta E_t = E_{t,0} - E_{v,0} , \quad (2.67)$$

where $E_{t,0}$ and $E_{v,0}$ are the trap level and the valence band edge in the absence of an electric field. The value of $|\Delta E_t|$ corresponds to minimal energy required for a transition. The latter, that is ΔE_b ,

represents only the remainder to the overall barrier $|\Delta E_t| + \Delta E_b$. For the $E_t > E_v$, the component $|\Delta E_t|$ vanishes and only ΔE_b remains. Using the above definitions of the barriers, the cross section can be written as

$$\sigma_p^{\text{SRH}} = \sigma_{p,0}^{\text{SRH}} \exp(-x_t/x_{p,0}) \begin{cases} \exp(-\beta\Delta E_b), & E_t > E_v \\ \exp(-\beta\Delta E_b) \exp(-\beta(E_v - E_t)), & E_t < E_v \end{cases}, \quad (2.68)$$

where $\sigma_{p,0}^{\text{SRH}}$ and $x_{p,0}$ denote a temperature-independent cross section and the characteristic tunneling length. It is remarked at this point that the transition barriers has been assumed to be independent of the energy of the holes.

$$1/\tau_{\text{cap},h} = \sigma_{p,0}^{\text{SRH}} \nu_{\text{th},p} p \exp(-x_t/x_{p,0}) \exp(-\beta\Delta E_b) \begin{cases} 1, & E_t > E_v \\ \exp(-\beta(E_v - E_t)), & E_t < E_v \end{cases}, \quad (2.69)$$

$$1/\tau_{\text{em},h} = \sigma_{p,0}^{\text{SRH}} \nu_{\text{th},p} p \exp(-x_t/x_{p,0}) \exp(-\beta\Delta E_b) \begin{cases} \exp(-\beta(E_t - E_f)), & E_t > E_v \\ \exp(-\beta(E_v - E_f)), & E_t < E_v \end{cases}. \quad (2.70)$$

Making use of

$$\begin{aligned} p &= N_v \exp(-\beta(E_f - E_v)), \\ E_v &= E_{v,0} - q_0\varphi_s, \\ E_t &= E_{t,0} - q_0\varphi_s - q_0F_{\text{ox}}x_t \end{aligned} \quad (2.71)$$

with $E_{t,0}$ and N_v being the trap level in the flat band case and the effective valence band weights, respectively, the rates (2.69) and (2.70) can be rewritten as

$$1/\tau_{\text{cap},h} = \frac{p}{\tau_{p,0}^{\text{SRH}} N_v} \exp(-x_t/x_{p,0}) \exp(-\beta\Delta E_b) \begin{cases} 1, & E_t > E_v \\ \exp(\beta\Delta E_t) \exp(-\beta q_0 F_{\text{ox}} x_t), & E_t < E_v \end{cases}, \quad (2.72)$$

$$1/\tau_{\text{em},h} = \frac{1}{\tau_{p,0}^{\text{SRH}}} \exp(-x_t/x_{p,0}) \exp(-\beta\Delta E_b) \begin{cases} \exp(-\beta\Delta E_t) \exp(\beta q_0 F_{\text{ox}} x_t), & E_t > E_v \\ 1, & E_t < E_v \end{cases} \quad (2.73)$$

with

$$\frac{1}{\tau_{p,0}^{\text{SRH}}} = N_v \nu_{\text{th},p} \sigma_{p,0}^{\text{SRH}}. \quad (2.74)$$

The corresponding expression for electron trapping from the conduction band can be derived in an analogous manner and reads

$$1/\tau_{\text{cap},e} = \frac{n}{\tau_{n,0}^{\text{SRH}} N_c} \exp(-x_t/x_{p,0}) \exp(-\beta\Delta E_b) \begin{cases} \exp(-\beta\Delta E_t) \exp(\beta q_0 F_{\text{ox}} x_t), & E_t > E_c \\ 1, & E_t < E_c \end{cases}, \quad (2.75)$$

$$1/\tau_{\text{em},e} = \frac{1}{\tau_{n,0}^{\text{SRH}}} \exp(-x_t/x_{p,0}) \exp(-\beta\Delta E_b) \begin{cases} 1, & E_t > E_c \\ \exp(\beta\Delta E_t) \exp(-\beta q_0 F_{\text{ox}} x_t), & E_t < E_c \end{cases} \quad (2.76)$$

with

$$\frac{1}{\tau_{n,0}^{\text{SRH}}} = N_c \nu_{\text{th},n} \sigma_{n,0}^{\text{SRH}}. \quad (2.77)$$

Finally, it should be mentioned that the conventional SRH theory as established in [127] does not account for charge carrier tunneling and the possible presence of thermal barriers.

3

Applied Methods

3.1 Schrödinger-Poisson Solver

All NBTI models share the same challenge, namely to explain the correct field acceleration and temperature activation of the ΔV_{th} degradation. These experimentally observed dependences must be traced back to the physics in a MOSFET. The most frequently used charge trapping models require the band diagram, the electric field across the insulator, and the spatial distribution of the inversion charge carriers. This information can easily be computed via a Poisson-solver (P-solver) or a Schrödinger-Poisson solver (SP-solver) [129] if quantum mechanics are assumed to play a crucial role.

The electrostatics within a MOS device are described by the Poisson equation

$$\epsilon \nabla_x \varphi(x) = -\rho(x) , \quad (3.1)$$

where $\varphi(x)$ denotes the electrical potential. The charge density

$$\rho(x) = q_0 (p(x) - n(x) - N_a(x) + N_d(x)) \quad (3.2)$$

is decomposed into the charge carrier densities of the electrons $n(x)$ and holes $p(x)$ and the ionized dopant concentration of acceptor $N_a(x)$ and donator $N_d(x)$ atoms. The charge carrier densities at the point x are expressed as

$$n(x) = \int_{E_c}^{\infty} D_n(E, x) f_{FD}(E) dE , \quad (3.3)$$

$$p(x) = \int_{-\infty}^{E_v} D_p(E, x) (1 - f_{\text{FD}}(E)) dE, \quad (3.4)$$

where f_{FD} stands for the Fermi-Dirac distribution, which determines the occupation of the conduction and valence band states and is given by

$$f_{\text{FD}}(E) = \frac{1}{1 + \exp(\beta(E - E_f))} \quad (3.5)$$

Its validity rests upon thermal equilibrium between the charge carriers in a specific region of the MOS device. This assumption is well justified when no voltage is applied between source and drain of a MOSFET during NBTI stress. In the parabolic band approximation the electron (D_n) and hole (D_p) DOS in equation (3.3) and (3.4) are defined by

$$D_n(E, x) = \sum_v \frac{g_v m_{n,v}^{3/2}}{\hbar^2 \pi^2} \sqrt{2(E - E_c(x))}, \quad (3.6)$$

$$D_p(E, x) = \sum_v \frac{g_v m_{p,v}^{3/2}}{\hbar^2 \pi^2} \sqrt{2(E_v(x) - E)}. \quad (3.7)$$

$m_{nn/p,v}$ is the electron/hole effective mass with a degeneracy of g_v , where v denotes the valley index. E_f , E_c , and E_v stand for the Fermi energy, the conduction, and the valence band edge, respectively. The electrostatic potential $\varphi(x)$ enters the calculation of the conduction ($E_c(x)$) and the valence ($E_v(x)$) band edge as follows:

$$E_c(x) = E_{c,0} - q_0 \varphi(x) \quad (3.8)$$

$$E_v(x) = E_{v,0} - q_0 \varphi(x) \quad (3.9)$$

$E_{c,0}$ and $E_{v,0}$ denote the conduction and the valence band edge energy in the flat band case, respectively. Due to the mutual dependence between $\varphi(x)$, on the one hand, and the carrier densities $n(x)$ and $p(x)$, on the other hand, the equations (3.1)-(3.9) must be solved self-consistently. This has been achieved by a P-solver, whose functionality relies on a numerical iteration scheme, visualized in Fig. 3.1.

More realistic simulations must account for the quantum confinement of the charge carriers in the inversion layer. This effect arises from the band bending, which forms a potential well for one type of charge carriers. As described in Section 2.1, this well enters as the potential in the one-dimensional Schrödinger equation, whose solution consists of the single quasi-bound states of electrons and holes. These states are required for the calculation of the carrier densities

$$n(x) = \int_{E_{n,0}}^{E_{\text{lim},n}} \sum_v g_v \frac{m_{n,v,yz}}{\hbar^2 \pi} \sum_i \Theta(E - E_{n,i}) |\psi_{n,i}(x)|^2 f_{\text{FD}}(E) dE, \quad (3.10)$$

$$p(x) = \int_{E_{\text{lim},p}}^{E_{p,0}} \sum_v g_v \frac{m_{p,v,yz}}{\hbar^2 \pi} \sum_i \Theta(E - E_{p,i}) |\psi_{p,i}(x)|^2 (1 - f_{\text{FD}}(E)) dE, \quad (3.11)$$

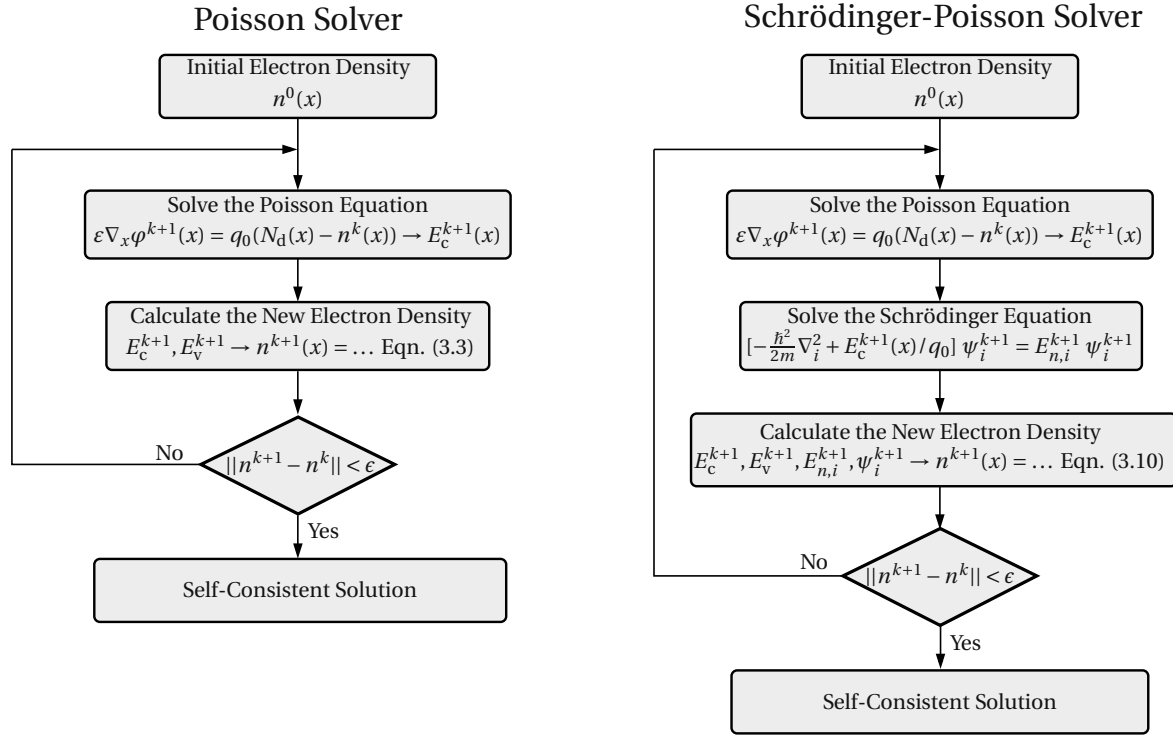


FIGURE 3.1: A flow chart diagram of the Newton iteration scheme used in the Poisson (left) and the Schrödinger-Poisson solver (right). The procedure is only discussed for electrons in the conduction band for simplicity but it also holds true for holes in the valence band using analogous formulas. In both iteration schemes, the old electron density $n^k(x)$ enters the Poisson equation and a new electrical potential $\varphi^{k+1}(x)$ is obtained, which is then required to calculate the new electron density $n^{k+1}(x)$. In a Poisson solver the new electron density $n^{k+1}(x)$ is evaluated using the semi-classical formula (3.3). By contrast, in the Schrödinger-Poisson solver the bound states must be determined, which are then taken to evaluate the new electron density $n^{k+1}(x)$ according to equation (3.10). Using the newly computed $n^{k+1}(x)$, the iteration loop is continued at the Poisson step until the update $\|n^{k+1}(x) - n^k(x)\|$ falls below a certain limit ϵ .

where $\Theta(x)$ stands for the Heaviside step function defined by

$$\Theta(x) = \begin{cases} 1, & x \geq 0 \\ 0, & x < 0 \end{cases}. \quad (3.12)$$

$E_{n,i}$ denotes the energy of the electron quasi-bound state i and $\psi_{n,i}(x)$ is the corresponding channel wavefunction. The single subbands of the quasi-bound states add up to the electron DOS within the potential well, which is formed by $E_c(x)$ and limited by $E_{\text{lim},n}$. Outside this region, the charge carriers are calculated according to equations (3.6) for the free states. Similarly, the hole quasi-bound states $E_{p,i}$ with the channel wavefunction $\psi_{p,i}$ form subbands within the energy range between E_v and $E_{\text{lim},p}$. For the calculation of the band diagram, the Poisson equation and the Schrödinger equation must be solved self-consistently since they are coupled through the electrostatic potential $\varphi(x)$ and the charge carrier concentrations, $n(x)$ and $p(x)$. In a SP-solver, this system of coupled equations is treated using a self-consistent iteration method, outlined in Fig. 3.1. Throughout this

thesis, the Vienna Schrödinger Poisson (VSP) solver [130] has been applied for the calculation of the band diagram and the charge carrier concentrations.

3.2 From Rates to Degradation Curves

The last section has been devoted to the possible physical explanations for the charge trapping process in NBTI. The involved mechanisms, such as quantum mechanical tunneling for instance, are characterized by their stochastic nature. This means that one must deal with probabilities instead of pre-determined transition times for the trapping events. Such problems can be best handled within the framework of homogeneous continuous-time Markov chain theory [131], which rests on the assumption that the transition rates do not depend on the past of the investigated system.

The continuous time Markov chain theory presumes a set of discrete states $S \in \{1, \dots, N\}$:

$$\Pi(t) = (\pi_1(t), \pi_2(t), \dots, \pi_N(t)) \quad (3.13)$$

The $\pi_i(t)$ are the time-dependent occupation probabilities, which fulfill the normalization condition

$$\sum_{i \in S} \pi_i(t) = 1. \quad (3.14)$$

This equation states that the probability of finding the system in one of the states $i \in S$ equals unity. The time-dependent probability p_{ij} for a transition from state i to state j can be formulated as

$$p_{ij}(\Delta t) = P\{X(t + \Delta t) = j | X(t) = i\} = r_{ij}\Delta t + O(\Delta t), \quad (3.15)$$

$$p_{ii}(\Delta t) = P\{X(t + \Delta t) = i | X(t) = i\} = 1 - \sum_{j \neq i} r_{ij}\Delta t + O(\Delta t), \quad (3.16)$$

where r_{ij} denotes the transition rate belonging to p_{ij} . The time evolution of the system can be described by the first-order partial differential equation

$$\partial_t \pi_i(t) = \underbrace{\sum_{j \neq i} \pi_j(t) r_{ji}}_{\text{transitions into state } i} - \underbrace{\sum_{j \neq i} \pi_i(t) r_{ij}}_{\text{transitions out of state } i}. \quad (3.17)$$

The above equation is referred to as the Master or rate equation and controls the time-dependent occupation probabilities. The first term on the right-hand side represents the transitions $T_{j \rightarrow i}$ while the second term stands for the opposite direction. With the definition

$$r_{ii} = - \sum_{j \neq i} r_{ij} \quad (3.18)$$

the rate equation (3.17) can be rewritten as

$$\partial_t \Pi(t) = \Pi(t) \cdot \mathbf{R}, \quad (3.19)$$

where \mathbf{R} denotes the matrix belonging to the elements r_{ij} . The solution of equation (3.19) is given by

$$\Pi(t) = \Pi(0) \cdot \exp(\mathbf{R}\Delta t) \quad (3.20)$$

and can be expanded into a truncated Taylor series.

$$\Pi(t) \approx \Pi(0) \cdot (1 + \mathbf{R}\Delta t) \quad (3.21)$$

Assuming detailed balance, the time derivative of $\Pi(t)$ vanishes and the equilibrium occupation probabilities Π_{eq} must satisfy

$$\Pi_{\text{eq}} \cdot \mathbf{R} = 0. \quad (3.22)$$

In the case of charge trapping, a single defect is represented by one vector $\Pi(t)$. When considering a large ensemble of defects, the stochastic behavior vanishes and $\pi_i(t)$ and $\Pi(t)$ can be replaced by their corresponding expectation values $f_i(t)$ and $\mathbf{F}(t)$, respectively. Then the equations (3.19) and (3.22) read

$$\partial_t \mathbf{F}(t) = \mathbf{F}(t) \cdot \mathbf{R} \quad (3.23)$$

and

$$\mathbf{F}_{\text{eq}} \cdot \mathbf{R} = 0, \quad (3.24)$$

respectively.

When applying Markov theory to charge trapping in NBTI, each state must be assigned to a certain configuration and a certain charge state of a defect. The rates r_{ij} linking the states i and j must be related to certain defect transitions, such as charge transfer reactions or thermally activated rearrangements of the defect structure. The trapping dynamics are then governed by equation (3.23), which must be solved as a function of time. The details of the applied numerical procedures are outlined in Fig. 3.2.

Before the real device is subject to stress, the device is assumed to be in equilibrium. The corresponding band diagram is computed by a P/SP-solver (A) for the equilibrium conditions $V_G = V_{\text{eq}}$ and $T = T_{\text{eq}}$. Based on this information, the transition rates $r_{\text{eq},ij,m}$ (B) can be evaluated for each defect m . With the rates $r_{\text{eq},ij,m}$ at hand, the equilibrium occupation probabilities $f_{\text{eq},i,m}$ are calculated using the equation (3.24) and must be subsequently stored (C). When stress sets in, the gate voltage V_G and the temperature T are changed to V_s and T_s , respectively. Since this alters the band diagram and in consequence the transition rates $r_{s,ij,m}$, the S/SP-solver step (D) and the calculation of the rates (E) must be repeated. Then the implicit Euler method is employed for the numerical time integration of equation (3.23). This iteration scheme must be continued until the end of the stress time t_s has been reached. At each t_k , the change in the defect occupancies $\Delta f_{i,m}(t_{k+1})$ (G) and the corresponding threshold voltage shift $\Delta V_{\text{th}}(t_{k+1})$ (H) are computed. With the beginning of the relaxation phase, V_G and T are modified again and the whole iteration loop including the steps D, E, F, G, and H must be repeated. This can be continued for several stress/relaxation cycles with different stress/relaxation conditions. The steps E, F, and G of numerical procedure in Fig. 3.2 must be repeated for each individual defect, where the calculation of the rates requires most of the computation time.

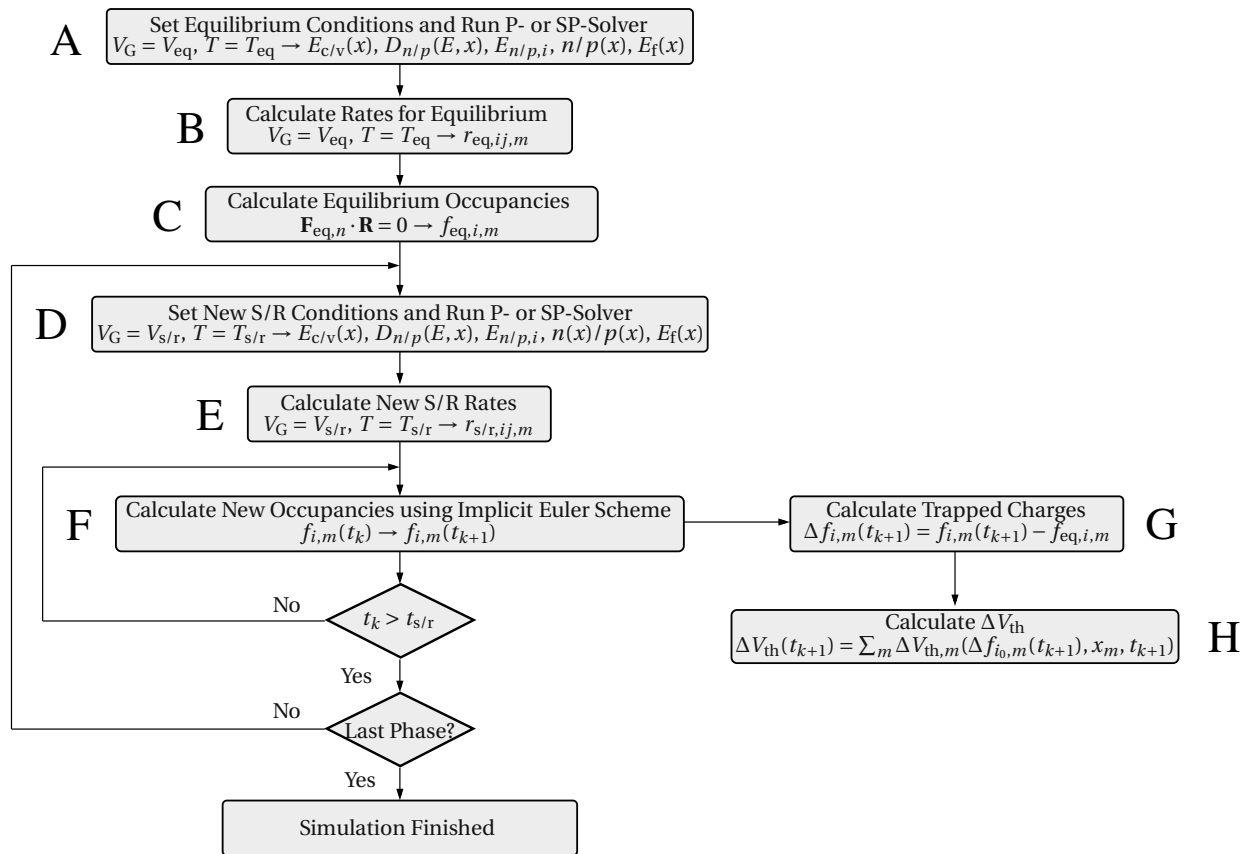


FIGURE 3.2: A flow chart diagram for the calculation of stress/relaxation curves. At first, the occupations for equilibrium conditions ($V_G = V_{eq}$, $T = T_{eq}$) are calculated in steps A, B, and C. During one stress or relaxation cycle, the band edges (D) and the transition rates (E) must be determined at first. Then the corresponding the time-dependent occupations (F) and the resulting threshold voltage shift (G,F) are evaluated at each time step t_k . This complete cycle must be performed for each stress or relaxation phase.

For the evaluation of ΔV_{th} , the charge sheet approximation is employed.

$$\Delta V_{th,m} = \frac{q_0 t_{ox}}{\epsilon_r \epsilon_0} \left(1 - \frac{x_m}{t_{ox}} \right) \Delta f_{i_0,m} \quad (3.25)$$

x_m and t_{ox} are the trap depth and the thickness of the dielectric, respectively. The above expression gives the threshold voltage shift $\Delta V_{th,m}$ due to a single trap m in the ‘charged’ state i_0 . It is noted that the term in the parentheses of equation (3.25) accounts for the trap depth dependence of $\Delta V_{th,m}$ according to which traps closer to the interface have a larger impact on the threshold voltage. However, there also exists a strong dependence on the lateral location of the traps, totally neglected in the above equation. Recall in this context that the V_{th} steps in the TDDS measurements have also been caused by single charged traps. The wide variations of these steps have been ascribed to the position of the traps relative to the current percolation path and follow an exponential distribution according to an investigation carried out by Kazcer *et al.* [50]. This issue has been intensively studied under the name random dopant fluctuations [50, 132–134] and gained large interest due to its serious influence on the lifetime projection. For instance, the charging of one defect can even produce step

heights in the threshold voltage beyond 30mV, which already violates typical lifetime criteria. By contrast, the charge sheet approximation rests on the assumption that a trapped charge is distributed over the whole plane parallel to the interface. Therefore, variations in the threshold voltage shift due to random dopant fluctuations remain unconsidered in this approximation.

Small-area devices often contain only a handful of defects. Then the steps B, C, E, F, G, and H can be performed at computationally feasible costs. But since the calculation time increases with the number of defects, the simulation of large-area devices can become time-consuming. In order to reduce computation time for these simulations, a certain number of defects with similar properties are grouped together and replaced by one representative trap. This approach implies that the channel area covers several defects with similar properties including the trap level and the spatial location among others¹. Furthermore, it is important to note here that the value of trap density is often quite inaccurate and can differ by some orders of magnitude. Therefore, the number of traps must be treated as a variable in the simulations. This means that the calculated degradation curves can be scaled to the experimental data in order to achieve reasonable agreement of the simulations with the measurements.

3.3 Density Functional Theory

3.3.1 Introduction

In material science, numerous research topics are related to microscopic processes. The description of these processes often relies on quantities which are not assessable by experiments but can be extracted from atomistic simulations. In the past, so-called first-principles calculations have been successfully employed for the determination of those quantities. These calculations solve the Schrödinger equation of the electrons for a given atomic configuration, and therefore, they do not depend on any fitting parameters. At this point it should be noted that the knowledge about the exact atomic configuration is often vague, which can sometimes be a serious issue. For instance, it is frequently debated whether the Si/SiO₂ interface is abrupt or graded or even has defects, such as suboxides or protrusions. One prominent example of first principle calculations is the Hartree-Fock method. It takes the fundamental exchange interactions² into account but suffers from a complete neglect of electron correlations and thus fails to reproduce some fundamental properties in solid state physics. Since Hartree-Fock simulations scale badly with the number of electrons, they perform unsatisfactorily with respect to the computational costs when more than only a few tens of atoms are considered. Therefore an alternative approach based on the electron density has been pursued. It is termed density functional theory (DFT) [91, 92, 136] and can be considered as the workhorse in the field of microscopic simulations. In the following, the basics of this method will be explained.

¹ Note that this assumption fails for small devices with only a few defects. In this case, the stochastic nature of the trapping process emerges and the device degradation must be understood in terms of expectation values and variances of the threshold voltage shift. Then, the calculations must be tackled with a stochastic simulation algorithm [135].

² The exchange interactions arise from the asymmetry of the many-electron wavefunction — a consequence of the fact that electrons are Fermions.

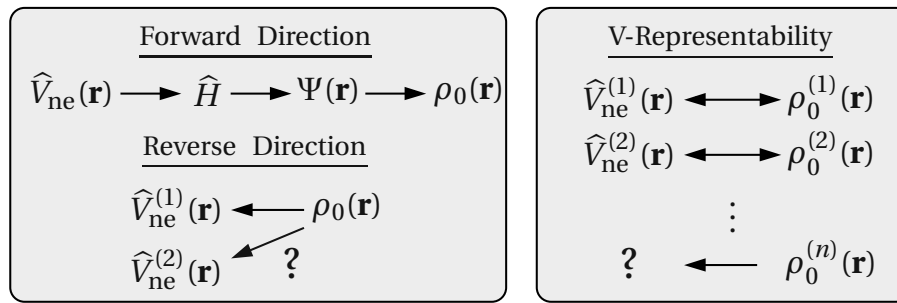


FIGURE 3.3: **Left:** The mapping of the external potential onto the electron density obviously holds true, however, its reverse direction is the central issue of the HK theorem. **Right:** Electron densities that do not correspond to any external potential violate the requirement of V-representability and thus pose in principle a problem to DFT.

3.3.2 The Basic Concepts of DFT

The first main idea of DFT is to reformulate the energy of an atomic system as a functional of the ground state electron density instead of the electron wavefunction. The proof of existence for such functionals relies on a one-to-one correspondence between the external potential $\hat{V}_{\text{en}}(\{\mathbf{R}_l\}, \{\mathbf{r}_m\})$ and the ground state electron density $\rho_0(\mathbf{r})$. The mapping of $\hat{V}_{\text{en}}(\{\mathbf{R}_l\}, \{\mathbf{r}_m\})$ onto $\rho_0(\mathbf{r})$ is obvious: Any Hamiltonian \hat{H} with a given external potential $\hat{V}_{\text{en}}(\{\mathbf{R}_l\}, \{\mathbf{r}_m\})$ has a ground state solution with an N -electron wavefunctions $\Psi_0(\mathbf{x})$, which can be uniquely identified with an electron density $\rho_0(\mathbf{r})$ using

$$\rho_0(\mathbf{r}) = N \int |\Psi_0(\mathbf{r}_1, \mathbf{r}_2, \dots, \mathbf{r}_N)|^2 \delta(\mathbf{r} - \mathbf{r}_1) d\mathbf{r}_1 \dots d\mathbf{r}_N. \quad (3.26)$$

The other direction of this mapping (see Fig. 3.3) was proven by the Hohenberg-Kohn (HK) theorem [137]. Due to the resulting one-to-one correspondence between $\hat{V}_{\text{ne}}(\mathbf{r})$ and $\rho_0(\mathbf{r})$, the energy of the atomic system E_i can be expressed as a functional of the electron density $\rho_0(\mathbf{r})$. Note that DFT is actually restricted to so-called ‘V-representable’ electron densities, however, this is not an issue in the practical use.

The many-electron wavefunction used in equation (3.26) reads

$$\Psi(\mathbf{x}) = \Psi(\mathbf{r}_1, \mathbf{r}_2, \dots, \mathbf{r}_N), \quad (3.27)$$

where its form depends on the ‘combination’ of all spatial electron coordinates. Unfortunately, such an approach would by far exceed any computational capabilities. However, this problem can be overcome using the Kohn-Sham (KS) ansatz, in which the fully-interacting system is replaced by a non-interacting one. This ansatz corresponds to a mean-field approach, where the wavefunction is decomposed into a product of single-electron orbitals $\psi_i(\mathbf{r})$. This simplification leads to a neglect of an energy contribution termed ‘correlations’. As a correction, the functional $E_{\text{cx}}[\rho(\mathbf{r})]$ must be introduced as an additional term in the Hamiltonian. It is noted that this term does not only account for the correlations but also for the unconsidered exchange interactions. Applying the variation principle to the modified Hamiltonian yields a single-particle Schrödinger equation, also referred to as Kohn-Sham equation in DFT. This equation includes an effective potential $\nu_{\text{eff}}(\mathbf{r})$, which is

produced by the Coulomb forces of all other electrons and nuclei and incorporates the exchange and correlation interactions.

$$\left(-\frac{\hbar^2}{2m_e}\nabla^2 + v_{\text{eff}}(\mathbf{r})\right) \psi_i^{\text{KS}}(\mathbf{r}) = \varepsilon_i^{\text{KS}} \psi_i^{\text{KS}}(\mathbf{r}) \quad (3.28)$$

$$v_{\text{eff}}(\mathbf{r}) = V_{\text{en}}(\mathbf{r}) + \underbrace{\int \frac{\rho_0(\mathbf{r}')}{|\mathbf{r}-\mathbf{r}'|} d\mathbf{r}'}_{=V_{\text{ee}}(\mathbf{r})} + \underbrace{\frac{\delta E_{\text{xc}}[\rho_0(\mathbf{r})]}{\delta \rho(\mathbf{r})}}_{=V_{\text{xc}}(\mathbf{r})} \quad (3.29)$$

The Kohn-Sham orbitals $\psi_i^{\text{KS}}(\mathbf{r})$ only reproduce the correct electron density but actually have no physical meaning. The total energy of the atomic system reads³:

$$E_i[\rho_0(\mathbf{r})] = \sum_i^{\text{occ}} \varepsilon_i^{\text{KS}} - \frac{1}{2} \int \int \frac{\rho_0(\mathbf{r})\rho_0(\mathbf{r}')}{|\mathbf{r}-\mathbf{r}'|} d\mathbf{r}d\mathbf{r}' - \int V_{\text{xc}}(\mathbf{r})\rho_0(\mathbf{r})d\mathbf{r} + E_{\text{xc}}[\rho_0(\mathbf{r})] \quad (3.30)$$

Up to now, DFT has been presented as a formally exact framework, however, the complicated part of physics, namely the exchange and correlation interactions, is incorporated in $E_{\text{xc}}[\rho(\mathbf{r})]$. The above eigen-value problem is solved using an iterative method that makes up the computationally expensive step of the DFT calculations. A schematic representation of a self-consistent loop in this numerical method is depicted in Fig. 3.4. With the forces at hands, the energy of a configuration can be minimized with respect to the atomic coordinates. Mathematically, this corresponds to finding the stationary point of a function whose exact form is generally unknown. This task is solved employing iterative methods [92], such as quasi-Newton methods or the conjugate gradient method for instance. The obtained energy minima corresponds to the stable configurations, which are physically realized and thus important for the determination of stable defect configurations.

When self-consistency is achieved for this loop, the electronic part of the system is solved. However, the nuclear part described by the Schrödinger equation (2.17) has not been addressed so far. Due to the relatively high nuclei mass, quantum mechanical considerations can be neglected so that the Schrödinger equation (2.17) can be replaced by Newton's law of motion. The required forces are evaluated according to the Hellmann-Feynman theorem [91, 92]:

$$\mathbf{F}_i = - \int \rho(\mathbf{r}) \frac{\partial V_{\text{en}}(\{\mathbf{R}_I\}, \{\mathbf{r}_m\})}{\partial \mathbf{R}_i} d\mathbf{r} - \frac{\partial V_{\text{nn}}(\{\mathbf{R}_I\})}{\partial \mathbf{R}_i} \quad (3.31)$$

3.3.3 Simulation Details

The simulations in this thesis are performed using the Vienna Ab-initio Simulation Package (VASP) [138–141], which is based on a plane-wave implementation of DFT. The computational details, especially those important for defect calculations, will be discussed in the following.

The correct description of the exchange-correlation functional takes a crucial role in DFT. The local-density approximation has already achieved satisfactory results for systems with a slowly varying

³ The last term \hat{V}_{nn} of the Hamiltonian in equation (2.16) describes the Coulomb interactions between nuclei. With respect to the electronic system, it yields a constant contribution, which has been left out in this derivation for simplicity.

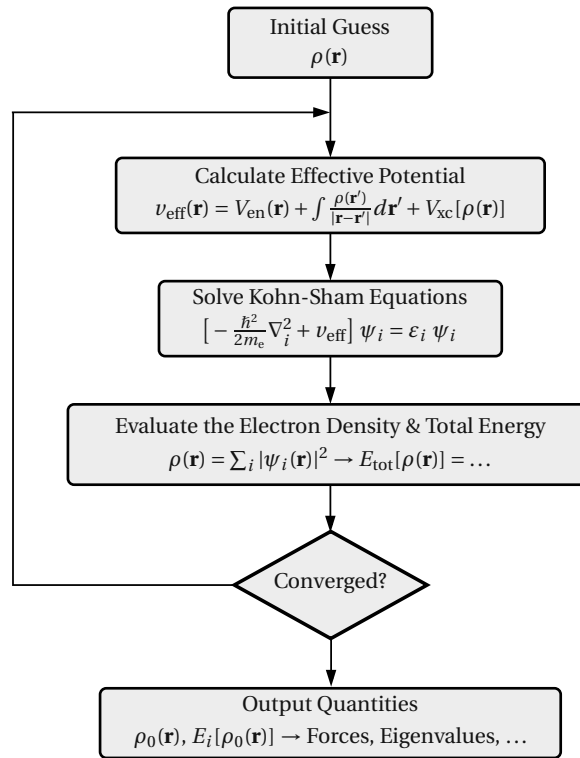


FIGURE 3.4: A flow chart of the iteration scheme. At first, an initial guess for the electron density is assumed, which is required for the calculation of $v_{\text{eff}}(\mathbf{r})$, the diagonalization of the Kohn-Sham equations, and the subsequent evaluation of $\rho(\mathbf{r})$ along with E_{tot} . As long as the convergence criterion is not fulfilled, the numerical procedure is continued with the last $\rho(\mathbf{r})$ instead of the initial guess. When the criterion is satisfied, various output quantities are computed.

electron density, such as metals [93]. However, it has a tendency termed overbinding, which overestimate binding energies and thus for instance predicts too strong hydrogen bonds with too short bonds lengths. The generalized gradient approximation is a systematic expansion, gives good results in most cases, and corrects for the overbinding [93]. Recently, hybrid functionals [142] have emerged, which achieve an improved accuracy, especially for the bandgap [143]. However, their use for large-scale investigations of atomic systems is time-demanding. Therefore, the functional based on the parametrization of Perdew, Burke, and Ernzerhof [144] and provided by the VASP code has been regarded as a reasonable trade-off between accuracy and computation time.

A realistic defect model must contain some of the surrounding atoms of its host material since the atoms of a real defect are connected to the surrounding atomic network and thus are not allowed to move around freely. In order to account for this, the long-range structural relaxations are handled using periodic supercells containing 108 atoms. The host structures have been produced using empirical potential molecular dynamics presented in Section 3.4. The resulting structures were optimized on DFT level employing a conjugate gradient algorithm that minimizes the force on each atom below $0.03 \text{ eV}/\text{\AA}$. In a further step, the defects were manually introduced by the addition or removal of single atoms, followed by a subsequent structural optimization. Due to the imposed

periodic boundary conditions in supercells, the Kohn-Sham orbitals $\Psi^{\text{KS}}(\mathbf{x})$ were represented by an expansion of plane waves up to a cut-off energy of 400 eV. Since the large size of the supercells ($> 1000\text{\AA}^3$) decreases the corresponding Brillouin zones, the k -point sampling was restricted to the Γ -point only.

VASP employs a sophisticated transformation of the Kohn-Sham equations based on the projector-augmented wave (PAW) method [145, 146], which smoothens the effective potential $v_{\text{eff}}(\mathbf{r})$ near the cores in order to spare the computationally expensive inclusion of the highly oscillating wavefunctions. The PAW method is one of the most powerful approaches which combines a good transferability to different atomistic configurations and chemical compositions with the required accuracy [93, 145].

Defect levels for charge capture or emission are calculated by means of the formation energies $U_{\text{f}}^q[X^q]$ [147, 148], which are defined for a certain charge state q and a certain atomic configuration X^q of the defect as

$$U_{\text{f}}^q[X^q] = E_{\text{tot}}[X^q] - E_{\text{tot}}[\text{bulk}] - \sum_j n_j \eta_j + q(\mu + \varepsilon_v + \Delta V) + E_{\text{corr}}. \quad (3.32)$$

$E_{\text{tot}}[\text{bulk}]$ stands for the total energy of a supercell containing pure bulk material while $E_{\text{tot}}[X^q]$ the supercell also contains the defect. The third term in equation (3.32) corrects for the different numbers of atoms in both supercells. n_j gives the number of added ($n_j > 0$) or removed ($n_j < 0$) atoms which are required to create the defect from a perfect bulk structure. The subscript j refers to the atom type and η_j denotes the corresponding energy in an atomic reservoir, which must be specified for each individual use case. The fourth term in equation (3.32) accounts for the charge state q of the defect. μ is defined as the electron chemical potential referenced with respect to the valence band edge ε_v in a bulk-like region. ΔV [147] corrects the shift in the reference level between two differently charged supercells and is obtained from the difference in the electrostatic potential far distant from the defect. Due to the periodic boundary conditions, charge neutrality must be ensured within a supercell. Thus a homogeneous compensating background charge must be introduced in calculations of charged defects. Its artificial Coulomb interactions are corrected by the term E_{corr} .

In DFT literature, one distinguishes between switching and thermodynamic transition levels. The former pertain to a charge capture or emission process, during which the atomic configuration is preserved, and thus they have the same meaning as the electron capture levels and hole emission levels presented in Section 2.3. In DFT they are defined as the difference of formation energies [113, 149] and can be written as

$$E_{+/0} = U_{\text{f}}^0[X^+] - U_{\text{f}}^+[X^+], \quad (3.33)$$

$$E_{0/+} = U_{\text{f}}^0[X^0] - U_{\text{f}}^+[X^0], \quad (3.34)$$

$$E_{-/0} = U_{\text{f}}^-[X^-] - U_{\text{f}}^0[X^-], \quad (3.35)$$

$$E_{0/-} = U_{\text{f}}^-[X^0] - U_{\text{f}}^0[X^0]. \quad (3.36)$$

Analogously to Section 2.3, energy levels $E^{+/0}$ and $E^{0/+}$ apply to a process which neutralizes a positive defect or introduces a positive charge into a neutral defect, respectively. An alternative possibility for the evaluation of the switching transition levels is provided by the Slater-Janak theorem [150].

The thermodynamic transition levels correspond to the difference between two energy minima, which is also the case for U_{ji} in the NMP theory (see section 2.4). In contrast to the switching transition levels, the relaxed configurations for each charge state must be used.

$$\varepsilon_{0/+} = E_f^0[X^0] - E_f^+[X^+] \quad (3.37)$$

$$\varepsilon_{-/0} = E_f^-[X^-] - E_f^0[X^0] \quad (3.38)$$

3.4 Empirical Potential Molecular Dynamics

Molecular dynamics has been established as a powerful tool for the generation of amorphous structures [151, 152]. It can simulate the time evolution of a group of atoms at a certain temperature, where the bonding between atoms is mimicked by interatomic empirical potentials. Even though it performs considerably fast, the simulation times are still restricted to a few thousand picoseconds [153–156]. For this reason, empirical potential molecular dynamics is not capable of simulating the processing of α -SiO₂. Nevertheless, a combination of experimental and theoretical investigations have shown that realistic amorphous structures [151, 152] can be produced by cooling down a random configuration of silicon and oxygen atoms from 3000K to room temperature within a few tens of a picosecond. It has been found [151–153, 155] that α -SiO₂ is composed of slightly deformed tetrahedral SiO₄ units with one Si atom in their centers. These units are randomly connected to each other so that they form Si-O-Si chains at their corners. In this way, each silicon atom is fourfold coordinated to oxygen atoms and each oxygen atom in turn is bonded to two silicon atoms. The distributions of the $d_{\text{Si-O}}$, $d_{\text{O-O}}$, and $d_{\text{Si-Si}}$ bond lengths as well as the $\phi_{\text{O-Si-O}}$ and $\phi_{\text{Si-O-Si}}$ angles have been used in the following to check the quality of the generated α -SiO₂ structures.

3.4.1 Fundamentals of Molecular Dynamics

The atomistic dynamics are accurately described by Newton's law of motion, which is applied for classical molecular dynamics [157].

$$m_i \frac{d}{dt} \mathbf{R}_i(t) = \mathbf{F}_i(t) \quad (3.39)$$

$$\mathbf{F}_i(t) = -\nabla_i V(\mathbf{R}_1(t), \dots, \mathbf{R}_N(t)) \quad (3.40)$$

$\mathbf{R}_i(t)$ and m_i denotes the position and the mass of atom i . The term on the right-hand side of equation (3.39) represents the force $\mathbf{F}_i(t)$ acting on the atom i and is evaluated by the derivative of the interatomic empirical potential $V(\mathbf{R}_1(t), \dots, \mathbf{R}_N(t))$ with respect to $\mathbf{R}_i(t)$. This differential equation is solved numerically using an appropriate time integration algorithm, such as the leap-frog Verlet algorithm.

$$\mathbf{R}_i(t + \Delta t) = \mathbf{R}_i(t) + \mathbf{v}_i(t + \frac{1}{2}\Delta t) \cdot \Delta t \quad (3.41)$$

$$\mathbf{v}_i(t + \frac{1}{2}\Delta t) = \mathbf{v}_i(t - \frac{1}{2}\Delta t) + \frac{\mathbf{F}_i}{m_i} \cdot \Delta t \quad (3.42)$$

In this procedure, the current positions $\mathbf{R}_i(t)$ and the accelerations \mathbf{F}_i/m_i are stored together with the mid-step velocities $\mathbf{v}_i(t - \frac{1}{2}\Delta t)$. The structure generation method used in this thesis is based on a rapid quench of a molten atomic system. Therefore, a thermostat is required to control the temperature of the atomic system during the quenching procedure. For this purpose, the Nose-Hoover thermostat [157] as implemented in the GULP code was employed throughout this thesis. It relies on a sophisticated method to couple the atomic system to a heat bath with the desired temperature. Since this method correctly produces the thermodynamical temperature fluctuations as well as the dynamics of the atomic system, the Nose-Hoover thermostat is usually considered as the working horse for molecular dynamics simulations.

3.4.2 Procedure for Structure Generation

The silicon and oxygen atoms were randomly placed in the periodic simulation cells. In order to avoid any overlapping between the atoms, exclusion radii ($r_{\text{Si-O}} = 1.5\text{\AA}$, $r_{\text{O-O}} = 2.5\text{\AA}$, $r_{\text{Si-Si}} = 3.1\text{\AA}$) were used. The edge length of the simulation cells (11.79\AA) was chosen to match a mass density of 2.19g/cm^3 [155]. The resulting random structures were taken as a starting configuration for the subsequent molecular dynamics equilibration step, which was performed at 3000 K for 30 ps with a time step of 1 fs. In this step the atomic structure is evolved from an unnatural random configuration to a liquid that should resemble molten SiO_2 . It was followed by a quenching step to 0 K for 30 ps with a time step of 1 fs, where the liquid was cooled down to an amorphous solid.

The simulations were performed using the popular Beest-Kramer-van Santen (BKS) potential [158]. This consists of Buckingham potentials, which were extended by a Coulombic term and parametrized to reproduce the interatomic interactions obtained from DFT. These two-body potentials feature artificial singularities at their origins and small separating barriers to the next energy minimum. But since the structures were not heated above 5000 K, corrections within a certain cut-off radii as applied in [159] could be omitted. The interatomic interactions were only represented by Si-O and O-O pair-potentials that describe the Si-O bonding and ensure the tetrahedral arrangement. Despite these strong simplifications, a series of studies have proven their successful application for SiO_2 structure generation [151, 152, 158, 159].

In order to prove the correctness of the applied production procedure, the obtained samples were evaluated based on the pair-correlation functions and angle distributions as shown in Fig. 3.5 and 3.6. Due to the fact that edge-sharing tetrahedra are energetically unfavored [152], only samples containing none of these edge-sharing tetrahedra were used for further investigations while the others were simply discarded. The remaining samples exhibited no miscoordination, such as broken Si-O bonds or threefold coordinated Si atoms. As demonstrated in Table 3.1, satisfying agreement has been achieved with previously published results [152, 153, 155]. The selected structures were minimized on a DFT level in order to prepare them for the following defect calculations. During this step, a small structural relaxation was observed indicating that no bonds had been broken.

| Ref. | $d_{\text{Si-O}}$ | $d_{\text{O-O}}$ | $d_{\text{Si-Si}}$ | $\phi_{\text{O-Si-O}}$ | $\phi_{\text{Si-O-Si}}$ |
|---------------|-------------------|------------------|--------------------|------------------------|-------------------------|
| Present study | 1.64 | 2.66 | 3.08 | 109.42 | 142.62 |
| [152] | 1.62 | 2.64 | 3.10 | 109.6 | 142.0 |
| [155] | 1.63 | 2.67 | 3.11 | 109.4 | 146.8 |
| [153] | 1.62 | 2.68 | 2.98 | 109 | 136 |

TABLE 3.1: Comparison of the characteristic properties of the produced $a\text{-SiO}_2$ structures. $d_{\text{Si-O}}$, $d_{\text{O-O}}$, and $d_{\text{Si-Si}}$ denote the first maximum in the corresponding pair-correlation functions. $\phi_{\text{O-Si-O}}$ and $\phi_{\text{Si-O-Si}}$ are the maxima of the respective angle distributions. The obtained values compare reasonably well with the published values in [152, 153, 155]. It should be mentioned here that the $\phi_{\text{O-Si-O}}$ angles are quite sensitive to the details of the used structure generation method. Thus, their values in the literature [152, 153, 155, 156, 159] are subject to a strong variation ranging from 136° and 152° and thus are still debated [156].

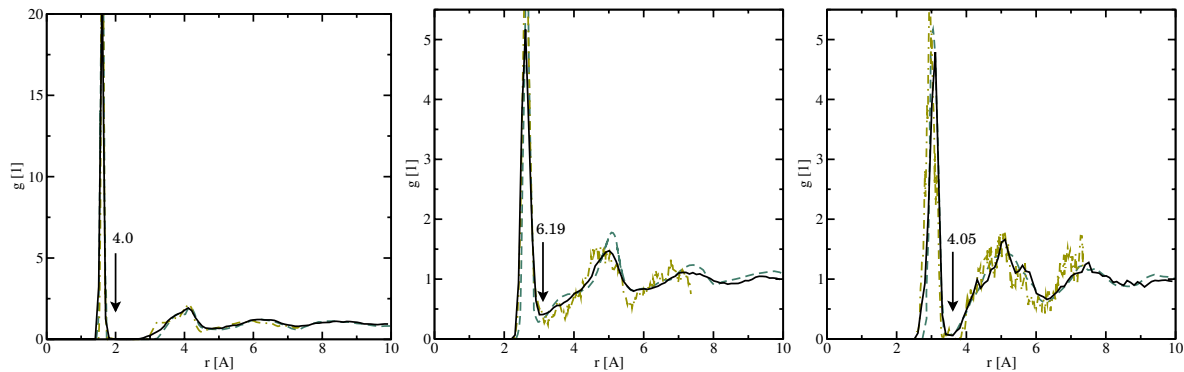


FIGURE 3.5: The pair-correlation functions [151] for the $d_{\text{Si-O}}$ (left), the $d_{\text{O-O}}$ (middle), and the $d_{\text{Si-Si}}$ (right) bonds. The solid black lines represent the data obtained in this thesis while the dashed ochre and the dashed-dotted green line are extracted from the studies of Sarnthein [153] and Rino [152], respectively. In order to improve the accuracy of statistics, the data have been collected from a 1 ps DFT molecular dynamics run at 300K for five different samples. The first sharp peak corresponds to the length of the respective bond type and compare well with the values from literature (see Table 3.1). It is noted that also the other features are found to be in qualitative agreement with the extracted data. The integral over the first peak yields the number of first nearest neighbors for the respective atom type. The values 4.0, 6.19, and 4.05 have been obtained for the $d_{\text{Si-O}}$, the $d_{\text{O-O}}$, and the $d_{\text{Si-Si}}$ bonds in agreement with [151, 153, 155]. The slight deviations have been attributed to the still small statistics associated with a small resolution with respect to r . Furthermore, the first peaks overlap with the next features at the right integration limit (indicated by the arrow) leading to an inaccurate determination of the numbers of first nearest neighbors.

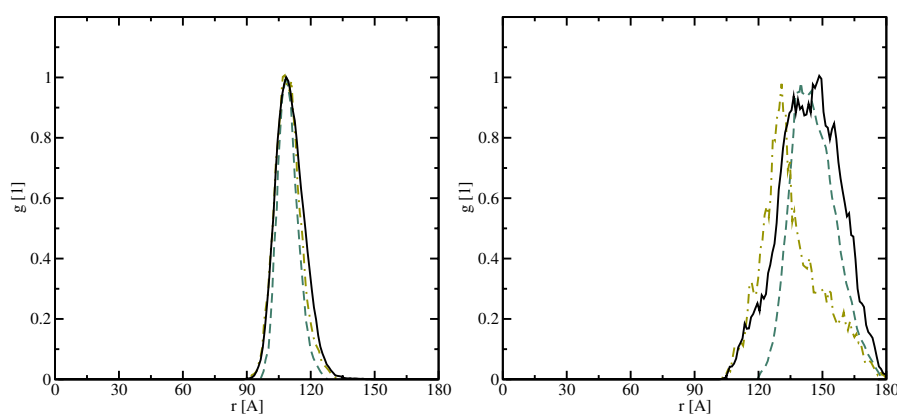


FIGURE 3.6: The angle distribution of the O-Si-O (left) and the Si-O-Si (right) chains for the data of this thesis and (ochre) Sarnthein [153] and (green) Rino [152]. The maxima as well as the full width at half maximum of the O-Si-O angle distribution are in reasonable agreement with the extracted data in [152, 153]. The values for the O-Si-O angles are subject to appreciable deviations, which originate from the complications mentioned in Table 3.1. Nevertheless, the maxima of Gaussian fits are found to be in an acceptable agreement.

4

Elastic Tunneling Model

It was long believed that NBTI is controlled by the creation of interface dangling bonds as it is the case in numerous variants of the reaction-diffusion and the reaction-limited models. With time, more and more authors [23, 70] considered trapped oxide charges as a possible cause for NBTI. One of the simplest trapping models has been proposed by Yang *et al.* [70]. It rests on the assumption that the capture and emission time constants follow certain distributions. Even though these distributions have been introduced in an ‘ad hoc’ manner and do not rely on any physical profound explanation, the basic concept is still present in each charge trapping model. Therefore, this phenomenological model will be briefly discussed in this chapter.

Tewksbury [23] explained charge trapping as an elastic tunneling process of substrate charge carriers into and out of oxide defects and ascribed the distribution of time constant to a wide range of trap depths. For an evaluation against experiments, his model has been implemented in a device simulator and tested whether it is consistent with the list of experimental findings presented in Section 1.4. In these investigations, a special focus has been put on the temperature dependence of charge trapping, which requires the consideration of quantization effects in the inversion layer. Since the oxide thickness has been reduced to a few nanometers, the model has also been extended to consider charge trapping from and to the gate contact.

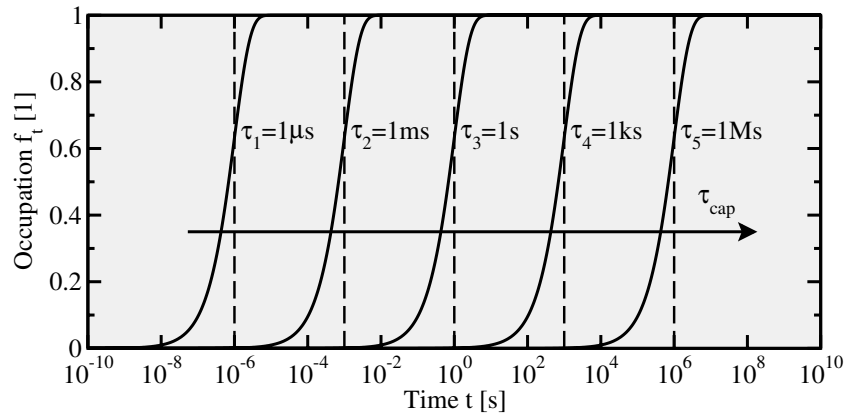


FIGURE 4.1: The time evolution of the trap occupancy for five traps with their different trapping time constant τ_i assuming $1/\tau = 1/\tau_{\text{cap}} + 1/\tau_{\text{em}}$ and $f_t(0) = 0$. τ_i gives the time point, when the trapping process should occur according to its expectation value $E\{\tau\}$. In a time-logarithmic plot, the time point of the transition shifts linearly with the order of magnitude of τ_i .

4.1 A Phenomenological Trapping Model

The trapping dynamics in the simplest case are governed by the first-order rate equation

$$\partial_t f_t(t) = \underbrace{\frac{1}{\tau_{\text{cap}}}}_{=k_t} (1 - f_t) - \underbrace{\frac{1}{\tau_{\text{em}}}}_{=k_r} f_t \quad (4.1)$$

with f_t being the electron occupancy of a single trap. Each of these traps is characterized by its own capture (τ_{cap}) and emission (τ_{em}) time constant, which are related to the forward (k_f) or the reverse (k_r) rate, respectively. The first term on the right-hand side of equation (4.1) has a positive sign, stands for electron trapping and increases f_t . By contrast, detrapping is represented by the second term with the negative sign and causes a reduction in f_t . It is emphasized that the defects have only discrete occupation numbers. This means that the defects carry an integer number of electrons and thus f_t must equal to either zero or unity. However, for a large number of defects, f_t corresponds to the average occupation number and thus takes values within the range $[0, 1]$. It is further mentioned that the physical trapping process is of a stochastic nature, as it has also been the case for electron tunneling and vibronic transitions in Chapter 2. These stochastic processes are characterized by the fact that the transition times are statistically distributed. As a consequence, τ_{cap} and τ_{em} correspond to the expectation value of the capture ($E\{\tau_{\text{cap}}\}$) or emission ($E\{\tau_{\text{em}}\}$) times, respectively, and the electron occupancy only changes gradually with time. The electron occupancy as a function of time is determined by the rate equation (4.1), which is a first-order differential equation with the solution

$$f_t(t) = \underbrace{\frac{\tau_{\text{em}}}{\tau_{\text{em}} + \tau_{\text{cap}}}}_{=f_t^{\text{eq}}} + \underbrace{\left(f_t(0) - \frac{\tau_{\text{em}}}{\tau_{\text{em}} + \tau_{\text{cap}}} \right)}_{=f_t(0) - f_t^{\text{eq}}} \cdot \exp \left(- \underbrace{\left(\frac{1}{\tau_{\text{em}}} + \frac{1}{\tau_{\text{cap}}} \right)}_{=1/\tau} t \right), \quad (4.2)$$

and is depicted in Fig. 4.1. The first term of equation (4.2) corresponds to the equilibrium occupancy f_t^{eq} , which approaches unity for the assumption $\tau_{\text{cap}} \ll \tau_{\text{em}}$. The second term describes an

exponential transition of $f_t(t)$ towards f_t^{eq} . In a time-logarithmic representation this leads to a step of $f_t(t)$, occurring within three decades around τ . This step is associated with the expectation value of the transition $E\{\tau\}$ in the trapping process and the stochastic nature of this process is reflected in the washed-out shape of the step. As demonstrated in Fig. 4.1, the step linearly shifts with the order of magnitude of τ . Furthermore, its height reaches the maximal value of 1 when the capture and emission time constant differ by some orders of magnitude. Note that hole detrapping requires that $\tau_{\text{em}} \ll \tau_{\text{cap}}$ and the time point of the transition is then determined by τ_{em} .

One has to consider that the atomic structure of defects strongly influences the defect properties. Dielectric host materials, in particular SiO_2 and SiON , exhibit an amorphous structure with large variations in the bond lengths and angles, which are assumed to have an impact on τ_{cap} and τ_{em} . As a result, the trapping time constants in equation (4.1) are subject to a dispersion. This will be accounted for by a probability density function $g(\tau_{\text{cap}}, \tau_{\text{em}})$, which is normalized by definition. Then the time evolution of trapped charges $N_{\text{ox}}(t)$ can be expressed as

$$N_{\text{ox}}(t) = N_t \int f_t(t, \tau_{\text{cap}}, \tau_{\text{em}}) g(\tau_{\text{cap}}, \tau_{\text{em}}) d\tau_{\text{cap}} d\tau_{\text{em}}, \quad (4.3)$$

where $g(\tau_{\text{cap}}, \tau_{\text{em}})$ is normalized and N_t stands for the concentration of traps. The integral in equation (4.3) can be interpreted as a superposition of individual and thus independent trapping processes. Note that this concept is in agreement with the findings of TDDS, in which the single trapping processes take place almost independently from each other.

In a phenomenological model of Yang *et al.* [58], the capture and emission time constants were correlated by the relation

$$\tau_{\text{cap}} = k\tau_{\text{em}} = \tau. \quad (4.4)$$

Furthermore, Yang *et al.* assumed a log-normal distribution of τ

$$g(\tau) = \frac{1}{\sqrt{2\pi\tau\sigma}} \exp\left(-\frac{1}{2}\left(\frac{\log(\tau) - \mu}{\sigma}\right)^2\right). \quad (4.5)$$

Although his model allows reasonable fits to single relaxation curves, it is inconsistent with the scalability of the experimental data (see Section 1.4). This is due to the fact that neither the probability density function nor the time constants have a field- or temperature dependence, which were not considered. Nevertheless, the above formulation of the rates already includes the central aspects of a charge trapping model and thus has served as a foundation for other models. The following points are suggested as an improvement for Yang's model:

- The probability density function has been phenomenologically introduced, where its shape was chosen to reproduce experimental data. Therefore, it is the goal to correlate the probability density function with certain physical properties of the defects and find reasonable shapes for $g(\tau_{\text{cap}}, \tau_{\text{em}})$.

- The model does not contain any information about the physics of the trapping process¹. Therefore, expressions for τ_{cap} and τ_{em} are sought, which are derived from physical considerations and must consequently depend on the temperature and the electrostatics in the device.

4.2 Elastic Tunneling

Tewksbury [23] assumed elastic tunneling of electrons and holes into and out of oxide defects as the mechanism responsible for charge trapping. The use of his model has been suggested by Huard *et al.* [58] in order to explain the recoverable part of the NBTI degradation. In this section, Tewksbury's model will be reviewed, extended for an application of present-day devices with small gate thicknesses, and referred to as the elastic tunneling model (ETM) in the following.

The approach applied in this thesis relies on rate equations for tunneling into one trap. The required rate expressions $r_e(E_t)$ and $r_h(E_t)$ are given by the equations (2.45) and (2.46), which already incorporate all elastic tunneling transitions between one trap and the numerous band states. Due to their analytical complexity, these rate equations are solved numerically using the numerical iteration scheme presented in Section 3.2. The used simple first-order partial differential equation reads

$$\partial_t f_t = \begin{cases} f_n(E_t) r_e(E_t) (1 - f_t) - f_p(E_t) r_e(E_t) f_t, & E_t \geq E_c \\ f_n(E_t) r_h(E_t) (1 - f_t) - f_p(E_t) r_h(E_t) f_t, & E_t \leq E_v \end{cases}, \quad (4.6)$$

with the electron and hole trapping times approximated as

$$\tau_{\text{cap,e}}(E_t, x_t) = \frac{1}{f_n(E_t) r_e(E_t)}, \quad (4.7)$$

$$\tau_{\text{em,e}}(E_t, x_t) = \frac{1}{f_p(E_t) r_e(E_t)}, \quad (4.8)$$

$$\tau_{\text{em,h}}(E_t, x_t) = \frac{1}{f_n(E_t) r_h(E_t)}, \quad (4.9)$$

$$\tau_{\text{cap,h}}(E_t, x_t) = \frac{1}{f_p(E_t) r_h(E_t)}. \quad (4.10)$$

The electron (f_n) and hole (f_p) occupancy are defined as

$$\begin{aligned} f_n(E) &= f_{\text{FD}}(E), \\ f_p(E) &= 1 - f_{\text{FD}}(E) \end{aligned} \quad (4.11)$$

with f_{FD} being the Fermi-Dirac distribution. The above rate equation features the same structure as that of equation (4.1). Therefore, the same mathematical implications as for the phenomenological model hold true for the ETM. Furthermore, equation (4.6) covers all four basic transitions illustrated Fig. 4.2 so that it can be viewed as a comprehensive description of elastic tunneling in MOSFETs.

¹It is remarked here that the exact nature of this mechanism is considered as an open issue in this thesis. As a consequence, the more general term 'trapping' is preferred to the term 'tunneling' when not referring to a special physical mechanism.

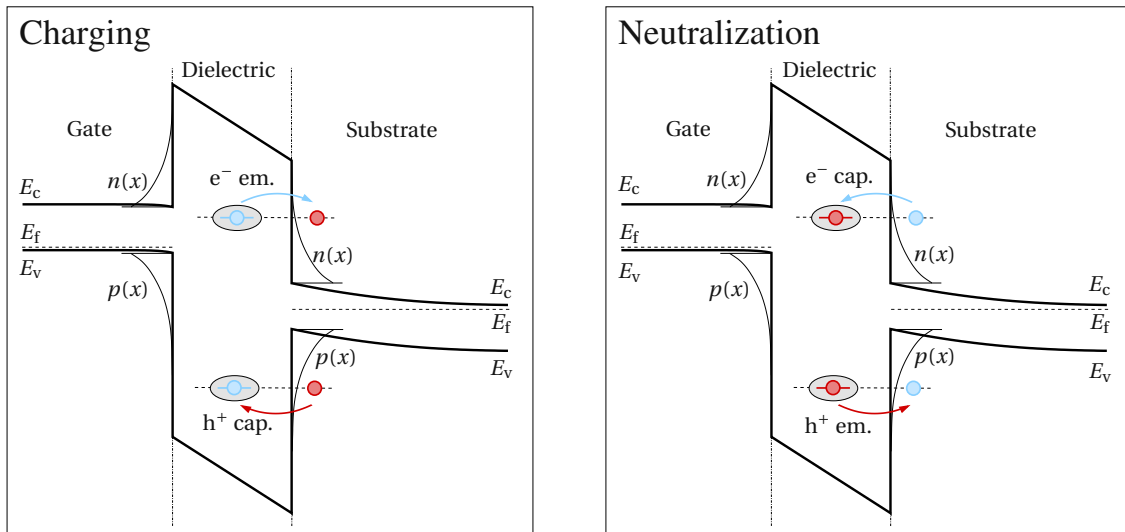


FIGURE 4.2: The basic tunneling transitions in a MOSFET for traps located above the conduction or below the valence band edge in the dielectric. Defects (gray filled ellipses) become positively charged in the left figure while they are neutralized in the right figure. The red arrows indicate a hole tunneling process, which always starts out from an empty state (marked by a red circle). It is noted here that this ‘empty state’ is located in the valence band and thus should be correctly referred to as a ‘hole’. However, the conduction and valence band states only differ in their effective masses — apart from their energetical position. These masses only affect the transport properties, such as the carrier mobilities, but marginally change the tunneling rates (2.45) and (2.46). In this respect, the terms ‘empty states’ and ‘holes’ are interchangeable and thus used synonymously in the remainder of this thesis.

4.2.1 The Behavior of A Single Trap

In this chapter, the investigations are focused on NBTI in pMOSFETs since these devices attract a large industrial interest at the moment. Therefore, only hole tunneling from the substrate valence band will be addressed in the following. Naturally, the basic statements will also remain valid for electron tunneling in the case of PBTI in nMOSFETs and for the different dielectric materials used in modern device technologies. For the trapping dynamics, f_{FD} and $\zeta_{WKB,V}^2(E_x, x_t)$ in $1/\tau_{cap,h}(E_t)$ and $1/\tau_{em,h}(E_t)$ of equation (4.6) are the most sensitive factors. These quantities determine the basic properties of the ETM and will be discussed in detail in this section.

The trapping dynamics are described by the rate equation (4.6), which has the same forward r_e and reverse r_h rate considering hole trapping ($E_t \leq E_v$).² This special form implies that the occupancy

²The equal forward and reverse rate originate from the assumption that the defect and the channel wavefunction are unchanged after a trapping or detrapping event. A consequence of this is that the overlap of the wavefunctions and thus the matrix element $|M_{v,tb}(E_x, x_t)|$ are unaffected, resulting in equaling rates r_h for the forward and the reverse mode of the tunneling process.

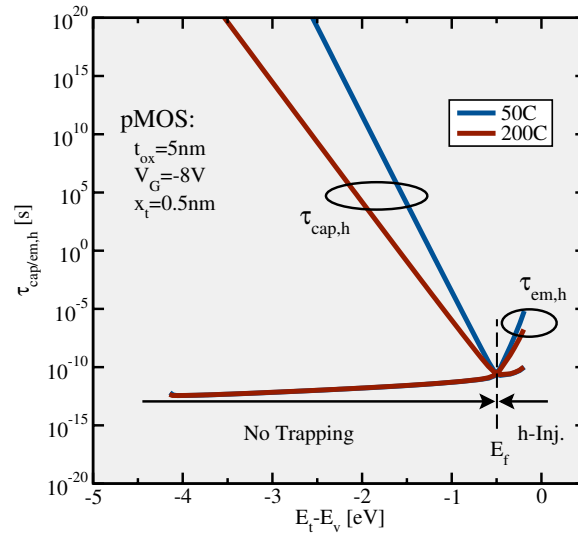


FIGURE 4.3: The hole capture ($\tau_{\text{cap,h}}$) and emission times ($\tau_{\text{em,h}}$) for two different temperatures as a function of the trap level E_t . The simulated device is subject to heavy stress conditions, at which tunneling ‘through’ the dielectric actually play a crucial role and should be taken into account. Nevertheless, V_G is set to a high gate voltage for illustration purposes only. The Fermi-Dirac distribution predicts a decrease in f_n above E_f , which leads to exponentially rising $\tau_{\text{em,h}}$. Analogously, f_p decays and $\tau_{\text{cap,h}}$ rises below the E_f . As a result, $\tau_{\text{em,h}}$ is larger than $\tau_{\text{cap,h}}$ in the region above the E_f so that hole trapping can occur there. By contrast, hole trapping is inhibited below E_f since $\tau_{\text{em,h}} \ll \tau_{\text{cap,h}}$. For higher temperatures, the exponential decay becomes weaker, which is reflected in smaller slopes of the $\tau_{\text{cap,h}}$ and $\tau_{\text{em,h}}$.

of the trap f_t equilibrates to that of the valence band states at the same energy E_t . For steady state conditions, f_t reads

$$f_t(t) = \frac{1}{1 + \tau_{\text{cap,h}}(E_t, x_t)/\tau_{\text{em,h}}(E_t, x_t)}, \quad (4.12)$$

where $\tau_{\text{cap,h}}$ and $\tau_{\text{em,h}}$ take the role of τ_{cap} and τ_{em} in (4.2), respectively. The above equation shows that the trap occupancy is eventually governed by the relative magnitude of $\tau_{\text{cap,h}}$ and $\tau_{\text{em,h}}$. Both time constants are most strongly affected by the exponential decay of the Fermi-Dirac distribution. This dependence is pointed out in Fig. 4.3, where the hole capture and emission times are plotted with respect to the trap energy E_t . In the region below E_f , the hole occupancy f_p decreases by several orders of magnitude per 1 eV so that the hole capture times $\tau_{\text{cap,h}}$ by far exceed the corresponding emission times $\tau_{\text{em,h}}$. Therefore, no effective hole trapping can take place in this region, irrespectively of the temperature. By contrast above E_f , the exponential decay of f_n causes an increase in the hole emission times $\tau_{\text{em,h}}$, which gives rise to hole trapping there. That is, E_f can be regarded as a demarcation energy between both regions. This fact is also reflected in the equilibrium solution (4.12) when using the definitions of $\tau_{\text{cap,h}}$ and $\tau_{\text{em,h}}$.

$$\begin{aligned} f_t(t) &= \frac{1}{1 + f_p(E_t)/f_n(E_t)} \\ &= \frac{1}{1 + e^{\beta(E_t - E_f)}} \end{aligned} \quad (4.13)$$

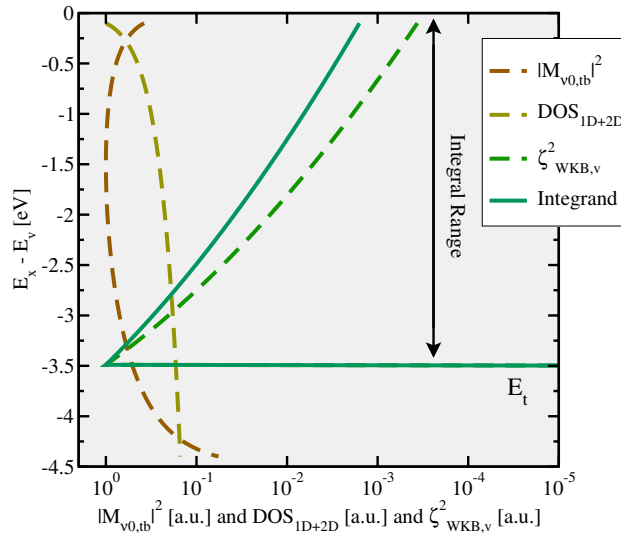


FIGURE 4.4: The functional form of $\text{DOS}_{p,1D+2D}(E_x)$, $|M_{v0,tb}(E_x, x_t)|^2$, the $\zeta_{WKB,v}^2(E_x)$, and their product for flat band conditions. For better visibility, all functions are normalized to their maximal values. While $\text{DOS}_{p,1D+2D}(E_x)$ and $|M_{v0,tb}(E_x, x_t)|^2$ remain within one order of magnitude, the WKB factor drops significantly. Since only the product of the three quantities enters the integrand of the rate equation (2.45) and (2.46), the largest contribution to the integral comes from the region slightly below the trap level E_t .

As a consequence, the trap occupancy is governed by the position of the substrate Fermi level in equilibrium³.

As mentioned before, the most sensitive factors in the tunneling rates of equation (4.6) are the Fermi-Dirac distribution and the WKB factor. In contrast to f_n and f_p , the latter is a function of E_x and cannot be taken out of the integrals in the rate expressions (2.45) and (2.46). As shown in Fig. 4.4, $\text{DOS}_{p,1D+2D}(E_x)$ and $|M_{v0,tb}(E_x, x_t)|^2$, the matrix element without the WKB factor, are subject to small variations so that they weakly affect the tunneling rates. Since the WKB factor falls off quickly with increasing E_x , the integral (2.46) delivers the largest contribution close to the trap level E_t . Therefore, it makes sense to approximate the rate integral (2.46) by dividing it through $\zeta_{WKB,v}^2(E_t, x_t)$ and define the resulting expression as $\tau_{p,0}^{\text{ETM}}(E_t)$. This new quantity incorporates the weak dependences on E_x while the sensitive factors, namely f_n or f_p and the WKB factor, are separated. Due to the small variations of $\text{DOS}_{p,1D+2D}(E_x)$ and $|M_{v0,tb}(E_x, x_t)|^2$, $\tau_{p,0}^{\text{ETM}}(E_t)$ shows small changes with E_t compared to $f_{\text{FD}}(E_t)$ and $\zeta_{WKB,v}^2(E_t, x)$ (see Fig. 4.5). This fact justifies approximations [23, 105, 106, 160], in which $\tau_{p,0}^{\text{ETM}}$ as a prefactor of the WKB factor is approximated as a constant. Using the above definitions, the rate equation for holes reads:

$$\partial_t f_t = f_n \underbrace{\frac{1}{\tau_{p,0}^{\text{ETM}}(E_t)} \zeta_{WKB,v}^2(E_t, x_t)}_{=1/\tau_{\text{em,h}}(E_t, x_t)} (1 - f_t) - f_p \underbrace{\frac{1}{\tau_{p,0}^{\text{ETM}}(E_t)} \zeta_{WKB,v}^2(E_t, x_t)}_{=1/\tau_{\text{cap,h}}(E_t, x_t)} f_t \quad (4.14)$$

³ Here, the term ‘equilibrium’ refers to the trapping kinetics but not to a thermal equilibrium. Therefore, it actually corresponds to steady state conditions, where the time derivative of f_t vanishes.

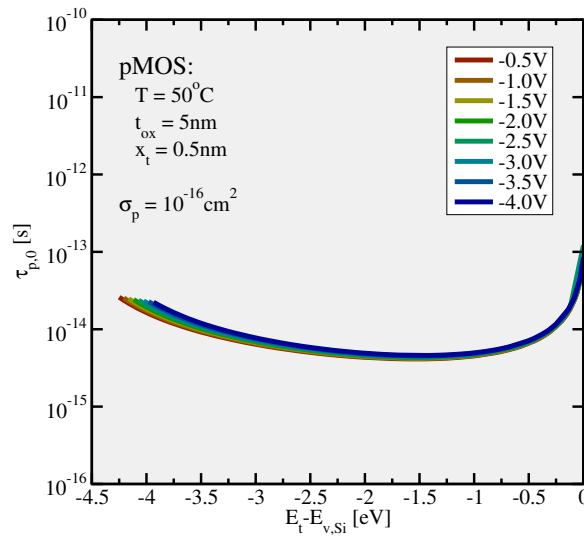


FIGURE 4.5: The quantity $\tau_{p,0}^{ETM}$ as a function of the trap level for different gate biases. Note that $\tau_{p,0}^{ETM}$ remains within one or two orders of magnitude. The peaks close to E_v can be traced back to a small kinetic energy of the holes within a classical picture. Quantum mechanically, the amplitude of the channel wavefunction at the interface is reduced for smaller charge carrier energies. This results in a decreased overlap of the wavefunction in the matrix element, a smaller tunneling probability, and ultimately in larger $\tau_{p,0}^{ETM}$ close to the band edges.

For the time evolution of charge trapping, $\zeta_{WKB,v}^2(E_t, x_t)$ becomes the essential factor (cf. Fig. 4.6). It shows an exponential decay with increasing trap depth, which results in a shift of τ_{cap} and τ_{em} towards larger times (cf. Fig. 4.7). Note that the energy of the tunneling charge carrier also impacts the WKB factor and the capture and the emission times. Since the energy dependence of the WKB factor enters both the capture and the emission times, their relative magnitude remains unaffected and the above argumentation of E_f as a demarcation energy remains valid.

In conclusion, the following findings have been made: The equilibrium charge state of an oxide defect is directly determined by the Fermi level in the substrate. When E_t is situated above E_f , the defect will capture a hole if the defect is initially occupied by an electron. Vice versa, positively charged defects with E_t below E_f will emit their holes. However, this relationship does not make any statement about the time point when the tunneling transitions occur. This is solely given by the respective capture ($\tau_{cap,h}$) or emission ($\tau_{em,h}$) time constant. The actual trapping times are given by the WKB factor, which predicts increasing capture ($\tau_{cap,h}$) and emission ($\tau_{em,h}$) times for larger tunneling distances.

4.2.2 Spatially and Energetically Distributed Traps

In the previous sections, only the behavior of single traps has been addressed but NBTI is actually caused by charging or discharging of a multitude of defects. This means that the degradation has to be understood as a superposition of several trapping events. It must be considered that the individual defects differ in their properties, such as their spatial depth and their energetical position within the

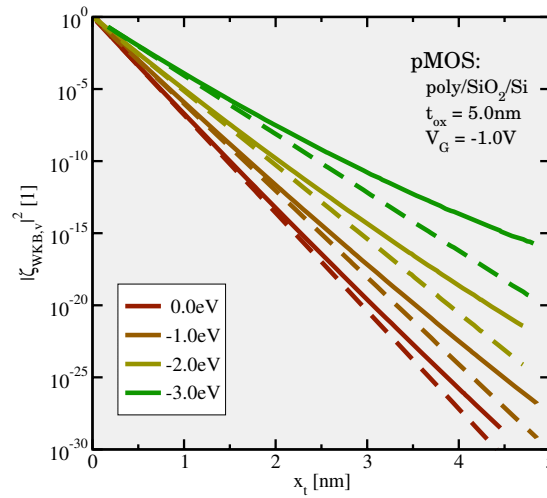


FIGURE 4.6: The WKB factor (solid line) versus its approximated variant through a rectangular barrier (dashed line) as a function of the trap level. A comparison between both coefficients reveals that the difference between them can be neglected for small tunneling distances. Especially, the rectangular approximation yields reasonable estimates of the accurate WKB factor for trap levels close to the valence band edge. Nevertheless, all simulation results in this chapter are computed using the accurate WKB factor. Note that the temperature does not enter the calculation of the matrix element and in consequence the WKB factor. This is why to first order elastic tunneling is expected to be a temperature independent process. However, there are small effects due to the temperature dependent shape of the channel wavefunction. They are not considered in the derivation of Section 2.5.2 but will be later shown to marginally affect the temperature dependence of hole trapping (see Section 4.2.7).

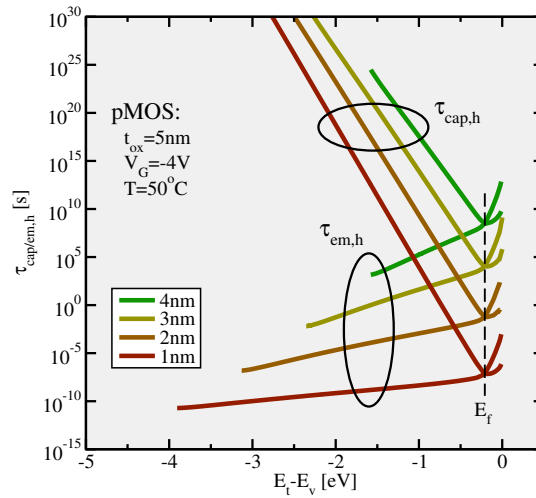


FIGURE 4.7: The spatial dependence of the hole capture ($\tau_{\text{cap,h}}$) and emission ($\tau_{\text{em,h}}$) times constants on the trap depths. The more distant the traps are located from the interface, the larger become $\tau_{\text{cap,h}}(E_t)$ and $\tau_{\text{em,h}}(E_t)$. This can be ascribed to the properties of the WKB factor, which decreases exponentially with the spatial depth of traps. Hence, the tunneling rates are reduced but the tunneling times are increased for deeper traps. Note that the crossing between $\tau_{\text{cap,h}}$ and $\tau_{\text{em,h}}$ always coincides with E_f , irrespectively of the tunneling distance. As a consequence, the energetical border to the trapping region does not vary with the trap depth.

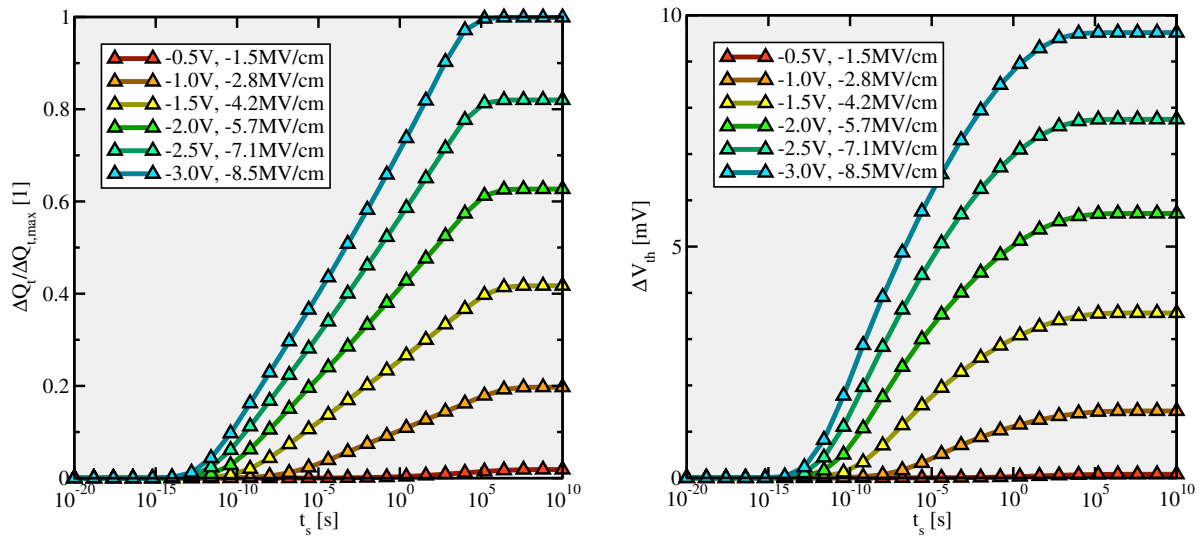


FIGURE 4.8: **Left:** A simulation of the trapped charges ΔQ_t as a function of stress time for different gate biases ($T = 125^\circ\text{C}$). Charge trapping occurs over up to approximately 15 decades and shows a logarithmic time dependence. The slopes in the plot increase linearly with the oxide field, which cannot be reconciled with the quadratic field dependence obtained from experiments. **Right:** The time evolution of the threshold voltage shift ΔV_{th} for different gate biases. The resulting curves roughly approximate a logarithmic time dependence in a small experimental window from $1\ \mu\text{s}$ to $1\ \text{ks}$.

oxide bandgap. The defects in this model are assumed to be bulk traps, which are scattered across the whole dielectric. The distribution in the trap levels can be attributed to variations in bond length and angles, which impact the energy levels of the defect orbitals according to quantum mechanical considerations [23, 161, 162]. Therefore, large variances up to a few electron Volts have been assumed in the ETM. However, the defect levels of the hydrogen interstitial [163] and the oxygen vacancy [164, 165] are found to have a spread below $0.5\ \text{eV}$. Hence, distributions of energy levels with a spread larger than $1\ \text{eV}$ seem to be unrealistic and must be verified by detailed atomistic investigations.

The following simulations, unless otherwise stated, are carried out on a pMOSFET ($N_d = 5 \times 10^{17}\ \text{cm}^{-3}$) with a strongly doped p-poly gate ($N_a = 2 \times 10^{20}\ \text{cm}^{-3}$) on top of a $3\ \text{nm}$ thick SiO_2 layer. The traps in the dielectric are uniformly distributed in space while their corresponding levels span a range from 0.3 to $4.3\ \text{eV}$ below E_v . The operation temperature is 125°C so that this value lies in the center of the temperature range relevant for NBTI. For simplicity, only charge injection from the valence band has been taken into account. Nevertheless, this does not affect the general findings of the model discussion.

4.2.3 Time Behavior during Stress

In the following, the ETM will be tested whether it is consistent with the experimental findings presented in Section 1.4. For this model evaluation, the temporal behavior during the stress phase is the most essential criterion. It is depicted in Fig. 4.8 as the evolution of trapped charges ΔQ_t and the threshold voltage shift ΔV_{th} . The former reveals a logarithmic time behavior, which is preserved for

a large time range and by far exceeds the measurement window ranging from $1\ \mu\text{s}$ to $1\ \text{ks}$. Recall that the behavior of one defect is described by the rate equation (4.6), which has the form of an ordinary first-order differential equation (4.1). It has been pointed out in Section 4.1 that the change in the occupancy $\Delta f_t(t)$ is given by the dominating time constants in the exponential term of equation (4.2). In the hole trapping region (cf. Fig. 4.3), $\tau_{\text{cap,h}} \ll \tau_{\text{em,h}}$ holds. Then equation (4.2) simplifies to

$$\Delta f_t(t, x_t, E_t) = \underbrace{f_t(0) - f_t(t \rightarrow \infty)}_{=\Delta f_{t,\text{max}}} \times \exp\left(-\frac{t}{\tau_{\text{cap,h}}(x_t, E_t)}\right). \quad (4.15)$$

Assuming a rectangular tunneling barrier for the WKB factor, one obtains

$$\Delta f_t(t, x_t, E_t) = \Delta f_{t,\text{max}} \times \exp\left(-\frac{t}{\tilde{\tau}_{p,0}^{\text{ETM}}(E_t)} e^{-x_t/x_{p,0}}\right) \quad (4.16)$$

using the definitions

$$\tilde{\tau}_{p,0}^{\text{ETM}}(E_t) = \tau_{p,0}^{\text{ETM}} / f_p(E_t) \quad (4.17)$$

and

$$x_{p,0} = \frac{\hbar}{2\sqrt{2m_p(E_{v,\text{sub}} - E_{v,\text{ox}})}}. \quad (4.18)$$

The exponential term on the right-hand side of equation (4.16) is characterized by a sharp drop at

$$x_B(t) = x_{p,0} \ln(t/\tilde{\tau}_{p,0}^{\text{ETM}}), \quad (4.19)$$

which suggests the following approximation

$$\Delta f_t(t, x) = \begin{cases} \Delta f_{t,\text{max}}, & x < x_B(t) \\ 0, & x > x_B(t) \end{cases}. \quad (4.20)$$

The sharp drop at $x_B(t)$ represents a border between defects which ‘already have’ and ‘still do not have’ captured holes from the substrate until the time t . This border moves away from the substrate towards deep into the dielectric as time progresses (see Fig. 4.9). Its shift follows a time logarithmic law according to equation (4.19) and results in straight lines in $\Delta Q_t(t)$ of Fig. 4.8. When the border arrives at the gate, hole trapping stops, which becomes visible as a saturation in $\Delta Q_t(t)$ and $\Delta V_{\text{th}}(t)$. According to the charge sheet approximation, charges more distant from the substrate oxide interface make a smaller contribution to ΔV_{th} due to their smaller weighting factors $(1 - x_t/t_{\text{ox}})$ in equation (3.25). This yields the curvature seen in $\Delta V_{\text{th}}(t)$ plots of Fig. 4.8. However, the resulting curves still roughly follow a logarithmic time behavior. When disregarding the oxide field and temperature dependence for the time being, this fact might be misinterpreted as an agreement with the experimentally observed logarithmic time behavior (1.8).

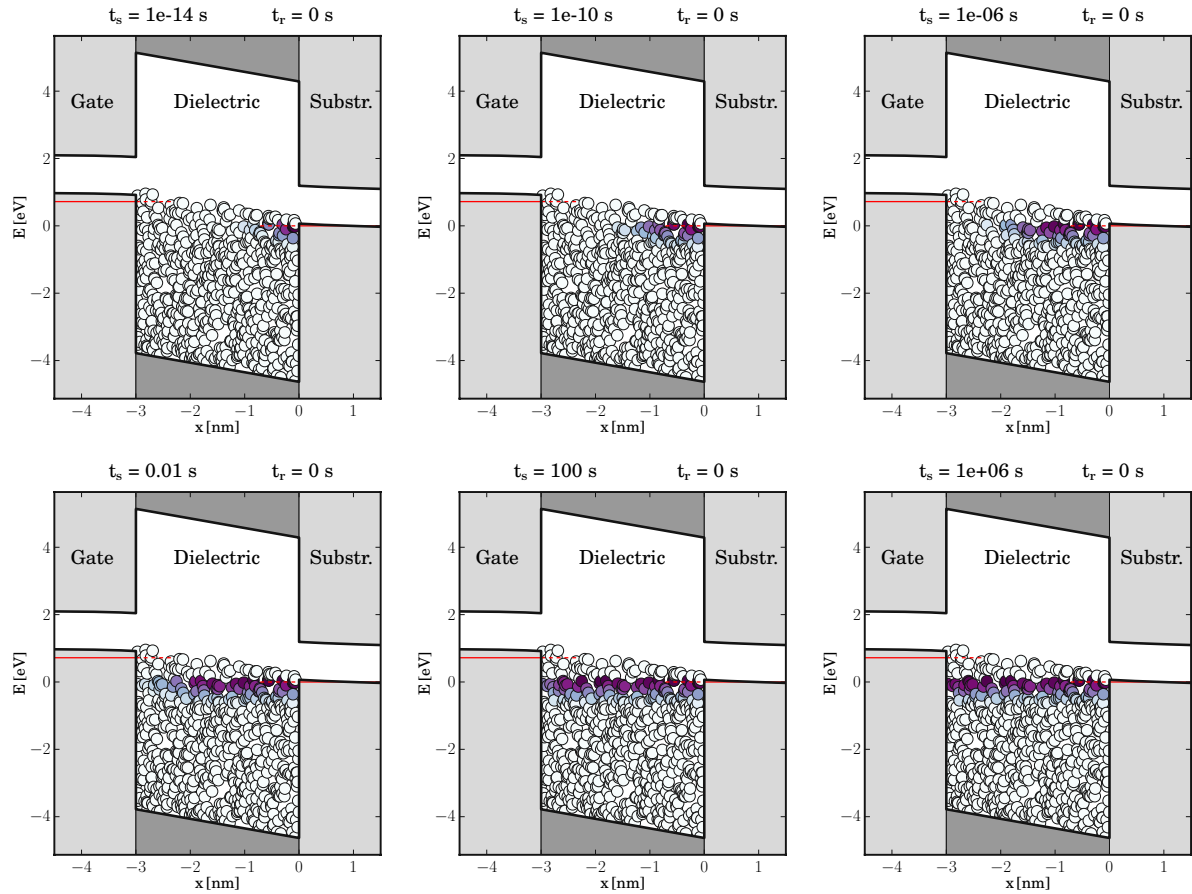


FIGURE 4.9: The hole filling of traps during the stress phase ($V_G = -1\text{ V}$). Single traps are represented by the small circles located in the lower part of the oxide bandgap, where the occupied and the empty states are depicted as purple and white filled circles, respectively. The hole occupation of traps in the band diagram is recorded for a series of stress times and demonstrates the filling of traps with time. One can recognize a tunneling hole front, which starts from the substrate (right) and penetrates deep into the dielectric (towards the left). For demonstration purposes, the simulations were performed with the upper edge of the trap band shifted slightly above the substrate valence band. Note that traps located above the Fermi level do not have captured holes. This is due to the fact that these traps are energetically located within the substrate bandgap and thus have no corresponding energy level which can serve as a hole source in a tunneling process. Furthermore, hole trapping from the poly-gate has been neglected in these simulations but this aspect will be addressed later in Section 4.2.8.

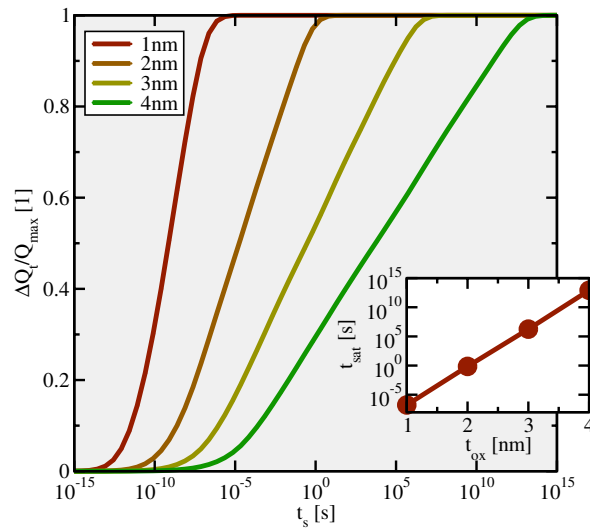


FIGURE 4.10: The time evolution of hole trapping for different thicknesses of the dielectric ($V_G = -1\text{V}$, $T = 125^\circ\text{C}$). For comparison with Section 4.2.8 uppermost trap level has been shifted -0.3eV below the substrate valence band edge in this simulation. One can observe an early saturation for devices with an oxide thickness equal or smaller than 2nm , not seen in experiments. The inset shows that the time point of saturation is shifted out of the measurement window for devices with an oxide thickness notably exceeding a value of 2nm .

4.2.4 Time Range of Trapping

The simulations in Fig. 4.8 reveal that hole trapping sets in around 1ps and lasts over approximately 15 decades. In this context one should consider that the electrical characterization methods used in NBTI have a limited time resolution of about $1\mu\text{s}$. Therefore, they can only assess the accumulated degradation within a small measurement window while a large part of the real degradation is invisible in the experimental data. However, note that despite the wide time range, hole trapping is limited to a few seconds in a 2nm thick device (cf. Fig. 4.10). By contrast, no sign of saturation has been experimentally observed in the stress phase of NBTI so far.

4.2.5 Oxide Field Dependence

The simulated curves in Fig. 4.8 have the same shape irrespective of the applied gate bias and can be made overlap by multiplying them with appropriate scaling factors $s(F_{\text{ox}}, T)$. According to measurement data, $s(F_{\text{ox}}, T)$ should follow a quadratic field dependence up to approximately 8MV/cm . However, the required scaling factors do not show the correct tendency. Recall that only defects energetically shifted above E_f are capable of capturing holes. Therefore, the amount of trapped charges per unit time is determined by the difference between E_v and E_f before and during the application of the stress voltage. The relative shift of these both energies is directly related to the surface potential φ_s according to equation (3.9). The simulations in Fig. 4.11 demonstrate that φ_s follows a nearly linear behavior over a wide range of the electric fields. As a result, one obtains

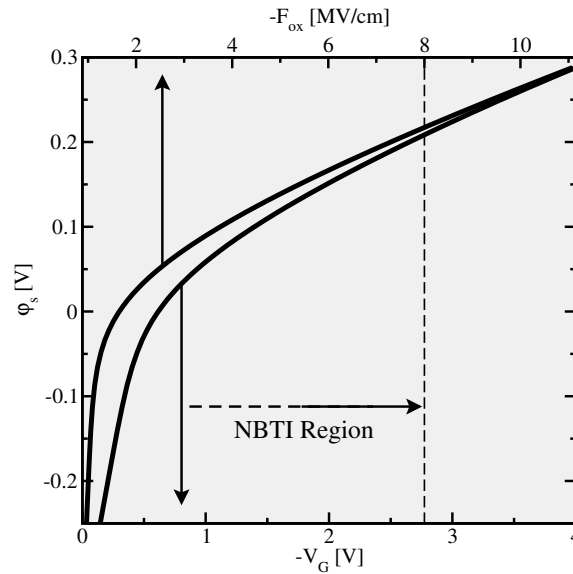


FIGURE 4.11: The surface potential ϕ_s versus the applied gate bias and the oxide field for the simulated pMOSFET ($T = 125^\circ\text{C}$). This quantity is proportional to the scaling factor $s(F, T)$ in the simulated curves of Fig. 4.8 and thus determines the field-acceleration of the ETM. In the region relevant for NBTI, ϕ_s shows a nearly linear dependence on the oxide field.

a linear dependence for $s(F, T)$ in the NBTI region (indicated in Fig. 4.11), opposed to the quadratic field-acceleration observed in experiments.

4.2.6 Time Behavior during Relaxation

In the simulated relaxation data in Fig. 4.12, the degradation returns back to its pre-stress value, meaning that all defects charged during the stress phase also take part in the recovery phase via hole emission. In these simulations it has been presumed that the trapped holes can only tunneling back to the substrate. However in devices with a small oxide thickness, the trapped charges can in principle be emitted to the poly-gate contact. This case will be addressed in detail in Section 4.2.8.

The simulations in Fig. 4.12 exhibit a logarithmic time behavior as observed in experiments (see Section 1.4). As for the stress phase, hole tunneling is determined by the WKB factor so that the tunneling times increase exponentially with larger x_t . This gives rise to a tunneling electron⁴ front, which starts out from the substrate and continues deep into the dielectric as illustrated in Fig. 4.13. The annihilation of trapped holes becomes visible as straight lines in Fig. 4.12, consistent with the experimental findings for the recovery phase. Against intuition, devices stressed at a higher gate bias recover faster. This can be traced back to the fact that spatially deeper traps have a reduced tunneling barrier when they are shifted down in the band energy diagram during relaxation (see Fig. 4.14). The above behavior has not been observed in measurements. This deviation from experimental data

⁴ Hole emission can be envisioned as electrons capture at a microscopic level, when disregarding the effective masses of the charge carriers.

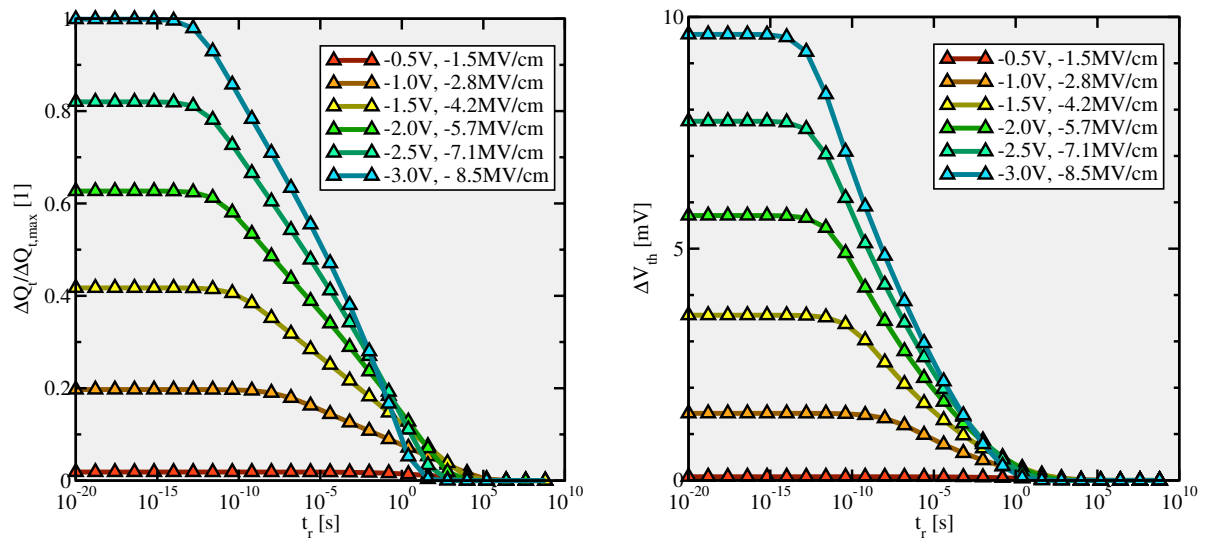


FIGURE 4.12: The same as Fig. 4.8 but for the relaxation phase. Note the accelerated recovery in the ΔQ_t curve for heavier stress conditions, which shifts the end of the relaxation phase below 1 s.

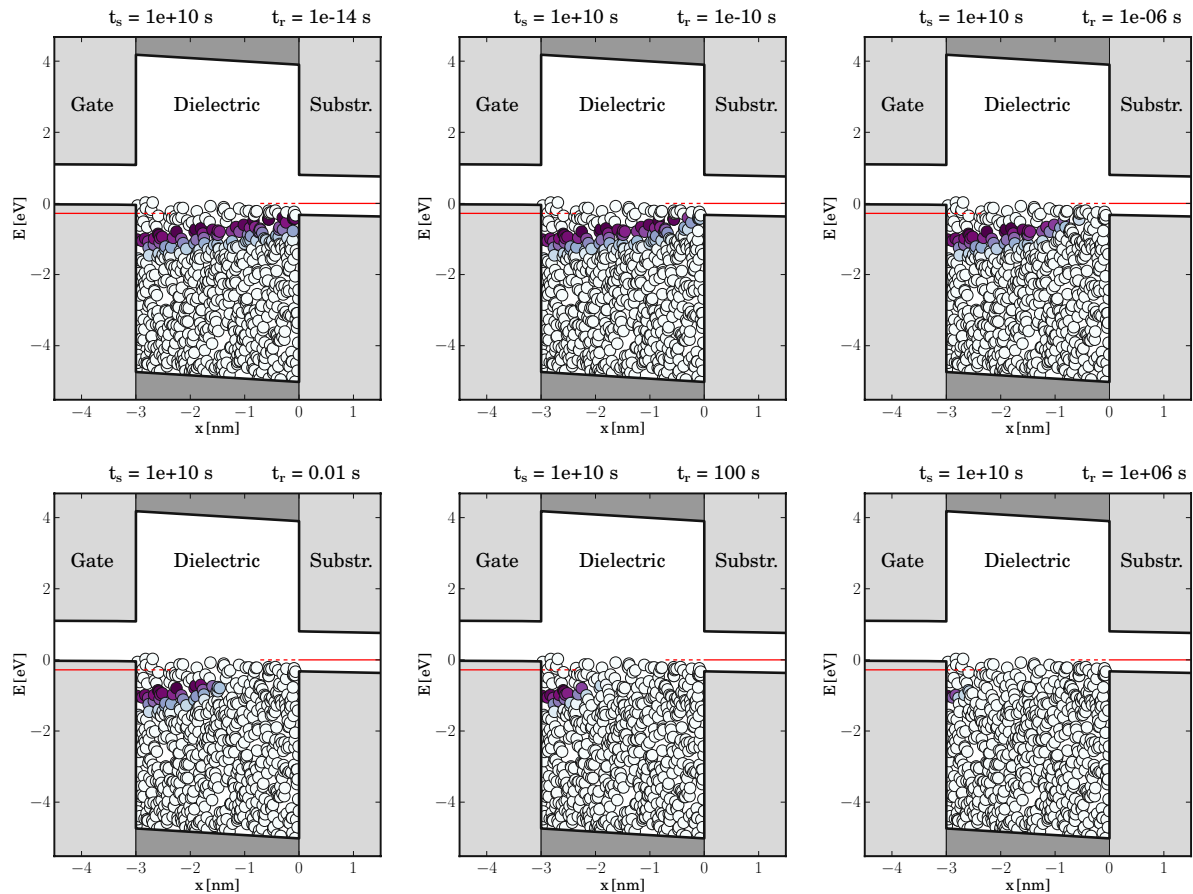


FIGURE 4.13: The same as Fig. 4.9 but for the relaxation phase. The tunneling electron front annihilates the trapped holes within the oxide, starting from the substrate.

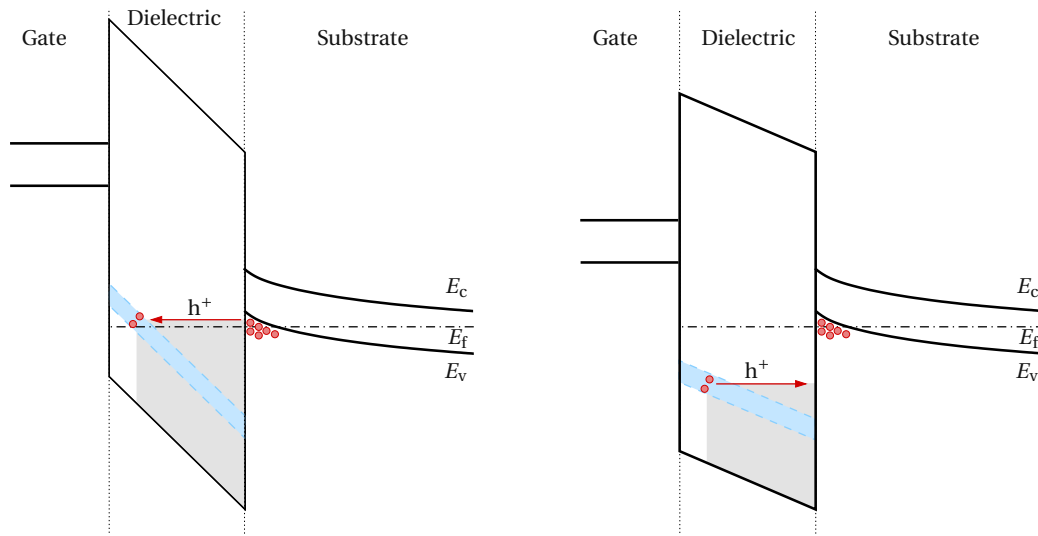


FIGURE 4.14: Hole trapping (left) and detrapping (right) during stress and recovery, respectively. The tunneling barrier during relaxation (indicated by the grey area) is appreciably reduced compared to stress, which is associated with shorter tunneling times and results in an accelerated recovery.

could, in principle, also originate from an additional permanent or slowly recovering component which is not accounted for in the present simulations. As compared to the stress phase, the time span for the relaxation phase is shortened for higher gate biases so that the recovery already ends before 1 s.

A remarkable peculiarity of NBTI is the asymmetry in the slopes during stress ($s_{\text{relax}}(T, F_{\text{ox,s}})$) and relaxation ($s_{\text{stress}}(T, F_{\text{ox,s}})$). It is related to the fact that the recovery phase exceeds the duration of the stress phase by a couple of decades. However, the ETM (see Fig. 4.15) predicts that the recovery proceeds at equal pace or even faster than the degradation during stress does. This is due to the fact that traps charged with $\tau_{\text{cap,h}}$ during stress emit their holes with approximately the same time constants $\tau_{\text{em,h}}$ during recovery.

4.2.7 Investigation of the Temperature Dependence using a Quantum Refinement

Another important issue concern the temperature dependence of the ETM. Recall that the experimental data exhibit an increased degradation at higher temperatures, which was thought to go hand in hand with an enhanced ‘total’ hole concentration p_{tot} ⁵. However, the simulations in Fig. 4.16 reveal an inverse tendency for the ETM. The discrepancy might be attributed to a shift of the hole centroid into the substrate and an associated reduction in the ‘interfacial’ hole concentration p_{if} (see insert of Fig. 4.16) for higher temperatures. In the band diagram, this is associated with a rise of E_f towards the center of the substrate bandgap and thus away from E_v . The relative position of E_f and E_v at the interface is the quantity which enters the calculation of the tunneling rates (2.46) and yields a reduction in the amount of hole trapping for higher temperatures. In a quantum mechanical

⁵ p_{tot} is defined as the hole concentration integrated over the direction perpendicular to the interface.

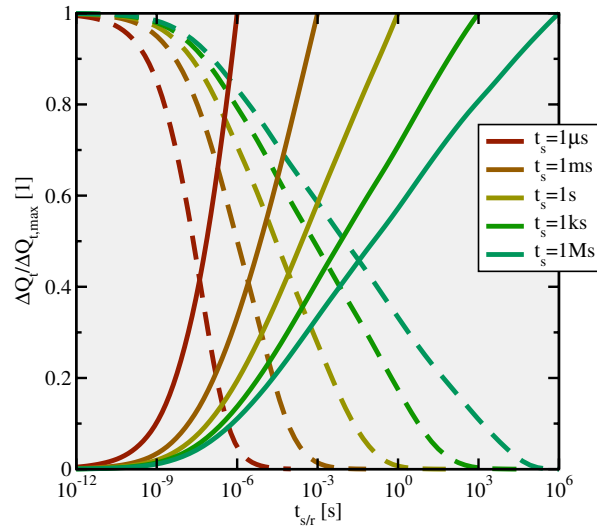


FIGURE 4.15: Trapping (solid) and detrapping (dashed) curves ($V_G = -1\text{ V}$, $T = 125^\circ\text{C}$) for different stress times. Each pair of curves is normalized to the last stress value. Note that both curves approximately cover the same number of decades, which is in disagreement with the experimentally obtained asymmetry in the slopes during the stress and the relaxation phase.

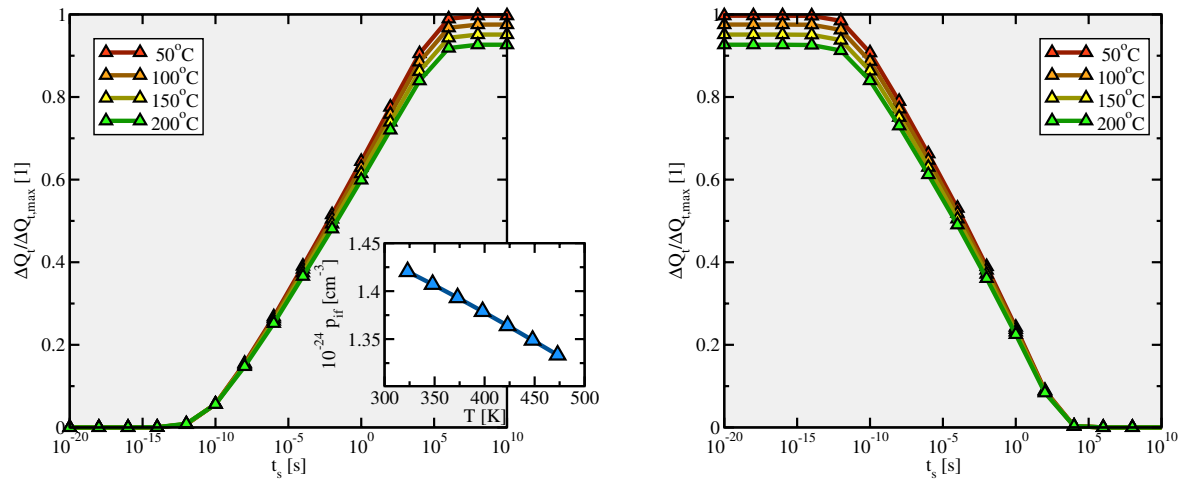


FIGURE 4.16: The time evolution of trapped holes during stress (left) and relaxation (right) for different temperatures. The applied gate bias has been set to -2 V . Surprisingly, the classical simulations predict a decrease in the amount of trapped holes for higher temperatures. This seems to be related to the reduction in the interfacial hole concentration p_{it} shown in the insert of the left plot.

treatment, the substrate holes are described by channel wavefunctions, which are spread over the whole channel region and penetrate deep into the dielectric. Tunneling and thus charge trapping are eventually induced by the overlap of the hole and trap wavefunctions. The ETM must be refined in order to account for the quantum mechanical nature of the confined charge carriers in the channel. Again equation (2.34) is taken as a starting point in the following derivation.

$$r = \sum_b \frac{2\pi}{\hbar} |M_{c/v,tb}(E_x, x_t)|^2 \delta(E_t - E_b) \quad (4.21)$$

Here, b stands for the initial states. The sum over these states is split into components parallel and perpendicular to the semiconductor-oxide interface, where the charge carriers are confined in the latter direction. As derived in the Appendix A.4, the number of states in an one-dimensional confined electron gas is

$$\sum_b = A_{yz} \left(\int_{E_{n,0}}^{\infty} dE D_{n,2D} \int_{E_{n,0}}^E dE_x \sum_{j_n} \delta(E_x - E_{n,j_n}) + \int_{-\infty}^{E_{p,0}} dE D_{p,2D} \int_E^{E_{p,0}} dE_x \sum_{j_p} \delta(E_x - E_{p,j_p}) \right), \quad (4.22)$$

$j_n, j_p = 0, 1, 2, \dots$ denote the quantum numbers and $E_{n/p,j_{n/p}}$ the respective eigenstates of the confined states in the conduction or the valence band, respectively. Note that the integrals run from the first confined eigenstate E_{n,j_n} or E_{p,j_p} since they are located closest to the conduction or valence band edges, respectively. Using (4.22), the rate (4.21) can be rewritten as

$$r = A_{yz} \frac{2\pi}{\hbar} \left(\int_{E_{n,0}}^{\infty} dE D_{n,2D} \int_{E_{n,0}}^E dE_x \sum_{j_n} \delta(E_x - E_{n,j_n}) |M_{c,tb}(E_x, x_t)|^2 \delta(E_t - E) + \int_{-\infty}^{E_{p,0}} dE D_{p,2D} \int_E^{E_{p,0}} dE_x \sum_{j_p} \delta(E_x - E_{p,j_p}) |M_{v,tb}(E_x, x_t)|^2 \delta(E_t - E) \right). \quad (4.23)$$

Due to the δ -function, the right-hand side of equation (4.22) can be simplified to

$$r = A_{yz} \frac{2\pi}{\hbar} \left(D_{n,2D} \int_{E_{n,0}}^{E_t} dE_x \sum_{j_n} \delta(E_x - E_{n,j_n}) |M_{c,tb}(E_x, x_t)|^2 + D_{p,2D} \int_{E_t}^{E_{p,0}} dE_x \sum_{j_p} \delta(E_x - E_{p,j_p}) |M_{v,tb}(E_x, x_t)|^2 \right). \quad (4.24)$$

The refined variant of the ETM shows an increase in the total hole concentration p_{tot} (see inset of Fig. 4.17), which would suggest an increased degradation for higher temperatures. Contrary to this ad hoc hypothesis, the simulations in Fig. 4.17 yield a reduced degradation, which is still in contrast to the experimental observations (see Section 1.4). Actually, not the change in the hole concentration — may it be p_{it} or p_{tot} — causes the inverse trend but the shift of E_f relative to E_v . From a statistical point of view, traps and band states at an energy E_t will equilibrate, meaning that their occupancies f_p and f_t will equalize. For higher temperatures, the raise of E_f in the band diagram implies a reduction

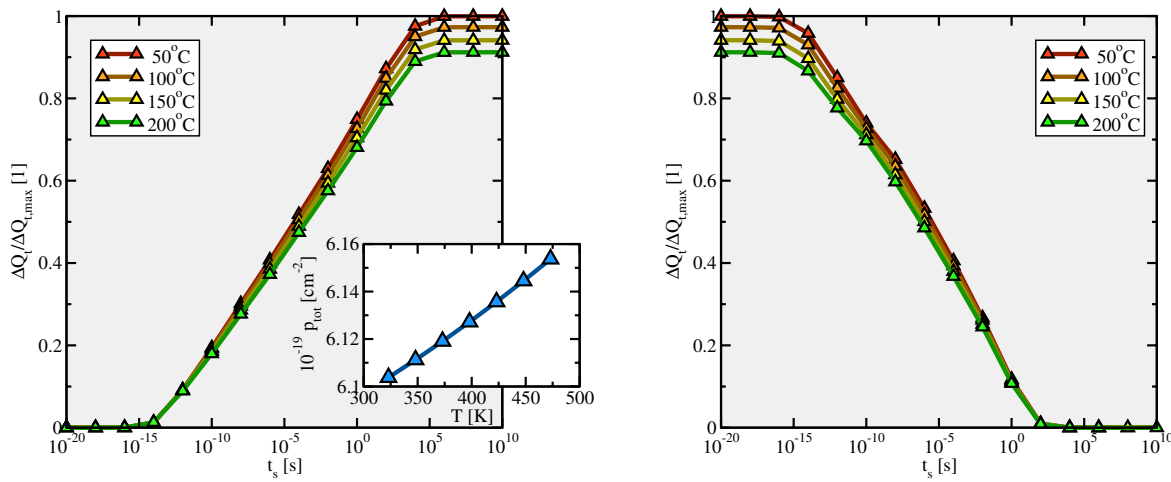


FIGURE 4.17: The same as in Fig. 4.16 but for the quantum mechanical variant of the ETM. The improved model delivers the same tendency as its classical variant even though the total hole concentration p_{tot} (see the insert of the left plot) would suggest an increased hole trapping for higher temperatures. In comparison to the classical variant, a shift of the whole set of curves towards earlier times is observed.

of f_p and in consequence f_t , which is related to the amount of trapped charges. It is important to note here that the density of states only affects the rates but not the equilibrium trap occupancies. In conclusion, the inverse temperature dependence cannot be ascribed to the deficiency of the classical variant of the ETM but it is inherent to elastic tunneling itself. Furthermore, the curves in Fig. 4.17 are shifted approximately two decades towards earlier times compared to the classical variant, which worsens the problem of the early saturation during stress.

4.2.8 Charge Injection from the Gate

So far, the existing description of charge trapping has been restricted to charge injection from the substrate. In device structures with thicker gate dielectrics, the large tunneling distances from the gate towards the defects are associated with small rates so that the presence of the gate contact as a source or sink of charge carriers could be neglected. As the oxide thickness of modern semiconductor devices has entered the nanometer range, this assumption has lost its justification. Therefore, the ETM needs to be extended by charge carrier injection from the gate. As illustrated in Fig. 4.18, this can be achieved by introducing additional terms into the rates equation:

$$\begin{aligned} \partial_t f_t = & (f_{n,s}(E_t) r_{e,s}(E_t) + f_{n,g}(E_t) r_{e,g}(E_t)) (1 - f_t) - (f_{p,s}(E_t) r_{e,s}(E_t) + f_{p,g}(E_t) r_{e,g}(E_t)) f_t \\ & + (f_{n,s}(E_t) r_{h,s}(E_t) + f_{n,g}(E_t) r_{h,g}(E_t)) (1 - f_t) - (f_{p,s}(E_t) r_{h,s}(E_t) + f_{p,g}(E_t) r_{h,g}(E_t)) f_t \end{aligned} \quad (4.25)$$

The subscripts s and g refer to quantities from the substrate or the poly-gate, respectively. The simulations presented in Fig. 4.19 underline the importance of the gate contact when thin dielectrics are considered. Recall that tunneling in the conventional ETM can be envisaged as a tunneling hole

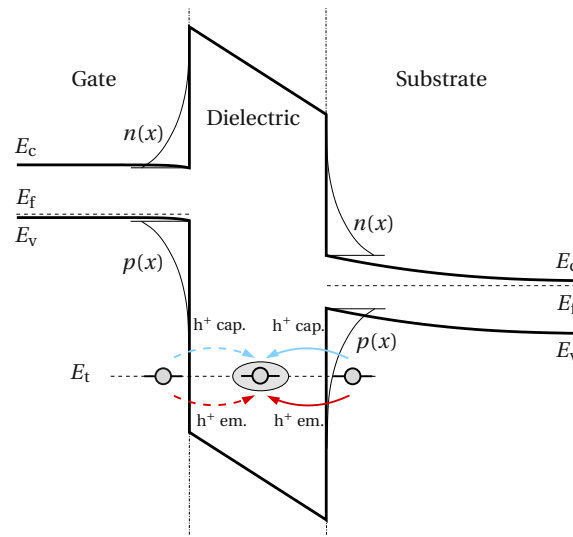


FIGURE 4.18: A schematic of the rates considered in the conventional and the extended ETM for a trap located below the substrate bandgap. The gray filled circles are hole states in the substrate, the dielectric, or the gate. The ellipse marks a trap within the dielectric. Tunneling rates from and towards the substrate are represented by the arrows with solid lines and already taken into account in the conventional ETM. For thinner gate dielectrics, the charge injection from the gate gains importance since the associated rates increase due to the shorter tunneling distances. These rates, indicated by the arrows with the dashed lines, must be incorporated the extended ETM.

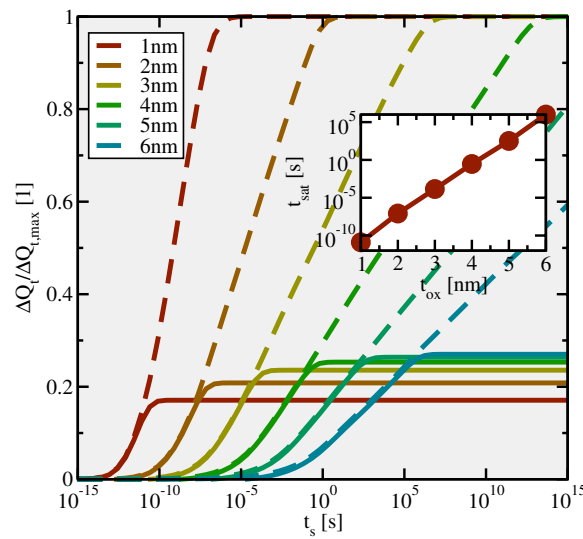


FIGURE 4.19: The same as in Fig. 4.10 but for the conventional (solid line) as well as the extended (dashed line) ETM ($V_G = -1V$, $T = 125^\circ C$). It is noted that the uppermost trap level is located 0.3eV below the substrate valence band edge in this simulation. In the case of the extended ETM, one can recognize an early saturation, which reflects the stopping of the hole front in the dielectric. As pointed out in the inset, this time point of saturation is moved towards an earlier time, which may lie within typical measurement windows for NBTI (ranging from 1 μs to 10ks). One should keep in mind that only devices with an oxide thickness thicker than 5.5nm show a logarithmic time behavior beyond 100ks, which corresponds to the largest investigated stress times.

front that starts at the substrate interface and continues towards the gate. Traps located in the second half of the dielectric are located closer to the gate and thus have shorter tunneling distances to the gate. For these traps, electron injection from the gate outbalances hole trapping from the substrate. Hence, the presence of the gate interface establishes a spatial border to the penetrating hole front. When this border is reached, the tunneling hole front stops, which causes an even earlier saturation during the stress phase. At this point it is important to note that, depending on the spatial and energetical distribution of traps, the band bending in the gate can also trigger electron injection from the gate. A comparison of both models is presented in Fig. 4.19. One may notice that the timescale for trapping is dramatically reduced in the case of the extended ETM. For devices with relatively thick gate dielectric of 4 nm, the saturation sets in before 1 s. In technologically more relevant device structures with a gate dielectrics thinner than 2.5 nm, the degradation due to hole trapping ends before 1 μ s and would even be not assessable with ultra-fast MSM measurements [27]. The fact that only traps with short tunneling times participate during the stress phase is also reflected in a fast removal of trapped charges during the relaxation phase. The complete removal of positive charges during the relaxation phase is achieved within approximately the same timescales than hole trapping during stress. By contrast, the relaxation seen in experiments is often described as a long-lasting process, which exceeds 10^5 s. More importantly, hole trapping is reduced below five decades for oxide thicknesses below 3 nm while the eMSM data on a 1.7 nm thick device (see Fig. 1.4) show at least seven decades.

4.2.9 Width of the Trap Band

Up to this point, only broad distributions of trap levels have been addressed. However, it is speculated that some high- κ dielectrics have a crystalline structure [166], which is characterized by small temperature-induced variations of bond distances and angles. These lattice distortions yield a small spreading of defect levels, seen as a small trap band in Fig. 4.20. In Fig. 4.20, the time evolution of ΔQ_t is plotted for a narrow distribution of defect levels. During stress, the onset of hole trapping is shifted towards earlier times for increasing gate voltages. This behavior can be traced back to different defects involved in charge trapping at different V_G (see Fig. 4.21). As the gate bias is increased, defects located closer to the substrate interface are moved into the region around the Fermi level. Due to their reduced tunneling distances, they feature shorter trapping times and therefore give rise to an earlier onset in the $\Delta Q_t(t)$ curves. Since the defects in the active trapping region are spatially concentrated to a small region, their corresponding tunneling distances are limited to a small range. Thus the distribution of trapping times is sharply peaked, which becomes visible as sudden jumps in the $\Delta Q_t(t)$ curves of Fig. 4.20. The shape of these curves is in stark contrast to the wide range of timescales usually involved in NBTI.

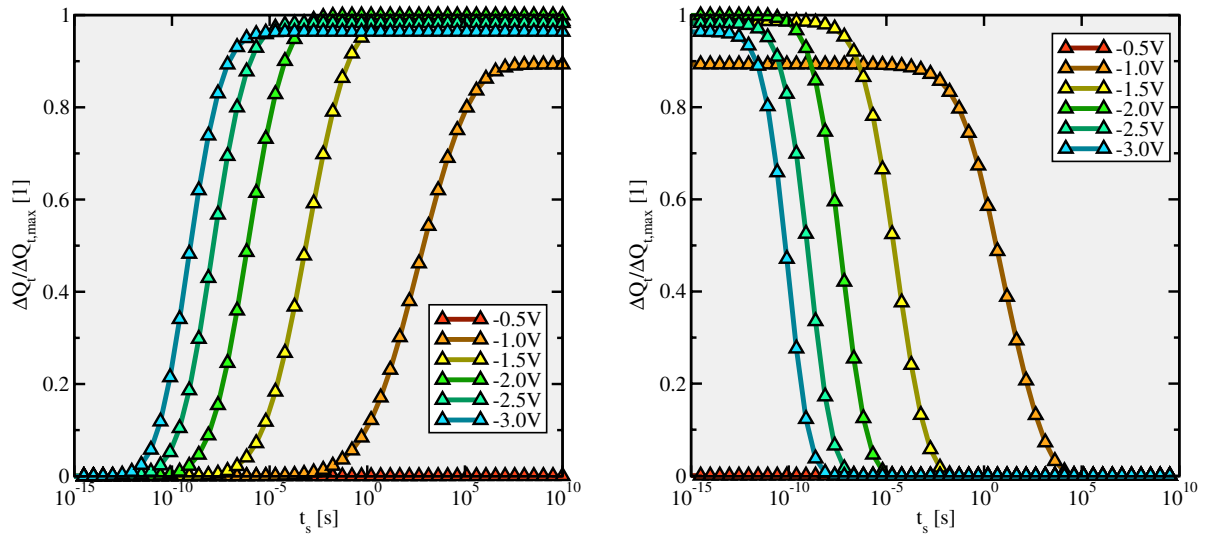


FIGURE 4.20: The time evolution of the normalized ΔQ_t ($T = 125^\circ\text{C}$) for stress (left) and relaxation (right) presuming a narrow distribution of defect levels (0.1 eV) centered around -0.75 eV below the substrate valence band edge. For this assumption, the ETM predicts short jumps or drops in ΔQ_t for both phases, which are limited to only a very few decades. This cannot be reconciled with NBTI data with a relaxation phase that spans over 10 decades. In the case of $V_G = 0.5\text{ V}$, the defect levels are not moved into the region around the Fermi level so that no trapping can occur.

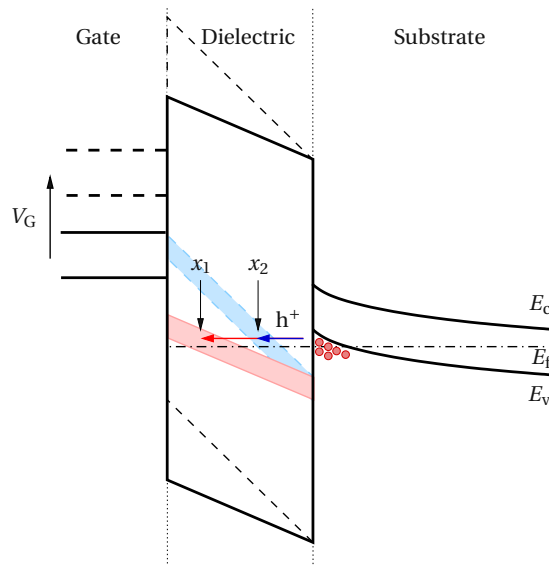


FIGURE 4.21: The band diagram for two different gate voltages. The crossing point between the Fermi level and the band of trap levels (shown as a purple and a blue region for a low and a high gate bias, respectively) is linked to the earliest trapping events and the beginning of charge trapping. When the gate bias is increased, the crossing point is shifted closer to the substrate interface ($x_1 \rightarrow x_2$) where traps with smaller tunneling time constants ($\tau_2 \ll \tau_1$) are situated. This leads to an earlier onset of charge trapping for higher gate voltages.

| Model Properties | | |
|------------------|----------------------------------|---|
| (i) | Involved Time Scales | X |
| (ii) | Log. Behavior during Stress | ✓ |
| (iii) | Log. Behavior during Recovery | ✓ |
| (iv) | Asymmetry Stress/Recovery | X |
| (v) | Quadratic Field Dependence | X |
| (vi) | Quadratic Temperature Dependence | X |

TABLE 4.1: Checklist for an NBTI model. This table contains the most important features of the NBTI stress and relaxation curves. The above features must be viewed as criteria which have to be fulfilled by an NBTI model candidate.

4.3 Conclusion

In this chapter, several peculiarities of the ETM have been analyzed and compared to the experimental findings of NBTI. It has been pointed out that this model predicts a logarithmic time behavior over several decades during stress and relaxation. However, the ETM fails to explain NBTI for several reasons:

- $\Delta V_{th}(t)$ saturates within or even before the experimental time window for devices with thin gate dielectrics as applied in modern semiconductor devices. This problem becomes even more severe if charge injection from the gate is considered.
- The asymmetry between stress and recovery cannot be reproduced by this model.
- The ETM shows the wrong temperature and field dependence, which are both inherent to the model and therefore cannot be improved by suitably chosen fitting parameters.

The above arguments summarized in Table 4.1 are a strong evidence that the NBTI degradation cannot be described by hole trapping according to the ETM. As a consequence, this model is discarded from the list of possible NBTI models, and other capture processes must be considered.

5

Level Shift Model

The ETM has been based on the concept that electrons tunneling into and out of a defect have the same energy. This implies that the corresponding trap level remains at the same energy within the oxide bandgap regardless of whether the defect has captured a charge or not. However, as pointed out in Section 2.3, this level is subject to a shift after each charging or discharging event. This is due to the fact that the defect undergo structural relaxation, which involves strengthening, weakening, or even disrupting bonds. With this deformation, the defect orbitals change which is accompanied by a shifts of the corresponding defect levels. This concept of the level shift has not received much attention so far but has important implications for the tunneling kinetics in α -SiO₂.

In the first part of this chapter it will be demonstrated that the charging and discharging of defects involves a non-negligible structural relaxation, which results in an appreciable level shift and thus impacts the trapping dynamics. Using DFT, the corresponding switching levels will be determined for a number of defects suspected to be present in α -SiO₂. Based on the position of these levels, the defects will be tentatively classified according to their expected trapping behavior in NBTI experiments. In order to allow for quantitative predictions, a new model accounting for the level shift will be developed in the second part of this chapter. This model will then be tested whether it can explain the NBTI experiments.

5.1 Defects in a – SiO_2

This section deals with the basic properties of defects, especially the position of their corresponding trap levels. Previous theoretical investigations were focused on defects in crystalline SiO_2 [112, 113] as a substitute for amorphous materials. At this point it is emphasized that one has to consider the amorphous nature of SiO_2 since it strongly affects the defect properties: For instance, oxygen molecules O_2 in c – SiO_2 have only discrete values for the barriers to migrate from one void to the next one. By contrast in a – SiO_2 , they encounter a distribution of barriers whose average eventually determines the effective activation energy for diffusion [167, 168]. Another example is the stability of the E' center, which can transform to an oxygen vacancy by overcoming a thermal barrier. The height of this barrier and thus the stability of the E' center have been found to strongly depend on the local surrounding silica network [19, 20]. These two examples suggest that small variations in the bond lengths and angles of the surrounding structure could result in a wide distribution of trap levels [161, 162] and thereby impact the trapping dynamics. Unfortunately most of the defect properties are difficult to determine experimentally so that theoretical methods, such as DFT, were chosen for the determination of defect levels. The empirical potential molecular dynamics was employed for the production of a – SiO_2 . The details of this procedure are described in Section 3.4.2. Pair-correlation functions, angle distributions, and the ring distribution have been evaluated in order to ensure that the obtained samples mimic real a – SiO_2 . The generated structures were used for DFT calculations, whose parameters are summarized in Section 3.3.3. The defect structures have been obtained by adding, shifting, or removing the silicon, the oxygen, or the hydrogen atoms. The switching trap levels for the created defects have been evaluated using the formulas (3.33)–(3.36). The calculated trap levels have been aligned to the silicon bandgap using the procedure proposed in [113]. The obtained valence band offset of 2.6 eV for the Si/ SiO_2 interface has been found to be in good agreement with the values extracted from [80, 169, 170]. In the following, a study of several prominent defects in a – SiO_2 will be presented. They will be discussed based on their configuration in their various charge states in order to check the correctness of the produced defect structures. Furthermore, their expected trapping behavior will be inferred from the switching levels gained from DFT simulations.

5.1.1 Oxygen Vacancy

In stoichiometric SiO_2 , two silicon atoms are always connected by one bridging oxygen atom. When this atom is removed, the two neighboring silicon atoms establish a common bond, the heart of the oxygen vacancy (see Fig. 5.1). In c – SiO_2 , the length of this bond is approximately 2.5 Å [19, 149], which compares well with the Si-Si distance of 2.35 Å in crystalline bulk silicon [171]. In the DFT simulations of this thesis, the defects are embedded in an amorphous SiO_2 host material so that this characteristic length is distributed. Our set of structures covers Si-Si bond lengths between 2.3 Å and 2.8 Å. These values are in reasonable agreement with the range (2.3 – 2.7 Å) obtained in the study of Mukhopadhyay *et al.* [172]. Nicklaw [162] extended his defect calculations to highly strained oxygen vacancies whose bond lengths reach values up to 3.2 Å. This kind of defects is associated with large

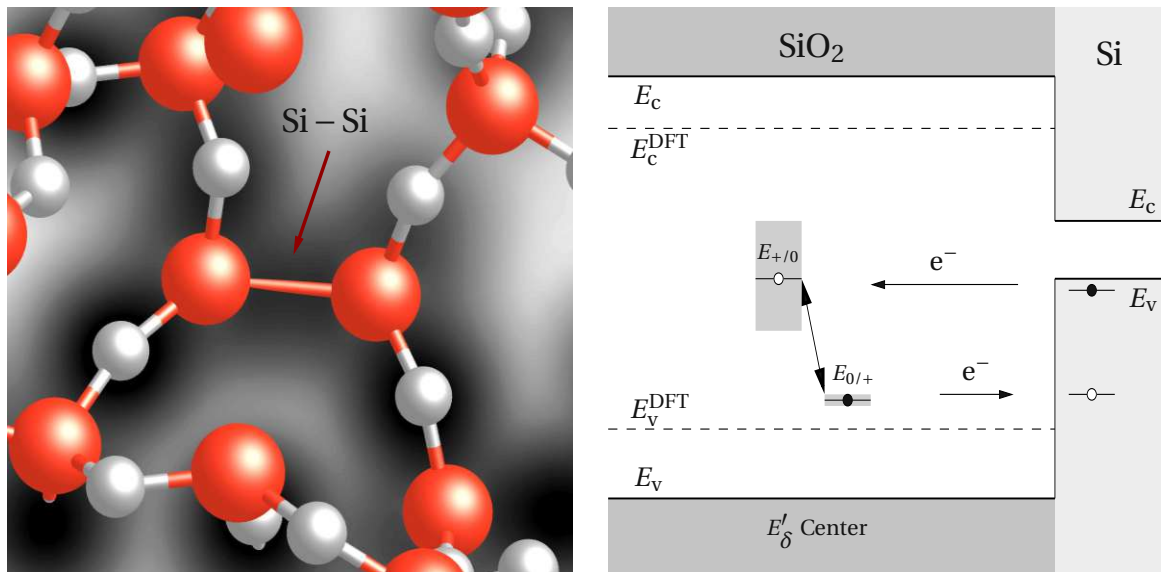


FIGURE 5.1: **Left:** An electron density plot of an oxygen vacancy. Red and white spheres represents silicon and oxygen atoms, respectively, and bonds are shown as the sticks connecting these atoms. The Si-Si bond, established after the removal of an oxygen atom, is indicated by a high charge density (dark area) between the neighboring silicon atoms. **Right:** The defect levels arising from oxygen vacancies (neutral) or E'_δ centers (positively charged) in α -SiO₂. $E_{c/v}^{\text{DFT}}$ (dashed line) denotes the conduction/valence band edge, extracted from the DFT simulations. The $E_{+/0}$ levels are related to the capture of electrons while the $E_{0/+}$ levels apply to electron emission. The double-sided arrow represents the shift of defect levels and the spreads of energy levels are visualized by the grey boxes.

formation energies [173], thus exists in small concentrations, and has a negligible contribution to the trapping kinetics of NBTI. The Si-Si bond is associated with the $E_{0/+}$ level, which is sharply peaked and situated far below the silicon valence band edge (cf. Fig. 5.1 and Table 5.1). For comparison, the corresponding defect calculations in c -SiO₂ [149] predict $E_{0/+}$ at approximately the same position.

In the context of EPR measurements, the positively charged counterpart of the oxygen vacancy is referred to as the E'_δ center. The missing negative charge within its bond causes a repulsion between the two electropositive silicon atoms and results in a stretching but not in a breakage of the Si-Si bond. In the c -SiO₂ reference, the Si-Si bond of E'_δ center was found to extend from $\sim 2.5\text{\AA}$ to $\sim 3.0\text{\AA}$ [19, 149], which is large in comparison to the bond length of a neutral oxygen vacancy. In the DFT simulations of this thesis, this kind of weak bonds experiences large tensile and compressive forces due the amorphous SiO₂ host material. The corresponding bond lengths are found to be distributed within a range of $2.6 - 3.5\text{\AA}$, consistent with the values used in [19] and [20]. This Si-Si bond is associated with a defect level close to the silicon valence band edge. Due to the amorphous nature of SiO₂, the defect levels $E_{+/0}$ are spread widely over an energy range from -1.5eV to $+0.4\text{eV}$ (cf. Fig. 5.1). By contrast in the case of the neutral oxygen vacancy the impact of the surrounding network can be neglected due to the strong Si-Si bond so that the distribution of $E_{+/0}$ levels is narrow as shown in Fig. 5.1.

| Defect | Trap Level | Min. | Max. |
|---------------------|------------|---------|---------|
| E'_δ | $E_{+/0}$ | -1.5 eV | +0.4 eV |
| | $E_{0/+}$ | -2.9 eV | -2.7 eV |
| E'_γ | $E_{+/0}$ | +0.7 eV | +0.9 eV |
| | $E_{0/+}$ | -1.1 eV | -0.8 eV |
| $E'_\delta\text{H}$ | $E_{+/0}$ | +1.2 eV | +1.7 eV |
| | $E_{0/+}$ | -1.5 eV | -0.9 eV |
| | $E_{0/-}$ | +0.9 eV | +1.1 eV |
| | $E_{-/0}$ | -2.0 eV | -0.6 eV |
| H | $E_{+/0}$ | +1.7 eV | +1.9 eV |
| | $E_{0/+}$ | -2.9 eV | -2.3 eV |
| | $E_{0/-}$ | +0.0 eV | +1.2 eV |
| | $E_{-/0}$ | -2.3 eV | -2.0 eV |

TABLE 5.1: Switching levels ($E_{+/0}$, $E_{0/+}$, etc.) referenced to the midgap of the substrate silicon. The first sign of $E_{\alpha/\beta}$ ($\alpha, \beta = +, 0, -$) indicates the equilibrium configuration of the defect in the corresponding charge state and the second sign gives the charge state of the defect for a given configuration.

Regarding the tunneling dynamics, one has to differentiate between two cases: If the defect level $E_{+/0}$ is located below the silicon valence band edge, electrons from the substrate valence band can be captured by the defect via elastic tunneling. For the reverse process, the defect level is already shifted downwards, where the electron in the defect is unlikely to find a high energetic hole in the substrate. From this argumentation it is expected that oxygen vacancy remains neutral if it is discharged once. In case the $E_{+/0}$ level is located above the silicon valence band edge, electron capture into the defect is inhibited, which suggests that this defect acts as a ‘fixed positive charge’. However, keep in mind that these charges may be neutralized via interface states instead.

5.1.2 E'_γ Center and Variants

The existence of the E'_γ center as an additional metastable configuration of the oxygen vacancy has been confirmed by a wide range of theoretical [19, 20] as well as experimental [15, 16] studies. Starting from the E'_δ center, one side of the defect undergoes a transformation called ‘puckered’. During this, the dimer bond is disrupted and the ‘puckered’ silicon atom moves through the plane defined by its three oxygen neighbors where this new configuration is stabilized via a back bond to a nearby oxygen atom. In the DFT simulations of this thesis, the back bond has typically a length of 1.8 – 2.0 Å, which is large compared to the Si-O bond in bulk SiO₂ (1.6 Å) [153–155, 174]. This indicates a weak bonding of the ‘puckering’ silicon atom to the back oxygen. On the other side of this defect, an unsaturated silicon dangling bond is left behind, which can carry up to two electrons and gives an EPR signal [17]. Only if the E'_γ center is neutralized, this defect is prone to a collapse into its oxygen vacancy configuration [20] again. The configuration of the E'_γ center is depicted in Fig. 5.2.

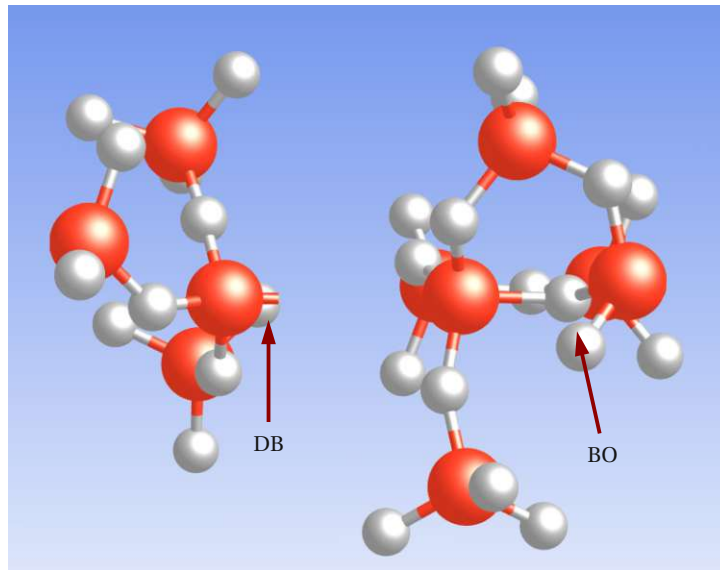


FIGURE 5.2: The structure of an E'_γ center. The silicon atom on the left of the oxygen vacancy can carry up to two electrons in the dangling bond (DB), which is indicated by the stick only connected to the silicon atom. The positively charged silicon atom on the right-hand side is bonded to the back oxygen (BO). The above atomic arrangement is also referred to as the puckered configuration.

In contrast to the oxygen vacancy, the defect levels $E_{+/0}$ and $E_{0/+}$ of the E'_γ center have only a small spread of about 0.2 eV since the silicon dangling bond along with the three other Si – O bonds almost preserve their tetrahedral symmetry during structural relaxation. The puckered side of the defect complex does not interact with the dangling bond and consequently does not impact its defect levels. The levels for tunneling into ($E_{+/0}$) or out of ($E_{0/+}$) the traps lie close to the silicon band edges (see Fig. 5.3). Therefore, only a small thermal excitation of the substrate charge carriers is required for a tunneling process. In this case, the band bending controls the concentrations of electrons in the silicon conduction band or holes in the silicon valence band, respectively, and consequently governs the tunneling rates. This means that the E'_γ centers can be repeatedly charged and discharged by electrons by switching the MOSFET between strong inversion and accumulation. The E'_γ configuration was already proposed by Lelis [15, 16] in the context of the temperature-dependent annealing behavior of oxide traps. The temperature dependence in his model was explained by a transition from a spin-triplet [15] to its corresponding spin-singlet state. The latter denotes the ground state of two electrons, which sit in the dangling bond of an E'_γ center and have their spins aligned anti-parallel. The spin-triplet state is the excited counterpart, which is characterized by a parallel alignment of the electron spins and decays immediately to the spin-singlet ground state after it is occupied. According to the argumentation of Lelis, the concentration of thermally excited electrons is increased at elevated temperatures. This gives rise to an enhanced tunneling probability and thus an accelerated annealing of positively charged E'_γ centers. Interestingly, the energy level of the excited spin-triplet state [15] coincides with the electron capture level $E_{+/0}$ obtained by the DFT simulations of this thesis. Thus, the level shift can explain the same trapping dynamics as in Lelis when replacing the spin-triplet state with the $E_{+/0}$ level. In this way, the defect levels

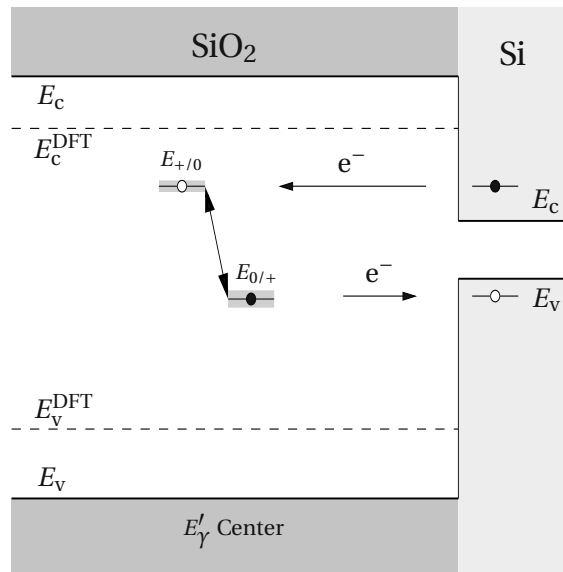


FIGURE 5.3: The defect levels originating from an E'_γ centers in a -SiO₂. The energy levels for the capture of electrons ($E_{+/0}$) as well as the energy levels for the emission of electrons ($E_{0/+}$) are found to lie close to the silicon conduction or valence band, respectively.

responsible for the annealing behavior in the Leleis model has been theoretically confirmed but with the interpretation based on the level shift. As highlighted in [20], most of the E'_γ centers immediately collapses into their oxygen vacancy configuration after neutralization. Then they feature defect levels, located down far below the silicon valence band edge. Therefore, once these defects are neutralized, they cannot be recharged again and will be permanently annealed out. However, this does not rule out the E'_γ center as a cycling charge. A considerable fraction of the neutralized E'_γ centers [20] have a large barrier for the relaxation to the oxygen vacancy configuration and thus may remain in the puckered configuration for time scales relevant for NBTI. In this configuration, they are capable of repeatedly exchanging electrons or holes with the Si/SiO₂ interface.

Another variant of the E'_γ center is the $E'_{\gamma 4}$ center (shown in Fig. 5.4), which has been extensively studied by Conley and Lenahan [40]. Its structure can be visualized by replacing one of the nearby oxygen atoms with an hydrogen atom. The DFT simulations in this thesis have revealed that the neighboring hydrogen atom does not affect the position of the defect levels originating from the dangling bond. As a result, this defect features the same distribution of trap levels and therefore can be repeatedly charged and discharged similarly to the simple E'_γ center.

5.1.3 Hydrogen Atom

In the context of reliability issues, the hydrogen atom [175, 176] is of special interest since it is available in appreciable amounts. Indeed it has been speculated in many investigations [149, 177] that hydrogen seriously affects the reliability of MOSFETs. Its configuration strongly differs with its

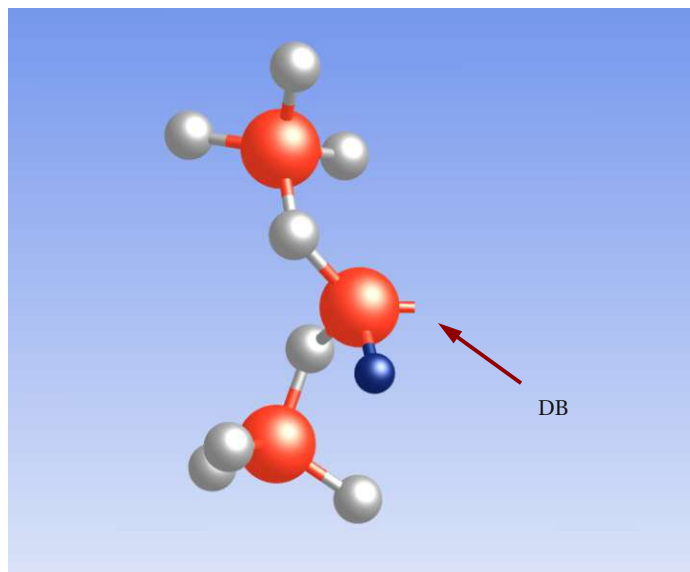


FIGURE 5.4: A representation of an E'_{74} center. The blue sphere represents an hydrogen atom. One of the neighboring O atoms is replaced by an hydrogen atom which shows a tendency to bond to a silica network atom.

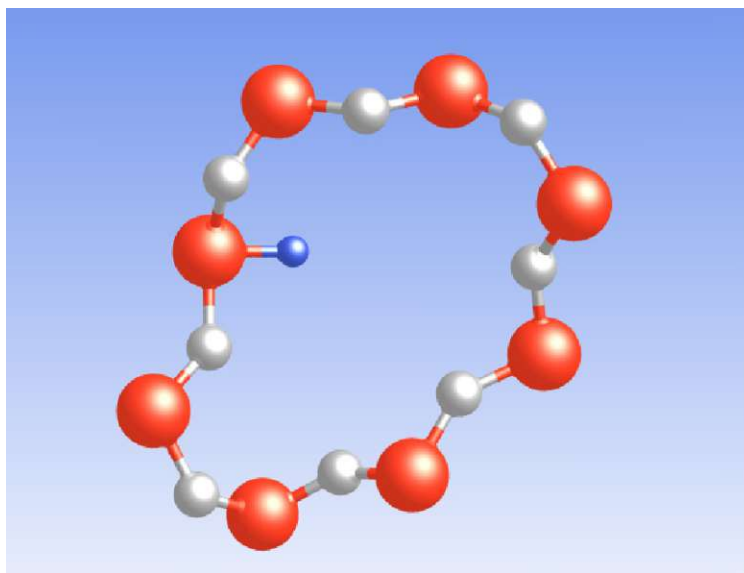


FIGURE 5.5: A representation of a negatively charged hydrogen bound to the silica network. H^+ attaches to the bridging oxygen atom, H^0 is situated in the middle of a void, and H^- forms a weak bond to a silicon network atom.

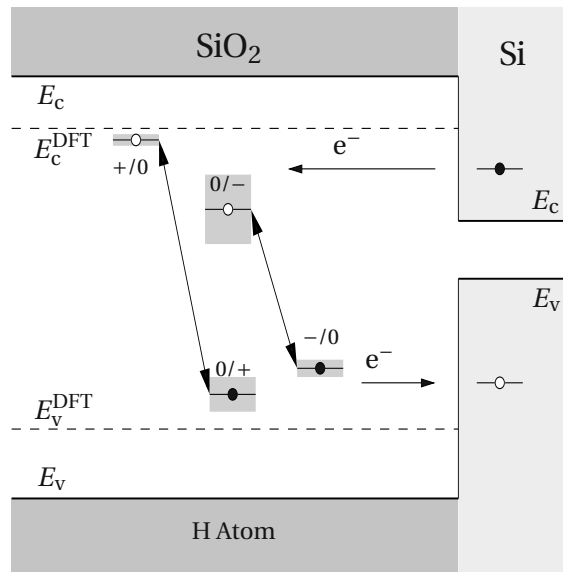


FIGURE 5.6: The defect levels of the hydrogen atom in *a*–SiO₂. The energy levels for charging and discharging are far away from the respective silicon band edges. Except of $E_{0/-}$, all defect levels are largely separated from the band edges and thus unlikely to find a high energetic charge carrier for a tunneling transition.

charge state: The DFT simulations of this thesis predict the neutral atom H^0 in the middle of a void where it does not form a bond with any SiO₂ network atom, consistent with DFT investigations in *c*–SiO₂ [175, 176]. The positively charged atom H^+ weakly binds to one of the electronegative oxygen network atoms as shown in Fig. 5.5. The corresponding Si–H bond length is found to be approximately 1.0 Å, which compares perfectly well with the values for *a*–SiO₂ (1.0 Å) in [164] and *c*–SiO₂ (1.02 Å) in [149, 176]. The negatively charged atom H^- attaches to an electropositive silicon atom with a bond distance of about 1.5 Å, in agreement with [149, 164, 176].

The energy levels of the hydrogen atom are visualized in Fig. 5.6 and listed in Table 5.1. The trap levels $E_{+/0}$, $E_{0/+}$, and $E_{-/0}$ are located far away from the silicon band edges and consequently require highly excited substrate charge carriers for a tunneling transition. By contrast, $E_{0/-}$ is centered around the silicon conduction band edge, resulting in a high tunneling probability. This suggests that the defect is preferredly found in its negative charge state at a weak oxide field. At a first glance, this result seems to contradict the findings of other groups [149, 175, 176]. According to them, the proton has been predicted to be the most stable charge state of the hydrogen atom. However, the calculations are based on a thermodynamic transition level, which only applies to thermally-activated processes, such as NMP transitions for instance.

5.1.4 Hydrogen Bridge

Hydrogen is frequently suspected to undergo reactions with oxide defects [178, 179]. Therefore, the present investigations include a hydrogenated variant of the E'_δ center, also referred to as the

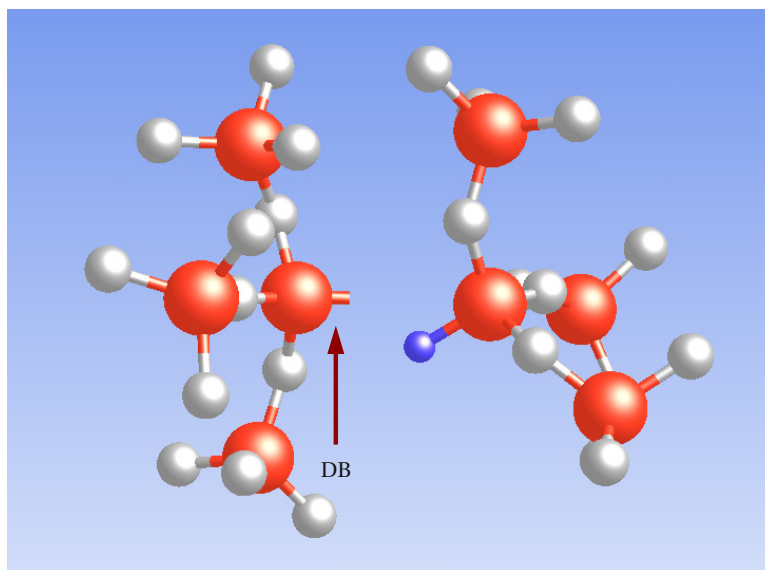


FIGURE 5.7: Representation of the hydrogen bridge in the neutral charge state. The positively charged defect is characterized by a Si-H-Si bond chain. After neutralization this chain is disrupted yielding a dangling bond on the left hand side of this complex and a saturated dangling bond on the right-hand side. In the case of a negatively charged hydrogen bridge, the Si-H bond is bent away from the dangling bond.

hydrogen bridge (see Fig. 5.7). This defect can be constructed by placing a hydrogen atom inbetween the silicon dimer of an oxygen vacancy. In the positive charge state, the hydrogen atom forms a three-center bond involving the two silicon atoms from the dimer and the hydrogen atom in the central position. Its relaxed structure exhibits an asymmetry in the Si-H distances with values of $1.5 - 1.7 \text{ \AA}$ and $1.6 - 2.0 \text{ \AA}$. This is in qualitative agreement with the corresponding defect structure generated in $c - \text{SiO}_2$ [149], however, there are small deviations in the Si-H distances attributed to variations in the atomic structure of the $a - \text{SiO}_2$ host structure. Note that although the aforementioned three-center bond is generally considered unusual in chemistry, the same Si-H-Si bond chain has also been observed for H^+ in $c - \text{Si}$ [180]. In the neutral charge state, the three-center bond is disrupted on the side with the long Si-H distance. The breakage is accompanied by a large structural relaxation which detaches the Si-H complex from the remaining dangling bond. The Si-H bond length reduces to its typical value of 1.5 \AA [181] for the unperturbed Si-H bond while the other silicon atom is separated from the hydrogen atom by about $2.2 - 2.9 \text{ \AA}$ and carries one electron in its dangling bond orbital. By contrast, Blöchl *et al.* [149] found that even in the neutral charge state the hydrogen atom interacts with both silicon atoms. This discrepancy may originate from the rigid network of the surrounding $c - \text{SiO}_2$, which keeps both silicon atoms together and thus prevents the Si-H-Si chain from bond breakage in the neutral charge state. In the negative charge state, the added electron sits on the dangling bond and causes a further repulsion between the dangling bond and the Si-H complex ($2.6 - 2.9 \text{ \AA}$).

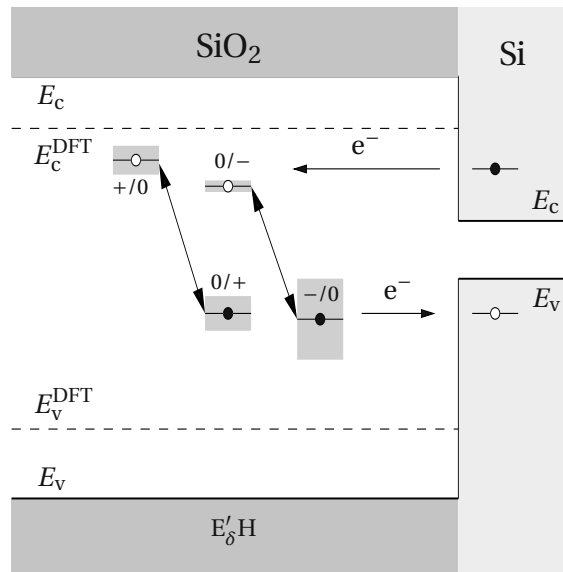


FIGURE 5.8: The defect levels of the hydrogen bridge in α -SiO₂. The hole ($E_{-/0}$ and $E_{0/+}$) capture levels lie slightly closer to the substrate bandgap compared to the electron ($E_{+/0}$ and $E_{0/-}$) levels. This indicates that the hydrogen bridge favors the positive charge state. In the end, the operation state of the MOSFET will eventually determine the charge state of the defect.

As shown in Fig. 5.8 and Table 5.1, all defect levels are located within a reasonable distance from silicon band edges on the energy scale. This suggests that none of the considered transitions can be ruled out based on the position of its corresponding trap level. Thus the trapping dynamics are eventually governed by the band bending in the substrate and the operation state of the MOSFET.

5.2 The Level Shift Model

So far, only qualitative statements about the defect behavior could be made based on the switching levels. In order to make quantitative predictions, the ETM must be generalized in a way to account for the levels shift. Recall that the conventional concept of the ETM is based on the assumption that the energy levels for tunneling ‘into’ and ‘out of’ a defect coincide. This is only the case for unrealistic defects which do not deform after a tunneling event. But as proven in the previous Section 5.1, defects do undergo structural relaxation and therefore feature two switching levels, say $E_{0/+}$ for hole capture and $E_{+/0}$ for hole emission for instance, which can even be separated by some electron Volts (see Fig. 5.9). To be precise, the switching levels $E_{0/+}$ and $E_{+/0}$ actually originate from the one defect orbital and thus must be correctly interpreted as one trap level, which shifts after each charging or discharging event. For the trapping kinetics, this means that only one of these levels can be present in the band diagram at a time. For instance, when the defect in Fig. 5.10 is in its neutral charge state, it has a trap level $E_{0/+}$ for hole capture while its corresponding trap level $E_{+/0}$ remains inactive for the time being. If a hole capture process takes place, the $E_{0/+}$ level vanishes and thus the $E_{+/0}$ level appears. Based on the considerations above, the ETM must be regarded as a special case of the level

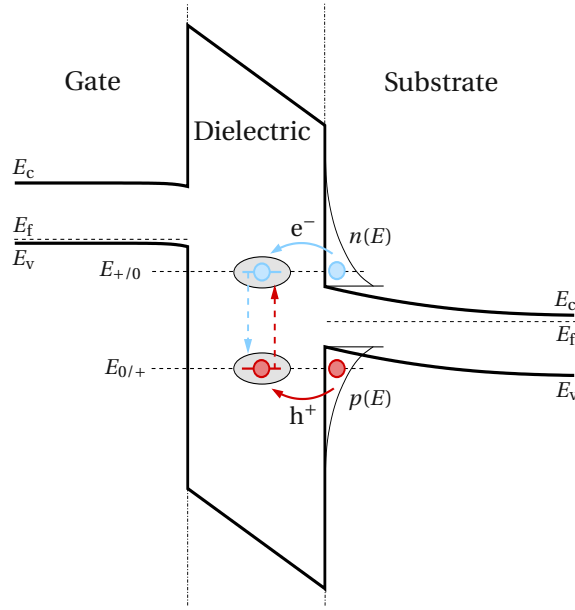


FIGURE 5.9: A schematic of the level shift model. As opposed to the ETM, two distinct defect levels must be considered — namely, $E_{+/0}$ and $E_{0/+}$ for electron and hole capture, respectively. When the positively charged trap (blue filled circle in gray ellipse) captures a substrate electron with an energy of $E_{+/0}$ (blue arrow), the defect level $E_{+/0}$ vanishes but reappears at $E_{0/+}$. The now neutral defect (red circle in gray ellipse) is only capable of capturing a hole from the silicon valence band (red arrow). Right after this process the defect level has returned to its initial position $E_{+/0}$ again.

shift model (LSM) but with a negligible defect relaxation. Consequently, the formulation of the ETM must be modified in order to account for the level shift. Thus equation (4.6) is rewritten as

$$\begin{aligned} \partial_t f_t = & + \underbrace{f_n(E_{q_1/q_2}) r_{e,q_1/q_2}(E_{q_1/q_2}, x_t)}_{=1/\tau_{\text{cap},e}(E_{q_1/q_2}, x_t)} (1 - f_t) - \underbrace{f_p(E_{q_2/q_1}) r_{e,q_2/q_1}(E_{q_2/q_1}, x_t)}_{=1/\tau_{\text{em},e}(E_{q_2/q_1}, x_t)} f_t \\ & + \underbrace{f_n(E_{q_1/q_2}) r_{h,q_1/q_2}(E_{q_1/q_2}, x_t)}_{=1/\tau_{\text{em},h}(E_{q_1/q_2}, x_t)} (1 - f_t) - \underbrace{f_p(E_{q_2/q_1}) r_{h,q_2/q_1}(E_{q_2/q_1}, x_t)}_{=1/\tau_{\text{cap},h}(E_{q_2/q_1}, x_t)} f_t, \end{aligned} \quad (5.1)$$

where the rates are defined as

$$r_{e,q_1/q_2}(E_{q_1/q_2}, x_t) = r_{e,q_2/q_1}(E_{q_1/q_2}, x_t) = \frac{1}{\tau_{n,0}^{\text{ETM}}(E_{q_1/q_2})} \zeta_{\text{WKB},c}^2(E_{q_1/q_2}, x_t), \quad (5.2)$$

$$r_{h,q_2/q_1}(E_{q_2/q_1}, x_t) = r_{h,q_2/q_1}(E_{q_2/q_1}, x_t) = \frac{1}{\tau_{p,0}^{\text{ETM}}(E_{q_2/q_1})} \zeta_{\text{WKB},v}^2(E_{q_2/q_1}, x_t). \quad (5.3)$$

q_1 and q_2 denote the two charge states involved in the tunneling process and the trap levels E_{q_1/q_2} and E_{q_2/q_1} corresponds to the switching traps introduced in Section 2.3. The above rate equation is reminiscent of the ETM presented in the previous Section 2.5.2. The peculiarity of the LSM is that the particular terms on the right-hand side of equation (5.1) must be evaluated for different energies, namely $E_{+/0}$ or $E_{0/+}$, depending on the charge state of the defect before the tunneling transition

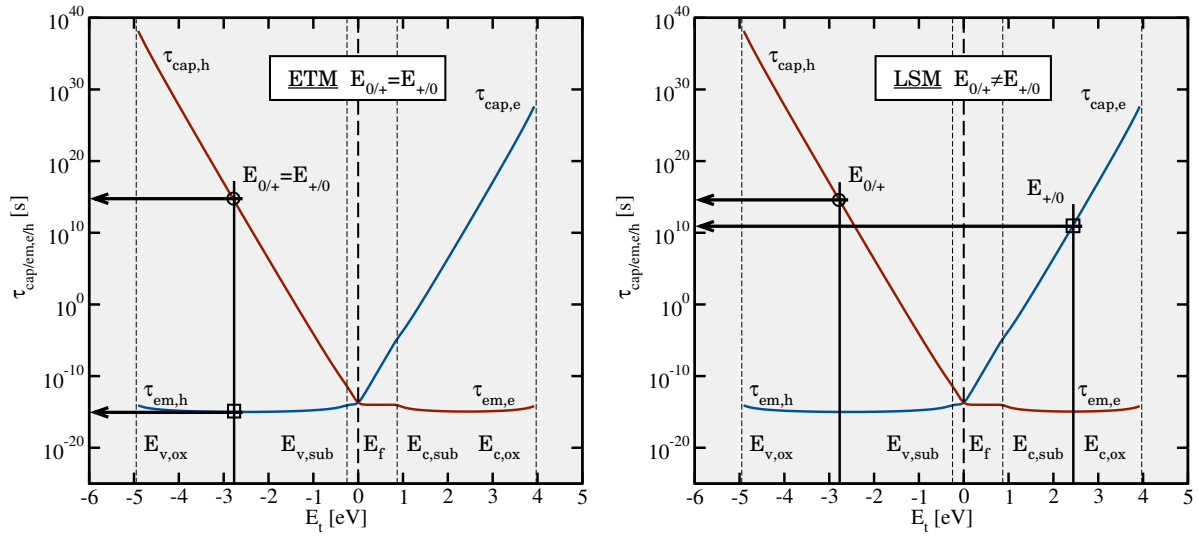


FIGURE 5.10: **Left:** The calculated time constants according to the ETM ($T = 50^\circ\text{C}$). The defect is placed close to the interface ($x_t = 2\text{\AA}$) of a pMOSFET in the off-state and features one single trap level $E_t = E_{+/0} = E_{0/+}$ indicated by the vertical dashed line. In the present case, the trap level lies 2.5 eV below the substrate valence band edge, where hole emission (circle) proceeds much faster than hole capture (box). Note that for trap levels within the substrate bandgap also tunneling from interface states [23] has been taken into account. **Right:** The same as in the left figure but for the LSM. Note that the form of the capture and emission times remain the same in both models whereas only the energy $E_{+/0}$ at which electron capture time is calculated has been changed ($E_{0/+} = E_{+/0}$). According to the equations (5.2) and (5.3), $\tau_{\text{cap},h}$ and $\tau_{\text{em},h}$ are evaluated at two different trap levels, namely one at $E_{+/0}$ for electron capture and another at $E_{0/+}$ for hole capture. For this case the relative magnitude of $\tau_{\text{cap},e}$ and $\tau_{\text{cap},h}$ depends on the energy distance of the respective trap level to E_f .

occurs. For instance, the positively charged defect of Fig. 5.9 has a trap level $E_{+/0}$, which must be applied for calculation of the electron capture rate $1/\tau_{\text{cap},e}(E_{+/0}, x_t)$ (see Fig. 5.10). By contrast, the neutralized defect features a trap level $E_{0/+}$ used for the hole capture rate $1/\tau_{\text{cap},h}(E_{0/+}, x_t)$. The calculation of the corresponding time constants is illustrated in Fig. 5.10. It is important to note here that the expressions for $\tau_{\text{cap},e}$, $\tau_{\text{cap},h}$, $\tau_{\text{em},e}$, and $\tau_{\text{em},h}$ remain the ‘same’ as in the ETM and only change in the energy they are evaluated for. This is due to the fact that the tunneling mechanism itself is not affected by the structural relaxation. Thus, analogously to the ETM, the tunneling process can be described by the tunneling rates (2.45) and (2.46) of the ETM and reasonably approximated by (5.2) and (5.3).

In the following, a new quantity, referred to as the demarcation energy¹, E_d will be introduced. It determines equilibrium occupancy of the defects and is defined by the condition

$$\tau_{\text{cap},e}(E_{+/0}, E_f) = \tau_{\text{cap},h}(E_{0/+}, E_f) \quad (5.4)$$

¹ Note that E_d must not be confused with the thermodynamic transition level, which only applies to thermally-activated processes, such as NMP transitions.

with

$$\tau_{\text{cap,e}}(E_{+/0}, E_f) = \frac{\tau_{n,0}^{\text{ETM}}(E_{+/0})}{\zeta_{\text{WKB,c}}^2(E_{+/0}, x_t) f_n(E_{+/0})}, \quad (5.5)$$

$$\tau_{\text{cap,h}}(E_{0/+}, E_f) = \frac{\tau_{p,0}^{\text{ETM}}(E_{0/+})}{\zeta_{\text{WKB,v}}^2(E_{0/+}, x_t) f_p(E_{0/+})}. \quad (5.6)$$

Assuming Boltzmann statistics, the energy dependences of the electron and hole occupation can be approximated as follows:

$$f_n(E) \approx \begin{cases} \exp(-\beta(E - E_f)), & E > E_f \\ 1, & E < E_f \end{cases} \quad (5.7)$$

$$f_p(E) \approx \begin{cases} 1, & E > E_f \\ \exp(-\beta(E_f - E)), & E < E_f \end{cases} \quad (5.8)$$

Suppose that $E_{0/+} > E_f$ and $E_{+/0} < E_f$ as it has been the case for the E'_γ center. Then only the exponential terms of f_n and f_p enter the time constants. The WKB factors in the expressions (5.5) and (5.6) can be replaced by their approximative variants for a rectangular barrier.

$$\zeta_{\text{WKB,c/v}}^2(E) \approx \exp\left(-2 \frac{\sqrt{2m_t}}{\hbar} x_t \sqrt{|E_{\text{c/v,ox}} - E|}\right). \quad (5.9)$$

Since $\tau_{n,0}^{\text{ETM}}(E_{+/0}) \approx \tau_{p,0}^{\text{ETM}}(E_{0/+}) \sim 10^{-14} \text{ s}^{-1}$ holds, equation (5.4) can be rewritten as

$$\begin{aligned} \exp\left(2 \frac{\sqrt{2m_t}}{\hbar} x_t \sqrt{E_{\text{c,ox}} - E_{+/0}}\right) \exp(\beta(E_{+/0} - E_f)) = \\ = \exp\left(2 \frac{\sqrt{2m_t}}{\hbar} x_t \sqrt{E_{0/+} - E_{\text{v,ox}}}\right) \exp(\beta(E_f - E_{0/+})). \end{aligned} \quad (5.10)$$

Taking the logarithm of this equation and after rearranging some terms, one obtains

$$E_d = E_f = \frac{E_{0/+} + E_{+/0}}{2} + \frac{\alpha}{\beta} \left(\sqrt{E_{\text{c,ox}} - E_{+/0}} - \sqrt{E_{0/+} - E_{\text{v,ox}}} \right) x_t \quad (5.11)$$

with

$$\alpha = 2 \frac{\sqrt{2m_t}}{\hbar}. \quad (5.12)$$

The factor $\alpha x_t / (\beta q_0)$ in equation (5.11) takes a value of approximately 0.094 at room temperature (23°C). Thus the last term is negligible compared to the remainder of equation (5.11) and E_d can be estimated by

$$E_d = \frac{E_{+/0} + E_{0/+}}{2}. \quad (5.13)$$

This quantity predicts the electron occupancy of a defect when equilibrium has been reached. For instance, when a stress voltage is applied to the gate of a pMOSFET, E_d is raised above E_f and the

initially neutral defect can capture a substrate hole during the stress phase. Conversely, when the MOSFET is switched from stress to relaxation, E_d falls below E_f and the positively charged defect will become neutralized in equilibrium. As an example, the E_d level of the oxygen vacancy varies between -1.7 eV and -0.5 eV according to the present DFT results. These values lie too low to be shifted above E_f for defects located close to the interface (< 1 nm). Therefore, the level E_d of the E'_γ center reveals that the LSM is incompatible with the concept of hole capture into oxygen vacancies. All other defect candidates, investigated by the DFT simulations in this thesis, feature values of E_d close to E_f and cannot be ruled out on the basis of the above argument.

While the equilibrium occupation of the defects is given by the demarcation energy, the trapping dynamics directly follow from the electron and hole capture time constants, whose dependence on the Fermi level and the trap depth will be discussed in the following. The ‘interesting’ instance is when the Fermi level is situated inbetween the levels $E_{+/0}$ and $E_{0/+}$ (cf. Fig. 5.10). Using Boltzmann statistics (5.7) and (5.8) and approximative WKB factor (5.9), the capture time constants can be estimated by

$$\tau_{\text{cap,e}}(E_{+/0}, x_t) = \tau_{n,0}^{\text{ETM}} \exp\left(2\alpha\sqrt{E_{\text{c,ox}} - E_{+/0}}x_t\right) \exp\left(\beta(E_{+/0} - E_f)\right) \quad (5.14)$$

$$\tau_{\text{cap,h}}(E_{0/+}, x_t) = \tau_{p,0}^{\text{ETM}} \exp\left(2\alpha\sqrt{E_{0/+} - E_{\text{v,ox}}}x_t\right) \exp\left(\beta(E_f - E_{0/+})\right). \quad (5.15)$$

In the equations above, the last term, originating from the Fermi-Dirac distribution, has the largest impact on both time constants. For instance, $\tau_{\text{cap,e}}$ exponentially depends on the energy difference $|E_{0/+} - E_f|$, that is, a higher $E_{0/+}$ level gives a larger $\tau_{\text{cap,e}}$. Analogous considerations hold true for the energy difference $|E_f - E_{+/0}|$ and $\tau_{\text{cap,h}}$. These dependences are also reflected in the exponential branches of the time constant plot in Fig. 5.10. Note that the simulated defect in this figure has been placed only 2\AA away from the interface where the time taken for the tunnel step can be almost neglected. However, when the defects are assumed to be situated deeper within the oxide, their time constants are increased due to the reduced tunnel probability. As demonstrated in Fig. 5.11 (left), this effect is more pronounced in the middle of the oxide bandgap while it almost diminishes towards the band edges due to the reduced tunneling barrier there. The ‘uninteresting’ instance is when the Fermi level is situated above $E_{0/+}$ as well as $E_{+/0}$ as shown Fig. 5.11 (right). In this case $\tau_{\text{em,h}}$ is larger than $\tau_{\text{cap,h}}$, implying that hole capture is effectively suppressed. Note that analogous consideration holds true for the electron capture when the Fermi level fall below $E_{+/0}$ and $E_{0/+}$.

5.2.1 Model Evaluation

In this section, the LSM will be employed to investigate the impact of the level shift on the trapping dynamics in NBTI experiments. Based on the NBTI checklist established in Section 1.4, it will be tested whether this model is capable of reproducing the NBTI degradation seen in experiments. The following simulations are carried out on a pMOSFET ($N_d = 5 \times 10^{17} \text{ cm}^{-3}$) with a strongly doped p-poly gate ($N_a = 3 \times 10^{20} \text{ cm}^{-3}$). The thickness of the oxide layer has been chosen to be 5 nm for demonstration purposes. Thereby, the traps can be homogeneously spread within the dielectric but are still sufficiently separated (2.0 nm) from the poly interface in order to be able to neglect trapping from the gate. Furthermore, this wide range of trap depths ensures a large distribution of capture and emission times over 14 decades in time (cf. Fig. 5.11). The energy levels of the traps have been

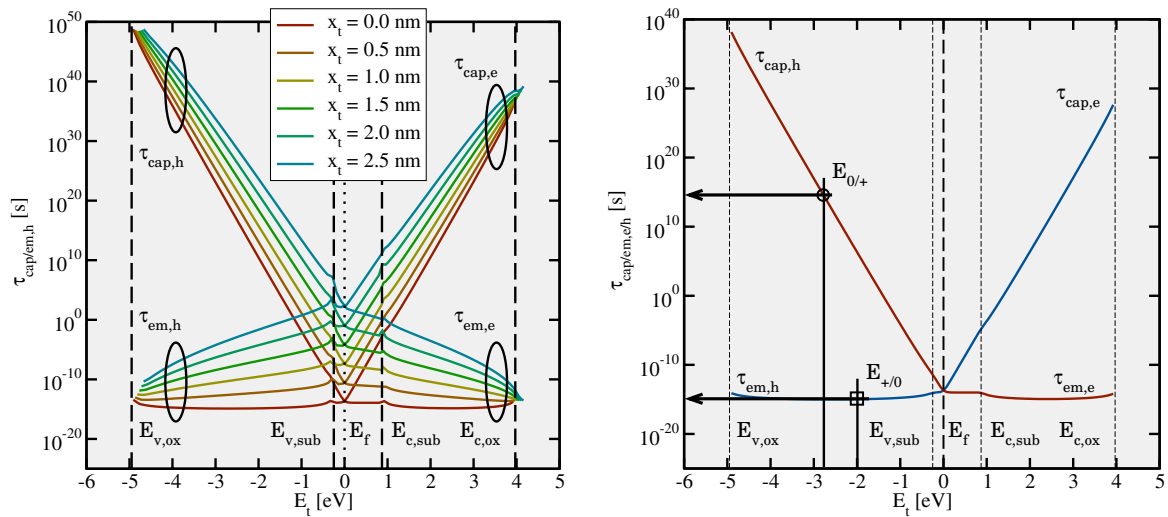


FIGURE 5.11: **Left:** The calculated time constants according to the LSM for various trap depths ($T = 50^\circ\text{C}$, $V_G = 0\text{V}$). The increase in the time constants is related to a larger tunneling distance for deeper traps. However, this effect, incorporated in the WKB factor, becomes weaker for energies closer to the oxide band edges since the tunneling barrier is dramatically lowered there. **Right:** The calculated time constants ($T = 50^\circ\text{C}$, $V_G = 0\text{V}$) for the case when the Fermi level is situated above both trap levels $E_{0/+}$ and $E_{+/0}$. Since $\tau_{\text{cap,h}}$ exceeds $\tau_{\text{em,h}}$, hole capture is overcompensated by hole emission and thus effectively suppressed.

assumed to be uniformly distributed with the $E_{0/+}$ and the $E_{+/0}$ levels being uncorrelated and thus independently calculated using a random number generator. The operation temperature is set to 125°C and thus lies in the middle of the range relevant for NBTI. It is noted that only charge injection from the substrate is accounted for in the following simulations for simplicity.

In the following, the basic properties of the LSM will be discussed on the basis of a simple showcase. Therefore, this model is evaluated for a type of defect whose trap level $E_{0/+}$ has a wide distribution below E_v while the $E_{+/0}$ counterpart is sharply peaked slightly above E_c (see Fig. 5.12). At the beginning of the stress phase nearly all defects are neutral and thus occupied by one electron. In this state, the traps are characterized by the hole capture levels $E_{0/+}$ located below the substrate valence band. The corresponding electron capture levels $E_{+/0}$ lie above the substrate conduction band but are inactive for the time being. During the stress phase, the substrate holes must be thermally excited to the defect level $E_{0/+}$ in order that a tunneling process can occur. In equation (5.6) their energy-dependent concentration is linked to the factor f_p , which decays exponentially with decreasing energies assuming Boltzmann statistics. This decay would lead to a temporal filling of traps from energetically higher towards lower traps in the band diagram. Furthermore, the tunneling of electrons and holes has an additional trap depth dependence, which is reflected in the WKB factor of equation (5.6). Analogously to the ETM, this would cause a temporal filling of traps starting from close to the interface and continuing deep into the oxide. As demonstrated in Fig. 5.13, the superposition of both effects results in a tunneling hole front which proceeds from high defect levels close to the interface towards lower ones deep in the oxide. The resulting time evolution of the trap occupancies is visualized in Fig. 5.12.

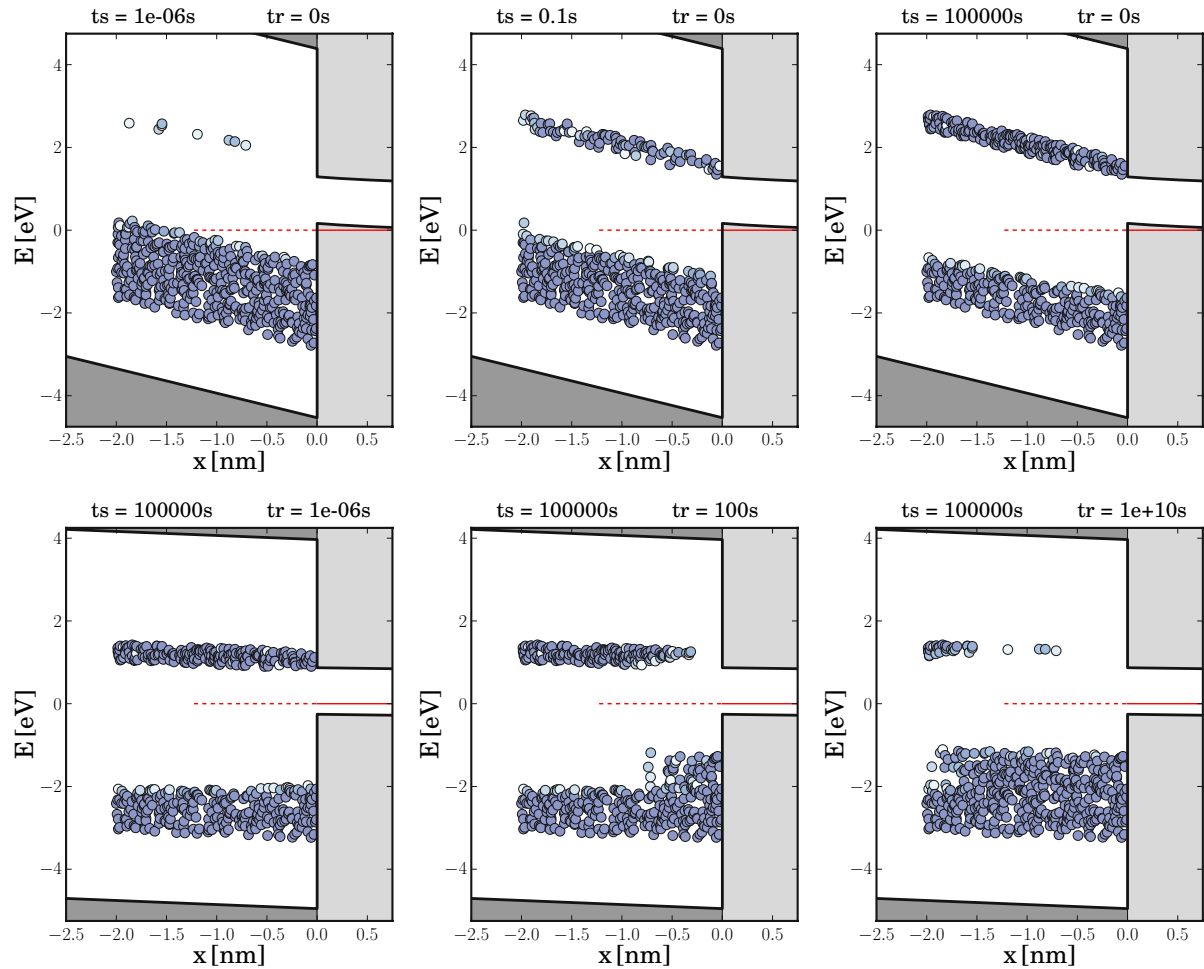


FIGURE 5.12: The time evolution of hole trapping during the stress (first row) and the relaxation (second row) phase ($V_s = -3.0\text{V}$, $T = 150^\circ\text{C}$). The substrate Fermi level is indicated by the red line and the small circles represent the trap levels $E_{+/0}$ and $E_{0/+}$ of the single defects. The neutral defects are assumed to have fully occupied defect orbitals and thus can only trap holes. Therefore, they feature hole capture levels $E_{0/+}$, which are located below the center of the substrate bandgap and are said to be ‘active’. By contrast, the positively charged defects are assumed to be able to trap electrons only. Accordingly, they have only electron capture levels $E_{+/0}$ above midgap but no energy levels $E_{0/+}$, which reappear once these defects are charged again. It is emphasized that the occupancy of one defect is related to which of its trap levels $E_{0/+}$ and $E_{+/0}$ is active at the moment. Therefore, the above figures also reflect the trap occupancies at a certain time. Since the trap levels are recorded at the beginning, the middle, and the end of the stress and the relaxation phase, these figures show the tunneling hole front, which is illustrated by the active trap levels and thus the occupancy of the defects.

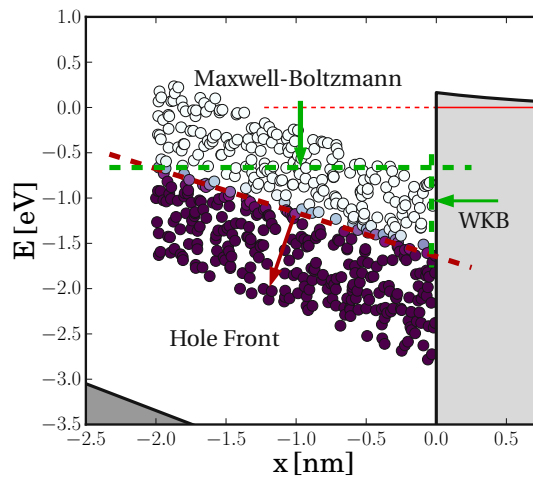


FIGURE 5.13: Motion of the tunneling hole front shown for a snippet of the hole occupancy in Fig. 5.12 after a stress time $t_s = 10^5$ s. The capture time constants are determined by the exponential decay in the WKB factor and the Fermi-Dirac distribution. The latter has been approximated by the Maxwell-Boltzmann distribution and shows an exponential energy dependence a few $k_B T$ away from the Fermi level. As indicated by the green vertical arrow, this dependence leads to a tunneling hole front moving downwards in the band diagram. By contrast, the WKB factor is most strongly affected by the trap depth, resulting in an tunneling hole from the substrate to deep into the oxide (green horizontal arrow). The resulting motion of the tunneling hole front is depicted by red arrow.

The temporal filling is also reflected in the occupancies of the demarcation energies, shown in Fig. 5.14. As already mentioned before, only defects located above E_f can participate in hole capture. As a consequence, the temporal filling of traps does not proceed below E_f , which thus marks a border to the tunneling hole front.

After the stress phase, a large part of the hole capture levels has disappeared and is replaced by their corresponding electron capture levels $E_{0/+}$. The latter are assumed to be concentrated in a small trap band slightly above the substrate conduction band. During the recovery phase, electrons in the substrate conduction band must be thermally excited up to the $E_{0/+}$ level where the trap depth-dependent tunneling process can take place. According to Fig. 5.12, the defects are found to be filled according to their trap depth, visible as a horizontally moving tunnel front. The small separation of the $E_{+/0}$ levels on the energy scale results in a narrow distribution of electron capture times. From this it follows that two particular charging events at the upper and the lower edge of the trap band can be hardly resolved in time. As a consequence, no vertical component in the motion of the tunnel front is observed during the recovery phase of Fig. 5.12. Analogously to the stress phase, the tunneling hole front also appears in the occupancies of the demarcation levels displayed in Fig. 5.14. During the relaxation phase, the E_d levels are shifted below E_f where they can be neutralized if equilibrium has been reached. However, Fig. 5.14 reveals that the discharging of traps has not been completed even until an unrealistic long relaxation time of 10^{10} s. It is important to note here that E_f during stress and relaxation determines the active area in which hole capture is possible. Defects above this area

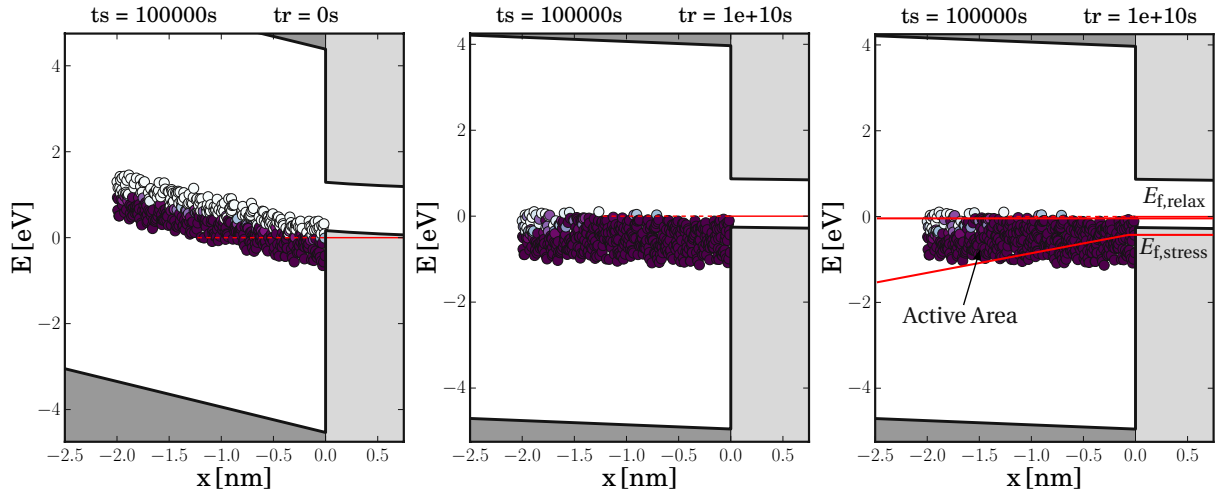


FIGURE 5.14: **Left:** The demarcation levels E_d at the end of the stress phase for the defects shown in Fig. 5.12 ($V_s = -3.0V$, $T = 150^\circ C$). The white circles represent neutral defects which have not trapped a hole during the stress phase. The purple filling color indicates that the defect is positively charged due to a finished hole capture event. Since there exist neutral defects with an E_d level above E_f , hole trapping has not reached saturation after a stress period lasting 10^5 s. **Middle:** The same as in the left figure but at the end of the relaxation phase. The figure indicates that not all trapped holes have been removed after a relaxation time of 10^{10} s. **Right:** Resulting active area for charge trapping in the LSM. The full red lines show the substrate Fermi levels during stress ($E_{f,stress}$) and relaxation ($E_{f,relax}$). The defects situated below $E_{f,stress}$ cannot capture a hole during stress while those located above $E_{f,relax}$ remain positively charged during relaxation and thus do not contribute to ΔV_{th} .

are already unoccupied before stress and thus cannot capture a further hole, while the ones below will remain neutral due to the high hole emission rate. As a result, only defects within this area can change their charge state and thus contribute to the net amount of captured holes and in further consequence to NBTI.

The LSM has been employed to simulate NBTI degradation in a pMOSFET for a wide range of different stress conditions. The calculated stress/relaxation curves for the aforementioned showcase are presented in Fig. 5.15. In contrast to the ETM, they exhibit a marked temperature dependence in addition to the obvious field acceleration. While the former one mainly stems from the temperature dependent Fermi-Dirac distribution in $\tau_{cap,h}$ (cf. equation (5.6)), the latter one cannot be simply interpreted by the lowering of the tunneling barrier at higher F_{ox} . The field acceleration originates from the larger shift of the trap levels at higher F_{ox} , as visualized in Fig. 5.16. As such, the field acceleration strongly depends on the distribution of the trap levels in space and energy but is not inherent to the LSM itself. For instance, a defect with $x_t = 0$ nm and $E_d < E_f$ during stress will not be able to capture a hole at all (see Fig. 5.17). In order to obtain more realistic results, tunneling from interface states [23] has been incorporated into LSM. The obtained degradation curves for defects with $E_{+/0} = E_v + 1.5 \pm 1.0$ eV and $E_{0/+} = E_v - 1.75 \pm 1.0$ eV are depicted in Fig. 5.18. Based on these results, it will be evaluated whether the LSM can satisfactorily reproduce the basic features seen in

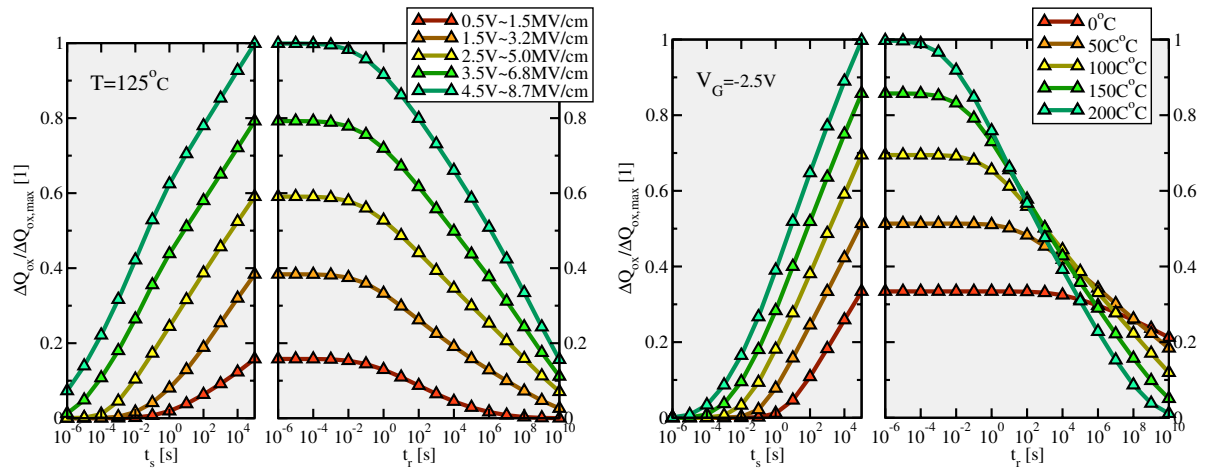


FIGURE 5.15: **Left:** The trapped charges $\Delta Q_{\text{ox}}(t)$ as a function of stress time for different gate biases. **Right:** The same as for the left figure but for different temperatures.

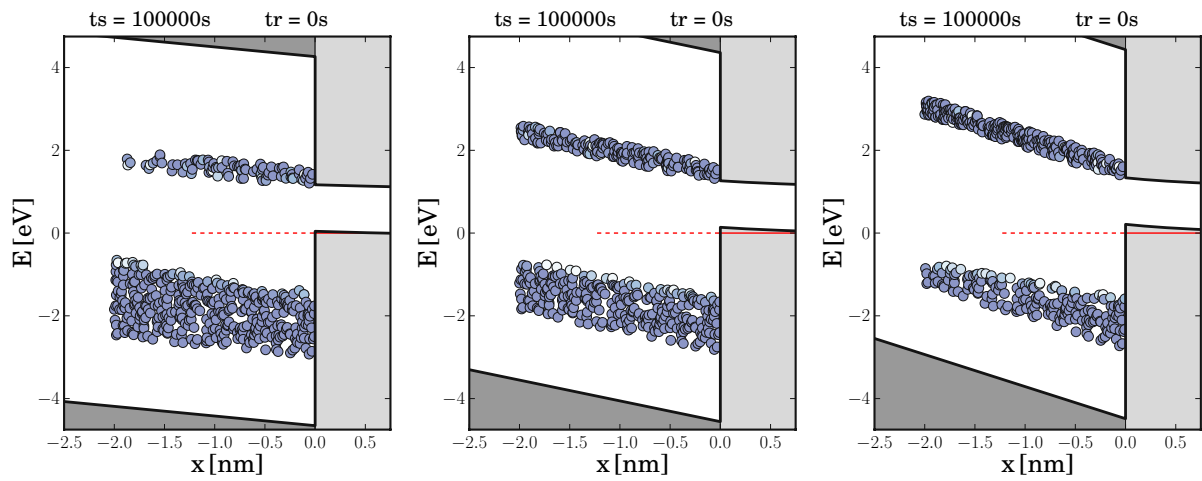


FIGURE 5.16: The trap levels $E_{0/+}$ and $E_{+/0}$ (both second row) after a stress time of 10^5 s for $V_s = -1.0 / -2.5 / -4.0$ V (from left to right) and $T = 150^\circ\text{C}$. The higher position of the $E_{0/+}$ levels goes hand in hand with shorter hole capture times and in consequence a larger amount of trapped charges after a stress time of 10^5 s. From this it can be concluded that the oxide field dependence of the LSM primarily originates from the upwards shift of the trap levels but is only marginally influenced by the reduced tunneling barrier at higher F_{ox} .

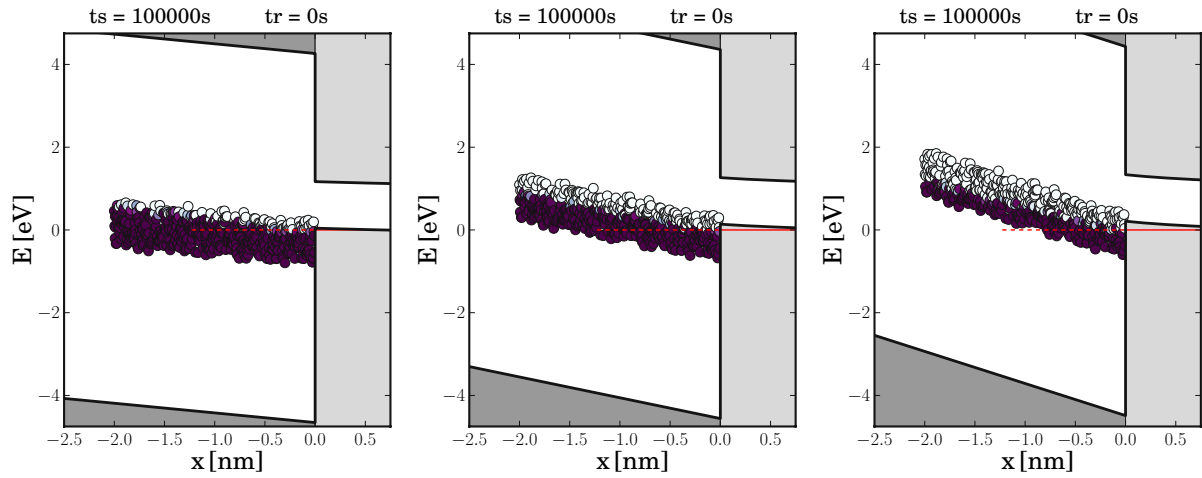


FIGURE 5.17: The position and the trap occupancy of E_d after a stress time of 10^5 s for $V_s = -1.0/-2.5/-4.0$ V (from left to right) and $T = 150^\circ\text{C}$. It can be recognized that a higher F_{ox} increases the portion of E_d levels above E_f and thus a larger number of traps are available for hole capture.

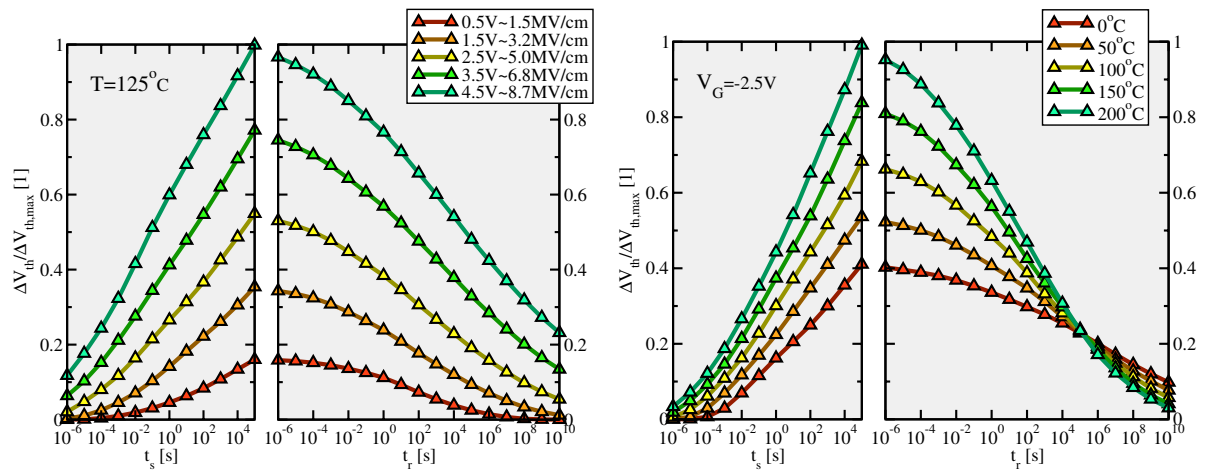


FIGURE 5.18: The same as in Fig. 5.15 but for a different distribution of defect levels and including tunneling from interface states. **Left:** During stress, charge trapping sets in later (10ms) when smaller biases are applied to the gate. The degradation curves follow a nearly logarithmic behavior over a wide time range, where the curves obtained for a small stress voltages can be better approximated by a power-law. Furthermore, none of the curves show a sign of saturation until a stress time of 10^5 s. It is noted that their slopes appear to be insensitive to the applied gate bias — except from small gate biases again. Regarding the relaxation phase, deviations from the time logarithmic behavior can be recognized below 10 ms. **Right:** For the stress as well as the relaxation phase, a very weak temperature dependence is obtained.

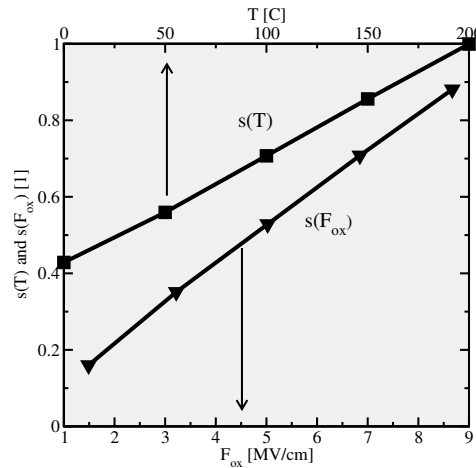


FIGURE 5.19: The field acceleration and temperature activation in the LSM during stress. Since the degradation roughly follows a logarithmic behavior in this phase, scaling factors can be extracted from Fig.5.18. $s(T)$ and $s(F_{ox})$ demonstrate that the LSM does not reproduce the quadratic field and temperature dependence seen in experiments.

NBTI experiments. In the NBTI checklist of Table 5.2, these features are formulated as necessary criteria, where each of them will be judged in the following.

- (i) Hole trapping during stress and relaxation is found to cover the time range from milliseconds to a few thousand seconds as in the reference data of Section 1.4. Moreover, it even extends from $1\ \mu\text{s}$ to $10^5\ \text{s}$ during stress and from $1\ \mu\text{s}$ to $10^{10}\ \text{s}$ during relaxation and thus even goes far beyond the experimental time window.
- (ii) At low stress voltages, the degradation curves feature only a weak curvature and thus roughly follow a logarithmic time behavior.
- (iii) Only small deviations from the logarithmic time behavior are present at low stress voltages in the relaxation phase. But one should kept in mind that the relaxation data cannot be scaled as there is an intersection point between the high and low temperature recovery curves.
- (iv) Since the degradation accumulated during the stress phase does not completely recover during the much longer relaxation phase, the LSM allows for the asymmetry between stress and relaxation. This can be ascribed to the fact that the $E_{+/0}$ levels are more widely spread on the energy scale than their $E_{0/+}$ counterparts. The wide separation of the $E_{+/0}$ levels is linked to a broad distribution of $\tau_{cap,e}$, giving rise to a retarded recovery.
- (v) The field acceleration is found to follow a nearly linear behavior (cf. Fig. 5.19), which is inconsistent with the NBTI criteria of Section 1.4.
- (vi) The elevated temperatures yield a weakly enhanced NBTI degradation during stress (cf. Fig. 5.19), while they reduce the electron capture times and thus lead to an accelerated recovery during relaxation. These tendencies cannot be reconciled with the quadratic temperature activation obtained in experiments.

| Model Properties | | |
|------------------|----------------------------------|---|
| (i) | Involved Time Scales | ✓ |
| (ii) | Log. Behavior during Stress | ✓ |
| (iii) | Log. Behavior during Recovery | ✗ |
| (iv) | Asymmetry Stress/Recovery | ✓ |
| (v) | Quadratic Field Dependence | ✗ |
| (vi) | Quadratic Temperature Dependence | ✗ |

TABLE 5.2: Checklist for an NBTI model validation. Since the LSM does not fulfill all of the criteria established in Section 1.4, it must be discarded as a possible model for NBTI.

The above list provides strong evidence that the LSM cannot be reconciled with the experimental NBTI data. As a consequence, pure tunneling must be discarded as a possible cause for hole trapping in NBTI.

5.2.2 Conclusion

In this chapter, the concept of the level shift has been incorporated in the ETM. The resulting LSM has been tested whether it is capable of explaining the NBTI phenomenon. By means of DFT simulations it has been proven that the structural relaxation after a tunneling process occurs for a series of defects suspected to be responsible for NBTI. Therefore, the ETM has been modified to account for the unquestionable occurrence of the level shift. This involves more complicated trapping dynamics but, for instance, allows for a temperature activation, missing in the ETM, as well as the asymmetry between stress and recovery. However, as pointed out in Table 5.2, the LSM is not capable of reproducing all of the essential NBTI features, such as the field and temperature dependence. As a consequence, it must be ruled out as an adequate model for charge trapping in NBTI.

6

SRH-Based Models

In the previous chapters, it has been demonstrated that the ETM as well as the LSM cannot explain charge trapping in NBTI. In particular the ETM, suggested by Huard *et al.* [58], suffers from several weaknesses, such as a too weak field dependence or a too short relaxation phase (see Section 4.2.9). However, the most severe deficiency is the lack of an appreciable temperature activation. As a result, there must exist an additional temperature-activated process coupled to elastic tunneling. Both subprocesses constitute a common trapping mechanism capturing the field as well as the temperature dependence.

The SRH equations (2.72) and (2.73) form the basis for the inelastic tunneling transitions mentioned before. They describe charge carrier transitions via an undefined temperature-activated process, which has not to be specified within the general framework of the standard SRH. Besides NBTI, the underlying concept has also been employed as a description for other charge trapping phenomena, such as random telegraph noise (RTN). The latter has been intensively investigated by means of time constant plots, which show τ_{cap} and τ_{em} as a function of the oxide field or the gate voltage [55, 56, 124, 125]. Recently, they have been used as one way to tackle the NBTI phenomenon experimentally [51, 53]. Since these plots reveal the behavior of single defects, they provide an insight into the microscopic processes behind a charge capture or emission event. Therefore, they will be used to evaluate the NBTI models presented in this chapter.

6.1 McWhorter Model

In the middle of the last century, McWhorter [182] dealt with the spectrum of $1/f$ -noise observed at germanium-oxide interfaces. This kind of noise is attributed to fluctuations in the trap occupancy f_t due to charge carriers tunneling forth and back between the bulk and the defects. McWhorter described these fluctuations using a simple SRH-based model, which can be considered as a prototype for other charge trapping models. His model extends the conventional SRH theory by the effect of charge carrier tunneling, which is accounted for by the factor $\exp(x_t/x_{p,0})$. Thus, the simplified time constants read as

$$\tau_{\text{cap,h}} = \tau_{p,0}^{\text{SRH}} \exp\left(\frac{x_t}{x_{p,0}}\right) \frac{N_v}{p}, \quad (6.1)$$

$$\tau_{\text{em,h}} = \tau_{p,0}^{\text{SRH}} \exp\left(\frac{x_t}{x_{p,0}}\right) \exp(\beta \Delta E_t) \exp(-\beta q_0 F_{\text{ox}} x_t). \quad (6.2)$$

The model presumes that all traps are energetically located within the substrate bandgap so that none of them will be found below E_v . Furthermore, they are assumed to be spatially distributed over the entire dielectric.

In the following, the McWhorter model will be evaluated against the findings of the TDDS experiments (see Section 1.3.4).

- (i) After equation (6.1) $\tau_{\text{cap,h}}$ shows a weak field dependence following $1/p$. The drop in the hole concentration p at small fields leads to a sharp peak, which is inconsistent with the field acceleration observed in TDDS experiments.
- (ii) Since the hole concentration weakly varies with changes in the temperature, the hole capture process is not thermally activated.
- (iii) The field dependence of $\tau_{\text{em,h}}$ is governed by the exponential term $\exp(-\beta q_0 F_{\text{ox}} x_t)$ and thus is inconsistent with the behavior of ‘normal’ defects. But one should keep in mind that some RTN investigations [55, 125] have revealed that there exist defects whose emission times increase exponentially with the gate bias.
- (iv) Consequently, the McWhorter model does also not agree with the linear dependence on p seen for $\tau_{\text{em,h}}$ in the case of the ‘anomalous’ defects. Beyond that, it does not give an explanation for the two distinct kinds of defects in general.
- (v) The McWhorter model predicts $\tau_{\text{em,h}}$ to be temperature-activated in agreement with the experimental findings.

The term $\exp(x_t/x_{p,0})$ in $\tau_{\text{cap,h}}$ and $\tau_{\text{em,h}}$ accounts for the trap depth dependence of tunneling and leads to an upwards shift of the entire $\tau_{\text{cap,h}}$ and $\tau_{\text{em,h}}$ curves with an increasing trap depth x_t . Due to the wide distribution of x_t , the McWhorter model allows a wide range of capture and emission times in thick oxides. In modern device technologies, however, the time constant of the devices with

an oxide thickness of 2 nm would be limited to 1 ms after the model. As such, this model cannot explain time constants larger than 1 ms for devices with an oxide thickness of 2 nm. This is in contrast to the experimental results (cf. Fig. 1.2), in which $\tau_{\text{em,h}}$ extends well into the kilosecond regime. In conclusion, this model cannot be reconciled with the findings of the TDDS and is thus inadequate to describe the traps involved in NBTI.

6.2 Standard Model of Kirton and Uren

Since the McWhorter model suffers from a weak temperature dependence of $\tau_{\text{cap,h}}$ and small time constants, Kirton and Uren [56] incorporated field-independent barriers ΔE_b in the cross sections σ_n^{SRH} and σ_p^{SRH} (see Section 2.5). The ‘ad hoc’ introduction of these barriers has been motivated by the theory of nonradiative multi-phonon transitions (NMP) process [115]. However, Kirton and Uren have not provided a detailed theoretical derivation based on this NMP theory. Nevertheless, their work is regarded as a substantial improvement in the interpretation of charge trapping at semiconductor-oxide interfaces and thus also referred to as the standard model throughout this thesis. In an extended version of the McWhorter model, the holes can also be captured by traps with an energy below the substrate valence band. As illustrated in Fig. 2.5 of Section 2.5.2, the required barriers consist of two components, namely ΔE_b and $|\Delta E_t|$. The latter is the required minimum energy for a hole capture process while ΔE_b is the barrier component which must be overcome for hole capture as well as emission. In this variant, the capture and emission time constants read

$$\tau_{\text{cap,h}} = \tau_{p,0}^{\text{SRH}} \exp\left(\frac{x_t}{x_{p,0}}\right) \exp(\beta \Delta E_b) \frac{N_v}{p} \begin{cases} 1, & E_t > E_v \\ \exp(-\beta \Delta E_t) \exp(\beta q_0 F_{\text{ox}} x_t), & E_t < E_v \end{cases}, \quad (6.3)$$

$$\tau_{\text{em,h}} = \tau_{p,0}^{\text{SRH}} \exp\left(\frac{x_t}{x_{p,0}}\right) \exp(\beta \Delta E_b) \begin{cases} \exp(\beta \Delta E_t) \exp(-\beta q_0 F_{\text{ox}} x_t), & E_t > E_v \\ 1, & E_t < E_v \end{cases}, \quad (6.4)$$

where the traps are not restricted to lie within the bandgap. Its behavior with respect to the temperature and the oxide field is illustrated in Fig. 6.1 and evaluated based on the TDDS checklist in Table 6.1. When the trap level lies below the valence band edge ($E_t < E_v$), $\tau_{\text{cap,h}}$ shows an exponential field dependence, which is superimposed by a sharp peak due to a drop of the hole concentration at weak oxide fields. Comparing the model to the experimental TDDS data (see Section 1.3.4), this exponential behavior allows for reasonable and approximative fits to $\tau_{\text{cap,h}}$ but it is incompatible with the observed curvature in $\tau_{\text{cap,h}}$. Furthermore, the model predicts $\tau_{\text{em,h}}$ to be field insensitive for $E_t < E_f$ according to the equations (6.4). It should be mentioned at this point that the derivation of the analytical expression (6.3) and (6.4) is based on Boltzmann statistics, leading to small deviations in $\tau_{\text{cap,h}}$ and $\tau_{\text{em,h}}$ compared to the simulations of Fig. 6.1 (left) using Fermi-Dirac statistics. The weak field dependence of the simulated $\tau_{\text{em,h}}$ reasonably agrees with the behavior of ‘normal’ (constant emission times) but is inconsistent with as well as ‘anomalous’ traps (a drop at weak oxide fields). Nevertheless, Fig. 6.1 reveals that the introduction of ΔE_b yields the required temperature activation and larger time constants in agreement with the points (ii) and (v) of the TDDS findings.

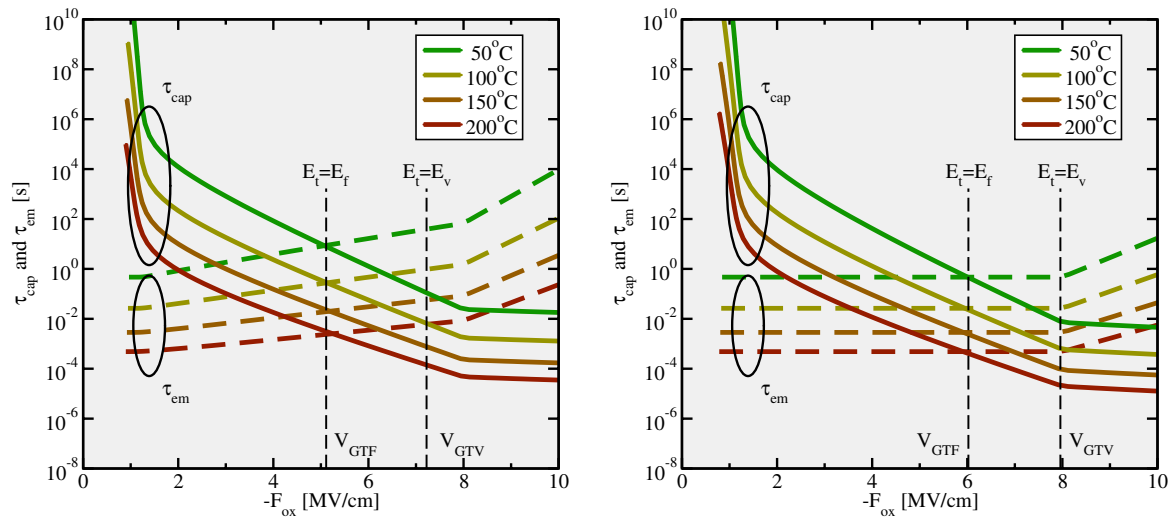


FIGURE 6.1: The simulated time capture and emission times according to the standard model of Kirton *et al.* [56] using Fermi-Dirac (left) and Boltzmann (right) statistics. The $\tau_{\text{cap},h}$ are plotted as solid lines, while the $\tau_{\text{em},h}$ are depicted by dashed lines. The vertical dashed lines mark the values of F_{ox} or V_G when the trap level E_t passes either the Fermi level or the valence band edge in the substrate, respectively. Equation (6.4), which is based on Boltzmann statistics, predicts that $\tau_{\text{em},h}$ remains constant in the region $E_t < E_v$ as shown in the right figure. Using more accurate Fermi-Dirac statistics the emission time constants are subject to a weak field dependence (cf. left figure). On the logarithmic scale, the $\tau_{\text{cap},h}$ follow a linear behavior in F_{ox} over a wide range but do not have the same curvature as present in the TDDS data. The $\tau_{\text{em},h}$ show neither a plateau nor a drop towards weak fields. Compared to the McWhorter model, $\tau_{\text{cap},h}$ and $\tau_{\text{em},h}$ exhibit a clear temperature activation over the whole range of oxide fields so that their values are moved to larger time scales relevant for NBTI.

A fit of the Kirton model to the experimental TDDS data is presented in Fig. 6.2. Although the model can reproduce some features seen in the TDDS data, except for the curvature in τ_{cap} , no reasonable agreement with the measurement data could be achieved. This discrepancy can be explained as follows: The exponential bias dependence extends up to a voltage V_{GTV} at which E_t coincides with E_v . In Fig. 6.2 (left) V_{GTV} is approximately 2.5V so that $\tau_{\text{cap},h}$ shows an exponential bias dependence up to this value and becomes constant afterwards. Therefore, E_t must be chosen such that V_{GTV} lies above the voltage range used in the measurements. This is only the case for defects whose trap levels E_t are situated sufficiently low. Note that those defects are also characterized by a large V_{GTF} , which marks the voltage where E_t coincides with E_f . After equation (2.66), their $\tau_{\text{cap},h}$ must equal their $\tau_{\text{em},h}$ at V_{GTF} , visible as the crossings between $\tau_{\text{cap},h}$ and $\tau_{\text{em},h}$ in Fig. 6.2. At a low gate bias, their trap levels are moved far below E_f so that their emission times fall several orders of magnitude below their corresponding capture time constants. The large difference between $\tau_{\text{cap},h}$ and $\tau_{\text{em},h}$ predicted by the Kirton model is inconsistent with the experimental TDDS data. Additionally, a fit of the Kirton model to $\tau_{\text{em},h}$ is presented in Fig. 6.1 (right). It clearly shows that the simulated $\tau_{\text{cap},h}$ fails to reproduce the experimentally obtained τ_{em} when a good match with $\tau_{\text{em},h}$ is achieved.

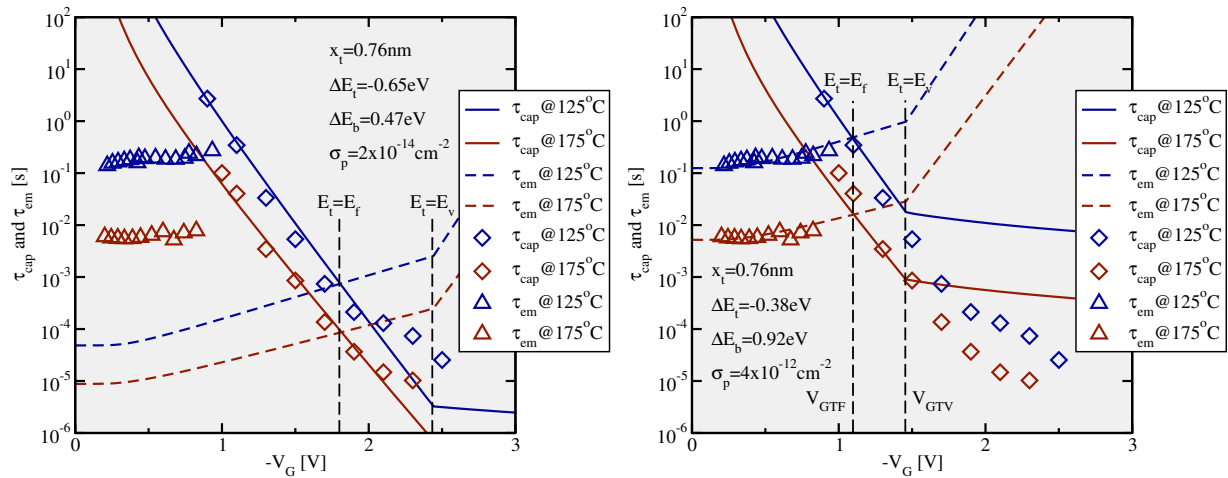


FIGURE 6.2: A fit of the Kirton model to the TDDS data. The symbols stand for the measurement data and the lines represent the simulated time constants. When the Kirton model is optimized to the hole capture times $\tau_{\text{cap},h}$ (left), reasonable fits can be achieved for them but $\tau_{\text{em},h}$ is predicted three orders of magnitudes too low. Alternatively, a good agreement (right) can be obtained for the hole emission times $\tau_{\text{em},h}$ but with a strong mismatch of the capture times $\tau_{\text{cap},h}$ for $V_G > V_{\text{GTV}}$. From this it is concluded that the Kirton model is not capable of fitting $\tau_{\text{cap},h}$ and $\tau_{\text{em},h}$ at the same time.

| Model | | McWhorter | Kirton |
|-------|---|-----------|--------|
| (i) | Curvature in τ_{cap} | X | X |
| (ii) | Temperature Activation of τ_{cap} | X | ✓ |
| (iii) | 'Normal' Defect Behavior | X | ✓ |
| (iv) | 'Anomalous' Defect Behavior | X | X |
| (v) | Temperature Activation of τ_{em} | ✓ | ✓ |

TABLE 6.1: Checklist for a TDDS defect. The individual criteria stem from the TDDS data addressed in Section 1.3.4. The McWhorter as well as the Kirton model do not fulfill all criteria and thus do not describe the defects seen in TDDS experiments.

6.3 Two Stage Model

The concept of NMP has been used in a slightly modified variant termed multiphonon field-assisted tunneling (MPFAT) [55, 115–117, 125], which was proposed for ionization of deep impurity centers. The underlying theory accounts for the fact that the emission of charge carriers out of bulk traps is accelerated in the presence of an electric field. This effect is eventually related to the shortened tunneling distance through a triangular barrier when considering thermal excitation of the charge carriers. According to theoretical calculations of Ganichev *et al.* [117], it yields a field enhancement factor $\exp(F^2/F_C^2)$, which is suspected to have a strong impact on hole capture processes in NBTI and has therefore been phenomenologically introduced in the two-stage model (TSM) [61].

6.3.1 Physical Description of the Model

The TSM relies on the Harry-Diamond-Laboratories (HDL) [15] model but is extended by a second stage accounting for the permanent component of NBTI (cf. Fig. 6.3). The defect precursor, an oxygen vacancy according to the HDL model, is capable of capturing substrate holes via the aforementioned MPFAT mechanism. The trap level $E_{t,1}$ of the precursor is located below the substrate valence band and subject to a wide distribution due to the amorphousness of SiO_2 . Upon hole capture, the defect undergoes a transformation to an E' center, which is visible in ESR measurements [43]. In this new configuration, it features a Si dangling bond associated with a defect level $E_{t,2}$ within or close to within the substrate bandgap in accordance to [162]. The level shift from $E_{t,1}$ to $E_{t,2}$ arises from the change to a new ‘stable’ defect configuration, namely the Si dangling bond. In the E' center configuration, the defect can be repeatedly charged and discharged by electrons tunneling in or out of its dangling bond. The associated switching behavior¹ is in agreement with the experimental observations made in electrical measurements [15, 16]. Only in the neutral state 3, in which the Si dangling bond is doubly occupied by an electron, the E' center can be annealed, thereby becoming an oxygen vacancy again.

The second stage involves an amphoteric trap, most probably a P_b center, which has been found to interact with the switching trap as observed in irradiation experiments [43]. That is, a hydrogen is detached from an interfacial Si-H bond and leaves behind a P_b center. In a subsequent reaction, it saturates the dangling bond of the E' center. This stage fixes the positive charge at the oxide defect and creates a new interface state, whose charge state is controlled by the substrate Fermi level. Since the hydrogen transition is assumed to last much longer than the hole capture or emission process, this stage corresponds to the permanent or slowly recoverable component of NBTI.

Mathematically, the dynamics of this complex mechanism are described by the set of the following rate equations:

¹ Once switching traps are created, they have a defect level within the substrate bandgap and thus their charge state can be repeatedly changed by small variations of the gate bias.

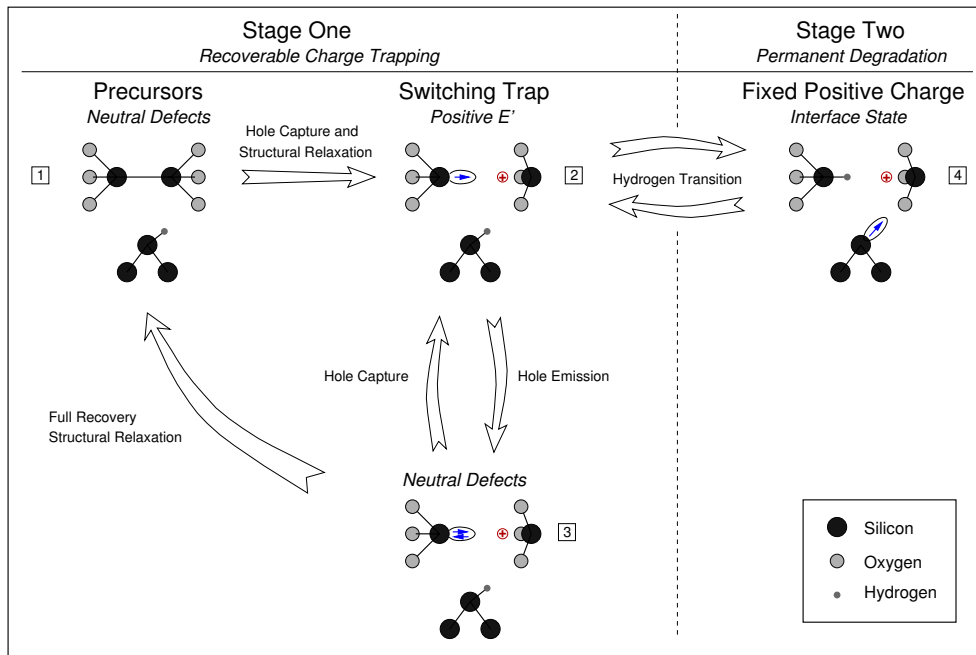


FIGURE 6.3: The transition state diagram for the trapping dynamics of the TSM. The recoverable component of NBTI constitutes the first stage of the TSM. The precursor (state 1) is transformed to a switching trap (state 2) via an irreversible MPFAT process. In this configuration, the defect can quickly respond to small variations of the gate bias by switching between the states 2 and 3. From the neutral charge state 3, the defect can undergo structural relaxation over a thermal barrier and arrives at its initial configuration. The second stage gives an explanation for the permanent component, which is attributed to a hydrogen transition from state 2 to 4. This transition fixes the positive charge (red plus sign) in the defect and creates a new interface state (ellipse with one or two blue arrows).

$$\partial_t f_1 = -f_1 r_{12} + f_3 r_{31}, \quad (6.5)$$

$$\partial_t f_2 = +f_1 r_{12} - f_2 r_{23} + f_3 r_{32} - f_2 r_{24} + f_4 r_{42}, \quad (6.6)$$

$$\partial_t f_3 = +f_2 r_{23} - f_3 r_{32} - f_3 r_{31}, \quad (6.7)$$

$$\partial_t f_4 = +f_2 r_{24} - f_4 r_{42}, \quad (6.8)$$

The subscript i of f_i stands for the state according to the numbering in Fig. 6.3. The transition rates are denoted as r_{ij} , with i and j as the initial and the final states, respectively. The rate r_{12} is derived from the SRH equations (2.69), in which the empirical enhancement factor $\exp(F_{\text{ox}}^2 / F_c^2)$ for the MPFAT transition² $T_{1 \rightarrow 2}$ has been phenomenologically introduced. Then the transition rates read

$$r_{12} = r_{\text{cap,h}}(\Delta E_{b,1}, E_{t,1}) \exp\left(\frac{F_{\text{ox}}^2}{F_c^2}\right) + r_{\text{em,e}}(\Delta E_{b,1}, E_{t,1}) \quad (6.9)$$

²The abbreviation $T_{i \rightarrow j}$ denotes transitions from state i to j while $T_{i \leftrightarrow j}$ stands for the bidirectional analogons. Furthermore, $T_{i \rightarrow j \rightarrow k}$ stands for a chain of two transitions $T_{i \rightarrow j}$ and $T_{j \rightarrow k}$.

with

$$r_{\text{cap,h}}(\Delta E_b, E_t) = \frac{1}{\tau_{p,0}^{\text{TSM}}} \frac{p}{N_v} \exp\left(-\frac{x_t}{x_{p,0}}\right) \exp(-\beta \Delta E_b) \begin{cases} 1, & E_t > E_v \\ \exp(-\beta(E_v - E_t)), & E_t < E_v \end{cases}, \quad (6.10)$$

$$r_{\text{em,e}}(\Delta E_b, E_t) = \frac{1}{\tau_{n,0}^{\text{TSM}}} \frac{n}{N_c} \exp\left(-\frac{x_t}{x_{n,0}}\right) \exp(-\beta \Delta E_b) \begin{cases} \exp(-\beta(E_f - E_c)), & E_t > E_c \\ \exp(-\beta(E_f - E_t)), & E_t < E_c \end{cases}. \quad (6.11)$$

The quantity $\tau_{p,0}^{\text{TSM}}$ is the equivalent of $\tau_{p,0}^{\text{SRH}}$ in the TSM and can be calculated according to equation (2.74). The barriers $\Delta E_{b,1}$ and $\Delta E_{b,2}$ are defined analogously to the barrier ΔE_b in Fig. 2.5. Therefore, they corresponds to the barrier component, which must be overcome in both directions of the transitions $T_{1 \leftrightarrow 2}$ and $T_{2 \leftrightarrow 3}$, respectively (cf. Fig 2.5). For the transitions between the states 2 and 3

$$r_{23} = r_{\text{cap,e}}(\Delta E_{b,2}, E_{t,2}) + r_{\text{em,h}}(\Delta E_{b,2}, E_{t,2}), \quad (6.12)$$

$$r_{32} = r_{\text{em,e}}(\Delta E_{b,2}, E_{t,2}) + r_{\text{cap,h}}(\Delta E_{b,2}, E_{t,2}), \quad (6.13)$$

the capture and emission of electrons as well as holes are taken into account.

$$r_{\text{em,h}}(\Delta E_b, E_t) = \frac{1}{\tau_{p,0}^{\text{TSM}}} \frac{p}{N_v} \exp\left(-\frac{x_t}{x_{p,0}}\right) \exp(-\beta \Delta E_b) \begin{cases} \exp(-\beta(E_t - E_f)), & E_t > E_v \\ \exp(-\beta(E_v - E_f)), & E_t < E_v \end{cases} \quad (6.14)$$

$$r_{\text{cap,e}}(\Delta E_b, E_t) = \frac{1}{\tau_{n,0}^{\text{TSM}}} \frac{n}{N_c} \exp\left(-\frac{x_t}{x_{n,0}}\right) \exp(-\beta \Delta E_b) \begin{cases} \exp(-\beta(E_t - E_c)), & E_t > E_c \\ 1, & E_t < E_c \end{cases} \quad (6.15)$$

The annealing of the defect ($T_{3 \rightarrow 1}$) is represented by the rate r_{31} , which is modeled by a structural relaxation over a thermal barrier $\Delta E_{b,3}$.

$$r_{31} = \nu_0 \exp(-\beta \Delta E_{b,3}) \quad (6.16)$$

ν_0 denotes the attempt frequency, which is usually in the order of 10^{13} s^{-1} . The hydrogen transition $T_{2 \rightarrow 4}$ is modeled assuming a field-dependent thermal barrier, as shown in Fig. 6.4.

$$r_{24} = \nu_0 \exp(-\beta(\Delta E_{b,4} - \gamma F_{\text{ox}})) \quad (6.17)$$

$$r_{42} = \nu_0 \exp(-\beta(\Delta E_{b,4} - E_4 + \gamma F_{\text{ox}})) \quad (6.18)$$

The occupancy of interface traps, present in state 4, is calculated using conventional SRH statistics as implemented in standard device simulators [183].

6.3.2 Model Evaluation

The following simulations are based on the same numerical scheme as has been presented in Section 3.2 and are used for the ETM and the LSM in Chapter 4 and 5. Each representative trap in this scheme is characterized by its individual set of defect levels and barriers. The generated random

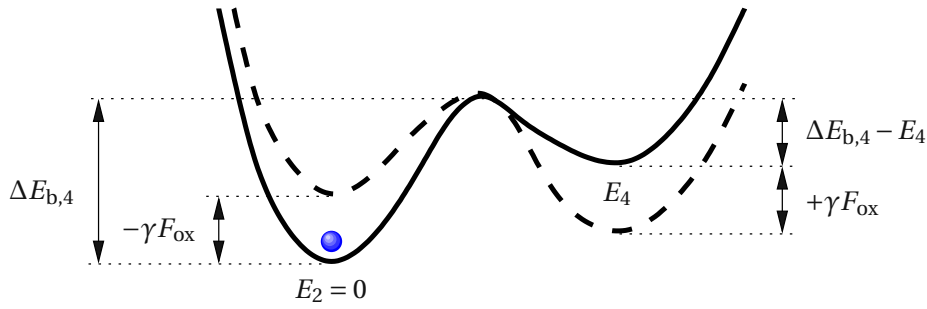


FIGURE 6.4: The schematic of the hydrogen transition. The solid line depicts the adiabatic potentials for a hydrogen reaction in a configuration coordinate diagram. When a bias is applied to the gate, the oxide field lifts the energy minimum of state 2 (E_2) but lowers that of state 4 (E_4). Since the interfacial Si-H bonds are associated with a dipole moment, the shift of the energy minima depends linearly on the oxide field with a proportionality constant of γ . The applied oxide field gives rise to a reduced forward barrier ($T_{2 \rightarrow 4}$) and an increased reverse barrier ($T_{4 \rightarrow 2}$). Without loss of generality, the value of E_2 is set to zero.

numbers are homogeneously distributed for $E_{t,1}$, $E_{t,2}$, $\Delta E_{b,1}$, and $\Delta E_{b,2}$ while they follow a Fermi-derivative (Gaussian-like) distribution [90] for $\Delta E_{b,4}$ and E_4 . The remaining quantities including $\sigma_{p,0}^{\text{TSM}} = \sigma_{n,0}^{\text{TSM}} \sim 3 \times 10^{-14} \text{ cm}^2$, $F_c \sim 2 \text{ MV/cm}$, $v_{\text{th},p} = v_{\text{th},n} \sim 10^7 \text{ cm/s}$, $x_{p,0} = 0.5 \text{ \AA}$, and $x_{n,0} = 0.5 \text{ \AA}$ are assumed to be single-valued.

In contrast to previous models, oxide charges (state 2) as well as interface traps (state 4) are incorporated into the TSM so that two states must be considered for the calculation of ΔV_{th} . It is important to note that only a part of the overall degradation during stress is observed within the experimental time window. As demonstrated in Fig. 6.5, a large fraction already occurs before the beginning of the OTF measurement ($t_0 = 1 \text{ ms}$) and only a part of the V_{th} degradation can be monitored by this technique (cf. Section 1.3.2). As a consequence, the measured threshold voltage shift must be calculated as

$$\Delta V_{\text{th}}(t_s) = V_{\text{th}}(t_s) - V_{\text{th}}(t_0). \quad (6.19)$$

Furthermore, the recovery during relaxation is monitored after $t_0 = 1 \text{ ms}$ so that only the tails of the real recovery curve can be assessed experimentally.

The TSM [61] has been compared to a large set of measurement data, including various combinations of stress voltages and temperatures. For illustration, a fit to the eMSM (cf. Section 1.4) data at 150°C is depicted in Fig. 6.6. The findings of this model are evaluated in the following:

- (i) Hole trapping during stress sets in before the first OTF measurement point (1 ms) is determined and no sign of saturation appears until 2 s. Detrapping during relaxation extends over the whole experimental time window ranging from 1 ms to 1000 s.
- (ii) $\Delta V_{\text{th}}(t)$ follows a logarithmic time behavior during the whole stress phase.

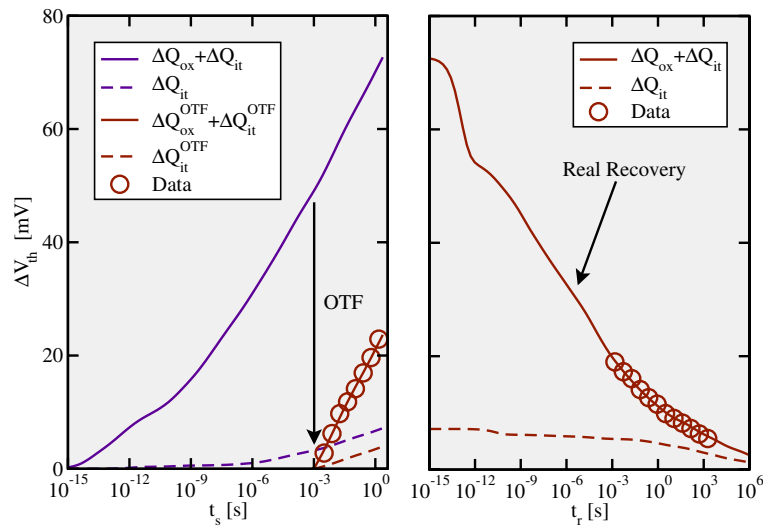


FIGURE 6.5: A comparison of the experimental and simulated degradation during stress (left panel) and relaxation (right panel). The data are extracted from eMSM measurements [25, 26], which employs OTF during stress and determines the V_{th} shift from the recorded drain current during the relaxation phase. Note that OTF only assesses the change of threshold voltage referred to the first measurement point, but disregards the degradation accumulated before. Analogously, the NBTI recovery may start already before 1 ms but the MSM technique can only monitor the tails of the degradation curves.

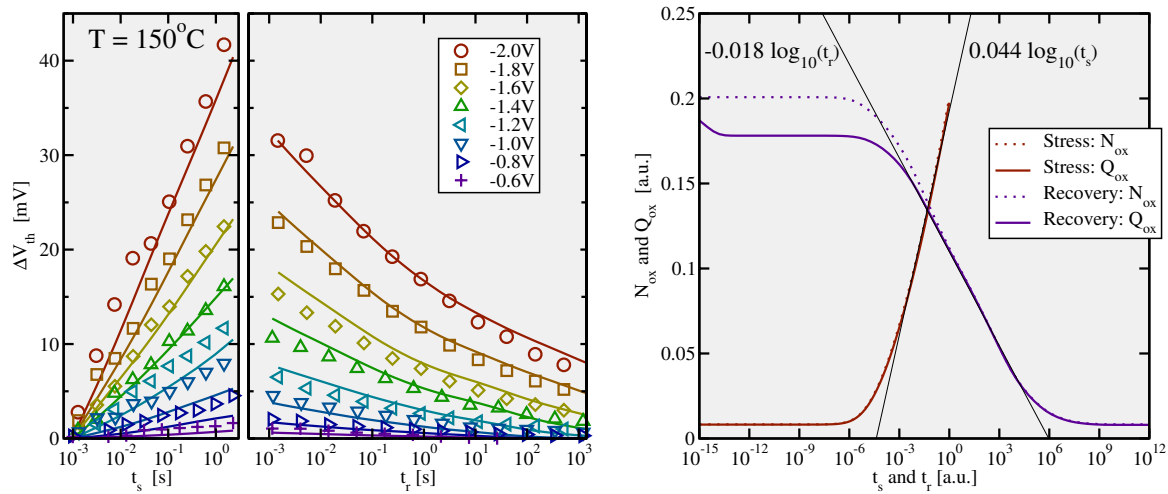


FIGURE 6.6: **Left:** An evaluation of simulation data (lines) against measurement data of a thin SiON device (symbols) for 8 different stress voltages at a temperature of 150°C . The field acceleration as well as the asymmetry between stress and relaxation have been nicely reproduced. **Right:** Averaged trap occupancy during stress and recovery for a single trap. The dotted lines refer to oxide defects in state 2 or 3, while the solid lines include the positively charged defects (state 3) only. The ratio between the slope of the stress (A_s) and the relaxation (A_r) curve yields $A_s/A_r \sim 2.5$, as observed experimentally in [61].

| Model Properties | | |
|------------------|----------------------------------|---|
| (i) | Involved Time Scales | ✓ |
| (ii) | Log. Behavior during Stress | ✓ |
| (iii) | Log. Behavior during Recovery | ✓ |
| (iv) | Asymmetry Stress/Recovery | ✓ |
| (v) | Quadratic Field Dependence | ✓ |
| (vi) | Quadratic Temperature Dependence | ✓ |

TABLE 6.2: Checklist for an NBTI model. The TSM fulfills all criteria established in Section 1.4. From this perspective the model can be justifiably regarded as a reasonable explanation for NBTI.

- (iii) During the initial phase of recovery, a logarithmic time dependence is clearly recognizable. However, this behavior is obscured for relaxation times larger than 1 s where the $\Delta V_{th}(t)$ curve starts to level off. This is due to the fact that the TSM also accounts for the permanent component of NBTI.
- (iv) The logarithmic slopes of ΔV_{th} during the stress and the relaxation phase exhibit a ratio of ~ 2.5 in agreement with [61]. This asymmetry is demonstrated by the temporal change of the trap occupancy in Fig. 6.6 (right). After the level shift from $E_{t,1}$ to $E_{t,2}$, when the defect transforms from an oxygen vacancy to an E' center, the trap level $E_{t,2}$ lies closer to the substrate valence bandedge than $E_{t,1}$. This results in higher trapping rates for hole capture (r_{32}) and emission (r_{23}) so that the subsystem of states 2 and 3 is only weakly affected by r_{31} during recovery. Therefore, this reduced system is close to equilibrium, meaning that

$$f_2 r_{23} = f_3 r_{32} \quad (6.20)$$

with $f_2 + f_3 = 1$. Then the occupation f_3 is given by

$$f_3 = \frac{1}{1 + \frac{r_{cap,h}(\Delta E_{b,2}, E_{t,2})}{r_{em,h}(\Delta E_{b,2}, E_{t,2})}} = \frac{1}{1 + \exp(\beta(E_{t,2} - E_f))} \quad (6.21)$$

and can be interpreted as the electron occupancy $f_{t,2}$ of the E' center with the defect level $E_{t,2}$. According to the above equation, the defect occupancy in the whole defect system of the TSM follows the substrate Fermi level, which thus controls the annealing rate r_{31} and can slow down the recovery. Due to this ‘occupancy effect’, the TSM is able to capture the asymmetry between stress and relaxation.

- (v) The simulations fit the experimental stress and relaxation curves for a wide range of gate biases meaning that the TSM correctly reproduces the field dependence seen in measurements.

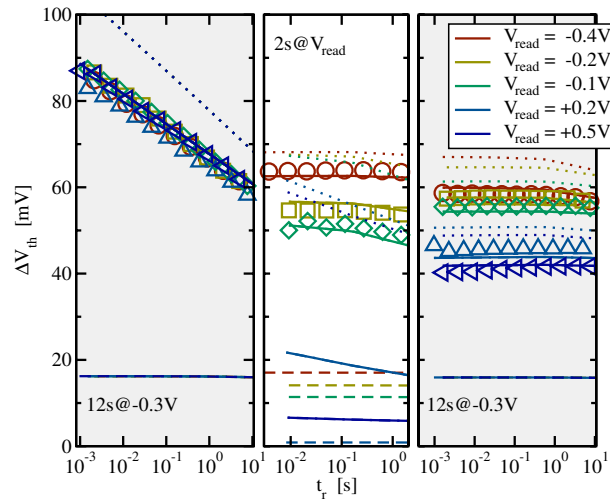


FIGURE 6.7: The field dependence of recovery [61]. Five devices were stressed for 6000s under the same conditions ($T = 125^\circ\text{C}$, $V_s = -2.0\text{V}$). The following recovery phase (left and right panel) was interrupted for a period of time during which V_G was switched from the recovery voltage of -0.13V to V_{read} for 2s (middle panel). The experimental data are marked by symbols, while the simulations are represented by lines (dotted: $\Delta N_{\text{ox}} + \Delta N_{\text{it}}$, solid: ΔV_{th} due to $\Delta Q_{\text{ox}} + \Delta Q_{\text{it}}$, dashed: ΔV_{th} due to ΔQ_{it}). The measurements demonstrate that the recovery is clearly affected by variations of the recovery bias. This effect is reminiscent of the field-dependent emission times seen in TDDS. The agreement of the simulations with the measurements shows that the TSM can explain the field-dependent NBTI recovery.

- (vi) An equal quality of fits (not shown here) has been achieved for other temperatures with the same set of parameters, meaning that the TSM is able to describe the temperature dependence observed experimentally.

The TSM is found to satisfy all criteria of Table 6.2 and therefore seems to properly describe NBTI degradation. Besides that, it also agrees well with the observation of a field-dependent recovery, which is demonstrated by the measurements shown in Fig. 6.7. Due to the occupancy effect, the substrate Fermi level E_f controls the portion of neutral E' centers (state 3) which can return to state 1 by structural relaxation and contribute to the NBTI recovery. Interestingly, this field dependence is compatible with the finding that the emission times of ‘anomalous defects’ are field-sensitive.

The distributions of trap levels obtained from the model calibration are depicted in Fig. 6.8. The trap levels $E_{t,1}$ of the precursors (state 1) are uniformly distributed between -1.68eV and -0.25eV in qualitative agreement with the values in [39]. The defects located the highest have also the highest substrate hole capture rates r_{12} and therefore have already been transformed E' centers (states 2 and 3) after a stress time of 1000s. In this new configuration, they feature a trap level $E_{t,2}$ in the range between -0.62eV and 0.39eV in qualitative agreement with the values published in [39]. According to equation (6.21), the occupancy of the $E_{t,2}$ levels is determined by the substrate Fermi energy and thus the number of neutralized defects in the E' center configuration (state 3) increases with a lower energies. Since only defects in this state transformed to a precursor (state 1) again, the number of traps in state 2 diminished towards the substrate Fermi energy (cf. Fig. 6.8). The donor levels of the

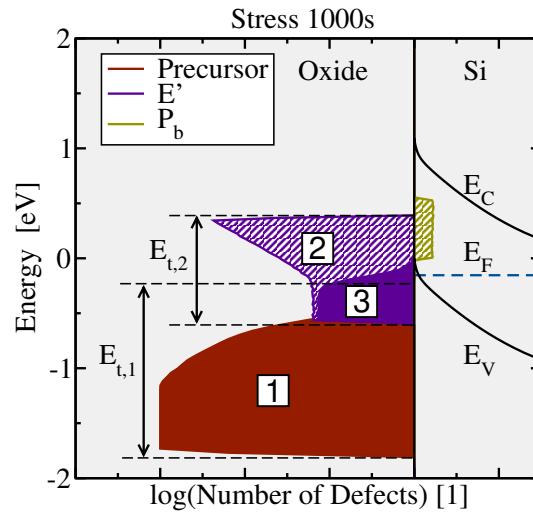


FIGURE 6.8: A histogram of energetically distributed defects after a stress time of 1000s. The numbers in the white filled boxes denote the state of the defects. The area in the plain red color gives the number of precursors (state 1) with the trap level $E_{t,1}$. The rest of the defects is in the E' center configuration, in which they can be positively charged (purple striped pattern) or neutralized (plain purple color) and have a trap level of $E_{t,2}$. The occupied (plain) and unoccupied (striped) interface states are depicted as beige areas. The beige striped area gives the density of interface states originating from the P_b centers.

interface states have been assumed to be uniformly distributed and are located within the lower part of the substrate bandgap consistent with [64].

6.3.3 Quantum Mechanical Simulations

So far, classical calculations of the band diagram have been performed to obtain the interface quantities, such as the position of the bandedges (E_C , E_V), the Fermi level (E_F), and the electric field (F) within the dielectric. These quantities enter the expressions of the rates and will significantly alter them due to their exponential dependences. However, the SRH rates (6.9) used in Section 6.3.1 are valid for a three-dimensional electron gas [55] but this assumption breaks down for an inversion layer of MOS structures. In the one-dimensional triangular potential well in the channel, quasi-bound states build up and form subbands, which correspond to the new initial or final energy levels for the charge carriers undergoing an NMP transitions. The quantum mechanical transition rates are obtained following the derivation in Section 2.5.2 but using the DOS for one-dimensionally confined holes. Then the rate equation (2.59) modifies to

$$\partial_t f_t = \int_{-\infty}^{E_v} \left((1 - f_t) \frac{e_p(E)}{c_p(E)} f_n(E) - f_t f_p(E) \right) c_p(E) D_{p,c3D}(E) f_p(E) dE. \quad (6.22)$$

It is noted here that the exact shape of $D_{p,c3D}(E)$ does not enter this derivation and consequently the DOS can be expressed as

$$D_{p,c3D}(E) = \tilde{D}_{p,c3D}(E) \Theta(E - E_{p,0}). \quad (6.23)$$

Using the above expression, the rate equation (6.22) simplifies to

$$\partial_t f_t = \left((1 - f_t) \frac{e_p(E)}{c_p(E)} f_n(E) - f_t f_p(E) \right) \int_{-\infty}^{E_{p,0}} c_p(E) \tilde{D}_{p,c3D}(E) f_p(E) dE \quad (6.24)$$

and the capture time $\tau_{cap,h}$ can be identified as

$$\frac{1}{\tau_{cap,h}} = \frac{\int_{-\infty}^{E_{p,0}} c_p(E) \tilde{D}_{p,c3D}(E) f_p(E) dE}{\underbrace{\int_{-\infty}^{E_{p,0}} \tilde{D}_{p,c3D}(E) f_p(E) dE}_{\equiv \sigma_p^{TSM} \nu_{th,p}}} p. \quad (6.25)$$

Analogously to the derivation in Section 2.5.2, the barrier dependence for the NMP transition is incorporated in the cross section σ_p^{TSM} (cf. Fig. 6.9).

$$\sigma_p^{TSM} = \sigma_{p,0}^{TSM} \exp(-x_t/x_{p,0}) \begin{cases} \exp(-\beta \Delta E_b), & E_t > E_{p,0} \\ \exp(-\beta \Delta E_b) \exp(-\beta(E_{p,0} - E_t)), & E_{p,0} < E_v \end{cases}, \quad (6.26)$$

where $E_{p,0}$ corresponds to the first bound state. Inserting the modified cross section in equation (2.65) and (2.66) yields

$$r_{cap,h}(\Delta E_b, E_t) = \frac{1}{\tau_{p,0}^{TSM}} \frac{p}{N_v} \exp(-x_t/x_{p,0}) \exp(-\beta \Delta E_b) \begin{cases} 1, & E_{p,0} > E_v \\ \exp(-\beta(E_{p,0} - E_t)), & E_{p,0} < E_v \end{cases} \quad (6.27)$$

and

$$r_{em,h}(\Delta E_b, E_t) = \frac{1}{\tau_{p,0}^{TSM}} \frac{p}{N_v} \exp(-x_t/x_{p,0}) \exp(-\beta \Delta E_b) \begin{cases} \exp(-\beta(E_t - E_f)), & E_{p,0} > E_v \\ \exp(-\beta(E_{p,0} - E_f)), & E_{p,0} < E_v \end{cases}. \quad (6.28)$$

These rates have been used to incorporate the aforementioned quantum effects into the TSM, which has been evaluated against the same set of experimental data. For a proper comparison with the classical variant of TSM, only the NMP parameters ($E_{t,1}$, $E_{t,2}$, $\Delta E_{b,1}$, and $\Delta E_{b,2}$) have been optimized while all other parameters have been held fixed. The simulated degradation curves show a good agreement with experimental data (see Fig. 6.10) so that the quantum mechanically refined variant of the TSM still fulfills all criteria listed in Table 6.2. It is noted here that these simulations yield an the uppermost trap levels $E_{t,1}$, which have been shifted downwards by about the same energy as the separation of E_1 and E_v (ranging between 169 and 277 meV). This can be explained when considering that, first, E_v is replaced $E_{p,0}$ in the rate equations (6.27) and (6.28) and, second, the NMP barrier for hole capture is reduced by this energy difference. From this it follows that also the trap levels $E_{t,1}$ must be shifted down by approximately the same energy in order to obtain hole capture rates of an equal magnitude. In summary, it has been assured that also the quantum mechanically refined variant of the TSM can explain the NBTI data and must therefore be considered as a reasonable NBTI model.

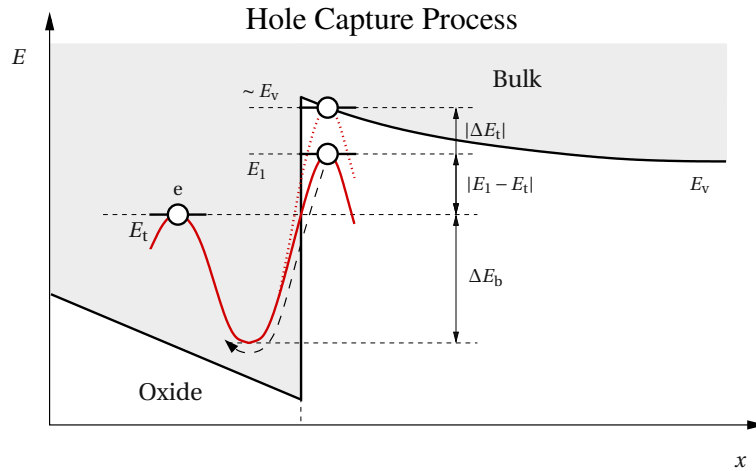


FIGURE 6.9: The band diagram of a pMOSFET. According to classical considerations the substrate holes initially lie at the valence band, however, they are concentrated around the first bound state E_1 when quantum confinement is taken into account. The shift of the initial energy level from E_v to E_1 reduces the corresponding NMP barriers (red lines) and thus enhances the hole capture rates. Note that the energy difference between E_v and E_1 varies with the oxide field and thus affects the field dependence of τ_{cap} and τ_{em} .

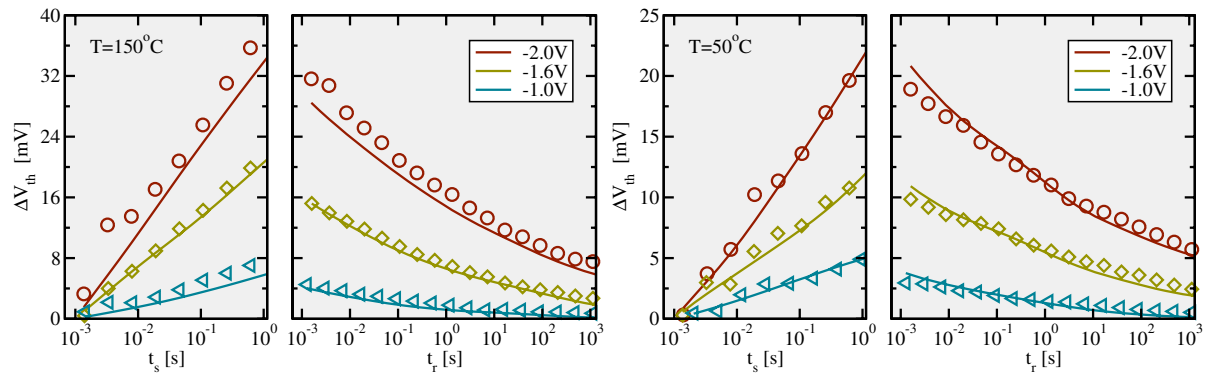


FIGURE 6.10: The temporal evolution of the trapped charges including quantization effects. A pMOSFET with a gate thickness of 1.75 nm is subjected to two different temperatures (50°C left panels, 150°C right panels) and three different gate voltages for 1 s during the first phase termed trapping/stress (left hand side). After the gate voltage is removed, the second phase called detrapping/relaxation phase (right-hand side) sets in. Symbols mark measurement data while solid lines belong to simulation data. Note that the temperature and field dependence is well reproduced simultaneously for relaxation phase. The slight tendency of the simulations to underestimate the measurements at high stress temperatures during the stress phase appear in the classical as well as in the quantum mechanical simulations. They may be traced back to the mobility degradation of the drain current during the MSM measurements [26].

6.3.4 Capture and Emission Time Constants

The criteria in Table 4.1 have been successfully satisfied by the TSM. With this respect, the TSM should be regarded as model qualified to describe NBTI. However, these criteria only evaluate the degradation produced by an ensemble of defects but do not consider whether the behavior of a single defect is correctly reproduced. For this reason, the TSM will be investigated using the time constant plots in the following. Since the TDDS measurements cannot capture the permanent component of NBTI, the transition state diagram must be reduced to stage one. This means that the equation (6.8) and the rates r_{24} and r_{42} in equation (6.6) must be omitted. Since the trap level $E_{t,2}$ is assumed to lie closer to the valence band edge than $E_{t,1}$, the associated rate r_{23} and r_{32} are much larger than r_{12} . Thus the fast switching between state 2 and 3 produces noise, which is undesired for the analysis of $\tau_{em,h}$ in the time constant plots. Therefore, a compact rate expression for the transition $2 \leftrightarrow 3 \rightarrow 1$ is sought. One can calculate the corresponding emission time τ_{21} as the mean first passage time in continuous time Markov chain theory [131] (discussed in Section 3.2).

$$\frac{1}{\tau_{21}} = r_{21} = \frac{r_{23}r_{31}}{r_{23} + r_{32} + r_{31}} \quad (6.29)$$

Assuming $r_{32} \gg r_{31}$ and $r_{23} \gg r_{31}$, the above expression can be simplified to

$$r_{21} = r_{31} \frac{1}{1 + \frac{r_{32}}{r_{23}}} \quad (6.30)$$

Since in a pMOSFET the trapping dynamics are dominated by the hole capture and emission from the valence band, the electron rates $r_{cap,e}(\Delta E_{b,1}, E_{t,2})$, $r_{cap,e}(\Delta E_{b,2}, E_{t,2})$, and $r_{23} = r_{em,e}(\Delta E_{b,2}, E_{t,2})$ can be neglected.

$$1/\tau_{cap,h} = \frac{1}{\tau_{p,0}^{TSM}} \frac{p}{N_v} \exp\left(-\frac{x_t}{x_{p,0}}\right) \exp(-\beta \Delta E_{b,1}) \exp\left(\frac{F_{ox}^2}{F_c^2}\right) \begin{cases} 1, & E_{t,1} > E_v \\ \exp(-\beta(E_v - E_{t,1})), & E_{t,1} < E_v \end{cases} \quad (6.31)$$

$$1/\tau_{em,h} = \nu_0 \exp(-\beta \Delta E_{b,3}) f_{t,2} \quad (6.32)$$

$$f_{t,2} = \frac{1}{1 + \exp(\beta(E_{t,2} - E_f))} \quad (6.33)$$

This reduced variant of the TSM is fitted against the TDDS data and will be evaluated according to the list of criteria established in Section 1.3.4.

- (i) The simulated τ_{cap} in the time constant plot of Fig. 6.11 has a wrong curvature. This can be traced back to the fact that τ_{cap} is proportional to $\exp(-F_{ox}^2/F_c^2)$ according to equation (6.31).
- (ii) The NMP barriers allow for a marked temperature activation of τ_{cap} .
- (iii) The TSM gives field-insensitive τ_{em} as demonstrated in Fig. 6.11. However, this is only true for defects with a trap level $E_{t,2}$ above E_f . In this case, $f_{t,2}$ approximates to 1 and τ_{em} is given by $\nu_0^{-1} \exp(\beta \Delta E_{b,3})$.

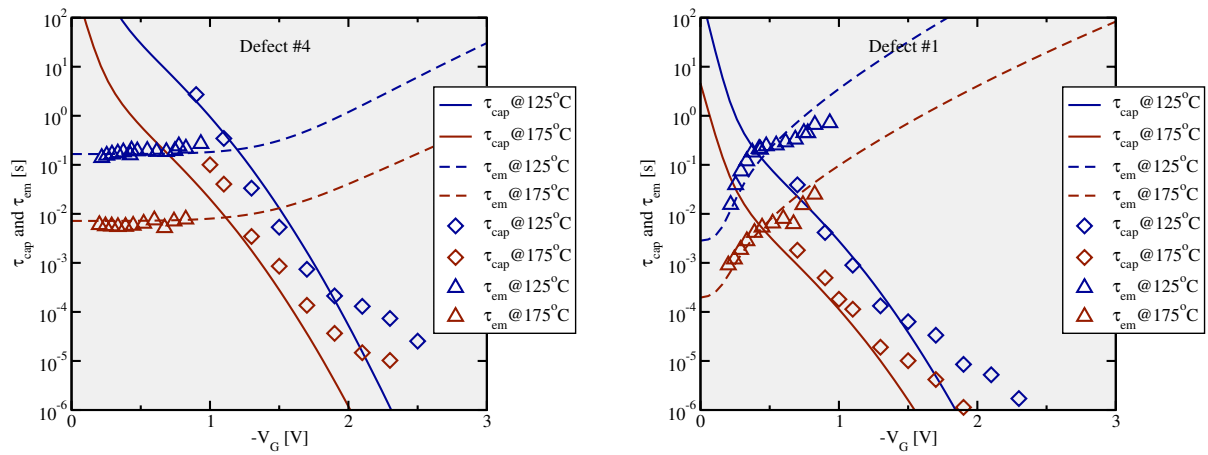


FIGURE 6.11: The TSM optimized against the TDDS data of ‘normal’ (left) and ‘anomalous’ (right) defects. Symbols mark measurement data while solid lines belong to simulations. Depending on the position of the trap level $E_{t,2}$, the TSM can explain both defect behaviors. However, it does not give the correct curvature of τ_{cap} due to the field enhancement factor.

| Model | McWhorter | Kirton | TSM |
|--|-----------|--------|-----|
| (i) Curvature in τ_{cap} | ✗ | ✗ | ✗ |
| (ii) Temperature Activation of τ_{cap} | ✗ | ✓ | ✓ |
| (iii) ‘Normal’ Defect Behavior | ✗ | ✓ | ✓ |
| (iv) ‘Anomalous’ Defect Behavior | ✗ | ✗ | ✓ |
| (v) Temperature Activation of τ_{em} | ✓ | ✓ | ✓ |

TABLE 6.3: The same as in Table 6.1 but including the TSM. In contrast to previous models the TSM can give an explanation for the ‘normal’ as well as the ‘anomalous’ defect behavior.

(iv) The TSM also allows for field-sensitive τ_{em} if $E_{t,2}$ is located slightly below E_f at the relaxation voltage. Then the field dependence is caused by the term $f_{t,2}$ in equation (6.32).

(v) In both defects, τ_{em} is thermally-activated.

As demonstrated in the previous section, the TSM is indeed an important improvement of the NBTI model. Regarding the time constant plots (cf. Table 6.3), the introduction of the state 3 gives an explanation for ‘normal’ as well as the ‘anomalous’ defect behavior. However, the TSM predicts a wrong curvature of τ_{cap} and thus cannot be reconciled with the TDDS data. As a consequence, it can be concluded that the TSM performs well for stress and relaxation curves but fails to describe the behavior of single defects.

6.4 Conclusion

In this chapter, several peculiarities of the TSM have been analyzed and compared to the findings of NBTI measurements. In contrast to the previous models, the TSM is capable of fulfilling all criteria in Table 6.2, including the logarithmic behavior during stress and relaxation, the quadratic field and temperature dependence, as well as the asymmetry of stress and relaxation. Furthermore, it exhibits a field dependence of recovery as noticed in NBTI measurements. Therefore, this model seems to reasonably describe the degradation process of NBTI. Furthermore, it evaluated for the time constant plots extracted from the TDDS measurements (cf. Table 6.3). Thereby it has been tested whether the TSM correctly reflects the behavior of a single defect. However, no reasonable agreement has been achieved, indicating that the TSM does not correctly describe the capture or emission process of a single trap.

7

The Extended Nonradiative Multi-Phonon Model

The Kirton model and the TSM rely on the concept of NMP processes and can therefore give an explanation for the experimentally observed temperature activation of τ_{cap} and τ_{em} . However, the energy barriers used in those models are not calculated by the crossing point of two adiabatic potentials, as it would be necessary according to theoretical considerations. Palma *et al.* [125] related the measured capture and emission time constants of RTN to the properties of oxide defects based on NMP theory. The success of their model was based on the effect of a Coulomb barrier, which was required to obtain the correct field dependence of τ_{cap} and τ_{em} . Irrespective of the physical correctness of this assumption, the Coulomb barrier was only successfully applied to MOSFETs with thick dielectrics [123, 125, 184]. In a few RTN studies [56] as well as in more recent TDDS measurements [53], interesting phenomena, such as aRTN and tRTN (both discussed in Section 1.3.4), have been observed. They are linked to quite complex trapping dynamics, which can only be explained by metastable defect states. Accordingly, a successful, physics-based NBTI model must incorporate additional metastable defect configurations in order to account for all experimental results. In a new modeling attempt, the theoretical framework of NMP charge transfer reactions has been combined with the concept of metastable states. The resultant model has been termed extended NMP (eNMP) and will be addressed in the following.

7.1 Transition Rates according to the NMP Theory

The transition rates of charge transfer reactions must be discussed on the basis of configuration coordinate diagrams. One such a diagram is depicted in Fig. 7.1 for the case of hole trapping. The

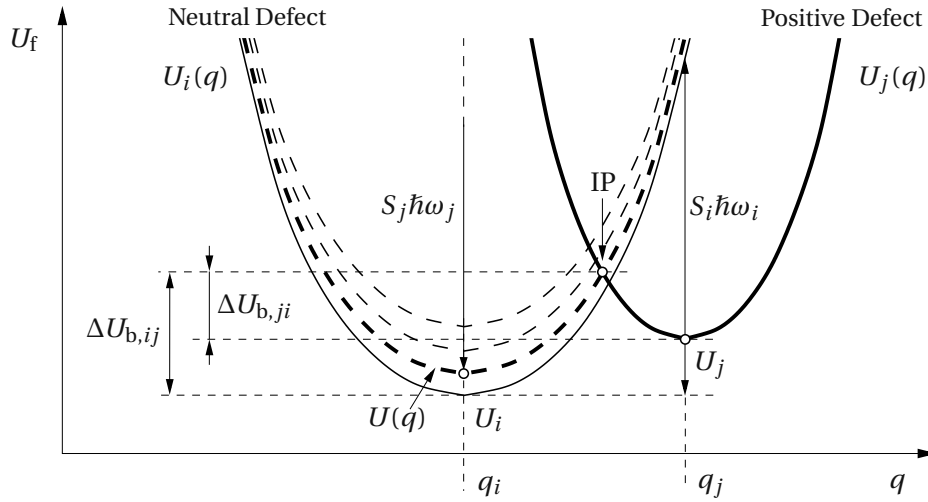


FIGURE 7.1: The configuration coordinate diagram for a hole trapping process. The left parabola corresponds to the case when the defect is neutral and the holes reside in the substrate valence band. Then the hole can be thermally excited by an energy ΔE , accompanied by an upwards shift of the left parabola from $U_i(q)$ (solid) to $U(q)$ (dashed). By contrast, when the defect is positively charged (right parabola), the whole system including the defect and the substrate is represented by the parabola $U_j(q)$ (solid). In general, the curvature of $U_i(q)$ and $U_j(q)$ do not need to be equal. As a consequence, both adiabatic potentials are characterized by their own oscillator frequency (ω_i , ω_j) and in further consequence their own Huang Rhys factor (S_i , S_j).

adiabatic potentials $U_i(q)$ and $U_j(q)$ in the configuration coordinate diagrams are approximated by the parabolas around their respective minima U_i and U_j assuming the harmonic approximation:

$$U_i(q) = \frac{1}{2} M \omega_i^2 (q - q_i)^2 + U_i \quad (7.1)$$

$$U_j(q) = \frac{1}{2} M \omega_j^2 (q - q_j)^2 + U_j \quad (7.2)$$

ω_i and ω_j denote the vibrational frequency of the oscillator potential when the defect is in the charge state i and j , respectively. It is stressed that these oscillator potentials of both charge states are assumed to have different curvatures $\omega_i \neq \omega_j$ in this derivation. The transition barriers $\Delta U_{b,ij}$ and $\Delta U_{b,ji}$ differ by the energy $U_j - U(q_i)$, which can be expressed as

$$\begin{aligned} U_j - U(q_i) &= U_j - U_i + U_i - U(q_i) \\ &= E_v - E_t - \Delta E \end{aligned} \quad (7.3)$$

using the relations

$$U_i - U_j = E_t - E_v, \quad (7.4)$$

$$U(q_i) - U_i = E_v - E_t = \Delta E. \quad (7.5)$$

$U_i - U_j$ corresponds to the separation of the trap level from the valence band edge and $U(q_i) - U_i$

gives the kinetic energy of the substrate hole. Making use of expression (7.3), the difference between the transition barriers can be expressed as:

$$\begin{aligned}\Delta U_{b,ij} - \Delta U_{b,ji} &= U_j - U(q_i) \\ &= -\Delta E - E_t + E_v\end{aligned}\quad (7.6)$$

Using the identity (2.62) and equation (7.6), one obtains the following relation:

$$\exp(-\beta\Delta U_{b,ji}) f_n(E) = \exp(-\beta\Delta U_{b,ij}) \exp(-\beta(E_t - E_f)) f_p(E) \quad (7.7)$$

Analogously to the equation (2.59), the trapping dynamics are governed by the rate equation

$$\partial_t f_t = \int_{-\infty}^{E_v} \left((1 - f_t) e_p^{\text{NMP}}(E) \exp(-\beta\Delta U_{b,ji}) f_n(E) - f_t c_p^{\text{NMP}}(E) \exp(-\beta\Delta U_{b,ij}) f_p(E) \right) D_p(E) dE \quad (7.8)$$

with

$$e_p^{\text{NMP}}(E) = e_{p,0}^{\text{NMP}} \exp(-\beta\Delta U_{b,ji}), \quad (7.9)$$

$$c_p^{\text{NMP}}(E) = c_{p,0}^{\text{NMP}} \exp(-\beta\Delta U_{b,ij}). \quad (7.10)$$

Making use of (7.6), the above rate equation can be simplified to

$$\partial_t f_t = \left((1 - f_t) e_{p,0}^{\text{NMP}} \exp(-\beta(E_t - E_f)) - f_t c_{p,0}^{\text{NMP}} \right) \int_{-\infty}^{E_v} \exp(-\beta\Delta U_{b,ij}) f_p(E) D_p(E) dE. \quad (7.11)$$

In order to evaluate the integral in the above equation, analytic expressions for $\Delta U_{b,ij}$ and $D_p(E)$ are required. The former is defined as the energy difference between U_i and the intersection point IP in the configuration coordinate diagram. The position of of this point can be derived from the condition

$$U_i(q) = U_j(q) \quad (7.12)$$

and reads

$$(q - q_i) = -\frac{q_j - q_i}{R_i - 1} \pm \sqrt{\frac{(q_j - q_i)^2}{(R_i - 1)^2} + \frac{(U_j - U_i) / (\frac{1}{2} M \omega_i^2) + (q_j - q_i)^2}{R_i - 1}} \quad (7.13)$$

with

$$R_i = \frac{\omega_i}{\omega_j}. \quad (7.14)$$

Inserting the expression (7.13) into equation (7.1), one obtains

$$\begin{aligned}\Delta U_{b,ij} &= U_i(q) - U_i \\ &= \frac{S_i \hbar \omega_i}{(R_i^2 - 1)^2} \left(1 - R_i \sqrt{1 + (R_i^2 - 1) \frac{U_j - U_i}{S_i \hbar \omega_i}} \right)^2,\end{aligned}\quad (7.15)$$

where the Huang Rhys factor S_i is defined by the equation

$$\frac{1}{2}M\omega_i^2(q_j - q_i)^2 = S_i\hbar\omega_i. \quad (7.16)$$

A second order expansion of equation (7.15) delivers

$$\Delta U_{b,ij} \approx \frac{S_i\hbar\omega_i}{(1+R_i)^2} + \frac{R_i}{1+R_i}(U_j - U_i) + \frac{R_i}{4S_i\hbar\omega_i}(U_j - U_i)^2. \quad (7.17)$$

According to equation (7.14), the oscillator frequencies ω_i and ω_j differ and thus the quantity R_i deviates from unity. Since R_i enters the above expression for the barrier height, the oscillator frequencies have a strong impact on the transition rates. When the kinetic energy of the substrate hole is taken into account, U_i must be replaced by $U(q_i)$ and equation (7.17) can be rewritten as

$$\Delta U_{b,ij} \approx \frac{S_i\hbar\omega_i}{(1+R_i)^2} + \frac{R_i}{1+R_i}((-\Delta E) + (E_v - E_t)) + \frac{R_i}{4S_i\hbar\omega_i}((-\Delta E) + (E_v - E_t))^2. \quad (7.18)$$

In the case of strong electron-phonon coupling, $S_i\hbar\omega_i \gg |\Delta E + E_t - E_v|$ holds and the third term can be neglected. Assuming parabolic bands (see Appendix A.4), the valence band density of states can be expressed as

$$D_p(E) = D_{p,0}\sqrt{\Delta E} \quad (7.19)$$

with

$$D_{p,0} = \frac{m_e^{3/2}}{\sqrt{2}\pi^2\hbar^3}. \quad (7.20)$$

Using (7.19), the integral in equation (7.11) can be evaluated as

$$\begin{aligned} \int_{-\infty}^{E_v} \exp(-\beta\Delta U_{b,ij}) f_p(E) D_p(E) dE = \\ = \exp\left(-\beta\frac{S_i\hbar\omega_i}{(1+R_i)^2}\right) \exp\left(-\beta\frac{R_i}{1+R_i}(E_v - E_t)\right) D_{p,0} \exp(\beta(E_v - E_t)) \left(\frac{\beta}{1+R_i}\right)^{-3/2} \Gamma(3/2) \end{aligned} \quad (7.21)$$

and simplifies to

$$\begin{aligned} \int_{-\infty}^{E_v} \exp(-\beta\Delta U_{b,ij}) f_p(E) D_p(E) dE = \exp\left(-\beta\frac{S_i\hbar\omega_i}{(1+R_i)^2}\right) \exp\left(-\beta\frac{R_i}{1+R_i}(E_v - E_t)\right) (1+R_i)^{3/2} p \\ = \exp\left(-\beta\Delta U_{b,ij}\Big|_{\Delta E=0}\right) (1+R_i)^{3/2} p \end{aligned} \quad (7.22)$$

with

$$p = D_{p,0} \exp(\beta(E_v - E_t)) \beta^{-3/2} \Gamma(3/2). \quad (7.23)$$

Here, $\Gamma(x)$ denotes the Gamma function, which is defined by

$$\Gamma(x) = \int_0^{\infty} t^{x-1} \exp(-t) dt. \quad (7.24)$$

With (7.22), the compact form of the rate equation (7.11) can be rewritten as

$$\partial_t f_t = \left((1 - f_t) e_p^{\text{NMP}} \exp(-\beta(E_t - E_f)) - f_t c_p^{\text{NMP}} \right) \exp\left(-\beta \Delta U_{b,ij} \Big|_{\Delta E=0}\right) (1 + R_i)^{3/2} p. \quad (7.25)$$

From this, it follows that

$$1/\tau_{\text{cap}} = c_{p,0}^{\text{NMP}} \exp\left(-\beta \Delta U_{b,ij} \Big|_{\Delta E=0}\right) (1 + R_i)^{3/2} p, \quad (7.26)$$

$$1/\tau_{\text{em}} = e_{p,0}^{\text{NMP}} \exp(-\beta(E_t - E_f)) \exp\left(-\beta \Delta U_{b,ij} \Big|_{\Delta E=0}\right) (1 + R_i)^{3/2} p. \quad (7.27)$$

Just as in the standard SRH theory (see Section 2.5), the right-hand side of equation (7.26) can be simplified using the definition

$$c_{p,0}^{\text{NMP}} \exp\left(-\beta \Delta U_{b,ij} \Big|_{\Delta E=0}\right) (1 + R_i)^{3/2} = \sigma_p^{\text{NMP}} \nu_{\text{th},p} \quad (7.28)$$

with

$$\sigma_p^{\text{NMP}} = \sigma_{p,0}^{\text{NMP}} \exp\left(-\beta \Delta U_{b,ij} \Big|_{\Delta E=0}\right). \quad (7.29)$$

Analogously to Section 2.5, thermal equilibrium can be assumed so that the trap occupation follows Fermi-Dirac statistics and detailed balance applies for the rate equation (7.25). Then c_p^{NMP} equals e_p^{NMP} and the hole capture and emission time constant reads

$$1/\tau_{\text{cap}} = \nu_{\text{th},p} \sigma_{p,0}^{\text{NMP}} \exp\left(-\beta \Delta U_{b,ij} \Big|_{\Delta E=0}\right) (1 + R_i)^{3/2} p \quad (7.30)$$

$$1/\tau_{\text{em}} = \nu_{\text{th},p} \sigma_{p,0}^{\text{NMP}} \exp(-\beta(E_t - E_f)) \exp\left(-\beta \Delta U_{b,ij} \Big|_{\Delta E=0}\right) (1 + R_i)^{3/2} p. \quad (7.31)$$

It is emphasized that the barrier heights are correctly calculated by determining the crossing point of two parabolas. Thereby, one avoids the artificial differentiation, whether E_t is located above or below E_v , as it has been the case in equation (6.10) of the TSM. Additionally, the NMP barriers have not been assumed to be independent of the energy of the hole in contrast to the Kirton model and the TSM.

7.2 States of a Bistable Defect

In the eNMP model, the defects are described by the form of their adiabatic potentials. Motivated by TDDS and EPR experiments [42, 53, 185], they are assumed to feature one stable and one metastable configuration. This bistability is reflected in the double well form of their adiabatic potentials (see Fig. 7.2). Note that it is the key aspect of the eNMP model since it can give an explanation for a plenty of challenging experimental observations, addressed later in this chapter.

The configuration coordinate diagram of such a bistable defect is depicted in Fig. 7.2. The numbers 1 and 2 denote the positive and neutral charge state of the defect, respectively, and the metastable states are marked by additional primes. In the configuration coordinate diagram, there exist two crossing points, where each of them is related to one of the two charge transfer reactions $T_{1 \leftrightarrow 2'}$ and $T_{1' \leftrightarrow 2}$.

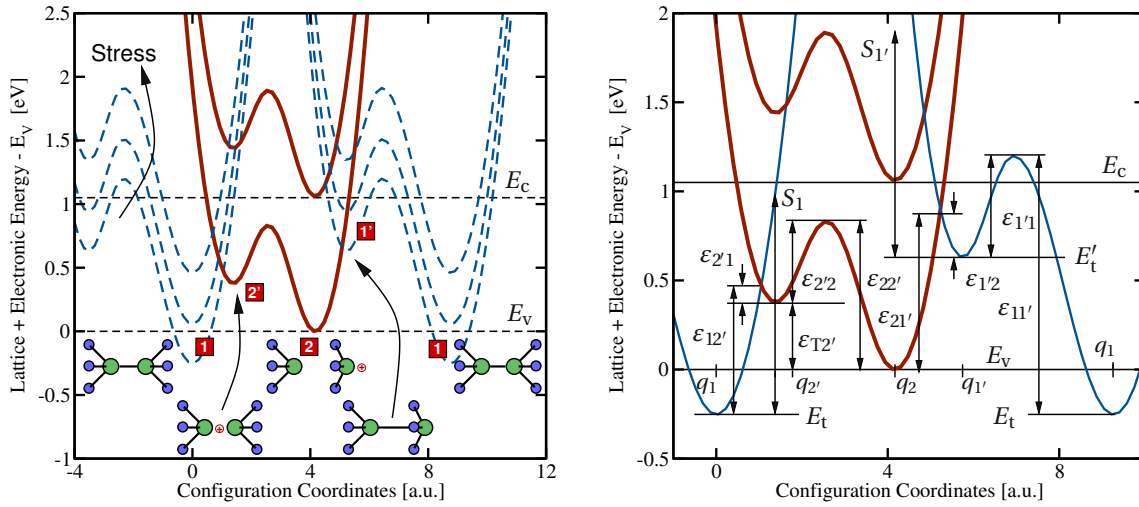


FIGURE 7.2: **Left:** A schematic of the configuration coordinate diagram for a bistable defect. The solid red and the blue dashed lines represent the adiabatic potentials for a defect in its positive and neutral charge state, respectively. The energy minima correspond to the stable or metastable defect configurations, labeled by i with $i = 1, 1', 2, 2'$. The present configuration coordinate diagram describes the exchange of holes with the valence band and thus is associated with a hole capture or emission process. The stick-and-ball models display a defect in its various stable and metastable configurations. A possible candidate for such a bistable defect might be the well-known E' center, which is frequently invoked in the context of noise in MOSFETs. **Right:** Definitions of the used energies and barriers in the eNMP model. Recall that two adiabatic potentials must be shown for one transition. It is assumed that an alternative transition pathway with an additional crossing point exists in the multi-dimensional atomic configuration space. In order to show both intersections (related to $T_{1 \leftrightarrow 2'}$ and $T_{2 \leftrightarrow 1'}$) in one configuration coordinate diagram, the ‘neutral’ potential must be plotted twice. Obviously, $\epsilon_{22'} = \epsilon_{2'2} + \epsilon_{T2'}$ and $\epsilon_{11'} = \epsilon_{1'1} + \Delta E'_t - \Delta E_t$ hold.

Their corresponding NMP barriers¹ $\Delta U_{b,12'}$ and $\Delta U_{b,1'2}$ are derived by evaluating equation (7.17) for the energy differences

$$U_{2'} - U_1 = E_v - E_t + \epsilon_{T2'} , \quad (7.32)$$

$$U_2 - U_{1'} = E_v - E'_t , \quad (7.33)$$

respectively (see Fig. 7.2). The resulting expressions for the NMP barriers read

$$\Delta U_{b,12'} \approx \frac{S_1 \hbar \omega_1}{(1 + R_1)^2} + \frac{R_1}{1 + R_1} (-\Delta E + E_v - E_t + \epsilon_{T2'}) , \quad (7.34)$$

$$\Delta U_{b,1'2} \approx \frac{S_{1'} \hbar \omega_{1'}}{(1 + R_{1'})^2} + \frac{R_{1'}}{1 + R_{1'}} (-\Delta E + E_v - E'_t) . \quad (7.35)$$

¹ The barrier for a transition from state i to j is denoted as ϵ_{ij} , irrespective of whether it belongs to an NMP process or a pure thermal transition.

Inserting them into the equations (7.30) and (7.31) delivers the transition rates

$$r_{12'} = (1 + R_1)^{3/2} \sigma_{p,0}^{\text{NMP}} \nu_{\text{th},p} p \exp(-\beta \varepsilon_{12'}) , \quad (7.36)$$

$$r_{2'1} = (1 + R_1)^{3/2} \sigma_{p,0}^{\text{NMP}} \nu_{\text{th},p} p \exp(-\beta \varepsilon_{12'}) \exp(-\beta(E_t - E_f - \varepsilon_{T2'})) , \quad (7.37)$$

$$r_{1'2} = (1 + R_{1'})^{3/2} \sigma_{p,0}^{\text{NMP}} \nu_{\text{th},p} p \exp(-\beta \varepsilon_{1'2}) , \quad (7.38)$$

$$r_{2'1'} = (1 + R_{1'})^{3/2} \sigma_{p,0}^{\text{NMP}} \nu_{\text{th},p} p \exp(-\beta \varepsilon_{1'2}) \exp(-\beta(E_t' - E_f)) , \quad (7.39)$$

with

$$\varepsilon_{12'} = \frac{S_1 \hbar \omega_1}{(1 + R_1)^2} + \frac{R_1}{1 + R_1} (E_v - E_t) , \quad (7.40)$$

$$\varepsilon_{1'2} = \frac{S_{1'} \hbar \omega_{1'}}{(1 + R_{1'})^2} + \frac{R_{1'}}{1 + R_{1'}} (E_v - E_t') . \quad (7.41)$$

In order to reduce the number of fitting parameters in the numerical simulations, the cross sections σ_p^{NMP} are expected to be within the same order of magnitude for all charge transfer reactions and are thus set equal. The field dependence of the charge transfer reactions $T_{1 \leftrightarrow 2'}$ and $T_{1' \leftrightarrow 2}$ is governed by the relative position of the ‘neutral’ and the ‘positive’ adiabatic potential. When a negative bias is applied to the gate of a pMOSFET (see Fig. 7.2), the ‘neutral’ potential is raised. As a result, the barriers $\varepsilon_{12'}$ and $\varepsilon_{1'2}$ are reduced, which facilitates the charge transfer reactions $T_{1 \rightarrow 2'}$ and $T_{1' \rightarrow 2}$, respectively. Conversely, the transitions $T_{2' \rightarrow 1}$ and $T_{2 \rightarrow 1'}$ are slowed down since the corresponding barrier heights $\varepsilon_{2'1}$ and $\varepsilon_{21'}$ have become larger.

The transitions $T_{1 \leftrightarrow 1'}$ and $T_{2 \leftrightarrow 2'}$ are thermally activated and do not vary with the applied gate bias. According to transition state theory, they can be expressed as

$$r_{11'} = \nu_0 \exp(-\beta \varepsilon_{11'}) , \quad (7.42)$$

$$r_{1'1} = \nu_0 \exp(-\beta \varepsilon_{1'1}) , \quad (7.43)$$

$$r_{22'} = \nu_0 \exp(-\beta \varepsilon_{22'}) , \quad (7.44)$$

$$r_{2'2} = \nu_0 \exp(-\beta \varepsilon_{2'2}) , \quad (7.45)$$

where the barriers ε_{ij} are defined as in Fig. 7.2 and ν_0 stands for the attempt frequency, which is typically of the order 10^{13} s^{-1} . Using $\varepsilon_{11'} = \varepsilon_{1'1} + \Delta E_t' - \Delta E_t$ and $\varepsilon_{22'} = \varepsilon_{2'2} + \varepsilon_{T2'}$, the rates $r_{11'}$ and $r_{22'}$ can be rewritten as

$$r_{22'} = \nu_0 \exp(-\beta(\varepsilon_{2'2} + \varepsilon_{T2'})) , \quad (7.46)$$

$$r_{11'} = \nu_0 \exp(-\beta(\varepsilon_{1'1} + \Delta E_t' - \Delta E_t)) . \quad (7.47)$$

The defect in the eNMP model has a state diagram as shown in Fig. 7.3. With the rates (7.36)-(7.47), the defect kinetics are described by

$$\partial_t f_1 = -f_1 r_{12'} + f_{2'} r_{2'1} - f_1 r_{11'} + f_{1'} r_{1'1} , \quad (7.48)$$

$$\partial_t f_{2'} = -f_{2'} r_{2'1} + f_1 r_{12'} - f_{2'} r_{2'2} + f_2 r_{22'} , \quad (7.49)$$

$$\partial_t f_2 = -f_2 r_{22'} + f_{2'} r_{2'2} - f_2 r_{21'} + f_{1'} r_{1'2} , \quad (7.50)$$

$$\partial_t f_{1'} = -f_{1'} r_{1'2} + f_2 r_{21'} - f_{1'} r_{1'1} + f_1 r_{11'} . \quad (7.51)$$

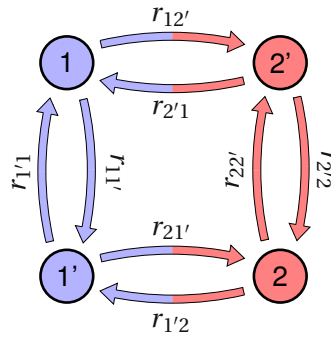


FIGURE 7.3: The state diagram of the eNMP model. The individual states are represented by the circles, where the red and the blue color indicate the positive and the neutral charge state of the defect, respectively. The transition rates between two states are denoted by the colored arrows. The vertical transitions correspond to pure thermal transitions while horizontal ones stand for charge transfer reactions, which are detectable in NBTI, RTN, and TDDS experiments.

7.3 Model Evaluation

The multitude of transition possibilities in the eNMP model results in quite complex defect kinetics, which allow to explain the defect behavior seen in TDDS. This is indeed important, since NBTI stress and relaxation processes are a superposition of several single trapping and detrapping events. Therefore, the degradation could in principle be reproduced by well-chosen distributions of model parameters. However, TDDS experiments give insight into the behavior of single defects and can therefore reveal whether a trapping model reflects the physics of a real defect.

The time constant plots in Fig. 7.4 depict a fit of the eNMP model against TDDS measurement data. An evaluation of the checklist in Table 7.1 is given below:

- (i) The curvature in τ_{cap} is reproduced by the eNMP model for the first time.
- (ii) τ_{cap} shows a marked temperature activation over the whole range of V_G , visible as a parallel upward shift.
- (iii) In general, the eNMP model yields field-insensitive τ_{em} as displayed in Fig. 7.4 left. It is important to note here that at larger oxide fields this model also predicts an exponential dependence, which has also been observed for some defects in RTN measurements [55].
- (iv) However, it also allows for a field-dependent τ_{em} provided that the energy minima of the states 1' and 2 are separated by only a few hundredth of an electron Volt at small V_G (cf. Fig. 7.4 right).
- (v) In both cases, τ_{em} is thermally-activated.

The above checklist demonstrates that the eNMP model predicts the key features of the hole capture and emission process correctly, strongly indicating that the eNMP model can describe the physics of the defects seen in TDDS.

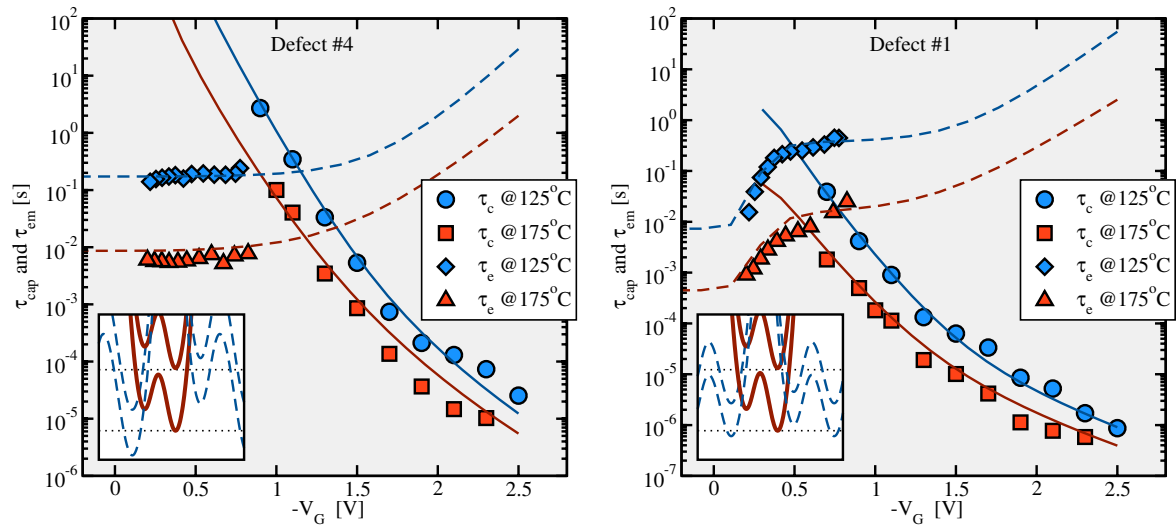


FIGURE 7.4: **Left:** The capture (solid lines) and emission (dashed lines) times of a ‘normal’ defect as a function of the gate bias. The symbols stand for the measurement data and the lines represent the simulation results of the eNMP model. The latter are shown to be in remarkable agreement with the experimental data. The inset (bottom left) depicts the adiabatic potential for the neutral (blue, dashed lines) and the positive (red, solid lines) charge state of the defect, when no bias is applied to the gate. Under these conditions the energy minima of the states $1'$ and 2 differ by at least a few tenth of an electron Volt. This fact eventually characterizes this trap as a ‘normal’ defect. **Right:** The same but for an ‘anomalous’ defect as presented in the Section 1.3.4. Compared to the defect #4, the present defect (#1) shows a strong voltage/field dependence of τ_{em} at low V_G or F_{ox} . In contrast to a ‘normal’ defect, the energy minima of the states $1'$ and 2 coincide, which allows for the strong sensitivity of τ_{em} to V_G .

| Model | McWhorter | Kirton | TSM | eNMP |
|--|-----------|--------|-----|------|
| (i) Curvature in τ_{cap} | ✗ | ✗ | ✗ | ✓ |
| (ii) Temperature Activation of τ_{cap} | ✗ | ✓ | ✗ | ✓ |
| (iii) ‘Normal’ Defect Behavior | ✗ | ✗ | ✗ | ✓ |
| (iv) ‘Anomalous’ Defect Behavior | ✗ | ✗ | ✗ | ✓ |
| (v) Temperature Activation of τ_{em} | ✓ | ✓ | ✗ | ✓ |

TABLE 7.1: Checklist for a defect model (see Section 1.3.4). The McWhorter model, the Kirton model, as well as the TSM do not fulfill all criteria and thus do not describe the defects seen in TDDS experiments. By contrast, the eNMP reproduces the correct field and temperature dependence and gives an explanation for the ‘normal’ and ‘anomalous’ defects.

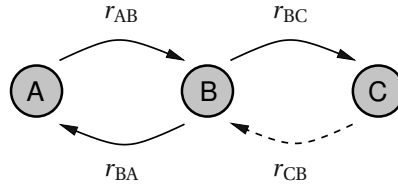


FIGURE 7.5: The state diagram for a two-step process from the state A to C . The first passage time of such a process is calculated by equation (7.52). Consider that the transition rate r_{CB} , indicated by the dashed arrow, does not enter this equation.

7.4 Analytics Derivation of the Capture and Emission Time Constants

In order to promote the understanding of the eNMP model, τ_{cap} and τ_{em} will be derived analytically in the following. The time constants observed in TDDS can be calculated on the basis of first passage times of a two-step process (see Fig. 7.5).

$$\tau = \frac{r_{AB} + r_{BC} + r_{BA}}{r_{AB}r_{BC}} \quad (7.52)$$

$$= \frac{1}{r_{AB}} + \frac{1}{r_{BC}} + \frac{1}{r_{BC}} \frac{r_{BA}}{r_{AB}} \quad (7.53)$$

This quantity corresponds to the mean time it takes the considered system to arrive at the state C , provided that it was in the state A but not in state B at the beginning. In the eNMP model, one is only interested in the transition times between the stable states 1 and 2, in which the defect dwells most of the time. Since the metastable states $1'$ and $2'$ are energetically higher than their corresponding stable counterparts 1 and 2, the defect only remains temporarily in these metastable states. This is in agreement with the condition for the first passage time that the system must not be in state B at the beginning. As a result, the transition rates between the states 1 and 2 can be reasonably described as the inverse of first passage times.

The various transition pathways allowed in the eNMP model are summarized in the state diagrams of Fig. 7.6. The corresponding first passage times for the hole capture or emission read

$$\tau_{\text{cap}}^{2'} = \frac{1}{r_{12'}} + \frac{1}{r_{2'2}} + \frac{1}{r_{2'2}} \frac{r_{2'1}}{r_{12'}}, \quad (7.54)$$

$$\tau_{\text{cap}}^{1'} = \frac{1}{r_{11'}} + \frac{1}{r_{1'2}} + \frac{1}{r_{1'2}} \frac{r_{1'1}}{r_{11'}}, \quad (7.55)$$

$$\tau_{\text{em}}^{2'} = \frac{1}{r_{22'}} + \frac{1}{r_{2'1}} + \frac{1}{r_{2'1}} \frac{r_{2'2}}{r_{22'}}, \quad (7.56)$$

$$\tau_{\text{em}}^{1'} = \frac{1}{r_{21'}} + \frac{1}{r_{1'1}} + \frac{1}{r_{1'1}} \frac{r_{1'2}}{r_{21'}}. \quad (7.57)$$

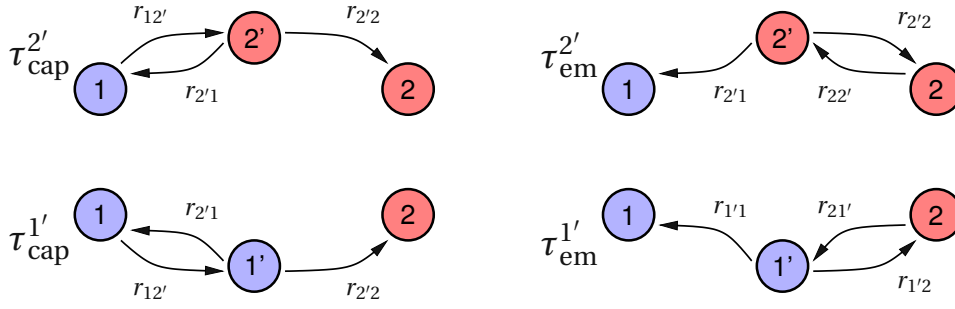


FIGURE 7.6: A simplified state diagrams of hole capture and emission over the metastable states $1'$ and $2'$. The superscript of τ denotes the intermediate state, which has been passed through during a complete capture or the emission event. Note that there exist two competing pathways for a hole capture event, namely one over the intermediate state $1'$ and one over $2'$. Of course, the same holds true for a hole emission event.

For studying the field dependence of these capture and emission times, the definition (2.67) is used for ΔE_t and $\Delta E_t'$ in the expression for the NMP barriers (7.17):

$$\begin{aligned} \varepsilon_{12'} &\approx \frac{S_1 \hbar \omega_1}{(1 + R_1)^2} + \frac{R_1 (E_v - E_t + \varepsilon_{T2'})}{1 + R_1} \\ &= \frac{S_1 \hbar \omega_1}{(1 + R_1)^2} - \frac{R_1 (\Delta E_t - \varepsilon_{T2'})}{1 + R_1} + \frac{R_1 q_0 x_t F_{\text{ox}}}{1 + R_1} \end{aligned} \quad (7.58)$$

$$\begin{aligned} \varepsilon_{1'2} &\approx \frac{S_{1'} \hbar \omega_{1'}}{(1 + R_{1'})^2} + \frac{R_{1'} (E_v - E_t')}{1 + R_{1'}} \\ &= \frac{S_{1'} \hbar \omega_{1'}}{(1 + R_{1'})^2} - \frac{R_{1'} \Delta E_t'}{1 + R_{1'}} + \frac{R_{1'} q_0 x_t F_{\text{ox}}}{1 + R_{1'}}. \end{aligned} \quad (7.59)$$

Using the definitions

$$\tau_{\text{c,min}}^{2'} = 1/r_{2'2}, \quad (7.60)$$

$$\tau_{\text{e,min}}^{2'} = 1/r_{22'}, \quad (7.61)$$

$$\tau_{\text{c,min}}^{1'} = 1/r_{11'}, \quad (7.62)$$

$$\tau_{\text{e,min}}^{1'} = 1/r_{1'1}, \quad (7.63)$$

$$\tau_{p,0}^{\text{NMP}} = \frac{1}{\sigma_{p,0}^{\text{NMP}} \nu_{\text{th},p} N_v} \quad (7.64)$$

the mean time constants (7.54)-(7.57) can be expressed as

$$\tau_{\text{cap}}^{2'} = \tau_0 \frac{N_2}{p} \exp \left(\beta \frac{R_1 q_0 x_t F_{\text{ox}}}{1 + R_1} \right) + \tau_{\text{c,min}}^{2'} \left(1 + \frac{N_1}{p} \exp(\beta q_0 x_t F_{\text{ox}}) \right), \quad (7.65)$$

$$\tau_{\text{cap}}^{1'} = \tau_{\text{c,min}}^{1'} + \tau_0 \frac{N_3}{p} \exp \left(\beta \frac{R_{1'} q_0 x_t F_{\text{ox}}}{1 + R_{1'}} \right), \quad (7.66)$$

$$\tau_{\text{em}}^{2'} = \tau_{\text{e,min}}^{2'} + \tau_{2'} \exp \left(-\beta \frac{q_0 x_t F_{\text{ox}}}{1 + R_1} \right), \quad (7.67)$$

$$\tau_{\text{em}}^{1'} = \tau_{1'} \exp \left(-\beta \frac{q_0 x_t F_{\text{ox}}}{1 + R_{1'}} \right) + \tau_{\text{e,min}}^{1'} (1 + \exp(\beta(E_t' - E_t))) \quad (7.68)$$

with

$$N_1 = N_v \exp(\beta(\varepsilon_{T2'} - \Delta E_t)) , \quad (7.69)$$

$$N_2 = \frac{N_v}{(1 + R_1)^{3/2}} \exp\left(\beta \frac{S_1 \hbar \omega_1}{(1 + R_1)^2}\right) \exp\left(-\beta \frac{R_1(\Delta E_t - \varepsilon_{T2'})}{1 + R_1}\right) , \quad (7.70)$$

$$N_3 = \frac{N_v}{(1 + R_{1'})^{3/2}} \exp\left(\beta \frac{S_{1'} \hbar \omega_{1'}}{(1 + R_{1'})^2}\right) \exp\left(-\beta \frac{R_{1'}}{1 + R_{1'}} \Delta E_t\right) (1 + \exp(\beta(\Delta E_t' - \Delta E_t))) , \quad (7.71)$$

$$\tau_{2'} = \frac{\tau_{p,0}^{\text{NMP}}}{(1 + R_1)^{3/2}} \exp\left(\beta \frac{S_1 \hbar \omega_1}{(1 + R_1)^2}\right) \exp\left(\beta \frac{\Delta E_t - \varepsilon_{T2'}}{1 + R_1}\right) (1 + \exp(\beta \varepsilon_{T2'})) , \quad (7.72)$$

$$\tau_{1'} = \frac{\tau_{p,0}^{\text{NMP}}}{(1 + R_{1'})^{3/2}} \exp\left(\beta \frac{S_{1'} \hbar \omega_{1'}}{(1 + R_{1'})^2}\right) \exp\left(\beta \frac{\Delta E_t'}{1 + R_{1'}}\right) . \quad (7.73)$$

Recall that the hole capture process can proceed from state 1 over one of the metastable states $2'$ or $1'$ to the final state 2 according to the state diagram of Fig. 7.3. The corresponding capture time constants are denoted as $\tau_{\text{cap}}^{2'}$ and $\tau_{\text{cap}}^{1'}$, respectively, and will be discussed in the following. When the transition pathway $T_{1 \rightarrow 2' \rightarrow 2}$ is preferred, the capture time constant in the form of (7.52) is given by

$$\tau_{\text{cap}}^{2'} = \frac{r_{12'} + r_{2'1} + r_{2'2}}{r_{12'} r_{2'2}} . \quad (7.74)$$

Each of the summands in the nominator can be dominant so that $\tau_{\text{cap}}^{2'}$ is characterized by three distinct regimes, namely B, C, and D in Fig. 7.7.

- At extremely high negative oxide fields (regime D), $r_{12'}$ is the dominant rate meaning that the transition² $T_{1 \rightarrow 2'}$ proceeds much faster than $T_{2' \rightarrow 2}$ (cf. Fig. 7.8). Thus the pace of the complete capture process ($T_{1 \rightarrow 2' \rightarrow 2}$) is determined by the second transition $T_{2' \rightarrow 2}$, which is much slower and has a time constant of $\tau_{\text{c,min}}^{2'}$. Since this second step is only thermally-activated, $\tau_{\text{cap}}^{2'}$ does not depend on the oxide field. This is consistent with equation (7.65) at extremely high negative oxide fields, at which both exponential terms become negligible compared to $\tau_{\text{c,min}}^{2'}$.
- At high negative oxide fields (regime C), the rate $r_{12'}$ approaches the order of magnitude of $r_{2'1}$ and even falls below $r_{2'2}$. Then the transition $T_{2' \rightarrow 2}$ over the thermal barrier $\varepsilon_{2'2}$ is undergone immediately after the defect has changed from the state 1 to $2'$. Thus the kinetics of the hole capture process are governed by the forward rate of the NMP process $T_{1 \rightarrow 2'}$. As a result, $\tau_{\text{cap}}^{2'}$ shows an exponential oxide field dependence, which is reflected in the first term of equation (7.65). Note that the second term is negligible due to its steeper exponential slope within this regime.
- At low negative oxide fields (regime B), $r_{12'}$ is already outbalanced by its reverse rate $r_{2'1}$ (see Fig. 7.8) and the ratio of both rates determines the oxide field dependence. This gives an increased exponential slope originating from the second term of equation (7.65).

² Keep in mind that the term 'transition' does not refer to the duration of the physical process itself, such as the time it takes an electron to tunnel through an energy barrier. It rather denotes the mean time until the physical process takes place and the defect change its state.

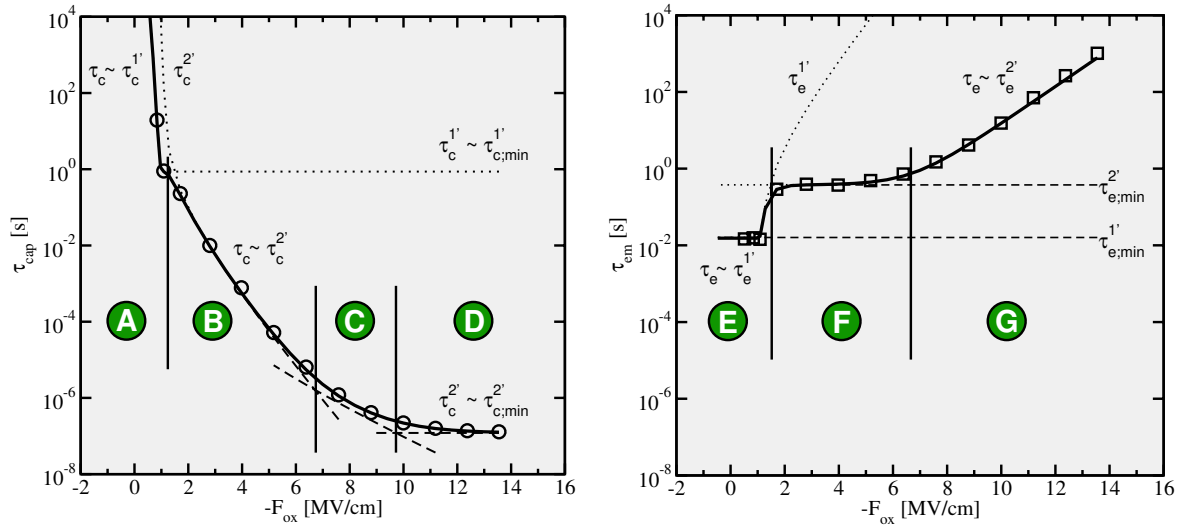


FIGURE 7.7: **Left:** The calculated hole capture time constants as a function of the oxide field. The different regimes of τ_{cap} (A, B, C, and D) are separated by the thin vertical lines and labeled by the green circles with the capital letters. The dotted curves τ_{cap}^i show the capture processes over a metastable state i . The field dependence of τ_{cap} within a certain regime is shown by the dashed curve, which becomes constant if τ_{cap} is insensitive to F_{ox} . **Right:** The same but for the hole emission time constants with the regimes (E, F, and G).

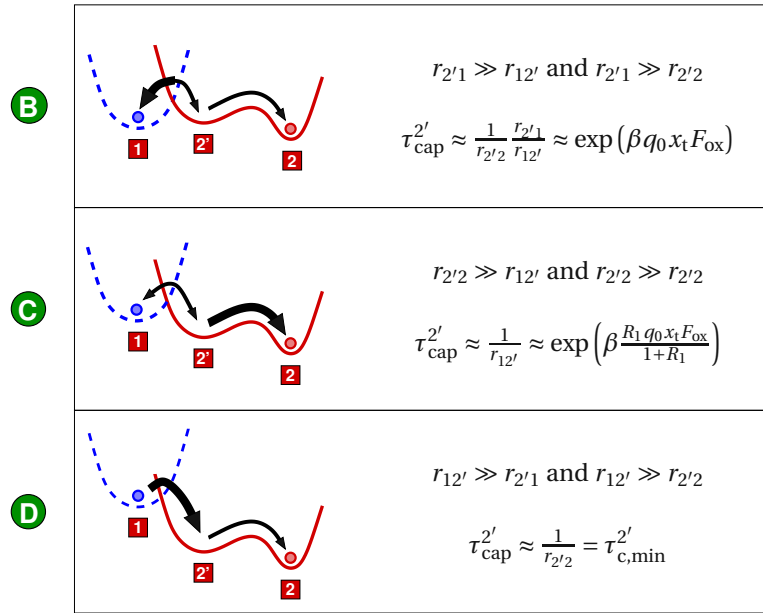


FIGURE 7.8: A schematic representation of adiabatic potentials in the regimes B, C, and D. The arrows show the possible directions of the transitions involved in the capture process. Their thicknesses indicate the magnitude of their rates, where the thinner arrows are associated with larger transitions times and thus governs the oxide field and temperature dependence of the complete capture process $T_{1 \rightarrow 2'}$. With higher oxide fields (B \rightarrow D) the blue potential (neutral defect) is raised relative to the red one (positive defect). This is associated with an increase of $r_{12'}$ and a decrease of the reverse rate $r_{2'1}$. In contrast to the charge transfer reactions $T_{1 \rightarrow 2'}$ and $T_{2 \rightarrow 1'}$, the thermal transition $T_{2' \rightarrow 2}$ is not affected by the oxide field.

The transitions between these three regimes are smooth so that a curvature appears in the time constant plots of τ_{cap} . However, when the transition over the metastable state $1'$ is favored (regime A), the capture time constant can be again formulated as a first passage time:

$$\tau_{\text{cap}}^{1'} = \frac{r_{11'} + r_{1'1} + r_{1'2}}{r_{11'} r_{1'2}} \quad (7.75)$$

Since the metastable state $1'$ is situated above the state 1 by definition, $r_{1'1} \gg r_{11'}$ holds. Therefore, the expression (7.75) can be approximated by

$$\tau_{\text{cap}}^{1'} \approx \frac{r_{1'1}}{r_{11'} r_{1'2}} + \frac{1}{r_{11'}} \quad (7.76)$$

which is characterized by only two regimes (A' and A'') now.

- At negative oxide fields (regime A'), the state $1'$ is located relatively high (see Fig. 7.9) and the transition rate $r_{1'2}$ exceeds $r_{11'}$. Therefore, the first term of expression (7.76) vanishes and the field-insensitive transition $T_{1 \rightarrow 1'}$ with a time constant of $\tau_{\text{c,min}}^{1'}$ dominates $\tau_{\text{cap}}^{1'}$.
- When reducing the oxide field, the state $1'$ is shifted downwards in the configuration coordinate diagram, thereby decreasing the transition rate $r_{1'2}$. At a certain oxide field, $r_{1'2}$ falls below $r_{11'}$ and the first term of the expression (7.76) becomes dominant (regime A''). As a consequence, $\tau_{\text{cap}}^{1'}$ governed by the field-dependent transition $T_{1' \rightarrow 2}$, which causes the exponential term of the expression (7.66). Depending on the value of $\tau_{\text{c,min}}^{1'}$, there exists a crossing point between the curves $\tau_{\text{cap}}^{2'}$ and $\tau_{\text{cap}}^{1'}$, marking the transition between the regime A and B. It is noted that the NMP transitions in the regimes A, B, and C also involve a nearly negligible $1/p$ field dependence, which has already been present in the TSM for instance.

The transition between A' and A'' yields a kink, which is visible in $\tau_{\text{cap}}^{1'}$ of Fig. 7.7 (dotted line) but not in the overall hole capture time given by

$$\frac{1}{\tau_{\text{cap}}} = \frac{1}{\tau_{\text{cap}}^{1'}} + \frac{1}{\tau_{\text{cap}}^{2'}} \quad (7.77)$$

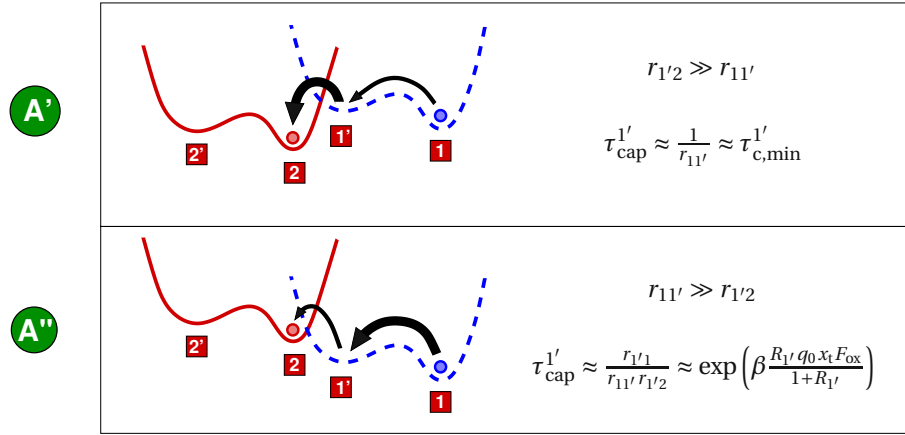
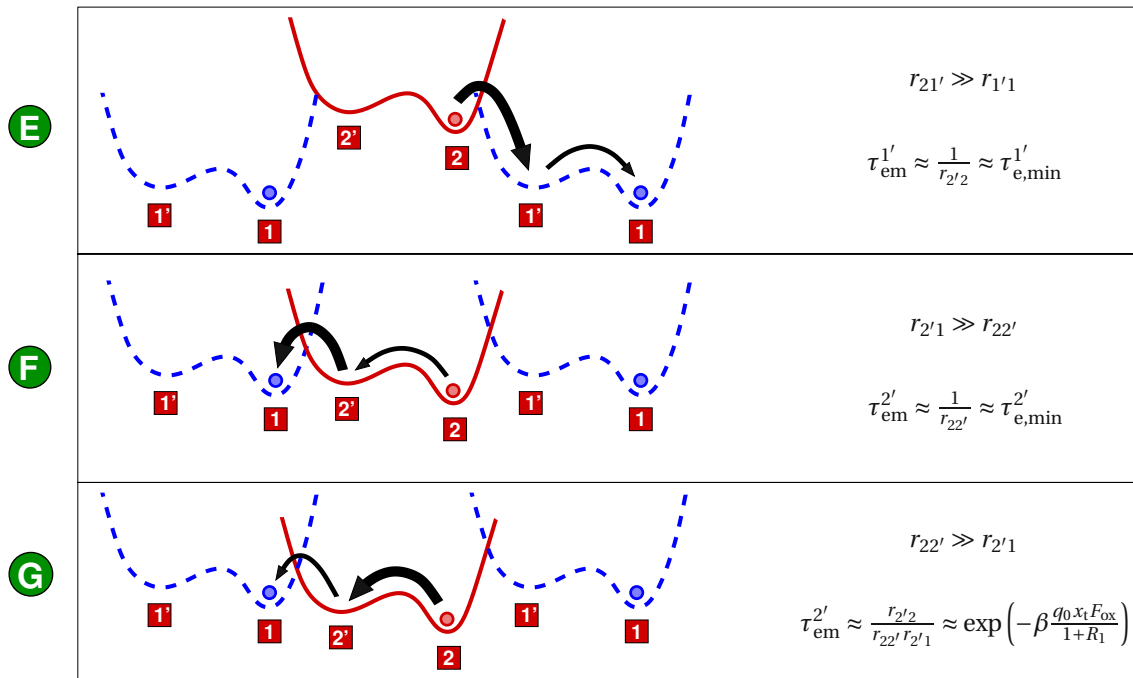
As a result, this transition has not been observed in TDDS experiments, the regimes A' and A'' are not differentiated in Fig. 7.8.

Also the hole emission process has the possibility to proceed over either the state $1'$ or $2'$, with $\tau_{\text{em}}^{1'}$ and $\tau_{\text{em}}^{2'}$ being the corresponding emission time constants (see Fig. 7.10). For the transition pathway over $2'$ the emission time constant can be expressed as:

$$\tau_{\text{em}}^{2'} = \frac{r_{22'} + r_{2'2} + r_{2'1}}{r_{22'} r_{2'1}} \quad (7.78)$$

Since $r_{2'2} \gg r_{22'}$ applies, $\tau_{\text{em}}^{2'}$ has only two regimes, labeled with the capital letters F and G in Fig. 7.7.

$$\tau_{\text{em}}^{2'} \approx \frac{r_{2'2}}{r_{22'} r_{2'1}} + \frac{1}{r_{22'}} \quad (7.79)$$


 FIGURE 7.9: The same as in Fig. 7.8 but for the regimes A' and A'' of the oxide field dependence of $\tau_{\text{cap}}^{1'}$.

 FIGURE 7.10: The same as in Fig. 7.8 but for the regimes E, F and G of the oxide field dependence of τ_{em} .

- At extremely high negative oxide fields (regime G), the state 1 is shifted upwards so that $r_{22'}$ dominates and the field-dependent NMP transition $T_{2' \rightarrow 1}$ determines the pace of $T_{1 \rightarrow 2' \rightarrow 2}$. The sensitivity of $T_{2' \rightarrow 1}$ to the oxide field is reflected in the exponential term of equation (7.67).
- At high negative oxide fields (regime F), the transition $T_{2' \rightarrow 1}$ proceeds much faster than $T_{2 \rightarrow 2'}$ over the purely thermal barrier $\varepsilon_{22'}$. Thus, $\tau_{em}^{2'}$ is determined by the field-insensitive transition $T_{2 \rightarrow 2'}$ with a time constant of $\tau_{e,min}^{2'}$. It is important to note that the field independence of this regime is experimentally observed in the time constant plots of 'normal' defects (cf. Fig. 7.4 left).

At a low oxide field (regime E), the state $1'$ is further shifted down, which speeds up the NMP transition $T_{2 \rightarrow 1'}$ and allows the pathway over the metastable state $1'$. The corresponding emission time constant $\tau_{em}^{1'}$ is given by

$$\tau_{em}^{1'} = \frac{r_{21'} + r_{1'2} + r_{1'1}}{r_{21'} r_{1'1}}. \quad (7.80)$$

For a sufficiently large barrier $\varepsilon_{1'1}$ the rate $r_{1'1}$ is negligible compared to $r_{21'}$ and $r_{1'2}$ and the above equation simplifies to

$$\tau_{em}^{1'} = \frac{1}{r_{1'1}} + \frac{r_{1'2}}{r_{21'} r_{1'1}}. \quad (7.81)$$

In this case, the state diagram reduces to a subsystem which includes the states $1'$ and 2 and is marginally disturbed by the rate $r_{1'1}$. Then the states $1'$ and 2 can be assumed to be in quasi-equilibrium.

$$f_{1'} r_{1'2} = f_2 r_{21'} \quad (7.82)$$

In this subsystem the condition $f_{1'} + f_2 = 1$ holds so that the trap occupancy $f_t' = f_{1'}$ is given by

$$f_{1'} = \frac{1}{1 + \frac{r_{21'}}{r_{1'2}}} \quad (7.83)$$

$$= \frac{1}{1 + \exp(\beta(E_t' - E_f))}. \quad (7.84)$$

In the above equation, it becomes obvious that the condition $r_{1'2} = r_{21'}$ is equivalent to $E_t' = E_f$. Furthermore, this equation can be used to simplify the equation (7.68) as follows:

$$\tau_{em}^{1'} = \tau_{1'} \exp\left(-\beta \frac{q_0 x_t F_{ox}}{1 + R_{1'}}\right) + \frac{\tau_{e,min}^{1'}}{f_t'}. \quad (7.85)$$

If E_t' falls below E_f at a certain relaxation voltage, the state $1'$ becomes occupied and the emission time $\tau_{em}^{1'}$ is determined by the field-independent transition $T_{1' \rightarrow 1}$ with the time constant $\tau_{e,min}^{1'}$. By contrast, if E_t' is raised above E_f , the state $1'$ is underpopulated thereby slowing down the hole emission process. This occupancy effect is reflected in the second term, which reacts sensitive to changes in E_f .

The overall hole emission time τ_{em} follows from

$$\frac{1}{\tau_{\text{em}}} \approx \frac{1}{\tau_{\text{em}}^{1'}} + \frac{1}{\tau_{\text{em}}^{2'}} \quad (7.86)$$

and is depicted in Fig. 7.7. At a certain oxide field, when the state $1'$ is shifted below state 2, $\tau_{\text{em}}^{1'}$ reaches its minimum value and falls below $\tau_{\text{em}}^{2'}$. The resulting drop in τ_{em} is observed as the field dependence characterizing ‘anomalous’ defects at weak oxide fields in TDDS experiments. As pointed out in Fig. 7.4, the drop of τ_{em} occurs when the minimum of the state $1'$ passes that of state 2, and is thus related to the exact shape of the configuration coordinate diagram.

7.5 Explanation for Noise in TDDS Measurements

So far it has been shown that the eNMP model accounts for all features seen in the time constant plots for the ‘normal’ as well as the ‘anomalous’ defects. Beyond that, the model can also give an explanation for tRTN observed in TDDS (see Section 1.3.4). The generated noise stems from defects switching forth and back between states 2 and $1'$. The associated charge transfer reactions $T_{2 \rightarrow 1'}$ do not involve any intermediate states and are therefore simple NMP processes. It is remarked here that the transitions $T_{2 \rightarrow 1'}$ require the energy minima 2 and $1'$ in the configuration coordinate diagram to be on approximately the same level at the relaxation voltage. This is only the case for a group of defects whose energy minima 1 and $1'$ are energetically not far separated. In a TDDS measurement, the investigated devices are stressed at a high V_G so that the defects are forced from the state 1 into the state 2 or $1'$. During this step, the defects undergo the transition $T_{1 \rightarrow 2' \rightarrow 2}$ into the state 2 or even further into $1'$. The other direct pathway $T_{1 \rightarrow 1'}$ into the state $1'$ or 2 is assumed to go over a large barrier $\varepsilon_{11'}$. Therefore, the transition $T_{1 \rightarrow 1'}$ proceeds on much larger timescales compared to $T_{1 \rightarrow 2' \rightarrow 2}$ and can be neglected. After stressing, the recovery traces are monitored at low V_G or F_{ox} , respectively, at which the energy minima of the states 2 and $1'$ coincide and noise is produced. However, the state 1 is thermodynamically preferred due to its energetically lower position compared to the states 2 and $1'$. When the defect returns to its initial state 1, the RTN signal disappears with a time constant of τ_{em}^s . The corresponding transition could be either $T_{2 \rightarrow 2' \rightarrow 1}$ or $T_{1' \rightarrow 1}$ with a time constant of $\tau_{\text{em}}^{2'}$ or $\tau_{\text{em}}^{1'}$, respectively (cf. Fig. 7.11). The termination of the noise signal after a time period of τ_{em}^s is determined by the minimum of these time constants. Consider that the NMP barriers $\varepsilon_{21'}$ and $\varepsilon_{1'2}$ must not be too large since otherwise trapping events will occur too fast and are therefore not detected using a conventional measurement equipment.

Interestingly, there also exists a sort of defects which repeatedly produce noise for a some time (see Section 1.3.4). This kind of noise has been referred to as aRTN and will be discussed for hole traps in the following. Just as in the case of tRTN, the noise signal is generated by charge transfer reactions between the states 2 and $1'$. The recurrent pauses of the noise signal (see Fig. 7.11) originate from transitions into the metastable state $2'$, which is electrically indistinguishable from the state 2. These interruptions correspond to the time during which the defect dwells in this state and no charge transfer reaction can take place. Thereby it has been presumed that the NMP transition $T_{2' \rightarrow 1}$ occurs on larger time scales than the return to the state 2 through the transition $T_{2' \rightarrow 2}$. The slow capture

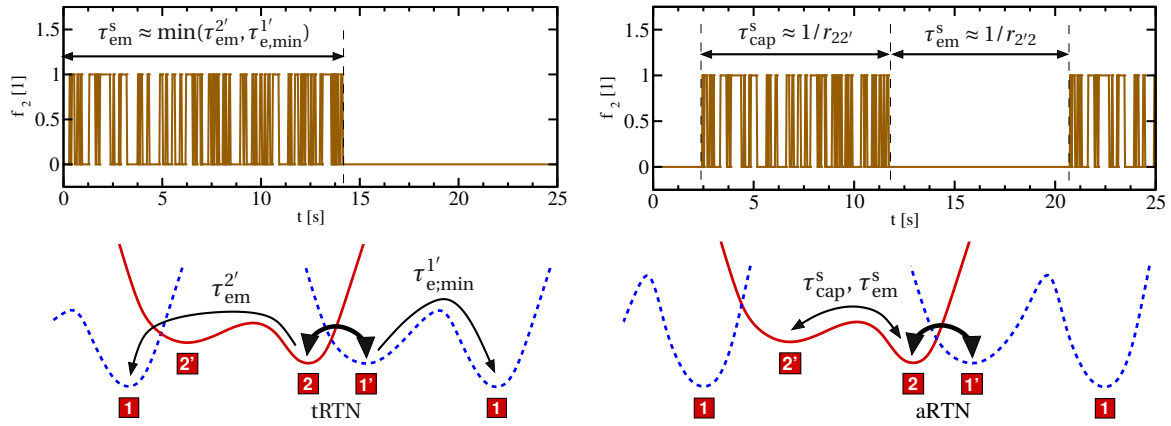


FIGURE 7.11: **Top Left:** The hole occupancy during tRTN. At $t = 0$ the stress voltage has been removed and the defect is in its positive state 2. After a time τ_{em}^s the defect ceases to produce noise. **Bottom Left:** Configuration coordinate diagram for a tRTN defect. The thick arrow indicates the fast switches between the states 2 and 1' related to the occurrence of noise. The possibilities to escape from these states are shown by the thin arrows. **Top Right:** Hole occupancy during aRTN. **Bottom Right:** Configuration coordinate diagram for an aRTN defect. Since this defect is a hole trap, the red solid and the blue dashed line correspond to the positive and neutral charge state, respectively. The double-sided thick arrow is associated with aRTN while the thin one represents the transitions into and out of the metastable state 2'.

time constant τ_{cap}^s in Fig. 7.11 defines the mean time interval during which noise is observed. Its value is given by the inverse of the transition rate $1/r_{22'}$. The slow emission time constant $\tau_{em}^s = 1/r_{2'2}$ corresponds to the mean time interval until the next noise period starts.

One should keep in mind that defects showing an aRTN behavior can also be responsible for tRTN seen in TDDS measurements. During TDDS stress, this sort of defects are forced into one of the states 2 and 1' where they produce an RTN signal. As in aRTN, they undergo a transition to the metastable state 2' thereby stopping to produce a noise signal. However, this special sort of defects is characterized by a slow emission time constant τ_{em}^s , which is much larger than the typical measurement time of TDDS. As a consequence, the next transition back to the state 2 and the subsequent noise period are shifted out of the experimental time window of TDDS and will not be recorded during the measurement run. According to this explanation, tRTN can also be explained as a stimulated variant of aRTN.

In summary, the eNMP can account for the features from the time constant plots and is consistent with the observation of tRTN as well as aRTN. This fact is presented here since it is regarded as an additional support for the validity of this model.

7.6 Discussion

As demonstrated in great detail, the eNMP model successfully reproduces the features of the time constants extracted from TDDS measurements. These experiments reveal the behavior of single

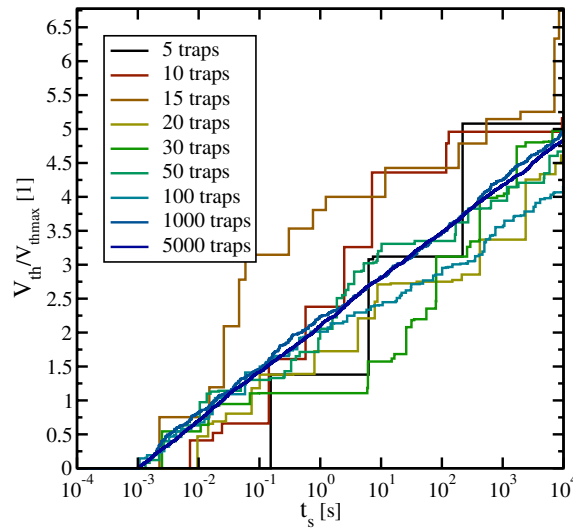


FIGURE 7.12: Normalized degradation curves for a varying number of defects. With an increasing number of traps, the stepped curve becomes smoothed out and approaches the expectation value of $\Delta V_{th}(t)$. The barriers for hole capture are assumed to be homogeneously distributed, resulting in a logarithmic time behavior. The step height due to one hole capture follow approximately an exponential dependence in agreement with [25].

defects by monitoring the response of single defects to different stressing conditions. This has made it possible to identify the underlying physical process involved in charge trapping. Reisinger *et al.* [54] established the link between single defects and NBTI by showing that the NBTI degradation is primarily caused by a large number of individual trapping events. The capture and emission times of these events are characterized by a wide distribution. In the eNMP this can be explained by large variations in the adiabatic potentials of defects, as usual for defects in an amorphous host materials [19, 20]. Fig. 7.12 illustrates how single hole capture events sum up to smooth degradation curves obtained in NBTI measurements. It becomes clear that the increase in the number of traps leads to an averaging of the $\Delta V_{th}(t)$ curves and the steps of single events cannot be resolved anymore. The distribution of hole capture times determines the form of the stress curves while the corresponding emission times yields the recovery curves. Consequently, the field acceleration and temperature activation of the time constants may explain the field and temperature dependences of the NBTI degradation curves. But one should keep in mind that the permanent component of NBTI is not captured by TDDS and thus have not been accounted for in the eNMP model. As a result, a significant contribution to the overall NBTI degradation is not described by the hole capture and emission process.

In the TSM the hole capture is modeled by an MPE process, which relies on a concept similar to the charge transfer reactions in the eNMP model. In both cases, the defect has to overcome an energy barrier resulting from the intersection of two adiabatic potentials in the configuration coordinate diagram. While the height of this barrier is a random variable in the TSM, it is determined from the shape of the adiabatic potentials in the eNMP model. In the latter, the intersection point varies with the relative position of the adiabatic potentials and consequently with the oxide field. Together

| Used Models | TSM | eNMP | |
|---------------------|-------------------------------------|--------------------------------------|--|
| Stress | $T_{1 \rightarrow 2}$ | $T_{1 \rightarrow 2' \rightarrow 2}$ | NMP Transfer Reaction + Intermediate State |
| 'Normal Defects' | \times | $T_{2 \rightarrow 2' \rightarrow 1}$ | |
| 'Anomalous Defects' | $T_{2 \rightarrow 3 \rightarrow 1}$ | $T_{2 \rightarrow 1' \rightarrow 1}$ | Field-Dependent Recovery |

TABLE 7.2: Comparison between the TSM and the eNMP model.

with the intermediate state $2'$, which is involved in the hole capture process, the eNMP model can reproduce the time constants seen in TDDS. By contrast, a field enhancement factor in the TSM had to be phenomenologically introduced in order to capture the field dependence observed in the experimental data. For the aforementioned reasons, the eNMP model is viewed as an improvement in the description of the hole capture process.

Apart from these physical details, the higher-level picture of the hole capture process remains the same for both models. In the precursor configuration (state 1 in both models), the defect features a trap level located far below the substrate valence band. Note that this level is referred to as $E_{t,1}$ in the TSM or E_t in the eNMP model. If $E_{t,1}/E_t$ is shifted upwards by the oxide field, the defect can capture a substrate hole. This is accompanied by a structural relaxation of the defect configuration and leads to a new trap level E'_t located within or at least close to the substrate bandgap.

The TSM as well as the eNMP model can describe defects which show a field dependence in the emission times and the recovery, respectively. This behavior is linked to a hole emission process, which neutralizes the defect via the transition $T_{2 \rightarrow 3}$ in the TSM or $T_{2 \rightarrow 1'}$ in the eNMP. As mentioned before, the corresponding trap level is $E_{t,2}$ in the TSM and E'_t in the eNMP model and lies within or close to the substrate bandgap. As a result, the occupation of $E_{t,2}$ or E'_t is strongly dependent of small variations of the substrate Fermi level, also known as the 'switching trap' behavior of defects. Only from the neutral charge state (the state 3 in the TSM and the state $1'$ in the eNMP model), the defect is allowed to return to its initial state 1 by structural relaxation. In the state diagrams, the last step corresponds to the transition $T_{3 \rightarrow 1}$ in the TSM or $T_{1' \rightarrow 1}$ in the eNMP model. It is important to note here that the hole emission times in both models are eventually controlled by the position of E_t relative to $E_{t,2}$ or E'_t . This effect is reflected in the field dependence of the 'anomalous' defects, on the one hand, and NBTI recovery, on the other hand. Consider that the transition $T_{2 \rightarrow 3}$ in the TSM and $T_{2 \rightarrow 1'}$ in the eNMP model are actually based on a different description of the hole capture and emission process. However, the corresponding transition barriers are assumed to be small in both models. Therefore, $T_{2 \rightarrow 3}$ in the TSM and $T_{2 \rightarrow 1'}$ in the eNMP model occur fast so that the occupancies of the involved states reach their equilibrium values, which are unaffected by the barrier heights. Insofar the different field dependences of both models do not enter the occupancies of the states and thus do not impact the model behavior.

Besides the 'anomalous' defects, the eNMP model also gives an explanation for 'normal' defects. They are characterized by the fact that the alternative pathway from the state 2 back to 1 is taken

over the metastable state $2'$. Thus the hole emission process is determined by the thermal transition $T_{2 \rightarrow 2'}$ resulting in field independent emission times as required for this kind of defects. But note that the TSM has no analog for the 'normal' defect behavior and thus must be viewed as an insufficient description of charge trapping in NBTI and TDDS.

In summary, it has been pointed that the physical picture behind of hole trapping in NBTI is the same for the TSM as well as for the eNMP model. Nevertheless, the eNMP model should be regarded as an improvement for the two reasons: First, it is extended by the metastable state $2'$, which allows for the curvature in τ_{cap} and the field independence of τ_{em} . Second, the NMP formalism is expected to be a better description of the investigated charge transfer reactions than its simplified MPE variant used in the TSM. In contrast to the TSM, the eNMP model has been rigorously derived from one configuration coordinate diagram, which is regarded as the most complete description of a defect with respect to energy.

7.7 Conclusion

In the previous chapter it has been demonstrated that the TSM captures the essential features of NBTI degradation curves but fails to explain the time constant plots obtained by TDDS experiments. This indicates that this model does not correctly reflect the nature of the microscopical trapping process behind NBTI. Therefore, the charge transfer reaction has been refined by using a more accurate description of the NMP process based on the adiabatic potentials of a defect. Furthermore, an additional metastable state has been introduced. With these extensions of the eNMP, it has also been able to reproduce the experimental findings of TDDS. In particular, the eNMP allows to reproduce the time constant plots and explain the 'normal' as well as the 'anomalous' defect behavior depending on the shape of the adiabatic potentials in the configuration coordinate diagram. Besides that, it gives an explanation for the occurrence of tRTN and aRTN, both seen in experiments.

8

Conclusion and Outlook

Due to the downscaling of semiconductor device geometries, modern MOS technologies are becoming increasingly prone to reliability issues, in particular to negative bias temperature instability (NBTI). This parasitic effect seriously limits the lifetime of the devices and has thus aroused considerable scientific interest. The data obtained by time-dependent defect spectroscopy (TDDS) provide experimental evidence that this NBTI issue is not related to a diffusion-controlled problem but rather to a hole trapping process. However, the exact nature of this process has remained vague and thus the charge transfer mechanism involved in hole trapping has shifted into the focus of interest. In this thesis, different kinds of mechanisms were taken into consideration and studied within the framework of rate equations. For each mechanism, the simulated NBTI degradation was compared to the data extracted from the extended measure-stress-measure (eMSM) technique. In these studies, only the short-term part of the NBTI degradation was considered since it is only weakly obscured by the permanent component of NBTI, which is attributed to another degradation mechanism.

The first charge trapping mechanism investigated was elastic tunneling of the charge carriers from the channel into the defects. The elastic tunneling model predicts a logarithmic time behavior, which is also observed for the short-term degradation of NBTI. Nevertheless, this concept has been ruled out for several reasons. First, the elastic tunneling model predicts a negligible temperature dependence, which is inconsistent with the experimental findings of the eMSM technique. Second, its field acceleration is linear instead of quadratic. It is noted that the temperature as well as the field dependence are inherently given by the physical foundations of this model and thus cannot be adjusted by any fitting parameters. Furthermore, modern device technologies have ever smaller oxide thicknesses so that the tunneling to and from the gate enters in the trapping dynamics. This aspect

was paid attention in an extended version of the elastic tunneling model used to study the impact of the gate contact. It was found that elastic tunneling is limited to a time range below 1 s for oxide thicknesses smaller than 4 nm. As a consequence, this concept cannot give an explanation of the wide distribution of time constants seen in NBTI experiments.

Another model attempt starts from the assumption that the defect configuration is closely linked to the position of the trap level. Since defects undergo structural relaxation after each charging event, the trap levels rise or fall within the oxide bandgap. This shift of the trap level was expected to have a strong impact on the trapping dynamics. As a consequence, it was incorporated in a new, rate-based model, which was considered as a possible explanation for hole trapping in NBTI. Using first principles calculations, it was verified that the level shift can be significant. These theoretical studies included the usually suspected defects, such as the oxygen vacancy, the E' centers, the hydrogen bridge, and the hydrogen interstitial, where each of them features a shift of at least one electron Volt. In a second step, the level shift model was investigated for its time dynamics as well as for its field and temperature dependence. Even though it shows a nearly logarithmic time behavior during stress and recovery, it can explain neither the field nor temperature dependence observed in NBTI experiments. As a consequence, this model must also be abandoned as an explanation for NBTI.

The level shift model was extended to account for the activation over thermal barriers. This modified variant, called nonradiative multi-phonon (NMP) theory, was used to describe the charge capture and emission process within bulk materials and has been employed in the two-stage model. This new model achieves a good match with the complicated NBTI stress and relaxation degradation curves for various different gate voltages and temperatures. As such, it fulfills all criteria inferred from the eMSM data and can thus be regarded as a successful model to describe NBTI. In order to test whether the two-stage model properly reflects the behavior of the microscopic processes, it had to be evaluated against the field and temperature dependent hole capture and emission of single defects. For this purpose, the simulated time constants were compared to results of TDDS experiments. The two-stage model was found to yield the correct temperature activation and successfully reproduce the field dependence of the 'normal' as well as the 'anomalous' defects. However, this model cannot explain the curvature in the experimentally obtained capture time constants. In an improved description of the NMP process, the heights of the thermal barriers were not assumed to be statistically distributed as in the two-stage model but derived from atomistic quantities, such as the vibrational frequencies of a defect. Furthermore, a second metastable state was introduced into the two-stage model in order to allow for temperature independent emission times and a curvature in the capture times. This refined model, called extended NMP model, was shown to capture all experimental feature seen in the TDDS data and, as such, gives an improved description of the microscopic charge transfer process. The validity of the extended NMP model was further supported by the fact that it can also give an explanation for anomalous and temporary random telegraph noise. Therefore, this new model is an important step forward in the understanding of NBTI.

In this work a new model has been devised, which captures the essential physics of charge trapping in MOSFETs. It depends on a couple of model parameters, which are directly linked to the physical properties, such as equilibrium configurations, barrier heights, and positions of the trap levels. By comparison to TDDS data, the range of these parameters could already be narrowed down. Given

that information, a very detailed list of requirements on the microscopic defect properties can be compiled. Unfortunately, a corresponding microscopic defect has still not been identified. The most prominent defect candidate has been the oxygen vacancy, which shows the bistability required in the extended NMP model, as already summarized in the Harry-Diamond-Laboratories model. However, recent first-principles simulations have shown that the trap levels of the oxygen vacancy are located far below the substrate valence band edge so that this defect must be ruled out for this model. Therefore, future investigations should be devoted to a systematic search for defects qualified according to the extended NMP model. These investigations should include defect candidates in the various dielectric materials, including silicon dioxide, silicon oxynitride, and high-k dielectrics. Most of these materials are expected to be amorphous so that the defect properties are subject to statistical variations. Furthermore, it has been realized that the defect properties can be seriously affected by the presence of a nearby interface. All these aspects should be accounted for in future investigations on hole trapping. When the question which defects is involved in charge trapping is solved, their occurrence could even be suppressed during processing.



Physical Basics

A.1 Fermi's Golden Rule

Fermi's golden rule provides one way to calculate the transition rate between two certain quantum mechanically defined states. Due to its generality, it has various applications in the field of atomic, nuclear, and solid-state physics. In the case of NBTI, it is of most interest for charge transfer reactions and electron tunneling in particular. In the following, Fermi's golden rule is derived for electron tunneling from the substrate into an oxide defect as illustrated in Fig. A.1. The system is divided into three separate regions, namely the channel, the insulator barrier, and the trap region. The electron wavefunctions $\psi_l(x)$ and $\psi_r(x)$ extend into the classically forbidden barrier region. Their overlap actually leads to a mutual influence between the channel and the trap system. However, this influence is assumed to be negligible so that both systems can be treated independently to first order. This justifies the assumption that in a first approximation the channel and the trap system can be described by their own Hamiltonians $H_{\text{ch}}(x)$ and $H_{\text{tr}}(x)$. For the derivation of the tunneling rate, the Hamiltonian of the common system is taken as a starting point.

$$H(x) = H_{\text{ch}}(x) + H'(x) \quad (\text{A.1})$$

$$H_{\text{ch}}(x) = -\frac{\hbar^2}{2m_e} \Delta + V_{\text{ch}}(x) \quad (\text{A.2})$$

$$H'(x) = V_{\text{tr}}(x) \quad (\text{A.3})$$

$H'(x)$ is viewed as the time-dependent perturbation that triggers the scattering from the band states $\psi_l(x)$ into the trap states $\psi_r(x)$. The solution $\psi(x, t)$ of the common system $H(x)$ can be written as a linear combination of the eigen wavefunctions $\psi_l(x)$ of the unperturbed system $H_{\text{ch}}(x)$.

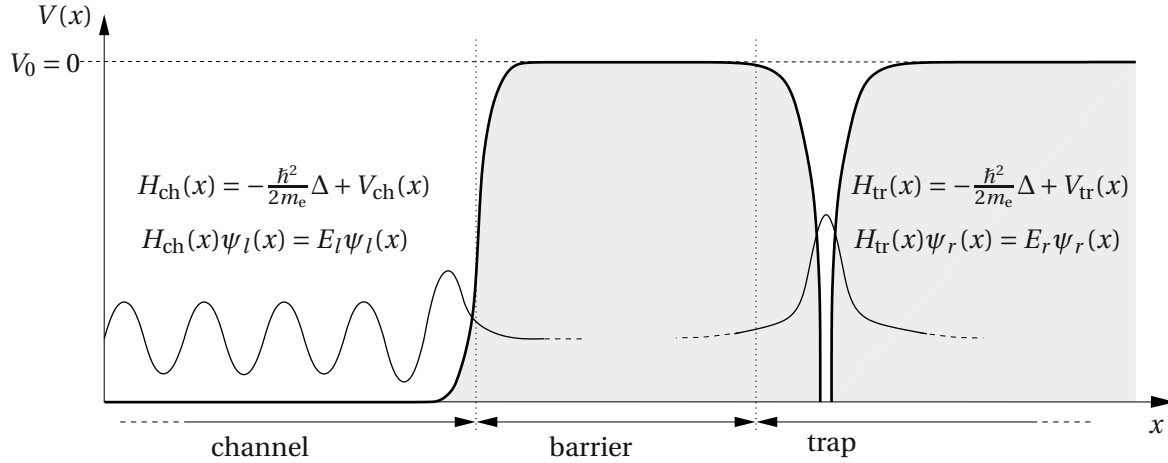


FIGURE A.1: Schematic representation of the channel, the barrier, and the trap region. Interactions between the channel and the trap system are neglected to first order so that both systems are characterized by a separate Hamiltonian $H_{\text{ch}}(x)$ and $H_{\text{tr}}(x)$, respectively. This means that the attractive trap potential $V_{\text{tr}}(x)$ is not accounted for in $V_{\text{ch}}(x)$ so that $V_{\text{ch}}(x) = V_0$ in the trap region. Vice versa, the channel potential $V_{\text{ch}}(x)$ is omitted in $V_{\text{tr}}(x)$, which consequently takes the value V_0 in the channel region.

$$\psi(x, t) = \sum_l a_l(t) \exp\left(-i \frac{E_l}{\hbar} t\right) \psi_l(x) \quad (\text{A.4})$$

This expansion of the wavefunction is inserted into the time-dependent Schrödinger equation

$$H(x) \psi(x, t) = i \hbar \partial_t \psi(x, t) \quad (\text{A.5})$$

and leads to

$$\begin{aligned} (H_{\text{ch}}(x) + V_{\text{tr}}(x)) \sum_l a_l(t) \exp\left(-i \frac{E_l}{\hbar} t\right) \psi_l(x) &= i \hbar \sum_l \left(\partial_t a_l(t) \exp\left(-i \frac{E_l}{\hbar} t\right) \psi_l(x) \right. \\ &\quad \left. + a_l(t) \left(-i \frac{E_l}{\hbar}\right) \exp\left(-i \frac{E_l}{\hbar} t\right) \psi_l(x) \right). \end{aligned} \quad (\text{A.6})$$

Due to $H_{\text{ch}}(x)\psi_l(x) = E_l\psi_l(x)$, the above equation simplifies to

$$V_{\text{tr}}(x) \sum_l a_l(t) \exp\left(-i \frac{E_l}{\hbar} t\right) \psi_l(x) = i \hbar \sum_l (\partial_t a_l(t)) \exp\left(-i \frac{E_l}{\hbar} t\right) \psi_l(x). \quad (\text{A.7})$$

Multiplying both sides by $\psi_r(x)^* \exp(i \frac{E_r}{\hbar} t)$ from the left and integrating over space yields

$$\partial_t a_r(t) = -\frac{i}{\hbar} \exp\left(-i \frac{E_l - E_r}{\hbar} t\right) \int \psi_r^*(x) (H - E_l) \psi_l(x) dx, \quad (\text{A.8})$$

$$= -\frac{i}{\hbar} \exp\left(-i \frac{E_l - E_r}{\hbar} t\right) \int \psi_r^*(x) (H - H_{\text{ch}}) \psi_l(x) dx, \quad (\text{A.9})$$

$$= -\frac{i}{\hbar} \exp\left(-i \frac{E_l - E_r}{\hbar} t\right) \underbrace{\int \psi_r^*(x) V_{\text{tr}}(x) \psi_l(x) dx}_{=M_{lr}}, \quad (\text{A.10})$$

where M_{lr} is referred to as the matrix element. $|a_r(t)|^2$ gives the transition probability $P_{lr}(t)$ that an electron initially located in the state $\psi_l(x)$, evolves into the final states $\psi_r(x)$ after a time t . Therefore, it must be divided by the time t in order to yield the transition rate r_{lr} .

$$r_{lr} = \frac{P_{lr}(t)}{t} = \frac{|a_r(t)|^2}{t} = |M_{lr}|^2 \frac{\left| \frac{1}{\hbar} \int_0^t \exp\left(\frac{i(E_l - E_r)t'}{\hbar}\right) dt' \right|^2}{t} \quad (\text{A.11})$$

The integrand is sharply peaked at $E_l = E_r$ and can be approximated as a δ -function.

$$\left| \frac{1}{\hbar} \int_0^t \exp\left(\frac{i(E_l - E_r)t'}{\hbar}\right) dt' \right|^2 \approx \frac{2\pi t}{\hbar} \delta(E_l - E_r) \quad (\text{A.12})$$

Substituting the integral in rate expression (A.11), one finally obtain ‘Fermi’s golden rule’.

$$r_{lr} = \frac{2\pi}{\hbar} |M_{lr}|^2 \delta(E_l - E_r) \quad (\text{A.13})$$

A.2 Wenzel-Kramers-Brillouin Method

The WKB method [102] is an approximative semiclassical approach to compute the stationary solution of the Schrödinger equation without struggling with the difficulties of a second order differential equation. Taking the time-independent, one-dimensional Schrödinger equation

$$\frac{\hbar^2}{2m_e} \partial_x^2 \psi(x) + (E - V(x)) \psi(x) = 0 \quad (\text{A.14})$$

as a starting point and inserting the ansatz

$$\psi(x) = \exp\left(i \frac{S(x)}{\hbar}\right) \quad (\text{A.15})$$

leads to

$$(\partial_x S(x))^2 = 2m_e (E - V(x)) + i\hbar \partial_x^2 S(x). \quad (\text{A.16})$$

Substituting the action $S(x)$ by its expansion in power series of \hbar/i

$$S(x) = S_0(x) + (i\hbar) S_1(x) + (i\hbar)^2 S_2(x) + \dots, \quad (\text{A.17})$$

one obtains

$$S_0(x) = \exp\left(\pm \frac{i}{\hbar} \int_{x_0}^x p(x') dx'\right), \quad (\text{A.18})$$

$$p(x)^2 \equiv 2m_e (E - V(x)) \quad (\text{A.19})$$

for terms of the order $\sim \hbar^0$ and

$$\partial_x S_1(x) = \frac{1}{2} \frac{\partial_x^2 S_0(x)}{\partial_x S_0(x)} = \frac{1}{2} \frac{\partial_x (p(x)/\hbar)}{(p(x)/\hbar)}. \quad (\text{A.20})$$

for terms of the order $\sim \hbar^1$. Integrating (A.20), one obtains

$$S_1(x) = \frac{1}{2} \ln |p(x)| + c \quad (\text{A.21})$$

which yields

$$\psi(x) = \frac{c}{\sqrt{|p(x)|}} \exp \left(\pm \frac{i}{\hbar} \int_{x_0}^x p(x') dx' \right), \quad (\text{A.22})$$

where the integration spans from x_0 to an arbitrary point x . x_0 is also referred to as the classical turning point, where the particle energy E equals the potential energy $V(x)$. Note that close to this point, the WKB approximation breaks down and the expression for the wavefunction diverges since $p(x)$ in the denominator approaches zero. As a result, the wavefunction left and right to this point cannot be adjusted, which is the case at the discontinuity of the semiconductor-dielectric interface for instance. One way to overcome this problem is to apply Langer's procedure [102], which is not presented here. The above formula also applies to classical forbidden regions where the particle energy E lies below the potential barrier $V(x)$.

A.3 WKB Formulas for Different Shapes of Energy Barriers

In the classical forbidden region, the shape of the wavefunction is dominated by the exponential term in equation (A.22).

$$\tilde{\psi}(x) \approx \exp \left(-\frac{1}{\hbar} \int_{x_1}^{x_2} \sqrt{2m_e(\phi(x) - E)} dx \right) \quad (\text{A.23})$$

$$\approx \exp \left(-\frac{\sqrt{2m_e}}{\hbar} \int_{x_1}^{x_2} \sqrt{\phi(x) - E} dx \right) \quad (\text{A.24})$$

x_1 and x_2 stand for the classical turning point at the semiconductor-dielectric interface and the position of the trap, respectively. Supposing that only a negligible amount of charges is located in the dielectric, the potential energy $\phi(x)$ can be expressed as

$$\phi(x) = \phi_1 + \underbrace{\frac{\phi_2 - \phi_1}{x_2 - x_1}}_{=q_0 F_{ox}} (x - x_1). \quad (\text{A.25})$$

For a trapezoidal barrier (see Fig. A.2), $\tilde{\psi}(x)$ simplifies to

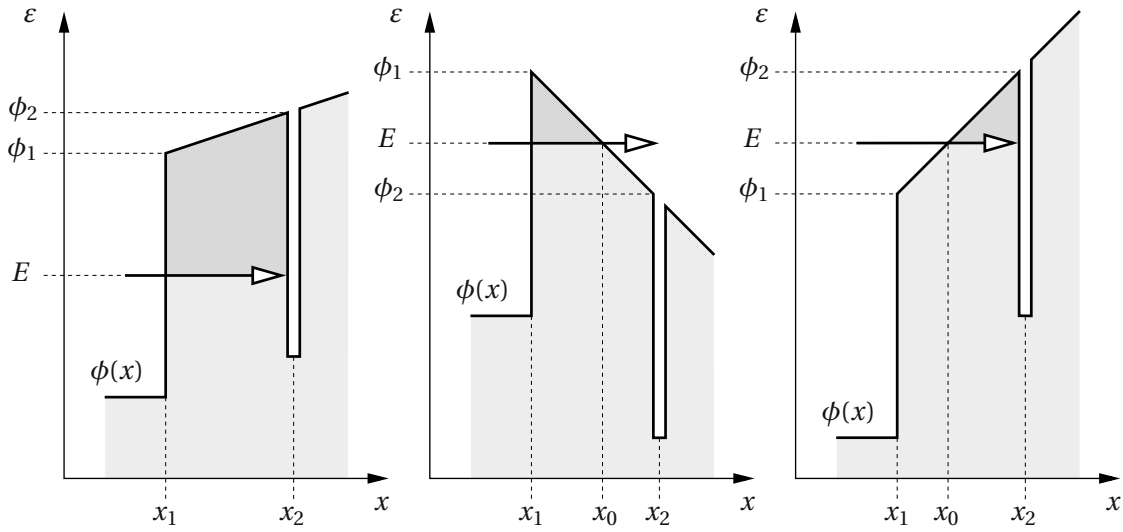


FIGURE A.2: Schematic representation of a trapezoidal (left) and a triangular barrier for a negative (middle) and a positive (right) gate bias. $\phi(x)$ displays the shape of the potential energy and takes the values ϕ_1 and ϕ_2 for the semiconductor-dielectric interface at x_1 and the trap at x_2 . For the case of triangular barriers, the classical forbidden region is decreased to the point x_0 .

$$\tilde{\psi}(x) \approx \exp \left(-\frac{\sqrt{2m_e}}{\hbar} \int_{x_1}^{x_2} \sqrt{\phi_1 + q_0 F_{\text{ox}} (x - x_1) - E} \, dx \right), \quad (\text{A.26})$$

$$\approx \exp \left(-\frac{2\sqrt{2m_e}}{3\hbar q_0 F_{\text{ox}}} (\phi_1 + q_0 F_{\text{ox}} (x - x_1) - E)^{\frac{3}{2}} \Big|_{x_1}^{x_2} \right), \quad (\text{A.27})$$

$$\approx \exp \left(-\frac{2\sqrt{2m_e}}{3\hbar q_0 F_{\text{ox}}} \left((\phi_2 - E)^{\frac{3}{2}} - (\phi_1 - E)^{\frac{3}{2}} \right) \right). \quad (\text{A.28})$$

If tunneling occurs through a triangular barrier (see Fig. A.2), the classically forbidden region extends to

$$x_0 = x_1 + \frac{E - \phi_1}{q_0 F_{\text{ox}}}. \quad (\text{A.29})$$

For negative electric fields ($\phi_2 < E < \phi_1$), one obtains

$$\tilde{\psi}(x) \approx \exp \left(-\frac{1}{\hbar} \int_{x_1}^{x_0} \sqrt{2m_e(\phi(x) - E)} \, dx \right), \quad (\text{A.30})$$

$$\approx \exp \left(-\frac{2\sqrt{2m_e}}{3\hbar q_0 F_{\text{ox}}} (\phi_1 + q_0 F_{\text{ox}} (x - x_1) - E)^{\frac{3}{2}} \Big|_{x_1}^{x_0} \right), \quad (\text{A.31})$$

$$\approx \exp \left(\frac{2\sqrt{2m_e}}{3\hbar q_0 F_{\text{ox}}} (\phi_1 - E)^{\frac{3}{2}} \right). \quad (\text{A.32})$$

while positive electric fields ($\phi_1 < E < \phi_2$) results in

$$\tilde{\psi}(x) \approx \exp \left(-\frac{1}{\hbar} \int_{x_0}^{x_2} \sqrt{2m_e(\phi(x) - E)} dx \right), \quad (\text{A.33})$$

$$\approx \exp \left(-\frac{2\sqrt{2m_e}}{3\hbar q_0 F_{\text{ox}}} (\phi_1 + q_0 F_{\text{ox}} (x - x_1) - E)^{\frac{3}{2}} \Big|_{x_0}^{x_2} \right), \quad (\text{A.34})$$

$$\approx \exp \left(-\frac{2\sqrt{2m_e}}{3\hbar q_0 F_{\text{ox}}} (\phi_2 - E)^{\frac{3}{2}} \right). \quad (\text{A.35})$$

The these two cases are commonly known as the Fowler-Nordheim formulas [186]. For a rectangular barrier with $E < \phi_1 = \phi_2 = \phi$, the integral in equation (A.23) simplifies to a multiplication.

$$\tilde{\psi}(x) \approx \exp \left(-\frac{\sqrt{2m_e(\phi - E)}}{\hbar} (x_2 - x_1) \right) \quad (\text{A.36})$$

A.4 Density of States

When going from small electron systems, such as atoms and molecules, to large electron systems, solids for instance, the number of available electron states reaches high values so that it is best expressed in terms of a density per energy and volume. In solid state theory the assumption of periodic boundary conditions is frequently employed and delivers simple first-order approximation of the density of states (DOS). However, in a few cases, such as tunneling, DOS decomposed in one energy component perpendicular (E_x) and one parallel (E_{yz}) to a certain plain is required. The corresponding derivation will be outlined in the following.

In each direction with periodic boundary conditions, each quantum number n is directly related to one wavevector k :

$$k = \frac{2\pi}{L} n, \quad (\text{A.37})$$

If the length of the periodicity L is increased, the single quantum states narrows in the k space and k becomes an continuous quantity. Then the summation over the single states can be replaced by an integral.

$$\sum_n = \int_{-\infty}^{+\infty} dn = \frac{L}{2\pi} \int_{-\infty}^{+\infty} dk \quad (\text{A.38})$$

Making use of the relation

$$E = \frac{\hbar^2 k^2}{2m_e} \quad (\text{A.39})$$

one obtains the number of states in the x -direction

$$N_x = \sum_{n_x} = 2 \frac{L_x}{2\pi} \int_0^{+\infty} dk_x = L_x \int_0^{+\infty} \underbrace{\frac{1}{\pi\hbar} \sqrt{\frac{m_e}{2E_x}}}_{=D_{1D}(E_x)} dE_x. \quad (\text{A.40})$$

For periodic boundaries in two dimensions, an integral transformation to polar coordinates is carried out in order to obtain the number of states in the yz -plane.

$$N_{yz} = \sum_{n_y, n_z} = \frac{L_y L_z}{(2\pi)^2} \int_0^{+\infty} \int_0^{+\infty} dk_y dk_z = \underbrace{L_y L_z}_{=A_{yz}} \int_0^{+\infty} \underbrace{\frac{m_e}{2\pi\hbar^2}}_{=D_{2D}} dE_{yz} \quad (\text{A.41})$$

with E_{yz} being the energy in the yz -plane. Combining both solutions yields

$$N_{xyz} = \sum_{n_x, n_y, n_z} = L_x A_{yz} \int_0^{+\infty} \int_0^{+\infty} \frac{m_e}{\pi^2 \hbar^3} \sqrt{\frac{m_e}{2E_x}} dE_{yz} dE_x, \quad (\text{A.42})$$

$$= L_x A_{yz} \int_0^{+\infty} \int_0^E \frac{m_e}{2\pi^2 \hbar^3} \sqrt{\frac{m_e}{2E_x}} dE_x dE, \quad (\text{A.43})$$

where an integral transformation from (E_{yz}, E_x) to (E, E_x) with the constraint $E = E_x + E_{yz}$ is performed. The split one/two dimensional DOS is defined as

$$D_{1D+2D}(E_x) = \frac{m_e}{2\pi^2 \hbar^3} \sqrt{\frac{m_e}{2E_x}} \quad (\text{A.44})$$

while the commonly known three dimensional DOS for a free electron gas reads

$$D_{3D}(E) = \int_0^E \frac{m_e}{2\pi^2 \hbar^3} \sqrt{\frac{m_e}{2E_x}} dE_x, \quad (\text{A.45})$$

$$= \frac{m_e}{2\pi^2 \hbar^3} \sqrt{2m_e E}, \quad (\text{A.46})$$

which is usually found in textbooks [129].

For the case that the electrons are confined in the x -direction, the number of states are counted in the following way:

$$N_x = \sum_{n_x} \theta(E_x - E_{n_x}) = \int_0^{+\infty} \sum_{n_x} \delta(E_x - E_{n_x}) dE_x \quad (\text{A.47})$$

Here, E_{n_x} denotes the quasi-bound states with the quantum number n_x . In order to refer N_x to the unit volume, one must introduce the the square of the wavefunction.

$$\sum_{n_x} \theta(E_x - E_{n_x}) = \int_0^{+\infty} \underbrace{\sum_{n_x} \delta(E_x - E_{n_x})}_{=D_{c1D}(E_x)} dE_x \quad (\text{A.48})$$

When $D_{c1D}(E_x)$ is multiplied with D_{2D} and the same integral transformation as for the derivation of $D_{3D}(E)$ is performed, one obtains the DOS for an one-dimensionally confined electronic system:

$$D_{c3D}(E) = \int_0^E D_{2D} \sum_{n_x} \delta(E_x - E_{n_x}) dE_x, \quad (\text{A.49})$$

$$= D_{2D} \sum_{n_x} \Theta(E - E_{n_x}) \quad (\text{A.50})$$

Note that in this derivation the spin degeneracy introducing a factor 2 has been neglected.

Bibliography

- [1] S. Rauch and G. L. Rosa, "CMOS Hot Carrier: From Physics to End Of Life Projections, and Qualification," in *Proc.IRPS*, 2010.
- [2] A. Bravaix and V. Huard, "Hot-Carrier Degradation Issues in Advanced CMOS Nodes," in *Proc.ESREF*, 2010.
- [3] A. Acovic, G. L. Rosa, and Y. Sun, "A Review of Hot Carrier Degradation Mechanisms in MOSFETs," *Microelectron.Eng.*, vol. 36, no. 7/8, pp. 845–869, 1996.
- [4] K. Schuegraf and C.Hu, "Reliability of Thin SiO₂," *Semicond.Sci.Technol.*, vol. 9, no. 5, pp. 989–1004, 1994.
- [5] A.Ghetti, "Gate Oxide Reliability: Physical and Computational Models," in *Predictive Simulation of Semiconductor Processing: Status and Challenges* (J.Dabrowski and E.R.Weber, eds.), pp. 201–258, Springer-Verlag, 2004.
- [6] S. Tan, T. Chen, J. Soon, K. Loh, C. Ang, and L. Chan, "Nitrogen-Enhanced Negative Bias Temperature Instability: An Insight by Experiment and First-Principle Calculations," *Appl.Phys.Lett.*, vol. 82, no. 12, pp. 1881–1883, 2003.
- [7] K. Sakuma, D. Matsushita, K. Muraoka, and Y. Mitani, "Investigation of Nitrogen-Originated NBTI Mechanism in SiON with High-Nitrogen Concentration," in *Proc.IRPS*, pp. 454 – 460, 2006.
- [8] P. Lenahan and J. Conley, "What Can Electron Paramagnetic Resonance Tell Us about the Si/SiO₂ System?," *J.Vac.Sci.Technol.B*, vol. 16, no. 4, pp. 2134–2153, 1998.
- [9] J. P. Campbell, P. M. Lenahan, A. T. Krishnan, and S. Krishnan, "Direct Observation of the Structure of Defect Centers Involved in the Negative Bias Temperature Instability," *Appl.Phys.Lett.*, vol. 87, no. 20, p. 204106, 2005.
- [10] A. Stesmans, "Passivation of P_{b0} and P_{b1} Interface Defects in Thermal (100)Si/SiO₂ with Molecular Hydrogen," *Appl.Phys.Lett.*, vol. 68, no. 15, pp. 2076–2078, 1996.
- [11] A. Stesmans and V. Afanas'ev, "Electrical Activity of Interfacial Paramagnetic Defects in Thermal (100)Si/SiO₂," *Phys.Rev.B*, vol. 57, no. 16, pp. 10030–10034, 1998.
- [12] K. L. Brower, "Passivation of Paramagnetic Si/SiO₂ Interface States with Molecular Hydrogen," *Appl.Phys.Lett.*, vol. 53, no. 6, pp. 508–510, 1988.

- [13] F. Z. J. C. Zhao, A. Chen, G. Groeseneken, and R. Degraeve, "Hole Traps in Silicon Dioxides—Part I: Properties," *IEEE Trans.Elect.Dev.*, vol. 51, no. 8, pp. 1267–1273, 2004.
- [14] D. Fleetwood, "'Border Traps' in MOS Devices," *IEEE Trans.Nucl.Sci.*, vol. 39, no. 2, pp. 269–271, 1992.
- [15] A. Lelis, T. Oldham, H. Boesch, and F. McLean, "The Nature of the Trapped Hole Annealing Process," *IEEE Trans.Nucl.Sci.*, vol. 36, no. 6, pp. 1808–1815, 1989.
- [16] A. Lelis and T. Oldham, "Time Dependence of Switching Oxide Traps," *IEEE Trans.Nucl.Sci.*, vol. 41, no. 6, pp. 1835–1843, 1994.
- [17] P. Lenahan, "Deep Level Defects Involved in MOS Device Instabilities," *Microelectron.Reliab.*, vol. 47, pp. 890–898, 2007.
- [18] J. Campbell and P. Lenahan, "Location, Structure, and Density of States of NBTI-Induced Defects in Plasma Nitrides PMOSFET," in *Proc.IRPS*, pp. 503–510, 2007.
- [19] M. Boero, A. Pasquarello, J. Sarnthein, and R. Car, "Structure and Hyperfine Parameters of E'_1 Centers in α -Quartz and in Vitreous SiO_2 ," *Phys.Rev.Lett.*, vol. 78, no. 5, pp. 887–890, 1997.
- [20] Z.-Y. Lu, C. Nicklaw, D. Fleetwood, R. Schrimpf, and S. Pantelides, "Structure, Properties, and Dynamics of Oxygen Vacancies in Amorphous SiO_2 ," *Phys.Rev.Lett.*, vol. 89, no. 28, p. 285505, 2002.
- [21] V. Huard, M. Denais, and C. Parthasarathy, "NBTI Degradation: From Physical Mechanisms to Modeling," *Microelectron.Reliab.*, vol. 46, no. 1, pp. 1–23, 2006.
- [22] D. Ang, S. Wang, and C. Ling, "Evidence of Two Distinct Degradation Mechanisms from Temperature Dependence of Negative Bias Stressing of the Ultrathin Gate p-MOSFET," *IEEE Elect.Dev.Let.*, vol. 26, no. 12, pp. 906–908, 2005.
- [23] T. Tewksbury, *Relaxation Effects in MOS Devices due to Tunnel Exchange with Near-Interface Oxide Traps*. Ph.D. Thesis, MIT, 1992.
- [24] T. Grassler, B. Kaczer, T. Aichinger, W. Goes, and M. Nelhiebel, "Defect Creation Stimulated by Thermally Activated Hole Trapping as the Driving Force Behind Negative Bias Temperature Instability in SiO_2 , SiON , and High-k Gate Stacks," in *Proc.IIRW*, pp. 91–95, 2008.
- [25] B. Kaczer, V. Arkhipov, R. Degraeve, N. Collaert, G. Groeseneken, and M. Goodwin, "Disorder-Controlled-Kinetics Model for Negative Bias Temperature Instability and its Experimental Verification," in *Proc.IRPS*, pp. 381–387, 2005.
- [26] B. Kaczer, T. Grassler, P. Roussel, J. Martin-Martinez, R. O'Connor, B. O'Sullivan, and G. Groeseneken, "Ubiquitous Relaxation in BTI Stressing-New Evaluation and Insights," in *Proc.IRPS*, pp. 20–27, 2008.

- [27] H. Reisinger, O. Blank, W. Heinrigs, A. Mühlhoff, W. Gustin, and C. Schlünder, "Analysis of NBTI Degradation- and Recovery-Behavior Based on Ultra Fast V_{th} -Measurements," in *Proc.IRPS*, pp. 448–453, 2006.
- [28] C. Shen, M.-F. Li, X. Wang, Y.-C. Yeo, and D.-L. Kwong, "A fast Measurement Technique of MOSFET $I_D - V_G$ Characteristics," *IEEE Elect.Dev.Let.*, vol. 27, no. 1, pp. 55–57, 2006.
- [29] D. Heh, R. Choi, C. Young, B. Lee, and G. Bersuker, "A Novel Bias Temperature Instability Characterization Methodology for High- k nMOSFETs," *IEEE Elect.Dev.Let.*, vol. 27, no. 10, pp. 849–851, 2006.
- [30] H. Reisinger, O. Blank, W. Heinrigs, W. Gustin, and C. Schlünder, "A Comparison of Very Fast to Very Slow Components in Degradation and Recovery Due to NBTI and Bulk Hole Trapping to Existing Physical Models," *IEEE Trans.Dev.Mater.Rel.*, vol. 7, no. 1, pp. 119–129, 2007.
- [31] T. Grasser, W. Goes, V. Sverdlov, and B. Kaczer, "The Universality of NBTI Relaxation and its Implications for Modeling and Characterization," in *Proc.IRPS*, pp. 268–280, 2007.
- [32] A. Krishnan, V. Reddy, S. Chakravarthi, J. Rodriguez, S. John, and S. Krishnan, "NBTI Impact on Transistor and Circuit: Models, Mechanisms, and Scaling Effects," in *Proc.IEDM*, pp. 1–4, 2003.
- [33] C. Schlünder, R.-P. Vollertsen, W. Gustin, and H. Reisinger, "A Reliable and Accurate Approach to Assess NBTI Behavior of State-Of-The-Art pMOSFETs With Fast-WLR," in *Proc.ESSDERC*, pp. 131–134, 2007.
- [34] H. Reisinger, U. Brunner, W. Heinrigs, W. Gustin, and C. Schlünder, "A Comparison of Fast Methods for Measuring NBTI Degradation," *IEEE Trans.Dev.Mater.Rel.*, vol. 7, no. 4, pp. 531–539, 2007.
- [35] A. Islam, E. N. Kumar, H. Das, S. Purawat, V. Maheta, H. Aono, E. Murakami, S. Mahapatra, and M. Alam, "Theory and Practice of On-the-fly and Ultra-fast V_T Measurements for NBTI Degradation: Challenges and Opportunities," in *Proc.IEDM*, pp. 1–4, 2007.
- [36] T. Grasser, P.-J. Wagner, P. Hehenberger, W. Goes, and B. Kaczer, "A Rigorous Study of Measurement Techniques for Negative Bias Temperature Instability," in *Proc.IIRW*, pp. 6–11, 2007.
- [37] T. Grasser, W. Goes, and B. Kaczer, "Dispersive Transport and Negative Bias Temperature Instability: Boundary Conditions, Initial Conditions, and Transport Models," *IEEE Trans.Dev.Mater.Rel.*, vol. 8, no. 1, pp. 79–97, 2008.
- [38] A. Stesmans, "Dissociation Kinetics of Hydrogen-Passivated P_b Defects at the (111)Si/SiO₂ Interface," *Phys.Rev.B*, vol. 61, no. 12, pp. 8393–8403, 2000.
- [39] E. Poindexter and W. Warren, "Paramagnetic Point Defects in Amorphous Thin Films of SiO₂ and Si₃N₄: Updates and Additions," *J.Electrochem.Soc.*, vol. 142, no. 7, pp. 2508–2516, 1995.

- [40] J. Conley and P. Lenahan, "Room Temperature Reactions Involving Silicon Dangling Bond Centers and Molecular Hydrogen in Amorphous SiO₂ Thin Films on Silicon," *IEEE Trans.Nucl.Sci.*, vol. 39, no. 6, pp. 2186–2191, 1992.
- [41] J. Conley and P. Lenahan, "Room Temperature Reactions Involving Silicon Dangling Bond Centers and Molecular Hydrogen in Amorphous SiO₂ Thin Films on Silicon," *Appl.Phys.Lett.*, vol. 62, no. 1, pp. 40–42, 1993.
- [42] J. Conley Jr., P. Lenahan, A. Lelis, and T. Oldham, "Electron Spin Resonance Evidence for the Structure of a Switching Oxide Trap: Long Term Structural Change at Silicon Dangling Bond Sites in SiO₂," *Appl.Phys.Lett.*, vol. 67, no. 15, pp. 2179–2181, 1995.
- [43] P. Lenahan, "Atomic Scale Defects Involved in MOS Reliability Problems," *Microelectron.Eng.*, vol. 69, pp. 173–181, 2003.
- [44] P. Lenahan, "Dominating Defects in the MOS System: P_b and E' Centers," in *Defects in Microelectronic Materials and Devices* (D. Fleetwood, R. Schrimpf, and S. Pantelides, eds.), Taylor and Francis/CRC Press, 2008. (invited).
- [45] E. Poindexter, P. Caplan, B. Deal, and R. Razouk, "Interface States and Electron Spin Resonance Centers in Thermally Oxidized (111) and (100) Silicon Wafers," *J.Appl.Phys.*, vol. 52, no. 2, pp. 879–884, 1981.
- [46] J. Conley and P. Lenahan, "Molecular Hydrogen, E' Center Hole Traps, and Radiation Induced Interface Traps in MOS Devices," *IEEE Trans.Nucl.Sci.*, vol. 40, no. 6, pp. 1335–1340, 1993.
- [47] J. Campbell and P. Lenahan, "NBTI: An Atomic-Scale Defect Persective," in *Proc.IRPS*, pp. 442–447, 2006.
- [48] B. Kaczer, T. Grasser, J. Martin-Martinez, E. Simoen, M. Aoulaiche, P. Roussel, and G. Groeseneken, "NBTI from the Perspective of Defect States with Widely Distributed Time Scales," in *Proc.IRPS*, pp. 55–60, 2009.
- [49] H. Reisinger, T. Grasser, and C. Schl nder, "A Study of NBTI by the Statistical Analysis of the Properties of Individual Defects in pMOSFETs," in *Proc.IIRW*, pp. 30–35, 2009.
- [50] B. Kaczer, T. Grasser, P. Roussel, J. Franco, R. Degraeve, L. Ragnarsson, E. Simoen, G. Groeseneken, and H. Reisinger, "Origin of NBTI Variability in Deeply Scaled PFETs," in *Proc.IRPS*, pp. 1095–1098, 2010.
- [51] T. Grasser, H. Reisinger, P.-J. Wagner, and B. Kaczer, "The Time Dependent Defect Spectroscopy for the Characterization of Border Traps in Metal-Oxide-Semiconductor Transistors," *Phys.Rev.B*, vol. 82, no. 24, p. 245318, 2010.
- [52] P.-J. Wagner, T. Grasser, H. Reisinger, and B. Kaczer, "Oxide Traps in MOS Transistors: Semi-Automatic Extraction of Trap Parameters from Time Dependent Defect Spectroscopy," in *Proc.IPFA*, pp. 249–254, 2010.

- [53] T. Grasser, H. Reisinger, P.-J. Wagner, F. Schanovsky, W. Goes, and B. Kaczer, "The Time Dependent Defect Spectroscopy (TDDS) for the Characterization of the Bias Temperature Instability," in *Proc.IRPS*, pp. 16–25, 2010.
- [54] H. Reisinger, T. Grasser, W. Gustin, and C. Schlünder, "The Statistical Analysis of Individual Defects Constituting NBTI and its Implications for Modeling DC- and AC-Stress," in *Proc.IRPS*, pp. 7–15, 2010.
- [55] N. Zanolta, D. Siprak, P. Baumgartner, E. Sangiorgi, and C. Fiegna, "Measurement and Simulation of Gate Voltage Dependence of RTS Emission and Capture Time Constants in MOSFETs," in *Ultimate Integration of Silicon*, pp. 137–140, 2008.
- [56] M. Kirton and M. Uren, "Noise in Solid-State Microstructures: A New Perspective on Individual Defects, Interface States, and Low-Frequency (1/f) Noise," *Adv.Phys.*, vol. 38, no. 4, pp. 367–486, 1989.
- [57] V. Huard, "Two Independent Components Modeling for Negative Bias Temperature Instability," in *Proc.IRPS*, pp. 33–42, 2-6 2010.
- [58] V. Huard, C. Parthasarathy, N. Rallet, C. Guerin, M. Mammase, D. Barge, and C. Ouvrard, "New Characterization and Modeling Approach for NBTI Degradation from Transistor to Product Level," in *Proc.IEDM*, pp. 797–800, 2007.
- [59] T. Grasser and B. Kaczer, "Negative Bias Temperature Instability: Recoverable versus Permanent Degradation," in *Proc.ESSDERC*, pp. 127–130, 2007.
- [60] T. Grasser, W. Goes, and B. Kaczer, "Towards Engineering Modeling of Negative Bias Temperature Instability," in *Defects in Microelectronic Materials and Devices* (D. Fleetwood, R. Schrimpf, and S. Pantelides, eds.), pp. 1–30, Taylor and Francis/CRC Press, 2008.
- [61] T. Grasser, B. Kaczer, W. Goes, T. Aichinger, P. Hehenberger, and M. Nelhiebel, "A Two-Stage Model for Negative Bias Temperature Instability," in *Proc.IRPS*, pp. 33–44, 2009.
- [62] T. Grasser, B. Kaczer, P. Hehenberger, W. Goes, R. O'Connor, H. Reisinger, W. Gustin, and C. Schlünder, "Simultaneous Extraction of Recoverable and Permanent Components Contributing to Bias-Temperature Instability," in *Proc.IEDM*, pp. 801–804, 2007.
- [63] T. Grasser, B. Kaczer, and W. Goes, "An Energy-Level Perspective of Bias Temperature Instability," in *Proc.IRPS*, pp. 28–38, 2008.
- [64] L.-A. Ragnarsson and P. Lundgren, "Electrical Characterization of P_b Centers in (100)Si/SiO₂ Structures: The Influence of Surface Potential on Passivation During Post Metallization Anneal," *Appl.Phys.Lett.*, vol. 88, no. 2, pp. 938–942, 2000.
- [65] E. Cartier and J. Stathis, "Hot-Electron Induced Passivation of Silicon Dangling Bonds at the Si(111)/SiO₂ Interface," *Appl.Phys.Lett.*, vol. 69, no. 1, pp. 103–105, 1996.
- [66] N. Johnson, D. Biegelsen, M. Moyer, S. Chang, E. Poindexter, and P. Caplan, "Characteristic electronic defects at the Si – SiO₂ interface," *Appl.Phys.Lett.*, vol. 43, no. 6, pp. 563–565, 1983.

- [67] B. Henderson, M. Pepper, and R. Vranich, "Spin-Dependent and Localisation Effects at Si/SiO₂ Device Interface," *Semicond.Sci.Technol.*, vol. 4, pp. 1045–1060, 1989.
- [68] S. Zafar, "Statistical Mechanics Based Model for Negative Bias Temperature Instability Induced Degradation," *J.Appl.Phys.*, vol. 97, no. 10, pp. 1–9, 2005.
- [69] V. Huard, M. Denais, F. Perrier, N. Revil, C. Parthasarathy, A. Bravaix, and E. Vincent, "A Thorough Investigation of MOSFETs NBTI Degradation," *Microelectron.Reliab.*, vol. 45, no. 1, pp. 83–98, 2005.
- [70] T. Yang, C. Shen, M.-F. Li, C. Ang, C. Zhu, Y.-C. Yeo, G. Samudra, S. Rustagi, M. Yu, and D.-L. Kwong, "Fast DNBTI Components in p-MOSFET with SiON Dielectric," *IEEE Elect.Dev.Let.*, vol. 26, no. 11, pp. 826–828, 2005.
- [71] K. Jeppson and C. Svensson, "Negative Bias Stress of MOS Devices at High Electric Fields and Degradation of MNOS Devices," *J.Appl.Phys.*, vol. 48, no. 5, pp. 2004–2014, 1977.
- [72] S. Ogawa and N. Shiono, "Generalized Diffusion-Reaction Model for the Low-Field Charge Build Up Instability at the Si/SiO₂ Interface," *Phys.Rev.B*, vol. 51, no. 7, pp. 4218–4230, 1995.
- [73] M. Houssa, M. Aoulaiche, S. D. Gendt, G. Groeseneken, M. Heyns, and A. Stesmans, "Reaction-Dispersive Proton Transport Model for Negative Bias Temperature Instabilities," *Appl.Phys.Lett.*, vol. 86, no. 9, pp. 1–3, 2005.
- [74] M. Alam, H. Kufluoglu, D. Varghese, and S. Mahapatra, "A Comprehensive Model for pMOS NBTI Degradation: Recent Progress," *Microelectron.Reliab.*, vol. 47, no. 6, pp. 853–862, 2007.
- [75] M. Alam and S. Mahapatra, "A Comprehensive Model of pMOS NBTI Degradation," *Microelectron.Reliab.*, vol. 45, no. 1, pp. 71–81, 2005.
- [76] S. Mahapatra, M. Alam, P. Kumar, T. Dalei, D. Varghese, and D. Saha, "Negative Bias Temperature Instability in CMOS Devices," *Microelectron.Eng.*, vol. 80, no. Suppl., pp. 114–121, 2005.
- [77] A. Krishnan, C. Chancellor, S. Chakravarthi, P. Nicollian, V. Reddy, A. Varghese, R. Khamankar, and S. Krishnan, "Material Dependence of Hydrogen Diffusion: Implications for NBTI Degradation," in *Proc.IEDM*, pp. 688–691, 2005.
- [78] M. Alam and H. Kufluoglu, "On Quasi-Saturation of Negative Bias Temperature Degradation," pp. 139–145, 2005.
- [79] S. Rangan, N. Mielke, and E. Yeh, "Universal Recovery Behavior of Negative Bias Temperature Instability," in *Proc.IEDM*, pp. 341–344, 2003.
- [80] S. Pantelides, S. Rashkeev, R. Buczko, D. Fleetwood, and R. Schrimpf, "Ab Initio Calculations of H⁺ Energetics in SiO₂: Implications for Transport," *IEEE Trans.Nucl.Sci.*, vol. 47, no. 6, pp. 2262–2268, 2000.

- [81] S. N. Rashkeev, D. M. Fleetwood, R. D. Schrimpf, and S. T. Pantelides, "Defect Generation by Hydrogen at the Si – SiO₂ Interface," *Phys.Rev.Lett.*, vol. 87, no. 16, p. 165506, 2001.
- [82] S. Rashkeev, D. Fleetwood, R. Schrimpf, and S. Pantelides, "Proton-Induced Defect Generation at the Si – SiO₂ Interface," *IEEE Trans.Nucl.Sci.*, vol. 48, no. 6, pp. 2086 –2092, 2001.
- [83] L. Tsetseris and S. Pantelides, "Migration, Incorporation, and Passivation Reactions of Molecular Hydrogen at the Si – SiO₂ Interface," *Phys.Rev.B*, vol. 70, no. 24, p. 245320, 2004.
- [84] S. Chakravarthi, A. Krishnan, V. Reddy, C. Machala, and S. Krishnan, "A Comprehensive Framework for Predictive Modeling of Negative Bias Temperature Instability," in *Proc.IRPS*, pp. 273–282, 2004.
- [85] J. Noolandi, "Multiple-Trapping Model of Anomalous Transit-Time Dispersion in *a*-Se," *Phys.Rev.B*, vol. 16, no. 10, pp. 4466–4473, 1977.
- [86] J. Orenstein, M. Kastner, and V. Vaninov, "Transient Photoconductivity and Photo-Induced Optical Absorption in Amorphous Semiconductors.," *Philos.Mag.B*, vol. 46, no. 1, pp. 23–62, 1982.
- [87] V. Arkhipov and A. Rudenko, "Drift and Diffusion in Materials with Traps," *Philos.Mag.B*, vol. 45, no. 2, pp. 189–207, 1982.
- [88] B. Kaczer, V. Arkhipov, R. Degraeve, N. Collaert, G. Groeseneken, and M. Goodwin, "Temperature Dependence of the Negative Bias Temperature Instability in the Framework of Dispersive Transport," *Appl.Phys.Lett.*, vol. 86, no. 5, pp. 1–3, 2005.
- [89] T. Grasser, W. Goes, and B. Kaczer, "Modeling of Dispersive Transport in the Context of Negative Bias Temperature Instability," in *Proc.IIRW*, pp. 5–10, 2006.
- [90] A. Haggag, W. McMahon, K. Hess, K. Cheng, J. Lee, and J. Lyding, "High-Performance Chip Reliability from Short-Time-Tests," in *Proc.IRPS*, pp. 271–279, 2001.
- [91] R. M. Martin, *Electronic Structure — Basic Theory and Practical Methods*. Cambridge University Press, 2004.
- [92] F. Jensen, *Introduction to Computational Chemistry*. John Wiley & Sons, 1999.
- [93] J. Kohanoff, *Electronic Structure Calculations for Solids and Molecules*. Cam, 2006.
- [94] T. Grasser, "Negative Bias Temperature Instability: Modeling Challenges and Perspectives," in *Proc.IRPS*, 2008. (Tutorial).
- [95] T. Grasser, W. Goes, and B. Kaczer, "Modeling Bias Temperature Instability During Stress and Recovery," in *Proc.SISPAD*, pp. 65–68, 2008.
- [96] P. Lenahan, P. Campbell, T. Krishnan, and S. Krishnan, "A Model for NBTI in Nitrided Oxide MOSFETs Which Does Not Involve Hydrogen or Diffusion," *IEEE Trans.Dev.Mater.Rel.*, vol. 99, p. 1, 2010.

- [97] S. Scharf, M. Schmidt, and D. Bränig, "Temperature-Dependent Positive Oxide Charge Annealing by Electron Tunneling," *Semicond.Sci.Technol.*, vol. 10, pp. 586–591, 1995.
- [98] A. Gnädinger and H. Talley, "Quantum Mechanical Calculation of the Carrier Distribution and the Thickness of the Inversion Layer of a MOS Field-Effect Transistor," *Sol.-St.Electr.*, vol. 13, no. 9, pp. 1301–1309, 1970.
- [99] K. H. Gundlach, "Zur Berechnung des Tunnelstroms durch eine trapezförmige Potentialstufe," *Sol.-St.Electr.*, vol. 9, pp. 949–957, 1966.
- [100] A. Messiah, *Quantenmechanik 1*. DeGruyter, 1991.
- [101] S. Gasiorowicz, *Quantum Physics*. John Wiley & Sons, 1995.
- [102] W. Nolting, *Grundkurs Theoretische Physik 5/2: Quantenmechanik - Methoden und Anwendungen*. Springer-Verlag, 2006.
- [103] L. Freeman and W. Dahlke, "Theory of Tunneling into Interface States," *Sol.-St.Electr.*, vol. 13, no. 11, pp. 1483–1503, 1970.
- [104] I. Lundstrom and C. Svensson, "Tunneling to Traps in Insulators," *J.Appl.Phys.*, vol. 43, no. 12, pp. 5045–5047, 1972.
- [105] F. Heiman and G. Warfield, "The Effects of Oxide Traps on the MOS Capacitance," *IEEE Trans.Elect.Dev.*, vol. 12, no. 4, pp. 167–178, 1965.
- [106] S. Christensson, I. Lundström, and C. Svensson, "Low Frequency Noise in MOS Transistors — I Theory," *Sol.-St.Electr.*, vol. 11, pp. 797–812, 1968.
- [107] K. Huang and A. Rhys, "Theory of Light Absorption and Non-Radiative Transitions in F-Centres," *Proceedings of the Royal Society of London. Series A*, vol. 204, pp. 406–423, 1950.
- [108] M. Lax, "The Franck-Condon Principle and Its Application to Crystals," *Journ.Chem.Phys.*, vol. 20, no. 11, pp. 1752–1760, 1952.
- [109] T. Keil, "Shapes of Impurity Absorption Bands in Solids," *Phys.Rev.*, vol. 140, no. 2A, pp. A601–A617, 1965.
- [110] K. Mikkelsen and M. Ratner, "Electron Tunneling in Solid-State Electron-Transfer Reactions," *Chemical Reviews*, vol. 87, no. 1, pp. 113–153, 1987.
- [111] M. Andersson, Z. Xiao, S. Norrman, and O. Engström, "Model based on Trap-Assisted Tunneling for Two-Level Current Fluctuations in Submicrometer Metal-Silicon-Dioxide Diodes," *Phys.Rev.B*, vol. 41, no. 14, pp. 9836–9842, 1990.
- [112] P. Blöchl and J. Stathis, "Hydrogen Electrochemistry and Stress-Induced Leakage Current in Silica," *Phys.Rev.Lett.*, vol. 83, no. 2, pp. 372–375, 1999.
- [113] P. Blöchl and J. Stathis, "Aspects of Defects in Silica Related to Dielectric Breakdown of Gate Oxides in MOSFETs," *Phys.B*, vol. 273-274, pp. 1022–1026, 1999.

- [114] W. Fowler, J. Rudra, M. Zvanut, and F. Feigl, "Hysteresis and Franck-Condon Relaxation in Insulator-Semiconductor Tunneling," *Phys.Rev.B*, vol. 41, no. 12, pp. 8313–8317, 1990.
- [115] C. Henry and D. Lang, "Nonradiative Capture and Recombination by Multiphonon Emission in GaAs and GaP," *Phys.Rev.B*, vol. 15, no. 2, pp. 989–1016, 1977.
- [116] S. Makram-Ebeid and M. Lannoo, "Quantum Model for Phonon-Assisted Tunnel Ionization of Deep Levels in a Semiconductor," *Phys.Rev.B*, vol. 25, no. 10, pp. 6406–6424, 1982.
- [117] S. Ganichev, W. Prettl, and I. Yassievich, "Deep Impurity-Center Ionization by Far-Infrared Radiation," *Phys.Solid State*, vol. 39, no. 1, pp. 1703–1726, 1997.
- [118] S. Ganichev, I. Yassievich, V. Perel, H. Ketterl, and W. Prettl, "Tunneling Ionization of Deep Centers in High-Frequency Electric Fields," *Phys.Rev.B*, vol. 65, p. 085203, 2002.
- [119] A. Avellan, D. Schroeder, and W. Krautschneider, "Modeling Random Telegraph Signals in the Gate Current of Metal-Oxide-Semiconductor Field Effect Transistors after Oxide Breakdown," *J.Appl.Phys.*, vol. 94, no. 1, pp. 703–708, 2003.
- [120] M. Isler and D. Liebig, "Enhanced Multiphonon Capture of Hot Electrons by Deep Centers with Strong Lattice Coupling: A Monte Carlo Study of InP : Fe," *Phys.Rev.B*, vol. 61, no. 11, pp. 7483–7488, 2000.
- [121] R. Siergiej, M. White, and N. Saks, "Theory and Measurement of Quantization Effects on Si – SiO₂ Interface Trap Modeling," *Sol.-St.Electr.*, vol. 35, no. 6, pp. 843–854, 1992.
- [122] N. Lukyanchikova, M. Petrichuk, N. Garbar, E. Simoen, and C. Claeys, "Influence of the Substrate Voltage on the Random Telegraph Signal Parameters in Submicron *n*-Channel Metal-Oxide-Semiconductor Field-Effect Transistors under a Constant Inversion Charge Density," *Appl.Phys.A*, vol. 70, no. 3, pp. 345–353, 2000.
- [123] M. Schulz, "Coulomb Energy of Traps in Semiconductor Space-Charge Regions," *J.Appl.Phys.*, vol. 74, no. 4, pp. 2649–2657, 1993.
- [124] M. Lu and M. Chen, "Oxide-Trap-Enhanced Coulomb Energy in a Metal-Oxide-Semiconductor System," *Phys.Rev.B*, vol. 72, no. 23, pp. 235417–1, 2005.
- [125] A. Palma, A. Godoy, J. A. Jimenez-Tejada, J. E. Carceller, and J. A. Lopez-Villanueva, "Quantum Two-Dimensional Calculation of Time Constants of Random Telegraph Signals in Metal-Oxide-Semiconductor Structures," *Phys.Rev.B*, vol. 56, no. 15, pp. 9565–9574, 1997.
- [126] A. Gehring, *Simulation of Tunneling in Semiconductor Devices*. Ph.d. thesis, Vienna University of Technology, 2003.
- [127] W. Shockley and W. Read, "Statistics of the Recombinations of Holes and Electrons," *Phys.Rev.*, vol. 87, no. 5, pp. 835–842, 1952.

- [128] M. Masuduzzaman, A. Islam, and M. Alam, "Exploring the Capability of Multifrequency Charge Pumping in Resolving Location and Energy Levels of Traps Within Dielectric," *IEEE Elect.Dev.Let.*, vol. 55, no. 12, pp. 3421–3431, 2008.
- [129] S. Datta, *Quantum Transport — Atom to Transistor*. Cambridge University Press, 2005.
- [130] M. Karner, A. Gehring, S. Holzer, M. Pourfath, M. Wagner, W. Goes, M. Vasicek, O. Baumgartner, C. Kernstock, K. Schnass, G. Zeiler, T. Grasser, H. Kosina, and S. Selberherr, "A Multi-Purpose Schrödinger-Poisson Solver for TCAD Applications," *Journ. of Computational Electronics*, vol. 6, pp. 179–182, 2007.
- [131] O. Ibe, *Markov Processes for Stochastic Modeling*. Academic Press, 2009.
- [132] A. Asenov, "Random Dopant-Induced Threshold Voltage Lowering and Fluctuations in Sub-0.1 μm MOSFET's: A 3-D "Atomistic" Simulation Study," *IEEE Trans.Elect.Dev.*, vol. 45, no. 12, pp. 2505–2513, 1998.
- [133] N. Sano, K. Matsuzawa, M. Mukai, and N. Nakayama, "On Discrete Random Dopant Modeling in Drift-Diffusion Simulations: Physical Meaning of "Atomistic" Dopants," *Microelectron.Reliab.*, vol. 42, no. 2, pp. 189–199, 2002.
- [134] A. Asenov, G. Slavcheva, A. Brown, J. Davies, and S. Saini, "Increase in the Random Dopant-Induced Threshold Fluctuations and Lowering in Sub-100 nm MOSFETs due to Quantum Effects: a 3-D Density-Gradient Simulation Study," *IEEE Trans.Elect.Dev.*, vol. 48, no. 4, pp. 722–729, 2001.
- [135] D. Gillespie, *Markov Processes: An Introduction for Physical Scientists*. Academic Press, 1992.
- [136] W. Kohn, "Nobel Lecture: Electronic Structure of Matter — Wave Functions and Density Functionals," *Rev.Mod.Phys.*, vol. 71, no. 5, pp. 1253–1266, 1999.
- [137] P. Hohenberg and W. Kohn, "Inhomogeneous Electron Gas," *Phys.Rev.*, vol. 136, no. 3B, pp. B864–B871, 1964.
- [138] G. Kresse and J. Hafner, "Ab Initio Molecular Dynamics for Liquid Metals," *Phys.Rev.B*, vol. 47, no. 1, pp. 558–561, 1993.
- [139] G. Kresse and J. Hafner, "Ab Initio Molecular-Dynamics Simulation of the Liquid-Metal-Amorphous-Semiconductor Transition in Germanium," *Phys.Rev.B*, vol. 49, no. 20, pp. 14251–14269, 1994.
- [140] G. Kresse and J. Furthmüller, "Efficiency of Ab-Initio Total Energy Calculations for Metals and Semiconductors using a Plane-Wave Basis Set," *Comput.Mat.Science*, vol. 6, no. 1, pp. 15–50, 1996.
- [141] G. Kresse and J. Furthmüller, "Efficient Iterative Schemes for Ab Initio Total-Energy Calculations using a Plane-Wave Basis Set," *Phys.Rev.B*, vol. 54, no. 16, pp. 11169–11186, 1996.

- [142] A. Alkauskas, P. Broqvist, and A. Pasquarello, “Charge State of the O₂ Molecule during Silicon Oxidation through Hybrid Functional Calculations,” *Phys.Rev.B*, vol. 78, no. 16, p. 161305, 2008.
- [143] P. Broqvist, A. Alkauskas, and A. Pasquarello, “Band Alignments and Defect Levels in Si – HfO₂ Gate Stacks: Oxygen Vacancy and Fermi-Level Pinning,” *Appl.Phys.Lett.*, vol. 92, no. 13, p. 132911, 2008.
- [144] J. Perdew, K. Burke, and M. Ernzerhof, “Generalized Gradient Approximation Made Simple,” *Phys.Rev.Lett.*, vol. 77, no. 18, pp. 3865–3868, 1996.
- [145] P. Blöchl, “Projector Augmented-Wave Method,” *Phys.Rev.B*, vol. 50, no. 24, pp. 17953–17979, 1994.
- [146] G. Kresse and D. Joubert, “From Ultrasoft Pseudopotentials to the Projector Augmented-Wave Method,” *Phys.Rev.B*, vol. 59, no. 3, pp. 1758–1775, 1999.
- [147] C. V. de Walle and J. Neugebauer, “First-Principles Calculations for Defects and Impurities: Applications to III-Nitrides,” *J.Appl.Phys.*, vol. 95, no. 8, pp. 3851–3879, 2004.
- [148] G. Lopez and V. Fiorentini, “Structure, Energetics, and Extrinsic Levels of Small Self-Interstitial Clusters in Silicon,” *Phys.Rev.B*, vol. 69, no. 15, p. 155206, 2004.
- [149] P. Blöchl, “First-Principles Calculations of Defects in Oxygen-Deficient Silica Exposed to Hydrogen,” *Phys.Rev.B*, vol. 62, no. 10, pp. 6158–6179, 2000.
- [150] J. Janak, “Proof that $\partial E/\partial n_i = \epsilon_i$ in Density-Functional Theory,” *Phys.Rev.B*, vol. 18, no. 12, pp. 7165–7168, 1978.
- [151] P. Vashishta, R. Kalia, J. Rino, and I. Ebbsjö, “Interaction Potential for SiO₂: A Molecular-Dynamics Study of Structural Correlations,” *Phys.Rev.B*, vol. 41, no. 17, pp. 12197–12209, 1990.
- [152] J. Rino, I. Ebbsjö, R. Kalia, A. Nakano, and P. Vashishta, “Structure of Rings in Vitreous SiO₂,” *Phys.Rev.B*, vol. 47, no. 6, pp. 3053–3062, 1993.
- [153] J. Sarnthein, A. Pasquarello, and R. Car, “Model of Vitreous SiO₂ Generated by an Ab Initio Molecular-Dynamics Quench from the Melt,” *Phys.Rev.B*, vol. 52, no. 17, pp. 12690–12695, 1995.
- [154] J. Sarnthein, A. Pasquarello, and R. Car, “Structural and Electronic Properties of Liquid and Amorphous SiO₂: An Ab Initio Molecular Dynamics Study,” *Phys.Rev.Lett.*, vol. 74, no. 23, pp. 4682–4685, 1995.
- [155] R. Van Ginhoven, H. Jónsson, and L. Corrales, “Silica Glass Structure Generation for Ab Initio Calculations using Small Samples of Amorphous Silica,” *Phys.Rev.B*, vol. 71, no. 2, p. 024208, 2005.
- [156] L. Giacomazzi, P. Umari, and A. Pasquarello, “Medium-Range Structure of Vitreous SiO₂ Obtained through First-Principles Investigation of Vibrational Spectra,” *Phys.Rev.B*, vol. 79, no. 6, p. 064202, 2009.

- [157] D. Frenkel and B. Smit, *Understanding Molecular Simulation: From Algorithms to Applications*. Academic Press, 1996.
- [158] B. van Beest, G. Kramer, and R. van Santen, "Force Fields for Silicas and Aluminophosphates Based on Ab Initio Calculations," *Phys.Rev.Lett.*, vol. 64, no. 16, pp. 1955–1958, 1990.
- [159] K. Vollmayr, W. Kob, and K. Binder, "Cooling-Rate Effects in Amorphous Silica: A Computer-Simulation Study," *Phys.Rev.B*, vol. 54, no. 22, pp. 15808–15827, 1996.
- [160] V. Huard, C. Parthasarathy, C. Guerin, and M. Denais, "Physical Modeling of Negative Bias Temperature Instabilities for Predictive Extrapolation," in *Proc.IRPS*, pp. 733–734, 2006.
- [161] D. Fleetwood, H. Xiong, Z.-Y. Lu, C. Nicklaw, J. Felix, R. Schrimpf, and S. Pantelides, "Unified Model of Hole Trapping, $1/f$ Noise, and Thermally Stimulated Current in MOS Devices," *IEEE Trans.Nucl.Sci.*, vol. 49, no. 6, pp. 2674–2683, 2002.
- [162] C. Nicklaw, D. Fleetwood, R. Schrimpf, and S. Pantelides, "The Structure, Properties, and Dynamics of Oxygen Vacancies in Amorphous SiO_2 ," *IEEE Trans.Nucl.Sci.*, vol. 49, no. 6, pp. 2667–2673, 2002.
- [163] C. Nicklaw, *Multi-Level Modeling of Total Ionizing Dose in α - SiO_2 : First-Principles to Circuits*. PhD thesis, Vanderbilt University, 2003.
- [164] J. Godet and A. Pasquarello, "Ab Initio Study of Charged States of H in Amorphous SiO_2 ," *Microelectron.Eng.*, vol. 80, pp. 288–291, 2005.
- [165] A. Alkauskas and A. Pasquarello, "Alignment of Hydrogen-Related Defect Levels at the Si – SiO_2 Interface," *Phys.B Condens.Matter*, vol. 401–402, p. 546–549, 2007.
- [166] H. Baik, M.K., G.-S. Park, S. Song, M.Varela, A. Franceschetti, S. Pantelides, and S. Pennycook, "Interface Structure and Non-Stoichiometry in HfO_2 Dielectrics," *Appl.Phys.Lett.*, vol. 85, no. 4, pp. 672–674, 2004.
- [167] A. Bongiorno and A. Pasquarello, "Oxygen Diffusion through the Disordered Oxide Network during Silicon Oxidation," *Phys.Rev.Lett.*, vol. 88, no. 12, p. 125901, 2002.
- [168] A. Bongiorno and A. Pasquarello, "Multiscale Modeling of Oxygen Diffusion through the Oxide during Silicon Oxidation," *Phys.Rev.B*, vol. 70, no. 19, p. 195312, 2004.
- [169] T. Yamasaki, C. Kaneta, T. Uchiyama, T. Uda, and K. Terakura, "Geometric and Electronic Structures of $\text{SiO}_2/\text{Si}(001)$ Interfaces," *Phys.Rev.B*, vol. 63, no. 11, p. 115314, 2001.
- [170] F. Giustino, A. Bongiorno, and A. Pasquarello, "Atomistic Models of the $\text{Si}(100)$ – SiO_2 Interface: Structural, Electronic and Dielectric Properties," *J.Phys.-Condens.Matter*, vol. 17, pp. S2065–S2074, 2005.
- [171] P. Denteneer, C. V. de Walle, and S. Pandelides, "Microscopic Structure of the Hydrogen-Boron Complex in Crystalline Silicon," *Phys.Rev.B*, vol. 39, no. 1, pp. 10809–10825, 1989.

- [172] S. Mukhopadhyay, P. Sushko, A. Stoneham, and A. Shluger, "Modeling of the Structure and Properties of Oxygen Vacancies in Amorphous Silica," *Phys.Rev.B*, vol. 70, no. 19, p. 195203, 2004.
- [173] L. Martin-Samos, Y. Limoge, J.-P. Crocombette, and G. Roma, "Neutral Self-Defects in a Silica Model: A First-Principles Study," *Phys.Rev.B*, vol. 71, no. 1, p. 014116, 2005.
- [174] T. Demuth, Y. Jeanvoine, J. Hafner, and J. Ángyán, "Polymorphism in Silica Studied in the Local Density and Generalized-Gradient Approximations," *J.Phys.-Condens.Matter*, vol. 11, p. 3833–3874, 1999.
- [175] A. Yokozawa and Y. Miyamoto, "First-Principles Calculations for Charged States of Hydrogen Atoms in SiO₂," *Phys.Rev.B*, vol. 55, no. 20, pp. 13783–13788, 1997.
- [176] P. Bunson, M. D. Ventra, S. Pantelides, R. Schrimpf, and K. Galloway, "Ab Initio Calculations of H⁺ Energetics in SiO₂: Implications for Transport," *IEEE Trans.Nucl.Sci.*, vol. 46, no. 6, pp. 1568–1573, 1999.
- [177] V. Afanas'ev, J. de Nijs, P. Balk, and A. Stesmans, "Degradation of the Thermal Oxide of the Si/SiO₂/Al System due to Vacuum Ultraviolet Irradiation," *J.Appl.Phys.*, vol. 78, no. 11, pp. 6481–6490, 1995.
- [178] R. Van Ginhoven, H. Hjalmarson, A. Edwards, and B. Tuttle, "Hydrogen Release in Si/SiO₂: Source Sites and Release Mechanisms," *Nucl.Instr.&Meth.Phys.Res.Sect.B*, vol. 250, no. 1-2, pp. 274–278, 2006.
- [179] P. Bunson, M. D. Ventra, S. Pantelides, D. Fleetwood, and R. Schrimpf, "Hydrogen-Related Defects in Irradiated SiO₂," *IEEE Trans.Nucl.Sci.*, vol. 47, no. 6, pp. 2289–2296, 2000.
- [180] C. V. de Walle, P. Denteneer, Y. Bar-Yam, and S. Pandelides, "Theory of Hydrogen Diffusion and Reactions in Crystalline Silicon," *Phys.Rev.B*, vol. 39, no. 15, pp. 10791–10808, 1989.
- [181] C. V. de Walle and R. Street, "Structure, Energetics, and Dissociation of Si-H Bonds at Dangling Bonds in Silicon," *Phys.Rev.B*, vol. 49, no. 20, pp. 14766–14769, 1994.
- [182] A. McWhorter, "1/f Noise and Germanium Surface Properties," in *Sem.Surf.Phys*, RH Kingston (Univ Penn Press), 1957.
- [183] *MiniMOS-NT Device and Circuit Simulator*, Institute for Microelectronic, TU Wien.
- [184] T. Grasser, H. Reisinger, W. Goes, T. Aichinger, P. Hehenberger, P. Wagner, M. Nelhiebel, J. Franco, and B. Kaczer, "Switching Oxide Traps as the Missing Link between Negative Bias Temperature Instability and Random Telegraph Noise," in *Proc.IEDM*, 2009.
- [185] Conley and Lenahan, "Electron Spin Resonance Evidence that E'_γ Centers Can Behave as Switching Traps," *IEEE Trans.Nucl.Sci.*, vol. 42, no. 6, pp. 1744–1749, 1995.
- [186] R. H. Fowler and L. Nordheim, "Electron Emission in Intense Electric Fields," in *Proc. R. Soc. Lond. A*, vol. 119, pp. 173–181, 1928.

Own Publications

- [1] W. Goes, F. Schanovsky, H. Reisinger, B. Kaczer, and T. Grassner, "Bistable Defects as the Cause for NBTI and RTN," *Solid State Phenomena*, vol. 178-179, pp. 473–482, 2011.
- [2] W. Goes, F. Schanovsky, H. Reisinger, B. Kaczer, and T. Grassner, "Bistable Defects as the Cause for NBTI and RTN," in *Gettering and Defect Engineering in Semiconductor Technology (GADEST) 2011: Abstract Booklet*, p. 153, 2011.
- [3] T. Grassner, B. Kaczer, W. Goes, H. Reisinger, T. Aichinger, P. Hehenberger, P.-J. Wagner, F. Schanovsky, J. Franco, M. Toledano-Luque, and M. Nelhiebel, "The Paradigm Shift in Understanding the Bias Temperature Instability: From Reaction-Diffusion to Switching Oxide Traps," *IEEE Transactions on Electron Devices*, 2011, (invited).
- [4] P. Hehenberger, W. Goes, O. Baumgartner, J. Franco, B. Kaczer, and T. Grassner, "Quantum-Mechanical Modeling of NBTI in High-k SiGe MOSFETs," in *Proceedings of the 15th International Conference on Simulation of Semiconductor Processes and Devices (SISPAD)*, pp. 11–14, 2011. Talk: SISPAD, Osaka, Japan; 2011-09-08 – 2011-09-10.
- [5] W. Goes, F. Schanovsky, T. Grassner, H. Reisinger, and B. Kaczer, "Advanced Modeling of Oxide Defects for Random Telegraph Noise," in *Proceedings of the 21st International Conference on Noise and Fluctuations (ICNF)*, 2011. Talk: ICNF, Toronto, Canada; 2011-06-12 – 2011-06-16.
- [6] F. Schanovsky, W. Goes, and T. Grassner, "Multiphonon Hole Trapping from First Principles," *Journal of Vacuum Science & Technology B*, vol. 29, no. 1, pp. 01A201–1–01A201–5, 2011.
- [7] T. Grassner, B. Kaczer, W. Goes, H. Reisinger, T. Aichinger, P. Hehenberger, P.-J. Wagner, F. Schanovsky, J. Franco, P. J. Roussel, and M. Nelhiebel, "Recent Advances in Understanding the Bias Temperature Instability," in *Proceedings of the 2010 IEEE International Electron Devices Meeting (IEDM)*, pp. 82–85, 2010. Talk: IEDM, San Francisco (invited); 2010-12-06 – 2010-12-08.
- [8] F. Schanovsky, W. Goes, and T. Grassner, "Ab-Initio Calculation of the Vibrational Influence on Hole-Trapping," in *Proceedings of the 14th International Workshop on Computational Electronics (IWCE)*, pp. 163–166, 2010. Talk: IWCE, Pisa; 2010-10-26 – 2010-10-29.
- [9] T. Grassner, H. Reisinger, P.-J. Wagner, W. Goes, F. Schanovsky, and B. Kaczer, "The Time Dependent Defect Spectroscopy (TDDS) for the Characterization of the Bias Temperature Instability." Talk: European Symposium on Reliability of Electron Devices, Failure Physics and Analysis (ESREF), Gaeta (invited); 2010-10-11, 2010.

- [10] W. Goes, F. Schanovsky, P. Hehenberger, P.-J. Wagner, and T. Grasser, "Charge Trapping and the Negative Bias Temperature Instability," in *Meet. Abstr. - Electrochem. Soc. 2010*, 2010. Talk: 218th ECS Meeting, Las Vegas, USA; 2010-10-10 – 2010-10-15.
- [11] W. Goes, F. Schanovsky, P. Hehenberger, P.-J. Wagner, and T. Grasser, "Charge Trapping and the Negative Bias Temperature Instability," in *Physics and Technology of High-k Materials 8*, pp. 565–589, ECS Transactions, 2010, (invited).
- [12] F. Schanovsky, W. Goes, and T. Grasser, "An Advanced Description of Oxide Traps in MOS Transistors and its Relation to DFT," *Journal of Computational Electronics*, vol. 9, no. 3-4, pp. 135–140, 2010, (invited).
- [13] F. Schanovsky, W. Goes, and T. Grasser, "Hole Capture into Oxide Defects in MOS Structures from First Principles," in *Abstract Book*, p. 435, 2010. Poster: Ψ_k - 2010 Conference, Berlin; 2010-09-12 – 2010-09-16.
- [14] F. Schanovsky, W. Goes, and T. Grasser, "Mult-Phonon Hole-Trapping from First-Principles," in *Book of Abstracts*, p. 54, 2010. Talk: Workshop on Dielectrics in Microelectronics (WODIM), Bratislava; 2010-06-28 – 2010-06-30.
- [15] T. Grasser, H. Reisinger, P. Wagner, B. Kaczer, F. Schanovsky, and W. Goes, "The Time Dependent Defect Spectroscopy (TDDS) for the Characterization of the Bias Temperature Instability," in *Proceedings of the International Reliability Physics Symposium (IRPS)*, pp. 16–25, 2010. Talk: IRPS, Anaheim; 2010-05-02 – 2010-05-06.
- [16] T. Grasser, B. Kaczer, W. Goes, T. Aichinger, P. Hehenberger, and M. Nelhiebel, "Understanding Negative Bias Temperature Instability in the Context of Hole Trapping," *Microelectronic Engineering*, vol. 86, no. 7-9, pp. 1876–1882, 2009, (invited).
- [17] T. Grasser, H. Reisinger, W. Goes, T. Aichinger, P. Hehenberger, P.-J. Wagner, M. Nelhiebel, J. Franco, and B. Kaczer, "Switching Oxide Traps as the Missing Link Between Negative Bias Temperature Instability and Random Telegraph Noise," in *Proceedings of the International Electron Devices Meeting (IEDM)*, 2009. Talk: IEDM, Baltimore; 2009-12-07 – 2009-12-09.
- [18] T. Grasser, W. Goes, and B. Kaczer, "Critical Modeling Issues in Negative Bias Temperature Instability," in *215th ECS Meeting* (R. Ekwil Sah, J. Zhang, J. Deen, J. Yota, and A. Toriumi, eds.), pp. 265–287, ECS Transactions, 2009, (invited).
- [19] B. Bindu, W. Goes, B. Kaczer, and T. Grasser, "Analytical Solution of the Switching Trap Model for Negative Bias Temperature Stress," in *2009 IEEE International Integrated Reliability Workshop Final Report (IIRW)*, pp. 93–96, 2009. Talk: IIRW, S. Lake Tahoe; 2009-10-18 – 2009-10-22.
- [20] W. Goes, T. Grasser, M. Karner, and B. Kaczer, "A Model for Switching Traps in Amorphous Oxides," in *Proceedings of the International Conference on Simulation of Semiconductor Processes and Devices (SISPAD)*, pp. 159–162, 2009. Talk: SISPAD, San Diego; 2009-09-09 – 2009-09-11.

- [21] S. Tyaginov, V. Sverdlov, W. Goes, and T. Grasser, "Impact of O-Si-O Bond Angle Fluctuations on the Si-O Bond-Breakage Rate," in *Proceedings of the 20th European Symposium on the Reliability of Electron Devices, Failure Physics and Analysis (ESREF)*, 2009. Talk: ESREF, Bordeaux; 2009-10-05 – 2009-10-09.
- [22] S. Tyaginov, V. Sverdlov, W. Goes, and T. Grasser, "Statistics of Si-O Bond-Breakage Rate Variations Induced by O-Si-O Angle Fluctuations," in *13th International Workshop on Computational Electronics (IWCE)*, pp. 29–32, 2009. Talk: IWCE, Beijing; 2009-05-27 – 2009-05-29.
- [23] T. Grasser, B. Kaczer, W. Goes, T. Aichinger, P. Hehenberger, and M. Nelhiebel, "A Two-Stage Model for Negative Bias Temperature Instability," in *2009 IEEE International Reliability Physics Symposium Proceedings (IRPS)*, pp. 33–44, 2009. Talk: IRPS, Montreal; 2009-04-26 – 2009-04-30.
- [24] S. Tyaginov, W. Goes, T. Grasser, V. Sverdlov, P. Schwaha, R. Heinzl, and F. Stimpfl, "Description of Si-O Bond Breakage Using Pair-Wise Interatomic Potentials Under Consideration of the Whole Crystal," in *2009 IEEE International Reliability Physics Symposium Proceedings (IRPS)*, pp. 514–522, 2009. Talk: IRPS, Montreal; 2009-04-26 – 2009-04-30.
- [25] P. Hehenberger, T. Aichinger, T. Grasser, W. Goes, O. Triebel, B. Kaczer, and M. Nelhiebel, "Do NBTI-Induced Interface States Show Fast Recovery? A Study Using a Corrected On-The-Fly Charge-Pumping Measurement Technique," in *2009 IEEE International Reliability Physics Symposium Proceedings (IRPS)*, pp. 1033–1038, 2009. Poster: IRPS, Montreal; 2009-04-26 – 2009-04-30.
- [26] S. Tyaginov, V. Sverdlov, W. Goes, P. Schwaha, R. Heinzl, F. Stimpfl, and T. Grasser, "Impact of the Surrounding Network on the Si-O Bond-Breakage Energetics," in *Proceedings of the 2009 Materials Research Society (MRS) Spring Meeting*, 2009. Talk: MRS, San Francisco; 2009-04-13 – 2009-04-17.
- [27] S. Tyaginov, V. Sverdlov, W. Goes, P. Schwaha, R. Heinzl, F. Stimpfl, and T. Grasser, "Si-O Bond-Breakage Energetics under Consideration of the Whole Crystal," in *Proceedings of the International Semiconductor Technology Conference & China Semiconductor Technology International Conference (CSTIC)*, p. 84, 2009. Talk: CSTIC, Shanghai; 2009-03-19 – 2009-03-20.
- [28] T. Grasser, W. Goes, and B. Kaczer, "Towards Engineering Modeling of Negative Bias Temperature Instability," in *Defects in Microelectronic Materials and Devices*, pp. 399–436, Taylor and Francis/CRC Press, 2008, (invited).
- [29] T. Grasser, P.-J. Wagner, P. Hehenberger, W. Goes, and B. Kaczer, "A Rigorous Study of Measurement Techniques for Negative Bias Temperature Instability," *IEEE Transactions on Device and Materials Reliability*, vol. 8, no. 3, pp. 526–535, 2008.
- [30] T. Grasser, B. Kaczer, T. Aichinger, W. Goes, and M. Nelhiebel, "Defect Creation Stimulated by Thermally Activated Hole Trapping as the Driving Force Behind Negative Bias Temperature Instability in SiO₂, SiON, and High-k Gate Stacks," in *2008 IEEE International Integrated Reliability Workshop Final Report (IIRW)*, pp. 91–95, 2008. Talk: IIRW, Fallen Leaf Lake; 2008-10-18 – 2008-10-22.

- [31] W. Goes, M. Karner, V. Sverdlov, and T. Grasser, "Charging and Discharging of Oxide Defects in Reliability Issues," *IEEE Transactions on Device and Materials Reliability*, vol. 8, no. 3, pp. 491–500, 2008.
- [32] T. Grasser, B. Kaczer, and W. Goes, "An Energy-Level Perspective of Bias Temperature Instability," in *Proceedings of the 19th European Symposium on Reliability of Electron Devices, Failure Physics and Analysis (ESREF)*, 2008. Talk: ESREF, Maastricht (invited); 2008-09-29 – 2008-10-02.
- [33] S. E. Ungersböck, W. Goes, S. Dhar, H. Kosina, and S. Selberherr, "The Effect of Uniaxial Stress on Band Structure and Electron Mobility of Silicon," *Mathematics and Computers in Simulation*, vol. 79, no. 4, pp. 1071–1077, 2008.
- [34] T. Grasser, W. Goes, and B. Kaczer, "Modeling Bias Temperature Instability During Stress and Recovery," in *International Conference on Simulation of Semiconductor Processes and Devices (SISPAD) 2008*, pp. 65–68, 2008. Talk: SISPAD, Hakone; 2008-09-09 – 2008-09-11.
- [35] W. Goes, M. Karner, S. Tyaginov, P. Hehenberger, and T. Grasser, "Level Shifts and Gate Interfaces as Vital Ingredients in Modeling of Charge Trapping," in *International Conference on Simulation of Semiconductor Processes and Devices (SISPAD) 2008*, pp. 69–72, 2008. Talk: SISPAD, Hakone; 2008-09-09 – 2008-09-11.
- [36] W. Goes, M. Karner, V. Sverdlov, and T. Grasser, "A Rigorous Model for Trapping and Detrapping in Thin Gate Dielectrics," in *Proceedings 15th International Symposium on the Physical and Failure Analysis (IPFA) of Integrated Circuits*, pp. 249–254, 2008. Talk: IPFA, Singapore; 2008-07-07 – 2008-07-11.
- [37] T. Grasser, W. Goes, and B. Kaczer, "Dispersive Transport and Negative Bias Temperature Instability: Boundary Conditions, Initial Conditions, and Transport Models," *IEEE Transactions on Device and Materials Reliability*, vol. 8, no. 1, pp. 79–97, 2008, (invited).
- [38] T. Grasser, B. Kaczer, and W. Goes, "An Energy-Level Perspective of Bias Temperature Instability," in *Proceedings of the International Reliability Physics Symposium (IRPS)*, pp. 28–38, 2008. Talk: IRPS, Phoenix; 2008-04-27 – 2008-05-01.
- [39] T. Grasser, B. Kaczer, P. Hehenberger, W. Goes, R. Connor, H. Reisinger, W. Gustin, and C. Schlünder, "Simultaneous Extraction of Recoverable and Permanent Components Contributing to Bias-Temperature Instability," in *International Electron Devices Meeting (IEDM) 2007*, pp. 801–804, 2007. Talk: IEDM, Washington, DC; 2007-12-10 – 2007-12-12.
- [40] M. Karner, A. Gehring, S. Holzer, M. Pourfath, M. Wagner, W. Goes, M. Vasicek, O. Baumgartner, C. Kernstock, K. Schnass, G. Zeiler, T. Grasser, H. Kosina, and S. Selberherr, "A Multi-Purpose Schrödinger-Poisson Solver for TCAD Applications," *Journal of Computational Electronics*, vol. 6, no. 1-3, pp. 179–182, 2007.
- [41] T. Grasser, P.-J. Wagner, P. Hehenberger, W. Goes, and B. Kaczer, "A Rigorous Study of Measurement Techniques for Negative Bias Temperature Instability," in *2007 IEEE International Integrated Reliability Workshop (IIRW) Final Report*, pp. 6–11, 2007. Talk: IIRW, Fallen Leaf Lake; 2007-10-15 – 2007-10-18.

- [42] W. Goes and T. Grasser, "Charging and Discharging of Oxide Defects in Reliability Issues," in *2007 IEEE International Integrated Reliability Workshop (IIRW) Final Report*, pp. 27–32, 2007. Talk: IIRW, Fallen Leaf Lake; 2007-10-15 – 2007-10-18.
- [43] M. Karner, S. Holzer, W. Goes, M. Vasicek, M. Wagner, H. Kosina, and S. Selberherr, "Numerical Analysis of Gate Stacks," in *Physics and Technology of High-k Gate Dielectrics 4, Vol. 3 No. 3*, pp. 299–308, ECS Transactions, 2006.
- [44] M. Karner, A. Gehring, M. Wagner, R. Entner, S. Holzer, W. Goes, M. Vasicek, T. Grasser, H. Kosina, and S. Selberherr, "VSP- A Gate Stack Analyzer," *Microelectronics Reliability*, vol. 47, no. 4-5, pp. 704–708, 2007.
- [45] W. Goes and T. Grasser, "First-Principles Investigation on Oxide Trapping," in *International Conference on Simulation of Semiconductor Processes and Devices (SISPAD) 2007* (T. Grasser and S. Selberherr, eds.), (12), pp. 157–160, Springer-Verlag Wien New York, 2007. Talk: SISPAD, Wien; 2007-09-25 – 2007-09-27.
- [46] T. Grasser, W. Goes, V. Sverdlov, and B. Kaczer, "The Universality of NBTI Relaxation and its Implications for Modeling and Characterization," in *45th Annual International Reliability Physics Symposium (IRPS)*, pp. 268–280, 2007. Talk: IRPS, Phoenix; 2007-04-15 – 2007-04-19.
- [47] M. Karner, S. Holzer, M. Vasicek, W. Goes, M. Wagner, H. Kosina, and S. Selberherr, "Numerical Analysis of Gate Stacks," in *Meeting Abstracts 2006 Joint International Meeting*, 2006. Talk: Meeting of the Electrochemical Society (ECS), Cancun; 2006-10-29 – 2006-11-03.
- [48] T. Grasser, W. Goes, and B. Kaczer, "Modeling of Dispersive Transport in the Context of Negative Bias Temperature Instability," in *2006 IEEE International Integrated Reliability Workshop (IIRW) Final Report*, pp. 5–10, 2006. Talk: IIRW, S. Lake Tahoe; 2006-10-16 – 2006-10-19.
- [49] M. Karner, A. Gehring, M. Wagner, R. Entner, S. Holzer, W. Goes, M. Vasicek, T. Grasser, H. Kosina, and S. Selberherr, "VSP-A Gate Stack Analyzer," in *WODIM 2006 14th Workshop on Dielectrics in Microelectronics Workshop Program and Abstracts (WODIM)*, pp. 101–102, 2006. Talk: WODIM, Catania; 2006-06-26 – 2006-06-28.
- [50] S. Tyaginov, V. Sverdlov, I. Starkov, W. Goes, and T. Grasser, "Impact of O-Si-O Bond Angle Fluctuations on the Si-O Bond-Breakage Rate," *Microelectronics Reliability*, vol. 49, pp. 998–1002, 2009.



Curriculum Vitae

- July 24th, 1979 Born in Vienna, Austria
- Jun. 1998 High school graduation, BRG 4 Wien
Focused on natural science
Finished grades 3 and 4 with honors
- Jul. 1998 - Mar. 1999 Compulsory military service
- Oct. 1999 Enrolled in Technical Physics
at the Technical University of Vienna
- Dec. 2001 Passed 1. Diplomprüfung
at the Technical University of Vienna
- Aug. 2003 - Sep. 2003 Summer internship at the company "Bosch"
Field: development of efficient fuel-injection control
- Oct. 2004 - Jun. 2005 Engaged as a tutor for the Course
"Laboratory Work I" and "Laboratory Work II"
at the Technical University of Vienna
- Oct. 2005 Finished Diploma Thesis
Title: "Grain Boundaries in Back Contact Solar Cells"
- Nov. 2005 Passed 2. Diplomprüfung with honors
at the Technical University of Vienna
- Dec. 2005 Received degree of "Diplomingenieur" (Dipl.-Ing.),
equivalent to Master of Science (MSc), in Technical Physics
from the Technical University of Vienna
Specialization: Material Science
- Jan. 2006 Enrolled in a PhD program
at the Institute for Microelectronics, Technical University Vienna
- Apr. 2007 - May 2007 Held a position as a visiting researcher
in the group of S.T. Pantelides at the Vanderbilt University, Nashville, TN